# Understanding the Depths of Brown Dwarfs and Giant Exoplanets: Modelling Substellar Atmospheres

## Mark Phillips

Submitted by Mark Phillips to the University of Exeter as a thesis for the degree of Doctor of Philosophy in Physics, August, 2020.

I certify that all material in this thesis which is not my own work has been identified and that no material has previously been submitted and approved for the award of a degree by this or any other University.

Signed: ...................................

Mark Phillips

Date: ....03/12/2020....

**Abstract**

The absence or lack of steady hydrogen fusion in the cores of brown dwarfs means these objects cool over time by radiating away their internal thermal energy. The rate at which these objects cool is regulated by the atmosphere, which imprints its complex and changing chemical composition of molecules and condensates onto the emitted radiation. A reliable model of the atmosphere and its evolution over time therefore lies at the core of our understanding of brown dwarfs and substellar objects. Over the last decade the WISE mission has uncovered the coolest spectral type known as the Y dwarfs. These objects have effective temperatures a few times greater than Jupiter, and thus provide excellent analogs for Jovian-like worlds outside of our solar system. Accurate and reliable atmosphere and evolution models are important for placing mass and age constraints on these newly discovered objects and understanding the rich chemistry and physics taking place in their atmospheres.

In this thesis, I present a new set of solar metallicity atmosphere and evolutionary models for very cool brown dwarfs and self-luminous giant exoplanets, which is termed `ATMO` 2020. Atmosphere models are generated with the state-of-the-art 1D radiative-convective equilibrium code `ATMO`, and are used as surface boundary conditions to calculate the interior structure and evolution of $0.0005 - 0.075\,M_\odot$ objects. These models include several key improvements to the input physics used in previous models available in the literature. First, the use of a new H-He equation of state including ab initio quantum molecular dynamics calculations has raised the mass by $\sim 1 - 2\%$ at the stellar-substellar boundary and has altered the cooling tracks around the hydrogen and deuterium burning minimum masses. A second key improvement concerns updated molecular opacities in our atmosphere model `ATMO`, which now contains significantly more line transitions required to accurately capture the opacity in these hot atmospheres. This leads to warmer atmospheric temperature structures, further changing the cooling curves and predicted emission spectra of substellar objects. I present significant improvement for the treatment of the collisionally broadened potassium resonance doublet, and highlight the importance of these lines in shaping the red-optical and near-infrared spectrum of brown dwarfs.

This is highlighted through improved comparisons to the observed spectra of benchmark objects. I generate three different grids of model simulations, one using equilibrium chemistry and two using non-equilibrium chemistry due to vertical mixing, all three computed self-consistently with the pressure-temperature structure of the atmosphere. I show the impact of vertical mixing on emission spectra and in colour-magnitude diagrams, and highlight wavelength regions which can be used of infer the strength of vertical mixing in cool brown dwarfs.

# Contents

# List of Figures

# List of Tables

# Declaration

The majority of the research presented in this thesis was performed by myself in collaboration with Isabelle Baraffe, Pascal Tremblin, Gilles Chabrier, Nicole Allard, Ben Drummond, Jayesh Goyal and Eric Hébrard. Here is a breakdown of contributions for each chapter.

## Chapter 2 & 3

The `ATMO` code described in these Chapters was initially begun by Wolfgang Hayek, with major rewriting, restructuring and improvements by Pascal Tremblin. Pascal Tremblin is now the lead developer of the code, with contributions from David Amundsen, Ben Drummond, Jayesh Goyal, Eric Hébrard and myself. I have contributed model improvements and testing, including the implementation of the SCVH95 EOS, the self-consistent coupling of a chemical relaxation scheme, and the calculation of gas phase Fe opacity.

## Chapter 4

The implementation, testing and comparisons of the potassium resonance line shapes presented in this Chapter were performed by myself, with input from Isabelle Baraffe, Pascal Tremblin and Nicole Allard.

## Chapter 5

The new set of atmosphere and evolution models was developed by myself, with input from Isabelle Baraffe, Pascal Tremblin and Gilles Chabrier. Isabelle Baraffe performed the evolutionary tracks calculations, with a new EOS provided by Gilles Chabrier. I computed

the grid of atmosphere models and performed all the comparisons to other models, with input on the interpretations of the results from Isabelle Baraffe, Pascal Tremblin and Gilles Chabrier.

**Chapter 6**

The comparisons of the new atmosphere and evolution models to observational datasets were performed by myself. Observational datasets were provided by Trent Dupuy and Sandy Leggett. The results were interpreted by myself, with input from Isabelle Baraffe, Pascal Tremblin and Gilles Chabrier.

# Acknowledgements

First and foremost, I would like to extend my thanks and gratitude to my PhD supervisor, Isabelle Baraffe. Isabelle has provided excellent guidance and support since the day I started in Exeter, and without her this work would not have been possible. I would also like to thank Pascal Tremblin, who throughout my PhD has always had time to explain things clearly to me and come to my rescue in early battles with ATMO. Similarly, I thank Ben Drummond and Jayesh Goyal, who spent many hours working with me at the start of my PhD helping me get started and debugging code. I have enjoyed being a part of the Exeter Exoplanet Theory Group, for which I thank Nathan Mayne and everyone involved, for cultivating an exciting and inclusive group to work in. I thank my PhD examiners Sasha Hinkley and Beth Biller for diligently reading my thesis and providing insightful comments on the manuscript.

I have enjoyed my time immensely in the Exeter Astrophysics Group, for which I thank everyone within it, both past and present. The countless tea breaks, crosswords, movie nights, game nights and pub trips have given me many fond memories, and helped me through the ups and downs of a PhD. In particular, my G27 office buddies - Aarynn Carter, Adam Finley, Brendan Retter and Tom Bending - have given me more laughs, excellent lunches and office merchandise than I could have ever hoped for. Thanks also to Angie Breimann, who helped me keep my resolve and gave me the support needed to finish this thesis in such uncertain and difficult times.

Lastly, my biggest thanks go to my family, my Mom Angela, Dad Richard and brother David. For as long as I can remember, they have supported and encouraged me unconditionally in everything I do. I am incredibly fortunate for this, and I owe them any success I have.

This work would not have been possible without the support of the people mentioned here. I dedicate this thesis to them.

Mark W. Phillips

Exeter, U.K.

3rd December 2020

# Chapter 1

# Introduction

Brown dwarfs are star-like objects with insufficient mass to sustain hydrogen fusion within their cores. The absence or lack of steady fusion means these objects cool over time by radiating away their internal thermal energy. This cooling leads to a degeneracy in mass, age and luminosity i.e. a relatively young, low mass object can have an equivalent luminosity to an older, higher mass object. This degeneracy makes the fundamental properties of brown dwarfs, particularly isolated field objects, difficult to determine. The rate at which brown dwarfs cool is regulated by the atmosphere, which imprints its complex and changing chemical composition of molecules and condensates onto the emitted radiation, forming the M-L-T-Y spectral sequence (Kirkpatrick 2005; Helling & Casewell 2014). A reliable model of the atmosphere and its evolution over time therefore lies at the core of our understanding of brown dwarfs and substellar objects.

Understanding the atmospheres of brown dwarfs has further motivation since the physics, chemistry, and composition is shared with giant extra-solar planets (exoplanets) (Burrows et al. 2001), meaning useful analogies can be drawn between these objects. Over the last decade the WISE mission (Wright et al. 2010) has uncovered the coolest brown dwarfs (known as the Y dwarfs; Cushing et al. 2011; Kirkpatrick et al. 2012), including the coldest known brown dwarf at $T_{\text{eff}} \sim 250\,\text{K}$ just $2\,\text{pc}$ from the sun (Luhman 2014). These objects have effective temperatures a few times greater than Jupiter ($T_{\text{eff}} \sim 124\,\text{K}$), providing excellent analogues for Jovian-like worlds outside of our solar system, and have

proved challenging for atmosphere models (Morley et al. 2018; Leggett et al. 2019). On-going projects are likely to discover more objects in this temperature range (e.g. Marocco et al. 2019; Meisner et al. 2020) that will become amenable to characterisation with future instrumentation such as the *James Webb Space Telescope* (Gardner et al. 2006).

In this thesis, I present my work on developing a state-of-the-art grid of atmosphere and evolution models for substellar objects, which encompass brown dwarfs and giant exoplanets. The new models aim to improve our understanding of these cool atmospheres and their evolution over time, and provide a toolkit for studying and characterising new discoveries of the coldest brown dwarfs and exoplanets. Ultimately, I hope this work contributes in some small way towards the grander question of whether our solar system is unique in the Universe.

I begin this thesis by first reviewing the history of the prediction and detection of the first brown dwarfs, as well as detailing the evolution of their main properties throughout their lifetime in Section 1.1. I then discuss the main observed features of brown dwarfs and giant exoplanets as they cool over time in Section 1.2, and assess our current under-standing and methods for modelling the physics driving these observations in Section 1.3. In Section 1.4 I provide the aims of this work. Finally, in Section 1.5 I give an overview of the structure of the chapters in this thesis, and provide my statement of contribution to publications in Section 1.6.

## 1.1 History and physical properties of brown dwarfs

### 1.1.1 The prediction of brown dwarfs and the hydrogen burning limit

Stars form through the gravitational collapse of gas and dust in cold interstellar clouds. As the cloud contracts it heats, radiating away energy until the central region is sufficiently dense to trap radiation. The temperature and density in the core of the forming star then increase over time until the conditions are hot and dense enough to fuse hydrogen into helium. The energy released from these thermonuclear reactions prevents further con-traction, and balances the energy radiated away from the stellar surface. This steady state configuration of hydrogen burning is known as the main-sequence stage of a star's life-

time.

It was first predicted by Kumar (1963) that electron degeneracy can play a key role in the cores of low mass contracting stars, and prevent objects of sufficiently low mass reaching the main sequence. This degeneracy occurs because electrons obey the Pauli exclusion principle, preventing them from occupying the same quantum state simultaneously and forcing them to occupy states of non-zero momentum even at absolute zero. This therefore provides a degeneracy pressure that in the dense core of a low mass forming star can prevent further gravitational collapse and hence the temperatures rising to that required for hydrogen burning. Kumar (1963) therefore proposed that there exists a hydrogen burning minimum mass (HBMM) of star formation due to the onset of electron degeneracy. Early calculations of the HBMM found its value to be $0.08\,M_\odot$ (Hayashi & Nakano 1963), while later calculations revised this value to be $\sim 0.07\,M_\odot$, dependent on metallicity (Chabrier et al. 2000b). The exact value of the HBMM is still being revised today, with improvements in the equation of state and the effect of metals altering the predicted value (Fernandes et al. 2019; Phillips et al. 2020b).

The absence or lack of steady hydrogen fusion in the cores of objects below the HBMM means that they will not attain a steady state like main sequence stars, and they will cool over time by radiating away their internal thermal energy. These objects were originally termed 'black' or infrared dwarfs, owing to their low observable luminosity, and the peak in emission moving to infrared wavelengths as they cool throughout their lifetime. The term 'brown' dwarf was first introduced by Tarter (1975), and has become the widely accepted term for star-like objects that do not sustain stable hydrogen burning.

### 1.1.2 The discovery of the first brown dwarfs

The search for the first unambiguous brown dwarfs proved a long and arduous process, as technology was not initially sensitive to their faint infrared emission. Searches focused on young clusters and star forming regions, in an effort to detect brown dwarfs when they are at their warmest and brightest, and hence most observable. The problem with this is that young brown dwarfs can have temperatures and luminosities similar to low mass main-sequence stars, making them difficult to distinguish between. It was first proposed

by Rebolo et al. (1992) that the detection of the element lithium (Li) can be used to distinguish a brown dwarf from a low mass star. Low mass stars are expected to be completely depleted in Li due to nuclear burning within $\sim 100\,\mathrm{Myr}$, whilst the cores of most brown dwarfs do not reach sufficient temperatures, and thus retain Li (Dantona & Mazzitelli 1985; Nelson et al. 1993). Therefore, for an age at which all main sequence stars have depleted their Li, it should only be found in objects of a substellar nature. This 'lithium test' was successfully used to confirm the first brown dwarfs in the Pleiades cluster, Teide 1 (Rebolo et al. 1995; Rebolo et al. 1996) and PPl 15 (Basri et al. 1996).

Concurrently to the brown dwarfs confirmed in the Pleiades, an extremely cool, red object was discovered orbiting the star Gliese 229 (Nakajima et al. 1995). The extremely faint luminosity implied that its companion, Gliese 229B, was a brown dwarf with a temperature of $\leq 1200\,K$. A further measurement of the near-infrared emission spectrum of Gl 229 B revealed absorption features attributable to methane (Oppenheimer et al. 1995), similar to that seen in Jupiter's emission. Since methane becomes stable at temperatures below $\sim 1200\,\mathrm{K}$, this unequivocally confirmed the substellar nature of Gl 229 B, and signalled that an entirely new class of astronomical object was now amenable to observational characterisation from Earth.

Remarkably, the discovery of the first methane brown dwarf Gl 229 B was announced at the same time as the detection of the first extra-solar planet orbiting a sun-like star (Mayor & Queloz 1995). The study and characterisation of over 2000 brown dwarfs and exoplanets has followed these discoveries, bridging the gap between stellar and planetary astrophysics. The brown dwarf and exoplanet fields have evolved in parallel, as both classes of object are governed by the same physics, chemistry and compositions (Burrows et al. 2001), meaning useful analogies can be drawn between these objects. Brown dwarfs can be most readily compared to giant exoplanets discovered at wide-separations (>30AU) from their host stars through high contrast adaptive optics imaging (Bowler 2016; Biller & Bonnefoy 2018). These directly imaged planets have atmospheres unaffected by host star irradiation, and therefore cool throughout their lifetimes similarly to field brown dwarfs.

### 1.1.3 Brown dwarf evolution

Figure 1.1 shows an artists view of some of the first discovered brown dwarfs compared to the Sun, a low mass red dwarf star Gliese 229 A, and the planet Jupiter. This graphic serves to illustrate several fundamental characteristics of brown dwarfs. First, the absence of a stable internal energy source means brown dwarfs cool over time by radiating away their internal energy. This leads to a degeneracy between mass, age and luminosity, which makes the fundamental properties of brown dwarfs hard to determine. For example, a relatively young, low mass object can have an equivalent luminosity to an older, higher mass object. Despite having similar masses, the young brown dwarf Teide 1 is significantly warmer and slightly larger than its older counterpart Gliese 229 B. Second, after an early contraction phase, all brown dwarfs have roughly the same size of $\sim 1$ Jupiter radius, regardless of their mass. This is brought about by the quantum mechanical effects of electron degeneracy within the cores brown dwarfs. Thus, Gliese 229B, WISE 1828 and Jupiter can be seen in Fig. 1.1 as having the same size, despite having masses ranging up to tens of Jupiter masses. Finally, the true colour of brown dwarfs as seen by the human eye is in fact not brown, and ranges from red to magenta, to a deep purple in the coldest objects. This is illustrative of the atmospheres of brown dwarfs imprinting complex and changing chemical compositions onto the emitted radiation, creating an ever-changing spectral appearance as they cool over time. It is in fact the broad absorption of the alkali metals sodium and potassium that give the coolest brown dwarfs their purple hue, as depicted in Fig. 1.1.

To more quantitatively review these characteristics of isolated substellar objects, Figures 1.2 through 1.6 show the evolution of the luminosity ($L$), core temperature ($T_c$), radius ($R$), effective temperature ($T_{\text{eff}}$) and surface gravity ($g$) as a function of age. In these Figures, objects in the mass range $0.001 - 0.2\,M_\odot$ (or approximately $1 - 200\,M_{\text{Jup}}$) are shown with colour coding based on the approximate hydrogen and deuterium burning limits ($\sim 0.075\,M_\odot$ and $0.012\,M_\odot$ respectively). It should be noted that this colour coding serves primarily to guide the eye, and should not be taken as indicative of what constitutes a planet or brown dwarf. While the deuterium burning minimum mass ($\sim 13\,M_{\text{Jup}}$) has been utilised as a dividing line between planets and brown dwarfs, a more physi-
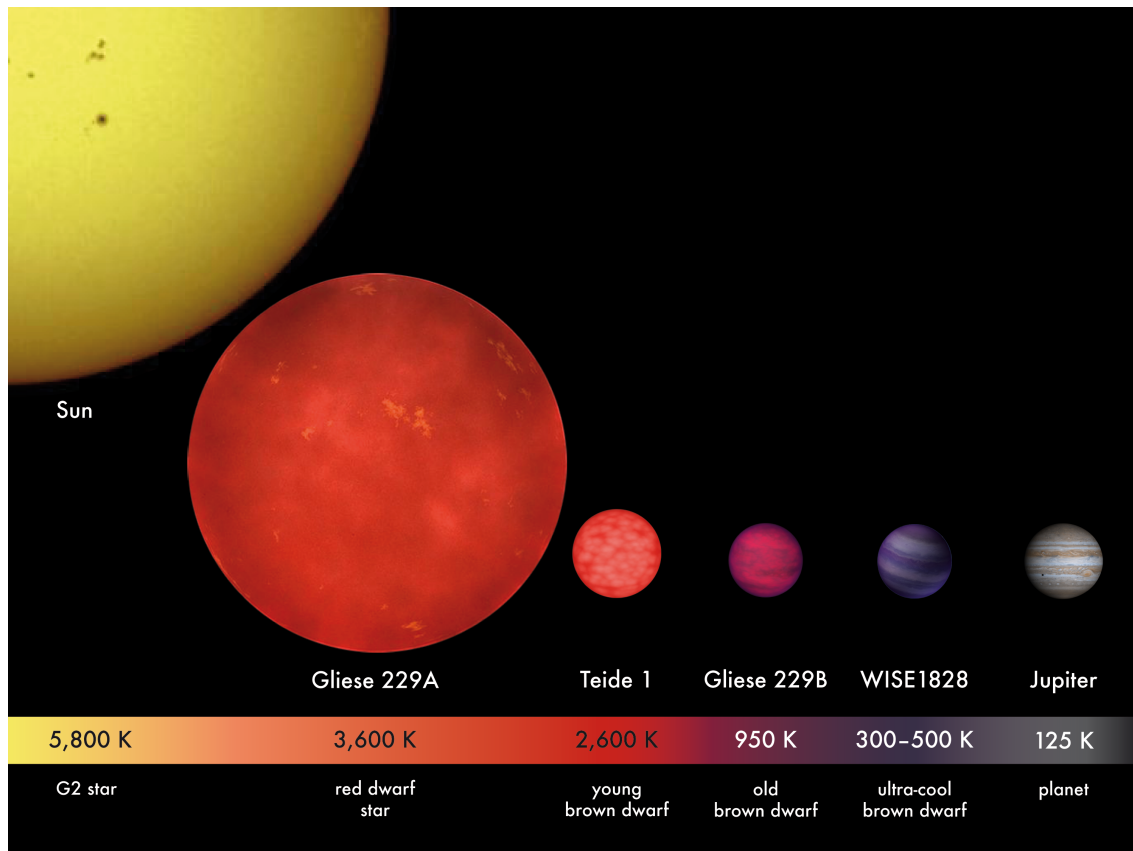
**Figure 1.1:** Illustration of the relative sizes, appearances and temperatures of the Sun, the M dwarf star Gliese 229A, the young brown dwarf Teide 1, the old brown dwarf companion Gliese 229B, one of the coldest brown dwarfs WISE 1828 Cushing et al. (2011), and Jupiter. The graphic was rendered using NASA satellite images (Sun, Jupiter) and NASA artist work (Gliese 229A+B, Teide 1, WISE 1828) and is taken from Joergens (2014) (Copyright MPIA/V. Joergens).

cally motivated way of distinguishing between the two objects is based on their formation (Schlaufman 2018). Objects forming through the collapse of interstellar material should be considered brown dwarfs, and objects forming through accretion in protostellar disks should be considered planets. Despite difficulties in determining the formation pathway of a substellar object, this is widely accepted to be the defining difference between planets and brown dwarfs.

The evolutionary tracks shown here are from the solar metallicity calculations of Burrows et al. (1997), and the Figures are based on those presented in Burrows et al. (2001). Evolutionary calculations from other authors exist in the literature (e.g. Chabrier et al. (2000b); Baraffe et al. (2003); Saumon & Marley (2008); Fernandes et al. (2019); Phillips et al. (2020b)), however these calculations differ minimally in the broad characteristics of brown dwarf evolution discussed in this Section. For further reading, the evolution of

brown dwarfs and giant planets is reviewed in more detail in Chabrier & Baraffe (2000); Burrows et al. (2001).

Figure 1.2 shows the luminosity of a given mass of object as a function of age. The luminosity is the amount of radiated power from the object's surface, and is often quoted in solar units. The luminosity of low-mass stars and brown dwarfs initially decreases over time at early stages in their evolution, as they contract after formation. In low-mass stars above the HBMM, i.e. $\geq 0.075\,M_\odot$, the core thermonuclear power eventually balances the photon radiative losses from the surface, stabilising the object's luminosity during the main sequence. This can be seen in Figure 1.2 for blue coloured lines representing low-mass stars above the HBMM, whereby the luminosity remains constant at later ages of $\geq 0.1 - 1\,Gyr$ depending on mass. In brown dwarfs below the HBMM, the absence or lack of steady hydrogen fusion means they cool over time becoming gradually less luminous. This can be seen in Figure 1.2 for orange and green coloured lines representing brown dwarfs and giant planets, whereby the luminosity continually decreases throughout their lifetimes.

Also shown in Fig. 1.2 are the ages at which a given mass has depleted 90% of its initial lithium and deuterium abundances through nuclear burning. Objects more massive than $\sim 0.06\,M_\odot$ will burn lithium, and objects more massive than $\sim 0.012\,M_\odot$ will burn deuterium. As discussed in Section 1.1.2, the presence of Li in sufficiently low-mass brown dwarfs can be used to distinguish them from low-mass stars through the 'lithium test'. Similarly, the presence of deuterium in the atmospheres of young brown dwarfs has been proposed as a method of inferring the mass and age of brown dwarfs (Chabrier et al. 2000a; Morley et al. 2019). Deuterium burning roughly stabilises the luminosity $L$ and radius $R$ of brown dwarfs with ages between $1\,Myr$ and $100\,Myr$ depending on mass. While deuterium does influence the evolution of young objects, it is not so abundant that its effects are as dominant as hydrogen burning in low mass stars. Most objects will have burnt the majority of their initial deuterium abundance by $\sim 100\,Myr$, with higher mass objects burning deuterium quicker (Burrows et al. 2001).

Figure 1.3 shows the evolution of the core temperature of a given object mass as a function of age. The gravitational contraction of low-mass stars and brown dwarfs leads to
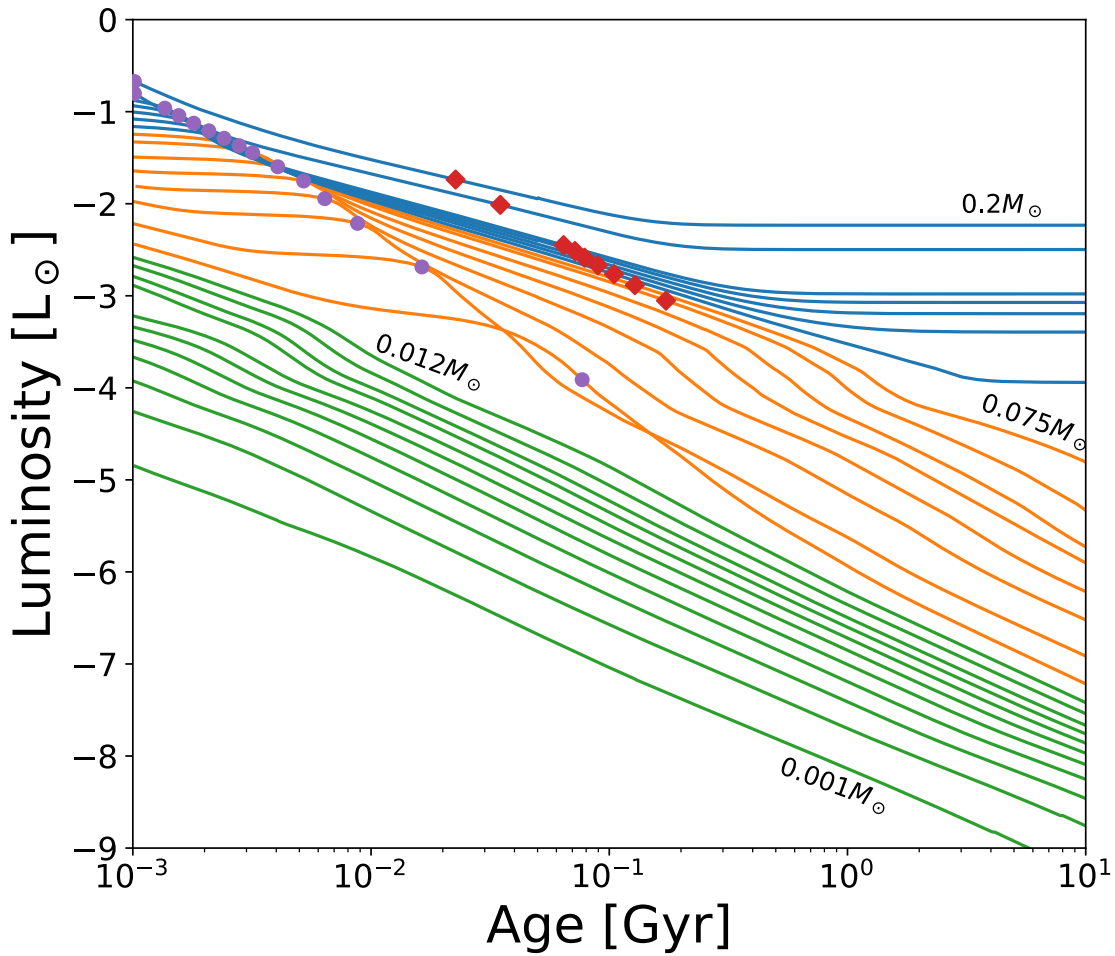
**Figure 1.2:** Evolution of the luminosity of low-mass stars and substellar objects as a function of age. Stars are shown in blue, brown dwarfs with masses $\leq 0.07\,M_\odot$ and above $> 0.012\,M_\odot$ are shown in orange, and brown dwarfs/giant planets with masses $\leq 0.012\,M_\odot$ are shown in green. These colour categories should be considered arbitrary, and are based on the approximate hydrogen and deuterium burning mass regimes. Red diamonds and purple circles indicate the ages at which a given mass has depleted 90% of the initial lithium and deuterium abundances respectively. The masses shown here, from top to bottom are, 0.001, 0.002, 0.003, 0.004, 0.005, 0.006, 0.007, 0.008, 0.009, 0.01, 0.012, 0.015, 0.02, 0.03, 0.04, 0.05, 0.06, 0.07, 0.075, 0.08, 0.085, 0.09, 0.095, 0.1, 0.15 and $0.2\,M_\odot$. Note that $0.001\,M_\odot \sim 1\,M_{\text{Jup}}$. Figure inspired by Fig. 1 of Burrows et al. (2001).

a steady increase in their core temperatures and densities. For objects above the HBMM, the temperatures and densities eventually reach that required to drive thermonuclear reactions fusing hydrogen to helium. The power derived from this nuclear burning balances the surface radiative losses, preventing further contraction and causing the core temperatures to remain constant for the rest of the object's lifetime. In brown dwarfs below the HBMM, the core becomes electron degenerate before the temperature reaches that required for thermonuclear power to balance the surface radiative losses, causing the core temperature to then decrease gradually over time.
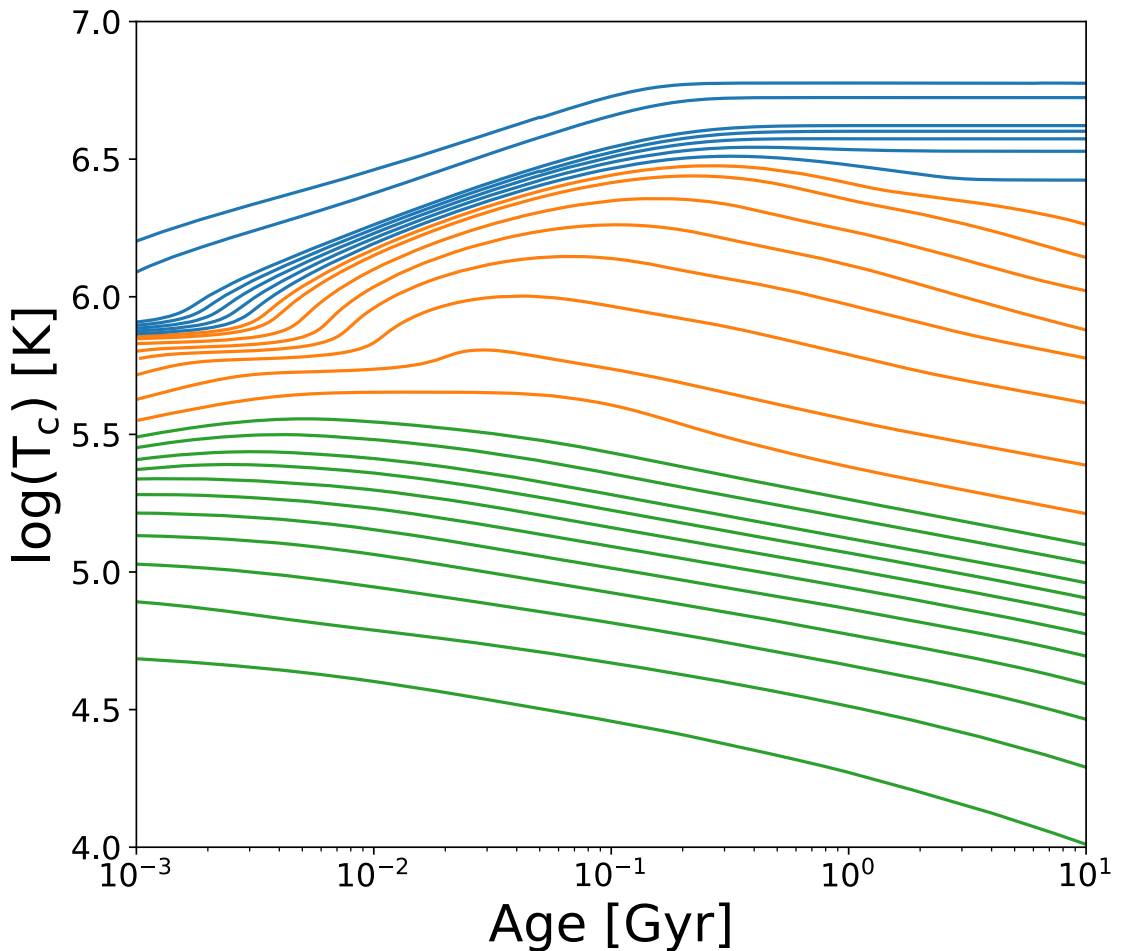
**Figure 1.3:** Evolution of the core temperature of low-mass stars and substellar objects as a function of age. The colour coding and mass-range is the same as in Fig. 1.2.

Figure 1.4 shows the evolution of the radius of a given mass of object as a function of age. At early ages in a substellar object's lifetime, the radius is a monotonically increasing function of mass, which decreases as a function of age as the object contracts after formation. Early plateaus in the radius of brown dwarfs coincide with deuterium burning. At later ages, the radii cluster around a value of $1R_{\text{Jup}}$ for objects spanning approximately $1 - 2$ orders of magnitude in mass between 0.001 and 0.075 $M_\odot$. Furthermore, within this clustering the dependence of the radius on mass reverses, with lower mass objects having larger radii. This is due to the competition of Coulomb and electron degeneracy effects in the equation of state. Coulomb forces set the mass-radius relationship as $R \propto M^{\frac{1}{3}}$, whereas electron degeneracy sets the relationship as $R \propto M^{-\frac{1}{3}}$. The interplay of these relationships cause the radii of brown dwarfs and giant planets to become independent of mass to within $\sim 30\%$ of the radius of Jupiter (Burrows et al. 2001).
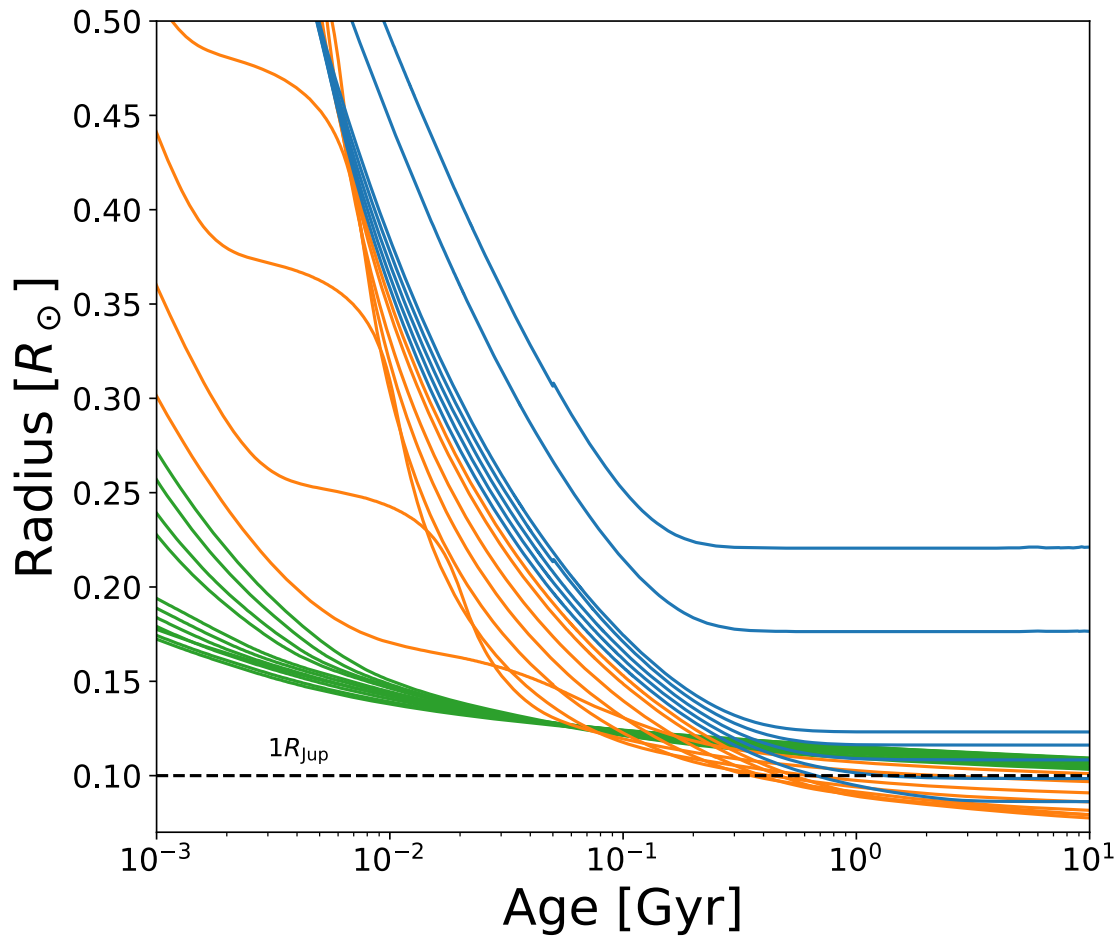
**Figure 1.4:** Evolution of the radius (in solar units) of low-mass stars and substellar objects as a function of age.  The colour coding and mass-range is the same as in Fig. 1.2.  The dashed black line shows the radius of Jupiter (1 $R_{Jup} \approx 0.1\,R_{\odot}$).

Figure 1.5 shows the evolution of the effective temperature of a given mass of object as a function of age.  The effective temperature is related to the luminosity of an object through the Stefan-Boltzmann law ($L \propto R^2 T_{eff}^4$), and thus a small drop in $T_{eff}$ leads to a large drop in $L$.  The $T_{eff}$ of low-mass stars eventually stabilises at late stages in their evolution, whereas the $T_{eff}$ of brown dwarfs and giant planets continuously decreases throughout their lifetime.  The continual decrease of $T_{eff}$ is the primary driver of chemical changes in the atmosphere that become imprinted onto the emitted thermal radiation.  These spectral imprints form a sequence characterised by the $M$, $L$, $T$ and $Y$ spectral types, and Fig. 1.5 is divided to indicate the approximate $T_{eff}$ ranges of these spectral types.  The defining features of these spectral types is discussed in detail in Section 1.2.1.

Finally, Fig. 1.6 shows the evolution of the surface gravity and effective temperature
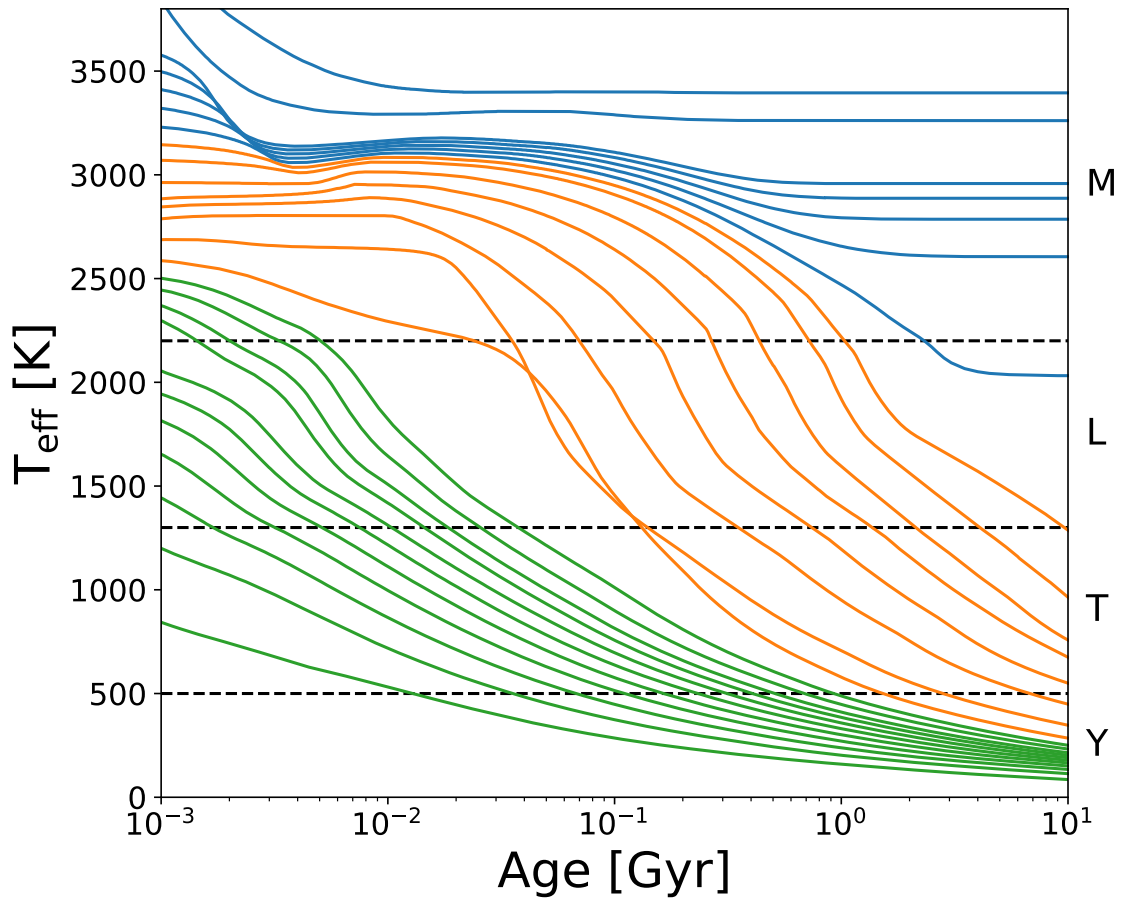
**Figure 1.5:** Evolution of the effective temperature of low-mass stars and substellar objects as a function of age. The colour coding and mass-range is the same as in Fig. 1.2. Dashed black lines divide the Figure into the approximate $T_{\text{eff}}$ ranges of the *MLTY* spectral sequence, as discussed in Section 1.2.1.

as a function of age. The surface gravity is related to the radius and mass of an object as $g \propto MR^{-2}$. The evolution in this Figure proceeds from right to left, as brown dwarfs and planets start with high $T_{\text{eff}}$ and low $g$, and then cool and contract moving to lower $T_{\text{eff}}$ and higher $g$. Brown dwarfs quickly increase their surface gravity during the deuterium burning phase, whereas lower mass objects which do not burn deuterium contract over a longer period of time, and thus increase their surface gravity more slowly. When brown dwarfs are young, they have similar surface gravities ($\log(g) \sim 3.5-4.0$) to planetary mass objects, making them ideal analogues to understand giant exoplanets. Furthermore, Fig. 1.6 illustrates that by knowing the $T_{\text{eff}}$ and $g$ of a brown dwarf can break the degeneracy between mass, age and luminosity.
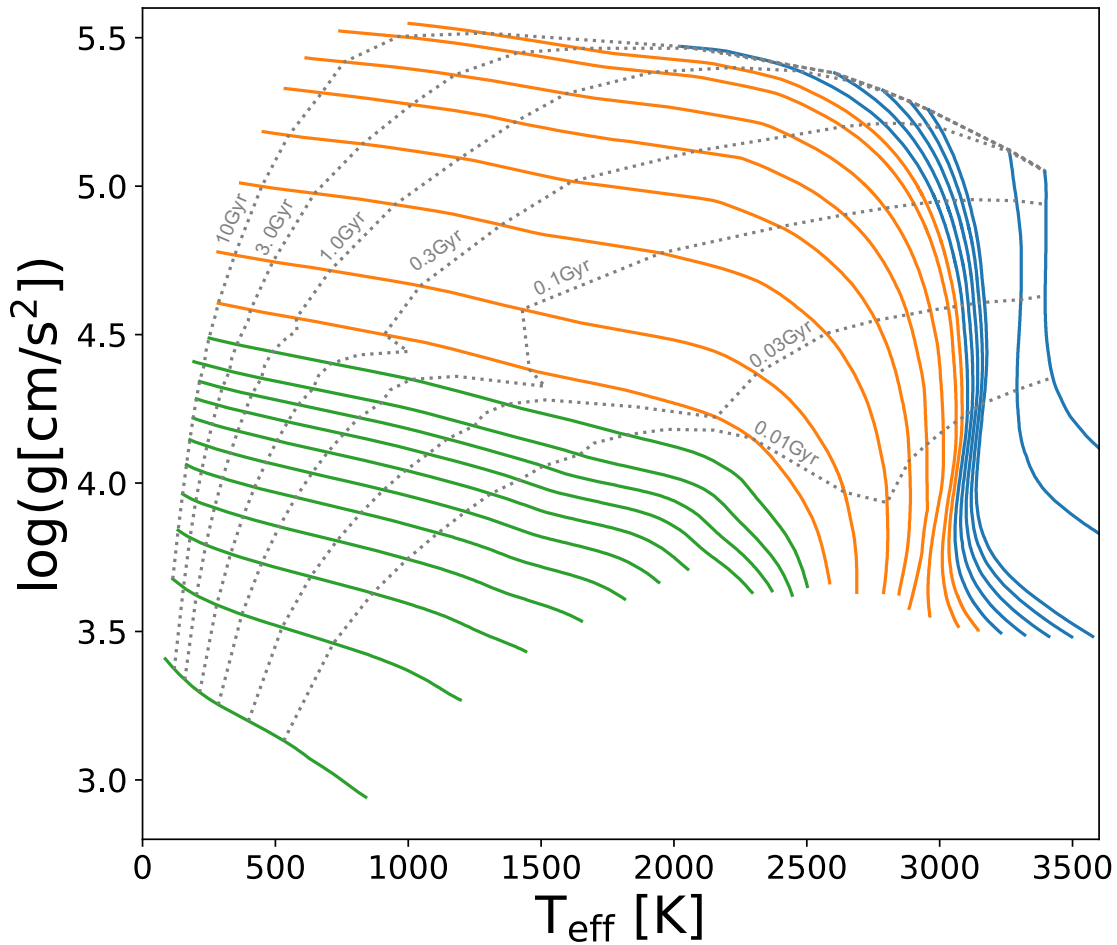
**Figure 1.6:** Evolution of the surface gravity and effective temperature of low-mass stars and substellar objects. The colour coding and mass-range is the same as in Fig. 1.2. Dotted grey lines are isochrones with ages as indicated on the plot.

## 1.2   Observations of the brown dwarf cooling sequence

### 1.2.1   The spectral sequence

Astronomers classify stars based on their emission spectra.  A star is assigned a letter out of OBAFGKM to indicate its spectral type, with O representing the hottest and M the coolest objects. This system is used to spectrally classify stellar objects, and is known as the MK system (Morgan & Keenan 1973).  M dwarf stars are classified as such based on the strength of the molecular absorption bands of titanium and vanadium oxide (TiO and VO respectively) in the red-optical emission spectra ($\sim 0.6 - 0.9\,\mu$m) (Kirkpatrick et al. 1991).  During the search for brown dwarfs, an early candidate displayed a spectrum lacking in the prominent in the TiO and VO absorption features characteristic of *M* dwarfs (Kirkpatrick et al. 1993).  Furthermore, one of the first confirmed brown dwarfs, Gl 229 B,

displayed methane absorption features in its near-infrared spectrum (Oppenheimer et al. 1995, 1998), a feature indicative of a planetary atmosphere rather than a stellar atmosphere. These observations hinted that the spectra of brown dwarfs differ from that of M dwarfs, and that at least one new spectral class would be needed to classify these objects.

Shortly after the first confirmed brown dwarfs in 1995, three surveys observing large areas of the sky at red-optical and near-infrared wavelengths began, allowing astronomers to detect and spectrally characterise hundreds of brown dwarfs. These surveys were 2MASS (Two Micron All Sky Survey) (Skrutskie et al. 1997), DENIS (Deep Near Infrared Southern Sky Survey) (Epchtein et al. 1997), and SDSS (Sloan Digital Sky Survey) (York et al. 2000). Observations by these surveys led to the development of two new spectral classes for brown dwarfs; the L and T spectral classes. More recently, the launch of the WISE (Wide field Infrared Survey Explorer) mission (Wright et al. 2010) has led to the discovery of the coldest brown dwarfs known, which have been assigned the Y spectral type. The MLTY spectral sequence is subdivided with numbers ranging from $0 - 9$, with e.g. L0 denoting the hottest L dwarfs and L9 the coolest. In this Section, I discuss the spectral characteristics of this sequence, and show the main observed features from red-optical to mid-infrared wavelengths in Figures 1.7 through 1.10.

A red-optical spectral classification scheme of L dwarfs was presented by Kirkpatrick et al. (1999) based on 2MASS discoveries. A red-optical classification scheme for T dwarfs was similarly presented by Burgasser et al. (2003b). The red-optical spectral sequence from early L dwarfs to late T dwarfs is shown in Figure 1.7. These spectra contain a mixture of atomic and molecular absorption features, including neutral alkali lines (Na I, K I, Rb I and Cs I), oxide bands (TiO and VO) and hydride bands (MgH, CaH, CaOH, CrH and FeH). The TiO and VO absorption features can be seen weakening in progressively cooler L dwarfs and have disappeared by the mid L5 spectrum (Martin et al. 1997; Kirkpatrick et al. 1999), while the neutral alkali lines and hydride bands strengthen. By late L and early T spectra, the hydride bands begin to weaken and $H_2O$ absorption bands appear in the spectrum while the alkali lines remain strong. $H_2O$ becomes a prominent absorber and the Na I and K I lines continue to strengthen throughout the T type sequence, becoming so broad they dominate throughout the red-optical.
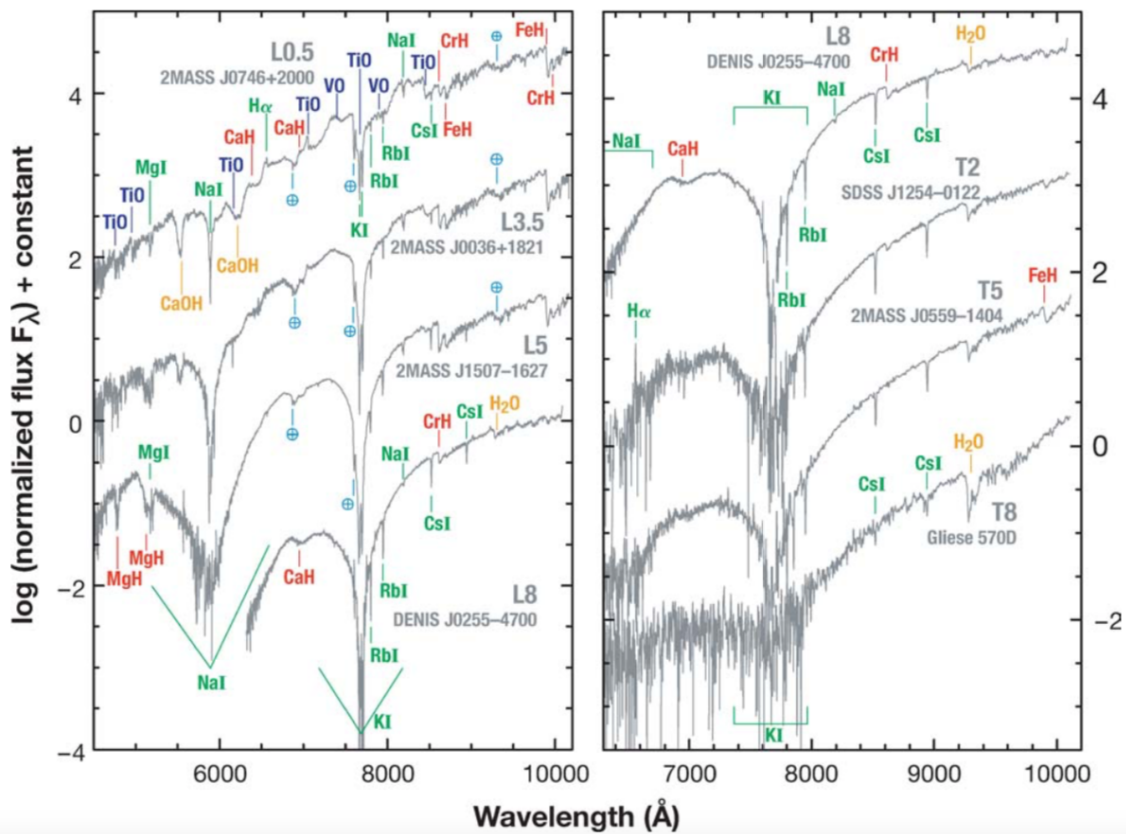
**Figure 1.7:** Red-optical spectral sequence of L and T type brown dwarfs. Neutral alkali lines are indicated by green annotations, oxides in yellow and hydrides in red. Figure from Kirkpatrick (2005).

The peak of the blackbody spectrum for L and early-mid T dwarfs lies in the near-infrared ($\sim 1.0 - 2.4\,\mu$m), and thus a spectral classification scheme at these wavelengths would be optimal. Kirkpatrick et al. (2010) and Burgasser et al. (2006) presented unified near-infrared spectral classification schemes for L and T dwarfs respectively. The near-infrared MLT spectral sequence is shown in Figure 1.8. The near-infrared spectra of L dwarfs is qualitatively similar to M dwarfs in that it is shaped by $H_2O$ and CO absorption bands, which increase in strength along the ML sequence. At short wavelengths between $0.95 - 1.35\,\mu$m, there are strong FeH bands along with neutral atomic lines from Na I, K I, Fe I, Al I and Ca I. These features can be seen in more detail in Figure 4 of Kirkpatrick (2005). $CH_4$ absorption features appear in the T dwarf spectra, which is the defining characteristic of this spectral class. The $CH_4$ and $H_2O$ bands deepen along the T sequence, shaping the spectrum into defined flux peaks by the latest T-type. The red wing of the K I resonance line shapes the short-wavelength side of the $1.05\,\mu$m flux peak, and collisionally induced absorption from $H_2$ flattens the $2.08\,\mu$m flux peak in the late T8 spectrum.
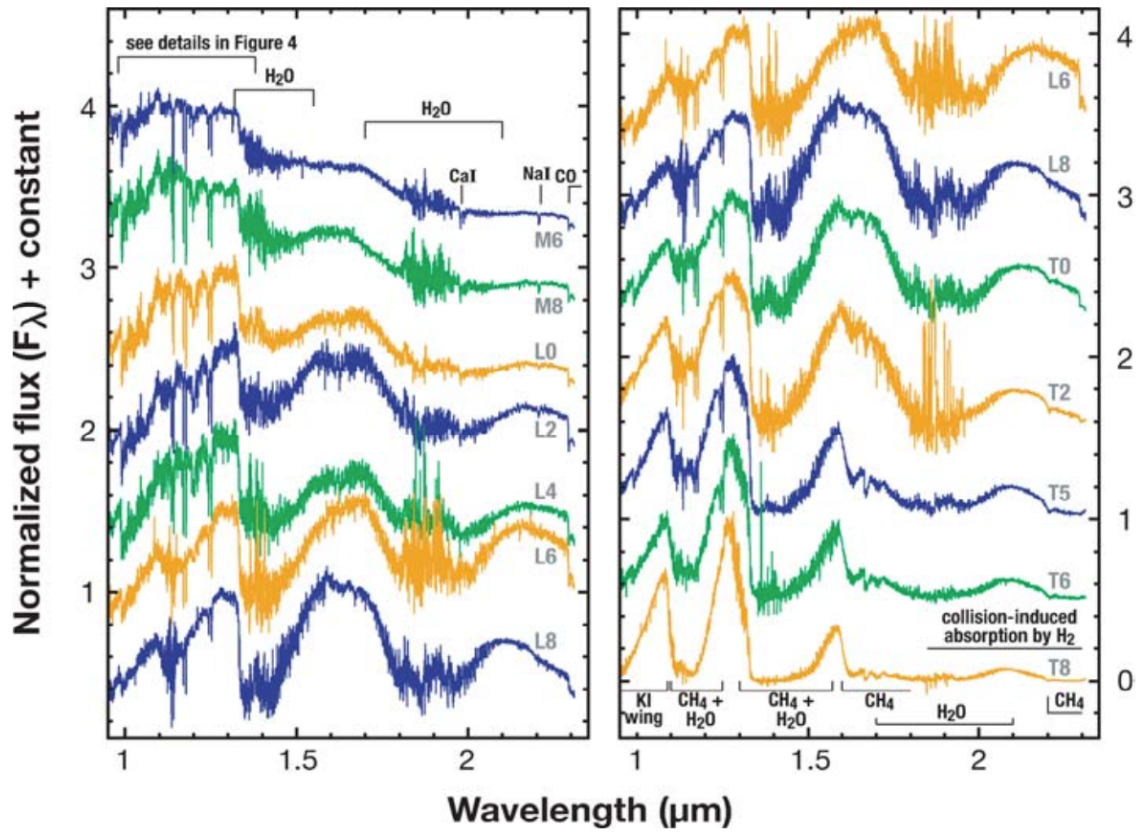
**Figure 1.8:** Near-infrared spectral sequence of M, L and T type dwarfs. Figure from Kirkpatrick (2005).

At longer wavelengths, $L-$band $(2.9 - 4.1 \, \mu m)$ and $M-$band $(4.5 - 5.0 \, \mu m)$ spectra of brown dwarfs have been obtained by Cushing et al. (2005); Leggett et al. (2019); Miles et al. (2020). These spectra have demonstrated the onset of a $CH_4$ absorption feature at $\sim 3.3 \, \mu m$ in mid-L dwarfs, which strengthens and dominates the $3.1 - 4.0 \, \mu m$ spectral region in T and Y dwarfs, as seen in Fig. 1.9. Carbon monoxide absorption is also seen peaking at $\sim 4.7 \, \mu m$, and is shown in the T6.5 object in Fig. 1.9.

The *Spitzer* space telescope has provided $5 - 15 \, \mu m$ spectra of a small sample of objects (Roellig et al. 2004; Cushing et al. 2006), as shown in Fig. 1.10. $M-$dwarf $5 - 15 \, \mu m$ spectra are relatively featureless with $H_2O$ the sole observed absorber in this wavelength range. The $H_2O$ absorption feature strengthens along the L sequence with $CH_4$ absorption features appearing by mid-L types. These features continue to strengthen in the $5 - 15 \, \mu m$ spectra of T dwarfs, with a strong $NH_3$ feature appearing between $10 - 11 \, \mu m$ in late T dwarf objects.

A comprehensive spectral classification scheme for $Y$ type brown dwarfs similar
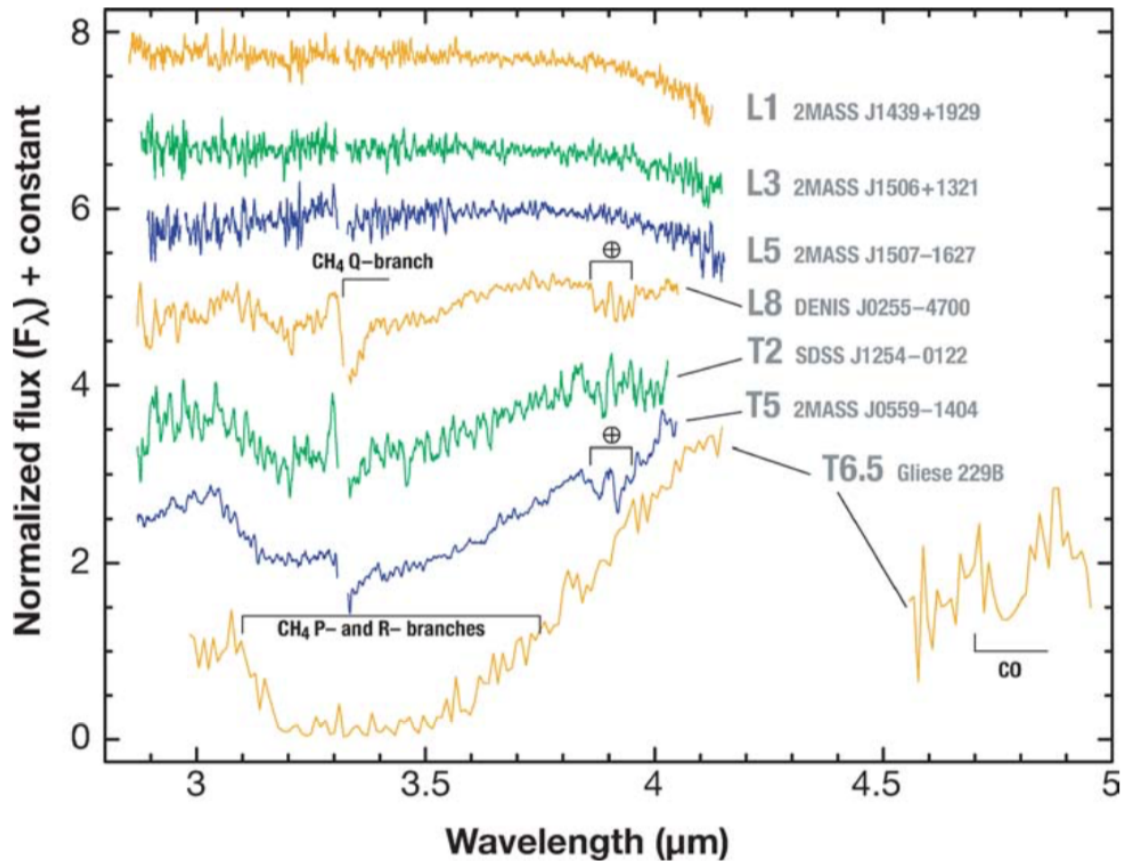
**Figure 1.9:** $L-$ and $M-$band spectra of $L$ and $T$ type brown dwarfs from Cushing et al. (2004) and Oppenheimer et al. (1998). Figure from Kirkpatrick (2005).

to the L and T dwarfs has yet to be developed. This due to their extremely faint nature making them challenging to detect and spectrally characterise. Nevertheless, Cushing et al. (2011) and Kirkpatrick et al. (2012) presented the first Y dwarfs and prototype Y0, Y1 and Y2 spectral standards based on observed ammonia absorption in the near-infrared ($\sim 1.0 - 2.4\,\mu$m), which was a long predicted hallmark of this spectral class (Burrows et al. 2003). While spectral classification in the near-infrared is useful, mid-infrared wavelengths increase in importance for and T and Y dwarf objects as the peak of the blackbody spectrum moves to ever longer wavelengths with decreasing temperature. Indeed, objects with $T_{\text{eff}} < 500\,$K emit around 50% of their flux through the $3.5 - 5.5\,\mu$m opacity window (Leggett et al. 2017), and thus a spectral sequence at these wavelengths would be optimal. The next generation of telescopes and instrumentation will be crucial for characterising and developing a comprehensive classification scheme for Y dwarfs. The *James Webb Space Telescope* (*JWST*) will be particularly suited for this, given its large aperture and increased sensitivity over existing instrumentation, along with its broad wavelength
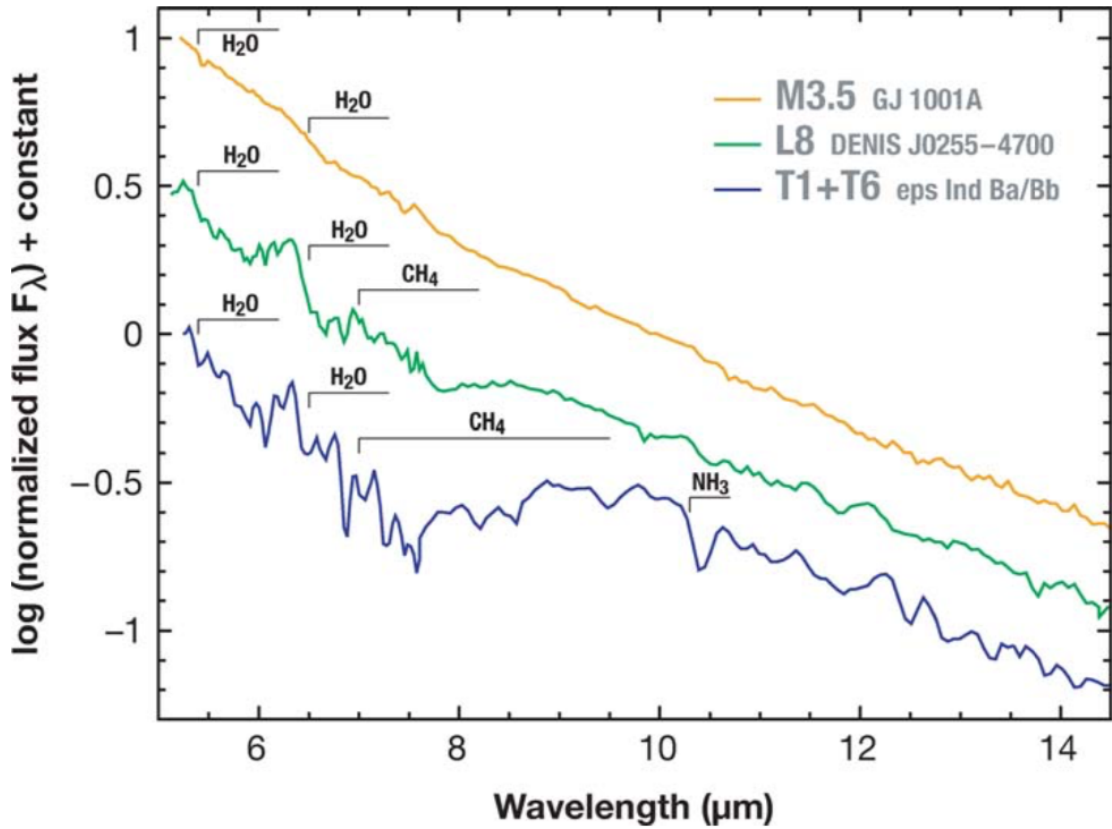
**Figure 1.10:** $5 - 15\,\mu$m *Spitzer* IRS spectra from Roellig et al. (2004) of *M*, *L* and *T* dwarfs. Figure from Kirkpatrick (2005).

coverage $(1 - 26\,\mu$m) (Gardner et al. 2006).

### 1.2.2 The spectral sequence in colour-magnitude diagrams

The brown dwarf spectral sequence can be represented photometrically in colour-magnitude diagrams (CMDs), which are similar to Hertzsprung-Russell diagrams for stars. Figure 1.11 shows two typical CMDs used to illustrate different classes of substellar object. The left panel shows a near-infrared diagram involving the *J*-band which ranges from $1.1-1.4\,\mu$m, and the *H*-band which ranges from $1.5-1.8\,\mu$m. The ground based near-infrared photometry of brown dwarfs from Dupuy & Liu (2012) in these bands has been converted to the Hubble Space Telescope (HST) channels for comparison with data from hot Jupiters (Manjavacas et al. 2019). The right panel shows a mid-infrared diagram with photometry using *Spitzer*/IRAC channels centred around 3.6 and 4.5 $\mu$m (Triaud et al. 2014). Also shown in Fig. 1.11 are young, low-gravity brown dwarfs (Liu et al. 2016) and directly imaged planets, which are discussed in more detail in Fig. 1.11.
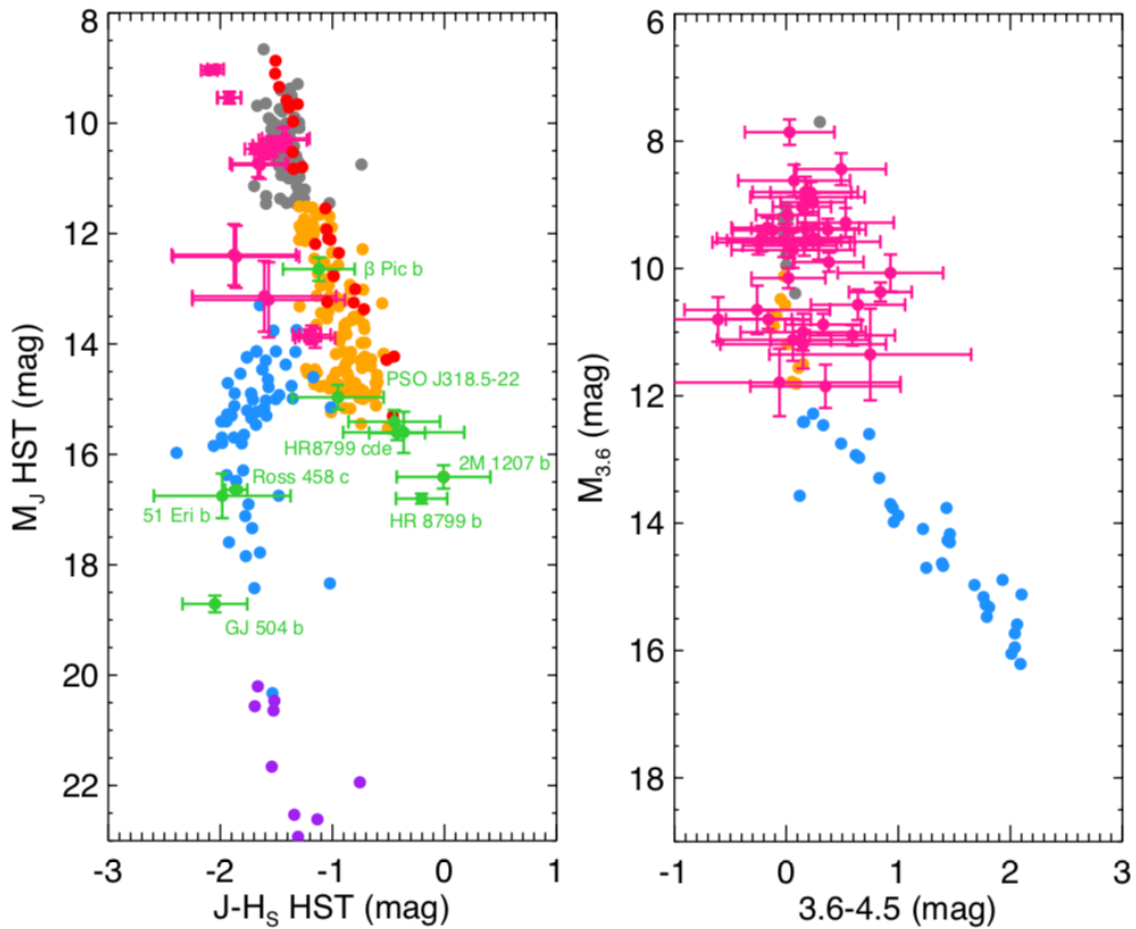
**Figure 1.11:** Colour-magnitude diagrams for multiple classes of substellar objects. Brown dwarfs are shown as grey, orange, blue and purple dots which represent the M, L, T and Y spectral classes respectively, with data from Dupuy & Liu (2012). Low gravity brown dwarfs from Liu et al. (2016) are shown as red dots. Hot Jupiters are shown in pink and directly imaged planets in green, with data from sources listed in Zhang (2020) from which this Figure was obtained.

In the near-infrared diagram, as the $J-$band magnitude decreases the $J-H$ colour of the M and L dwarfs gets progressively redder, before a sudden brightening of the $J-$band and a shift to bluer colours for early T dwarfs. After the L-T transition, the T dwarfs become progressively bluer as $CH_4$ absorption increases in the $H-$band, before eventually turning back to redder colours for late-T and Y dwarf objects. In the mid-infrared diagram, the $[3.6] - [4.5]$ colours remain roughly constant for the M and L dwarfs as the [3.6]-band magnitude decreases. There is then a clear transition to redder colours for T type objects, as $CH_4$ begins absorbing in the [3.6]-band. As $CH_4$ absorption increases along the T sequence, the colours become progressively redder as the [3.6]$-$band magnitude decreases.

Figure 1.11 also shows photometry of hot Jupiters; close-in exoplanets that orbit

their host stars on short periods (< 10 days). The atmospheric emission from hot Jupiters is strongly impacted by the intense stellar irradiation they experience, which leads to a hot dayside and cooler nightside causing drastically different atmospheric dynamics to brown dwarfs. These objects cannot therefore be compared directly to brown dwarfs and directly imaged planets, whose emission is formed solely from their internal energy. Nevertheless, the dayside near- and mid-infrared emission of hot-Jupiters shows similar colours to M and mid-L dwarfs, indicating that the same underlying physical processes may be taking place in their atmospheres. The sample of hot Jupiters shown in Fig. 1.11 display a wider scatter in near- and mid-infrared colours, a diversity that could be driven by the host-star irradiation (along with surface gravity, metallicity, internal heat and radius effects).

### 1.2.3 Low-gravity objects

In addition to effective temperature, surface gravity can also affect the spectral morphology of substellar objects. Young brown dwarfs (< 300 Myr; see Fig. 1.6) have low surface gravities ($\log(g) < 4.5$) as they are still undergoing contraction, and share similar gravities to self-luminous giant exoplanets. Identifying spectral indicators of low gravity enables the characterisation of young brown dwarfs, which act as useful proxies for directly imaged planets (Faherty et al. 2013, 2016). Brown dwarfs can be identified as young objects from host star age-indicators if they are found as companions to stars (e.g. Phillips et al. 2020a), or from having proper motions associated with young moving groups (e.g. Best et al. 2017; Zhang et al. 2018; Lodieu et al. 2018).

Cruz et al. (2009) and Allers & Liu (2013) presented spectral indices and spectral typing methods for low-gravity M and L dwarfs. Young, low-gravity brown dwarfs exhibit a 'triangular' or 'peaky' H band (Allers & Liu 2013), which can be used to identify young substellar objects in star forming regions (Jose et al. 2020). Further spectral features sensitive to surface gravity include the J-band FeH feature, and the K I, Na I, Rb I and Cs I lines in the optical and near-infrared which appear weaker and narrower in younger objects (McGovern et al. 2004).

Low-gravity brown dwarfs are consistently fainter and redder at near-infrared wavelengths (Faherty et al. 2016; Liu et al. 2016). This can be seen in Fig. 1.11, in which low-

gravity brown dwarfs from Liu et al. (2016) form a tight continuous sequence from M to late-L dwarfs which is systematically redder than the field M to L dwarf sequence. Several of the directly imaged planets (or planetary mass objects) shown in Fig. 1.11 photometrically resemble L and T dwarfs, further emphasising the synergy between these two classes of object. These directly imaged planetary mass objects can be seen extending the 'elbow' of the L-T transition to fainter J-band magnitudes and redder $J-H$ colours, indicating that the L-T transition depends on surface gravity. The gravity dependence of the L-T transition was most recently investigated by Zhang et al. (2020), who found that low-gravity brown dwarfs pass through the transition at $T_{\text{eff}} \sim 200-300\,\text{K}$ cooler than older, higher gravity objects, exhibit larger amplitude $J-$band brightening and also brighten in the $H-$band across the transition.

At present, there is a significantly smaller sample of confirmed young low-gravity and planetary mass T dwarfs (e.g. Macintosh et al. 2015; Gagné et al. 2015, 2017, 2018) than L dwarfs. However, the gravity dependence of the spectral morphology appears to weaken in T type objects, as they have been found to have comparable near-infrared photometry and are $T_{\text{eff}} \sim 100\,\text{K}$ cooler than older, higher gravity T dwarfs (Zhang et al. 2020).

### 1.2.4 Non-solar metallicity objects

Astronomically, 'metals' are considered as any element heavier than helium. The interstellar medium (ISM) is progressively enriched over time with metals from supernovae and the stellar winds of giant stars. Since brown dwarfs are formed within the ISM, they have metal contents representative of their formation environments. Metal-poor and metal-rich brown dwarfs have generally formed earlier and later in galactic history respectively. Metal-poor brown dwarfs, known as subdwarfs, therefore provide a key insight into the early history of our galaxy, and the current state of knowledge on these objects is reviewed in detail in Lodieu (2018).

Subdwarfs can often be identified from their large kinematic velocities which are caused by energetic dynamical interactions throughout the galaxy, implying older ages (Burgasser et al. 2003a). They typically have bluer near-infrared colours compared to

equivalent field brown dwarfs (Mace et al. 2013; Burningham et al. 2014; Lodieu et al. 2017; Gonzales et al. 2018), and are rare compared to solar metallicity objects (Zhang et al. 2017b,a, 2019).

### 1.2.5 Variability

It has been suggested since the discovery of the first brown dwarfs that meteorological processes may lead to rotationally induced photometric and spectral variability (Tinney & Tolley 1999). Such modulations are of great interest as they act as probes into the spatial variations of large scale surface features on the object. The reliability of observing rotational modulations from the atmospheres of brown dwarfs depends on relatively short rotation periods. High resolution spectroscopy has provided projected rotational velocities of brown dwarfs in the range of $10 - 60 \, \mathrm{km s^{-1}}$, which given the radii of brown dwarfs ($\sim 1 \, \mathrm{R_{Jup}}$) gives an upper limit on the rotation period of $\sim 12.5 \, \mathrm{hrs}$ (Mohanty & Basri 2003; Zapatero Osorio et al. 2006). These relatively short rotation periods mean multiple object rotations can be observed during single observing runs, making observing brown dwarf variability feasible. Brown dwarf variability has become an active research field, and is reviewed in detail in Biller (2017) and Artigau (2018). Here I briefly summarise key observational results of brown dwarf variability.

Ground- and space-based photometric surveys have found that variability is common within field L and T dwarfs. Typically, ground-based surveys have revealed that $> 10\%$ of brown dwarfs have variability $> 1\%$ in the J-band (Radigan et al. 2014; Wilson et al. 2014; Radigan 2014), while the *Spitzer* space telescope (which is more sensitive to smaller variability amplitudes) has shown that $> 50\%$ of these objects are variable at mid-infrared wavelengths, with amplitudes in the range $0.2 - 4.6\%$ (Metchev et al. 2015). A number of early T dwarfs that exhibit variability with high amplitudes and lie within the L-T transition have been found (Artigau et al. 2009; Radigan et al. 2012; Biller et al. 2013), with the highest amplitude being 26% in the J-band on a period of 7.7 hrs. The ground-based near-infrared survey of Radigan et al. (2014) also found increased variability amplitudes in objects close to the L-T transition, hinting that the physical process behind the sharp change in colours from late-L to early-T types may also be driving the observed

high amplitude variability. In addition to high amplitude variable objects found at the L-T transition, low-gravity brown dwarfs and planetary mass objects have also been found to have high variability amplitudes (Biller et al. 2015; Lew et al. 2016; Zhou et al. 2016). Vos et al. (2019) performed a ground-based survey of L dwarfs, finding that low-gravity objects have a higher variability occurrence rate than field dwarfs. Despite the faint nature of Y dwarfs, *Spitzer* has also found them to be variable in the mid-infrared, with variability amplitudes of $\sim 3 - 5\%$ and rotation periods in the range $6 - 8.5$ hrs (Cushing et al. 2016; Leggett et al. 2016; Esplin et al. 2016).

Spectroscopic variability of brown dwarfs has been primarily observed with the Wide Field Camera 3 (WFC3) onboard the *Hubble Space Telescope* (HST) (Buenzli et al. 2012; Apai et al. 2013). The WFC3 has a wavelength coverage of $1.1 - 1.7\,\mu$m, covering a deep $H_2O$ absorption band at $1.45\,\mu$m which is inaccessible from the ground due to telluric absorption. There is evidence that the spectroscopic variability of L and T dwarfs differ based on the behaviour of this water feature. Yang et al. (2015) demonstrated that a small sample of L dwarfs show similar variability amplitudes both in and out of the water feature, whereas T dwarfs show significantly lower variability amplitudes within the water feature compared to out of it.

Simultaneous HST and *Spitzer* time-resolved observations have found prominent phase shifts between lightcurves observed in the near-infrared (HST) and mid-infrared (*Spitzer*) (Buenzli et al. 2012; Yang et al. 2016), a feature that has also been found in planetary mass objects (Biller et al. 2018). Since different wavelengths probe different pressure-levels in the atmosphere (Marley & Robinson 2015), the phase-shifted light curves provide useful probes of spatial variations in the vertical structure of brown dwarf atmospheres. Medium resolution spectroscopy ($R \sim 4000$) has been used to study variability at the resolution of the K I spectral lines in the closest known brown dwarf binary to the Sun, Luhman 16AB (Faherty et al. 2014; Kellogg et al. 2017). Finally, high resolution spectroscopy has enabled Doppler imaging to construct a brightness map of Luhman 16B (Crossfield et al. 2014), showing large scale surface inhomogeneities.

## 1.3 The physics driving the cooling sequence

### 1.3.1 Modelling the cooling sequence

Traditionally, the atmospheres of brown dwarfs and giant planets are modelled with 1D codes which convert a given internal heat flux from the convective interior to radiation which departs the top-of-the atmosphere. Energy transport in these atmospheres is dominated by convection at high pressures (treated as an adiabatic process), and radiative transfer at low pressures (accounting for the opacities of abundant atoms and molecules). Such models aim to solve for the atmospheric temperature structure in radiative-convective flux balance with a given internal heat flux, while maintaining self-consistency between the temperature structure, chemical abundance profiles and opacities in the model atmosphere. This type of model is typically referred to as a radiative-convective equilibrium model, and I refer the reader to Marley & Robinson (2015); Fortney (2018); Zhang (2020) for detailed reviews of these 1D atmosphere models.

Radiative-convective equilibrium models are used to compute grids of model atmospheres spanning effective temperature and surface gravity. These grids contain temperature structures and top of the atmosphere emission spectra, which both have useful applications. The temperature structures can be coupled as surface boundary conditions (Chabrier & Baraffe 1997) to interior structure models to compute the cooling and evolution over time. Such evolutionary tracks have already been discussed in Section 1.1.3. The fundamental properties of brown dwarfs can be then obtained by fitting synthetic emission spectra from grids of atmosphere models and then inferring the mass and age of the object using evolutionary calculations (e.g. Saumon et al. 2006; Saumon et al. 2007; Burningham et al. 2011; Leggett et al. 2019; Zhang et al. 2020).

Some of the earliest model sets that follow this coupled atmosphere and evolutionary model framework and that are widely used in the literature include Burrows et al. (1997), and the AMES-Dusty and AMES-Cond models of Chabrier et al. (2000b) and Baraffe et al. (2003) respectively. Saumon & Marley (2008) presented coupled atmosphere and evolutionary calculations, additionally varying the cloud sedimentation efficiency (Ackerman & Marley 2001) within their atmospheric outer boundary condition, in order

to investigate the impact of clouds on brown dwarf evolution (see Section 1.3.3 for more information on clouds). More recently, Fernandes et al. (2019) used existing atmosphere models in the literature as surface boundary conditions to a stellar evolution code to investigate the effects of including additional metals in the interior equation of state on the substellar boundary.

Beyond these coupled evolutionary models numerous improvements and complexities have been added to radiative-convective equilibrium codes in an attempt to reproduce and explain various features of the brown dwarf cooling sequence. I now discuss some of these complexities regarding atmospheric chemistry (Section 1.3.2), clouds (Section 1.3.3) and thermo-compositional convection (Section 1.3.4), and our current understanding of the physics driving the brown dwarf cooling sequence.

### 1.3.2   Atmospheric chemistry

Stars are predominantly composed of hydrogen, with the second most abundant element being helium. M dwarfs and brown dwarfs are sufficiently cool for hydrogen to be in a molecular state ($H_2$) (Burrows & Liebert 1993), with some hydrogen being contained in metal hydrides. The high densities in these cool atmospheres mean that the frequency of collisions between $H_2$ molecules (and other species) is high enough to produce collisionally induced absorption (CIA) (Linsky 1969), which peaks at $\sim 2.4\ \mu$m (Saumon et al. 2012). The $H_2 - H_2$ CIA is stronger in the denser atmospheres of higher gravity brown dwarfs than lower gravity brown dwarfs, and is partially responsible for producing the redder $J - H$ and $J - K$ of low-gravity objects seen in Fig. 1.11.

Aside from $H_2$ and He in M dwarf atmospheres, oxygen is primarily found in $H_2O$, TiO and VO, carbon in CO and nitrogen in $N_2$ (Allard et al. 1997; Burrows & Sharp 1999), which have prominent features in the M dwarf spectral sequence. The change in spectral morphology from the M to L class is thought to be the result of the formation of condensates as the pressures and temperatures of these atmospheres become amenable to harbor liquid and solid phase species. At atmospheric temperatures less than $\sim 2400\,$K, condensates form from the refractory elements Ti, V, Ca, Al, Fe, Mg and Si, which gravitationally settle in the atmosphere to form cloud layers as depicted in Fig. 1.12. The weakening of the
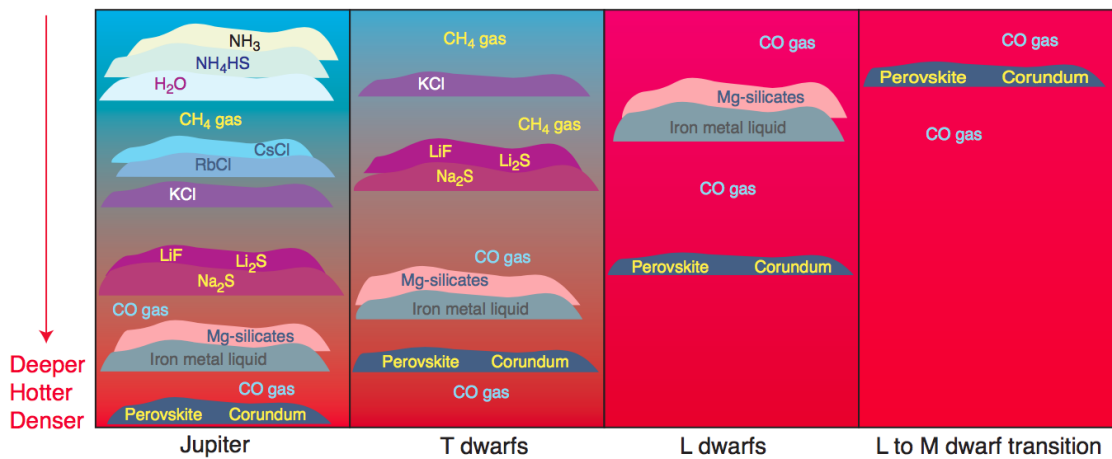
**Figure 1.12:** Illustration of the condensate cloud layers and carbon chemistry that drives changes along the brown dwarf spectral sequence. Figure from (Lodders 2004).

TiO and VO bands in L dwarfs is a result of the condensate perovskite ($CaTiO_3$) and solid solutions of $VO_2$ and $V_2O_3$ forming in the atmosphere (Fegley & Lodders 1996; Jones & Tsuji 1997). Al also condenses into corundum ($Al_2O_3$), and at slightly lower temperatures ($< 1800\,K$), Mg and Si condense into forsterite ($Mg_2SiO_4$) and enstatite ($MgSiO_3$), and Fe into liquid iron (Fegley & Lodders 1996; Allard et al. 1997; Burrows & Sharp 1999). The removal of Fe from the gas phase causes the weakening of the FeH spectral signature in late L dwarf spectral types (Kirkpatrick et al. 1999; Burgasser et al. 2002).

In cooler T type brown dwarfs, the perovskite, corundum, Mg-silicate and liquid iron clouds sink deeper into the atmosphere, as depicted in Fig. 1.12. As these clouds sink deeper, the alkali metals Na and K condense into sodium sulfide ($Na_2S$) and potassium chloride (KCl) for atmospheric temperatures below $\sim 1000\,K$ and $\sim 800\,K$ respectively (Lodders 1999; Morley et al. 2012). This removal of Na and K from the gas phase is the cause of the disappearance of their strong resonance lines in the red-optical spectra of late T dwarfs (Burgasser et al. 2003b). Moving to cooler objects still, cloud layers continue to sink (Fig. 1.12), and $H_2O$ and $NH_3$ are predicted to condense in Y dwarf atmospheres with $T_{\text{eff}} < 350\,K$ and $T_{\text{eff}} < 200\,K$ respectively (Morley et al. 2014b).

Alongside condensation, gas phase chemistry also strongly influences the brown dwarf cooling sequence. The change in spectral morphology from the L to T class is dominated by the appearance of $CH_4$ absorption features, as the dominant form of carbon transitions from CO at high temperatures to $CH_4$ at lower temperatures. Similarly, the

transition from the T to Y spectral classes is characterised by the appearance of $NH_3$ absorption, as the dominant form of nitrogen transitions from $N_2$ at high temperatures to $NH_3$ at lower temperatures. At the atmospheric pressures relevant in brown dwarf atmospheres ($0.1 - 10$ bar), these transitions occur at $\sim 1300 \pm 200$ K and $\sim 700 \pm 200$ K respectively (Fegley & Lodders 1996; Lodders & Fegley 2006). The net chemical reactions converting CO to $CH_4$ and $N_2$ to $NH_3$ are (Lodders & Fegley 2006)

$$CO + 3H_2 \longleftrightarrow CH_4 + H_2O, \tag{1.1}$$

$$N_2 + 3H_2 \longleftrightarrow 2NH_3. \tag{1.2}$$
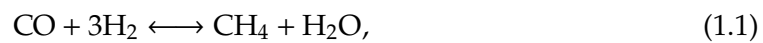
It is well known from chemical network studies that the rightward chemical reactions of Eq. (1.1) and Eq. (1.2) are typically slow (Moses et al. 2011; Venot et al. 2012). These species can therefore be driven away from chemical equilibrium by rapid vertical mixing which may be induced by a number of complex processes common in planetary and stellar atmospheres (e.g. gravity waves, convective overshooting (Freytag et al. 1996; Kupka et al. 2018)). The abundances of these species is therefore not determined by chemical equilibrium predictions, but rather the competition between the rate of transport and the rate of chemical conversion. For example, if CO from the hotter, deeper layers of the atmosphere is rapidly vertically mixed into the cooler, upper layers faster than the chemical conversion to $CH_4$, then CO will remain in the cooler observable part of the atmosphere, in contrast to chemical equilibrium predictions.

Signatures of non-equilibrium chemistry due to vertical mixing are present in solar system planet observations, and an observed excess of CO is seen in Jupiter's upper atmosphere (Bézard et al. 2002). Fegley & Lodders (1996) suggested that non-equilibrium chemistry due to vertical mixing could also occur in brown dwarf atmospheres, with excess CO and depleted $CH_4$ predicted in T-type objects, and excess $N_2$ and depleted $NH_3$ in cooler late T-Y type objects (Zahnle & Marley 2014). Indeed, observational studies have revealed vertical mixing is prevalent throughout the brown dwarf cooling sequence, through observations of excess CO in T dwarfs (Noll et al. 1997; Oppenheimer et al. 1998; Geballe

et al. 2009; Miles et al. 2020) and depleted $NH_3$ in late T and Y dwarfs (Saumon et al. 2000, 2006; Leggett et al. 2015; Tremblin et al. 2015).

### 1.3.3 Clouds

The main parameter driving the spectral sequence is the effective temperature, which steadily decreases throughout the M-L sequence before plateauing at $T_{eff} = 1400 \pm 200\,$K at the L-T transition, and then continuing to steadily decrease from mid-T types onwards (Golimowski et al. 2004; Kirkpatrick 2005; Stephens et al. 2009; Marocco et al. 2013; Filippazzo et al. 2015). The occurence of the L-T transition over a narrow $T_{eff}$ range implies that another parameter is responsible for the dramatic change in spectral morphology.

The widely accepted process driving the change from red L dwarfs to blue T dwarfs is the evolution of clouds in brown dwarf atmospheres. As previously discussed in Section 1.3.2, perovskite, corundum, Mg-silicates and liquid iron condense in L dwarf atmospheres to form cloud layers. These clouds have an intrinsic opacity, and block flux emerging from the hot, deep layers of the atmosphere. This suppresses the flux at near-infrared wavelengths (in particular in the J- and H-bands), causing the colours of L dwarfs to become progressively redder with decreasing $T_{eff}$ (Chabrier et al. 2000b; Cushing et al. 2008; Stephens et al. 2009; Witte et al. 2011). The sharp change to bluer colours at the L-T transition is thought to be due to a sudden reduction in the cloud opacity (Allard et al. 2001; Ackerman & Marley 2001). The extremely red colours of low-gravity objects and directly imaged planets are also generally considered to be the result of thick cloud decks, which persist to lower effective temperatures than in typical, higher gravity brown dwarfs (Barman et al. 2011; Marley et al. 2012).

There are two main proposed causes for this sudden drop in cloud opacity at the L-T transition. The first proposal suggests that there is a break up in the cloud cover, allowing flux from the hot, deep layers of the atmosphere to emerge through holes in the clouds, brightening the J-band at the L-T transition and producing bluer near-infrared colours (Ackerman & Marley 2001; Burgasser et al. 2002; Marley et al. 2010). This scenario is demonstrated in Fig. 1.13, which shows synthetic photometry from clear, cloudy, and patchy model atmospheres. The red near-infrared colours of L dwarfs can only be
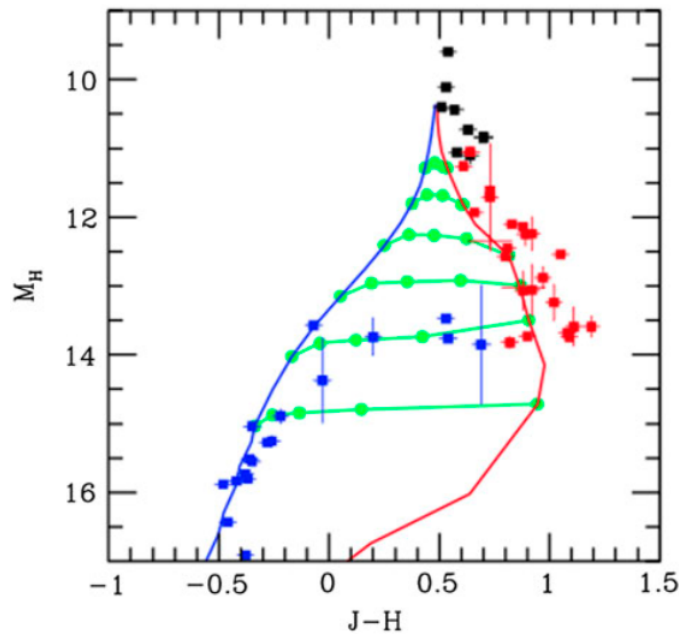
**Figure 1.13:** Near-infrared CMD from Marley et al. (2010). M, L and T dwarfs are shown as black, red and blue data points respectively. The red line is a completely cloudy model, the blue line is a completely clear model, and the green lines are patchy cloud models with different values of cloud sedimentation efficiency (Ackerman & Marley 2001).

reproduced by cloudy model atmospheres, whereas the bluer colours of T dwarfs are reproduced by clear model atmospheres, with the transition between the two captured by model sequences with varying cloud patchiness (Marley et al. 2010).

Another key spectroscopic feature of the L-T transition indicative of patchy clouds is the behaviour of the 0.99 $\mu$m FeH spectral feature. FeH absorption weakens and disappears in mid to late L dwarfs, before re-emerging in early to mid T dwarfs (Burgasser et al. 2002; Burrows et al. 2003). The weakening of this feature along the L sequence is interpreted as evidence of Fe being sequestered in condensates which gradually sink below the photosphere. The re-emergence of FeH absorption in T dwarfs can be interpreted as holes in the cloud cover allowing deeper regions of the atmosphere, where Fe is not sequestered in condensates and still present in gas phase species such as FeH, to be probed (Burgasser et al. 2002).

The second suggested explanation for the apparent drop in cloud opacity at the L-T transition, is a sudden downpour (or rainout) of condensates due to a change in the dynamical state of the atmosphere, increasing the cloud particle sizes and leading to a clearing of the cloud layers (Tsuji & Nakajima 2003; Tsuji et al. 2004; Knapp et al. 2004;

Burrows et al. 2006; Saumon & Marley 2008; Charnay et al. 2018). Similarly to the cloud break-up scenario, changes in the cloud sedimentation efficiency parameter $f_{sed}$ (Ackerman & Marley 2001), can reproduce the sharp change in near-infrared colours at the L-T transition in CMDs (e.g. Saumon & Marley 2008; Charnay et al. 2018), and can also lead to an increase in the strength of the FeH absorption feature in early T dwarfs. This is due to the opacity of the atmosphere decreasing as the cloud sedimentation efficiency increases across the L-T transition, allowing a larger column density of FeH to be observed (Cushing et al. 2008).

Since L-T transition objects exhibit increased variability, it is natural to suggest that the physical process driving the sharp change in colours is also behind the observed variability. Indeed, it has been shown that the high amplitude variability of L-T transition objects can be best fit by 1D model combinations of thin and thick cloud decks, rather than combinations of clear and cloudy models (Radigan et al. 2012; Apai et al. 2013; Buenzli et al. 2015). However, while the FeH spectral feature might be expected to be variable given this cloudy explanation of the L-T transition, Buenzli et al. (2015) observed a lack of variability within this spectral feature.

Clouds have also been invoked to explain the red near-infrared colours of late-T and Y dwarfs. $Na_2S$ and $H_2O$ clouds are expected to form in these atmospheres, and including opacity from these condensates in 1D radiative-convective models has been shown to improve comparisons to observations (Morley et al. 2012, 2014b). The variability seen in Y dwarfs is also attributed to patchy water clouds (Morley et al. 2014a).

Given the importance of clouds in shaping the observed cooling sequence, numerous cloud models have been developed for use in 1D radiative-convective models, which determine the cloud particle size and distribution in the atmosphere. These models can be divided into two classes. The first class is perhaps the most sophisticated, and corresponds to models which self-consistently compute cloud particle sizes and vertical distributions from microphysics (e.g. Helling et al. 2008; Allard et al. 2012). The second class, while not as sophisticated, is perhaps more versatile and suited for use in large grids of atmosphere models. It represents models in which the cloud particle sizes and vertical distributions are defined by free parameters (e.g. Ackerman & Marley 2001; Tsuji 2002;

Burrows et al. 2006; Madhusudhan et al. 2011), and it is these parameterised models that have predominantly been used to study the role of clouds throughout the brown dwarf cooling sequence.

### 1.3.4  Thermo-compositional convection

The cloudy picture of the brown dwarf cooling sequence discussed in Section 1.3.3 has advanced the understanding of the role of clouds in brown dwarf and exoplanet atmospheres. However, cloudy models can only reproduce the spectral evolution of brown dwarfs by manually adjusting the cloud parameters, such as the cloud patchiness (Marley et al. 2010) or cloud sedimentation efficiency (Saumon & Marley 2008). In particular, the physical mechanism causing the sudden drop in cloud opacity at the L-T transition remains unclear.

Over the past half decade, a new theory has been developed suggesting that chemical transitions such as $CO \rightarrow CH_4$ and $N_2 \rightarrow NH_3$ in brown dwarf atmospheres can be responsible for triggering convective instabilities. This can reduce the temperature gradient in the atmosphere and reproduce several observed features of brown dwarfs, including the L-T transition (Tremblin et al. 2016), extremely red young low-gravity objects (Tremblin et al. 2017b), and the red colours of cool late T dwarf objects (Tremblin et al. 2015). To date the reduction in the temperature gradient has been modelled in radiative-convective equilibrium models by adjusting the adiabatic index $\gamma$, which sets the pressure $P$ and temperature $T$ in the convective regions of the atmosphere through $P^{1-\gamma}T^{\gamma}$ = constant (this is discussed in more detail in Chapter 2). For an ideal gas, $\gamma$ is the ratio of the specific heats at constant pressure and volume and for a diatomic gas such as a $H_2$ dominated brown dwarf atmosphere, $\gamma = 1.4$. Reducing the value of $\gamma$ in the model atmosphere reduces the temperature gradient, leading to cooler temperatures in the deep atmosphere.

The proposed explanation of brown dwarf spectral evolution according to reductions in the temperature gradient can be seen in Fig. 1.14, which shows a near-infrared CMD comparison between observed field brown dwarfs and the model atmospheres of Tremblin et al. (2016). L dwarf atmospheres are expected to be unstable to convective instabilities driven by the $CO \rightarrow CH_4$ chemical conversion. The reddening L dwarf sequence
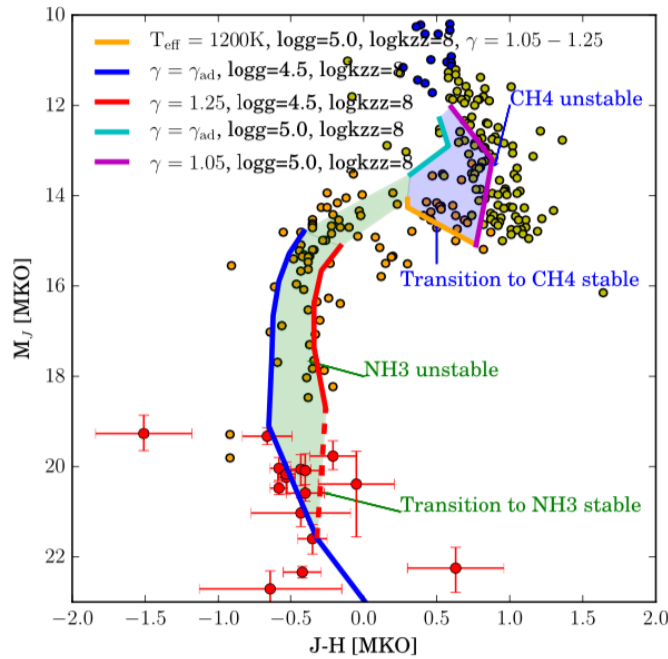
**Figure 1.14:** Near-infrared CMD from Tremblin et al. (2016). Unmodified atmosphere models are shown as blue and cyan solid lines, and models with modified adiabatic indexes are shown as red, orange and magenta solid lines. M, L, T and Y dwarf photometry from Dupuy & Liu (2012); Faherty et al. (2012); Dupuy & Kraus (2013); Beichman et al. (2014) are shown as blue, light green, orange and red data points respectively.

is reproduced with model atmospheres with $\gamma = 1.05$, which reduces the temperature gradient, lowering the flux emitted through the J-band and reddening the emission spectrum. Brown dwarf atmospheres become stable to $CO \rightarrow CH_4$ convective instabilities across the L-T transition as the atmosphere becomes $CH_4$ dominated. This increases the temperature gradient of the atmosphere, causing a re-emergence of the FeH spectral feature and a brightening of the *J*-band that reproduces the sharp change in colours from late-L to early T-type objects. Cooler objects become unstable to convective instabilities induced by the $N_2 \rightarrow NH_3$ chemical conversion, and the colours of late-T dwarfs are best reproduced by model atmospheres with $\gamma = 1.25$.

To investigate the potential mechanism at play reducing the temperature gradient, Tremblin et al. (2019) generalised the theory of convection to include diabatic processes through thermal and compositional source terms, demonstrating that a number of convective systems in the Earth's atmosphere and oceans derive from the same instability criterion. In brown dwarf atmospheres, the thermal and compositional source terms are represented by radiative transfer and $CO \rightarrow CH_4$ or $N_2 \rightarrow NH_3$ chemistry, respectively, with the convective instability driven by opacity and/or mean molecular weight differ-

ences in the different chemical states.  The idealised 2D hydrodynamics simulations of
Tremblin et al. (2019) reveal that by including such source terms the temperature gradient
can indeed be reduced to that required to qualitatively reproduce brown dwarf observa-
tions.

Thermo-compositional convection provides a promising mechanism by which to
explain observational features of the brown dwarf cooling sequence. However, the study
of such convection in brown dwarf atmospheres is in its infancy compared to the mod-
elling of clouds, and shares the same drawback in that currently it uses a free parameter ($\gamma$)
to reproduce the L-T transition. More detailed, larger simulations, beyond the idealised
small-scale simulations shown in Tremblin et al. (2019), are required to establish whether
the spatial scales associated with the thermo-chemical instability are large enough to in-
fluence brown dwarf atmospheres. Further work is currently being undertaken to assess
whether temperature fluctuations naturally arising from thermo-compositional convec-
tion could also provide an explanation for observed brown dwarf variability.

## 1.4    Aims of this thesis

As discussed in Section 1.3, there have been numerous complexities concerning clouds
and convection used in 1D radiative-convective models in an attempt to reproduce various
features of the observed brown dwarf cooling sequence. Along with these additional com-
plexities, there has also been significant improvement in the fundamental input physics
to 1D atmosphere models. The opacity for important molecular absorbers has improved
through more complete high-temperature line lists (Tennyson & Yurchenko 2018), which
has altered the temperature structures and synthetic emission spectra in 1D model grids
(Saumon et al. 2012; Malik et al. 2019). There has been significant theoretical improvement
in the pressure-broadened line shapes of the alkali metals Na and K (Allard et al. 2016,
2019), which shape the red-optical and near-infrared spectra. To further aid in the study of
non-equilibrium processes, complex chemical kinetics networks containing thousands of
reactions between important molecules in exoplanet and brown dwarf atmospheres have
been developed and refined (Moses et al. 2011; Venot et al. 2012, 2019; Tsai et al. 2017,
2018).

Motivated by these theoretical improvements, and driven by ever-improving instrumentation becoming sensitive to cooler objects, I have developed a state-of-the-art grid of coupled atmosphere and evolution models for cool T/Y type brown dwarfs and self-luminous giant exoplanets. This grid, which is named `ATMO` 2020, includes numerous key improvements to the input physics for modelling substellar objects used in previous models available in the literature. The aims of these new models, and this thesis as a whole, are to:

- Determine the pressure-temperature structure, abundance profiles and key processes impacting the observable emission from brown dwarf and giant exoplanet atmospheres

- Identify observable atomic and molecular spectral features of brown dwarf and giant exoplanet atmospheres

- Determine the impact of modelling improvements on the atmospheric temperature structures, emission spectra and cooling tracks of brown dwarfs and giant exoplanets

- Provide a publically available set of atmosphere and evolutionary models for the community to use in interpretation of existing and future observations of brown dwarfs and giant exoplanets.

## 1.5 Chapter overview

The Chapters in this thesis are structured as follows. In Chapter 2 I introduce the fundamentals of one-dimensional forward modelling of substellar atmospheres, such as radiative transfer and convection. I focus on how these processes are modelled in the `ATMO` code, which is used throughout this work. In Chapter 3 I describe the chemistry schemes and opacities used by `ATMO`. I present improvements regarding the equation of state, discuss the self-consistent coupling of a chemical relaxation scheme to model non-equilibrium chemistry, and detail the calculation of gaseous Fe opacity. Chapter 4 focuses on the implementation of new potassium resonance line shapes in opacity tables used by `ATMO`. I

compare these line shapes to those previously used, and demonstrate the impact on atmosphere models. I present the `ATMO` 2020 model grid in Chapter 5, and highlight numerous theoretical modelling improvements by comparing to other model sets in the literature. These improvements are further highlighted and validated through comparisons to observational datasets in Chapter 6. These comparisons also serve to highlight current shortcomings in the modelling of cool brown dwarfs in reproducing the cooling sequence, thus motivating future work in these areas. Finally, in Chapter 7, I summarise and conclude the results, and provide future prospects for this work.

## 1.6   Statement of contribution to publications

Many of the results from Chapters 4, 5 and 6 have been published in Phillips et al. (2020b). The results were obtained and analysed by myself, with contributions and input from Pascal Tremblin, Isabelle Baraffe, Gilles Chabrier, Nicole Allard, Ben Drummond, Jayesh Goyal and Eric Hébrard. The writing of the manuscript was led by myself.

I am a co-author on the paper Tremblin et al. (2019), where I provided model fits to observational data and was involved in the discussion of the manuscript. Results from this paper are not presented in this thesis, however its implications are discussed.

I am a co-author on the paper Goyal et al. (2020), which has recently been accepted for publication in the Monthly Notices of the Royal Astronomical Society. I provided the Fe opacity used in the atmosphere models in this work, and discussed its role in forming temperature inversions in hot Jupiter exoplanets. I present the Fe opacity used in this work in Chapter 3.

Some of the results in Chapter 6 regarding comparisons of the `ATMO` 2020 and `Sonora` models in CMDs, and modelling the late-T dwarf UGPS 0722 with a reduced temperature gradient, are yet to be published. However these results will likely appear in work led by Sandy Leggett, in collaboration with Pascal Tremblin, in the near-future.

# Chapter 2

# One-dimensional forward modelling of substellar atmospheres

This Chapter outlines the physics and techniques commonly used in brown dwarf and planetary atmosphere models, with a particular focus on the atmosphere code `ATMO`. `ATMO` is a 1D/2D atmosphere model developed to study hot Jupiters (Amundsen et al. 2014; Drummond et al. 2016; Tremblin et al. 2017b; Goyal et al. 2018; Goyal et al. 2019; Drummond et al. 2019) and brown dwarfs (Tremblin et al. 2015; Tremblin et al. 2016; Tremblin et al. 2017a). The model (in 1D) solves for the pressure-temperature structure of an atmosphere that is self-consistent with radiative-convective flux balance for a given internal heat flux, and hydrostatic equilibrium for a given surface gravity. This type of model, often termed a radiative-convective equilibrium model, has a long history of being used to study brown dwarf and giant planet atmospheres, and the reader is referred to Marley & Robinson (2015); Hubeny (2017); Fortney (2018) for further reviews of these models in this context.

I begin by reviewing the fundamental atmospheric physics used in one-dimensional forward models of substellar atmospheres in Section 2.1. I discuss and demonstrate how radiative transfer and convection shape the temperature structure of a model atmosphere, and lead to observable emission from the top of the atmosphere. I provide more detail on the radiative transfer scheme used in `ATMO` in Section 2.2, and mixing length theory

used to model convection in Section 2.3. Finally, I discuss how the model iterates towards a final pressure-temperature profile in Section 2.4. The chemistry schemes and opacities used by `ATMO` are discussed in Chapter 3.

## 2.1 One-dimensional atmospheric physics

### 2.1.1 Discretisation and optical depth

One-dimensional forward models assume a vertical atmospheric column of gas which is split into a grid of model levels defined in either pressure ($P$), altitude ($z$), or in the case of `ATMO` optical depth ($\tau$). Optical depth is an appropriate vertical coordinate for a 1D atmosphere model over, for instance, altitude, since it indicates the transparency/absorbency of the material, encompassing information regarding the density and opacity of abundant atoms, molecules and condensates. The optical depth $\tau$ at a given wavenumber $\tilde{\nu}$ (inverse of the wavelength $\lambda$), is defined as

$$d\tau = \kappa(\tilde{\nu})dz, \tag{2.1}$$

where $\kappa(\tilde{\nu})$ is the extinction coefficient, which is the change in intensity of light due to absorption or scattering over a given path length $dz$. The extinction coefficient is typically defined as per unit number density or per unit mass density.

### 2.1.2 Hydrostatic Equilibrium

It is assumed each model level obeys hydrostatic equilibrium, whereby the pressure in each model level must support the weight of the atmosphere above it. Balancing the gravitational force acting on a parcel of gas with the pressure-gradient force, the condition for hydrostatic equilibrium can be simply derived as

$$\frac{dP}{dz} = -\rho g, \tag{2.2}$$

where $\rho$ is density, and $g$ is acceleration due to gravity. Replacing the gradient $d/dz$ with

the derivative with respect to optical depth in Eq. (2.1) gives the hydrostatic equilibrium condition as

$$\frac{dP}{d\tau} = -\frac{\rho g}{\kappa(\tilde{\nu})}.$$ (2.3)

A 1D model atmosphere must satisfy this equation in each model level, for a given surface gravity. The radial extension of the atmosphere should be negligible compared to the total radius of the object, and thus the gravity can assumed to be constant throughout the atmosphere. While the hydrostatic equilibrium equation does depend weakly on temperature through the extinction coefficient, it is this equation that predominantly defines the pressure levels in an `ATMO` model atmosphere.

### 2.1.3 Pressure scale height

A useful quantity for describing atmospheres is the pressure scale height $H_P$. This represents the vertical distance over which the pressure in an isothermal atmosphere drops by a factor of $1/e$. The value of $H_P$ can be easily derived by inserting the ideal gas law into the equation for hydrostatic equilibrium (Eq. (2.2)) to eliminate the density $\rho$, and integrating from a reference pressure $P_0$ (defined at $z = 0$) to a given pressure and altitude to obtain

$$P = P_0 e^{-\frac{\mu m_u g}{kT} z}.$$ (2.4)

Here $\mu$ is the mean molecular weight, $m_u$ is the atomic mass constant, $k$ is Boltzmann's constant, and $T$ is temperature. The pressure scale height of the atmosphere can then be seen to be

$$H_P = \frac{kT}{\mu m_u g}.$$ (2.5)

The pressure scale height gives useful insight into the effect of gravity on an atmosphere. Lower gravity atmospheres will have a larger pressure scale height, meaning the vertical extent of a low gravity atmosphere will be larger than a higher gravity atmosphere.

### 2.1.4 Internal heat flux and radiative-convective equilibrium

Alongside the surface gravity, another key model input parameter is the internal heat flux ($F_i$), which (for a non-irradiated object) is set by the effective temperature ($T_{\text{eff}}$) through the Stefan-Boltzmann law

$$F_i = \sigma T_{\text{eff}}^4, \tag{2.6}$$

where $\sigma$ is the Stefan-Boltzmann constant. This heat flux is assumed to be constant throughout the atmosphere, and is carried by two energy transport mechanisms: radiation and convection. The internal heat flux is conserved by the radiative ($F_{\text{rad}}$) and convective ($F_{\text{conv}}$) fluxes throughout the atmosphere such that

$$F_i = F_{\text{rad}} + F_{\text{conv}}, \tag{2.7}$$

is satisfied in each model level. This is shown in Fig. 2.1, which shows an example pressure-temperature profile from the 1D atmosphere model `ATMO`. The right panel of this Figure illustrates how the radiative and convective fluxes satisfy the internal heat flux throughout the atmosphere. This conservation of energy flux leads to 1D atmosphere models such as `ATMO` being commonly referred to as radiative-convective equilibrium models.

### 2.1.5 Convection

The internal heat flux in brown dwarfs is large ($T_{\text{eff}} = 200 - 2400\,\text{K}$), and leads to thermal structures unstable to vertical convection. If a parcel of gas is displaced upwards and finds itself in an environment with a density greater than the parcel's own internal density, then it will continue to rise, and vice versa for a parcel displaced downwards. This leads to a density gradient for which convection occurs when the gradient is too steep. This density gradient can be related to a temperature gradient in the atmosphere, known as the lapse rate, which can be used to define the limit between convectively stable and unstable thermal structures.
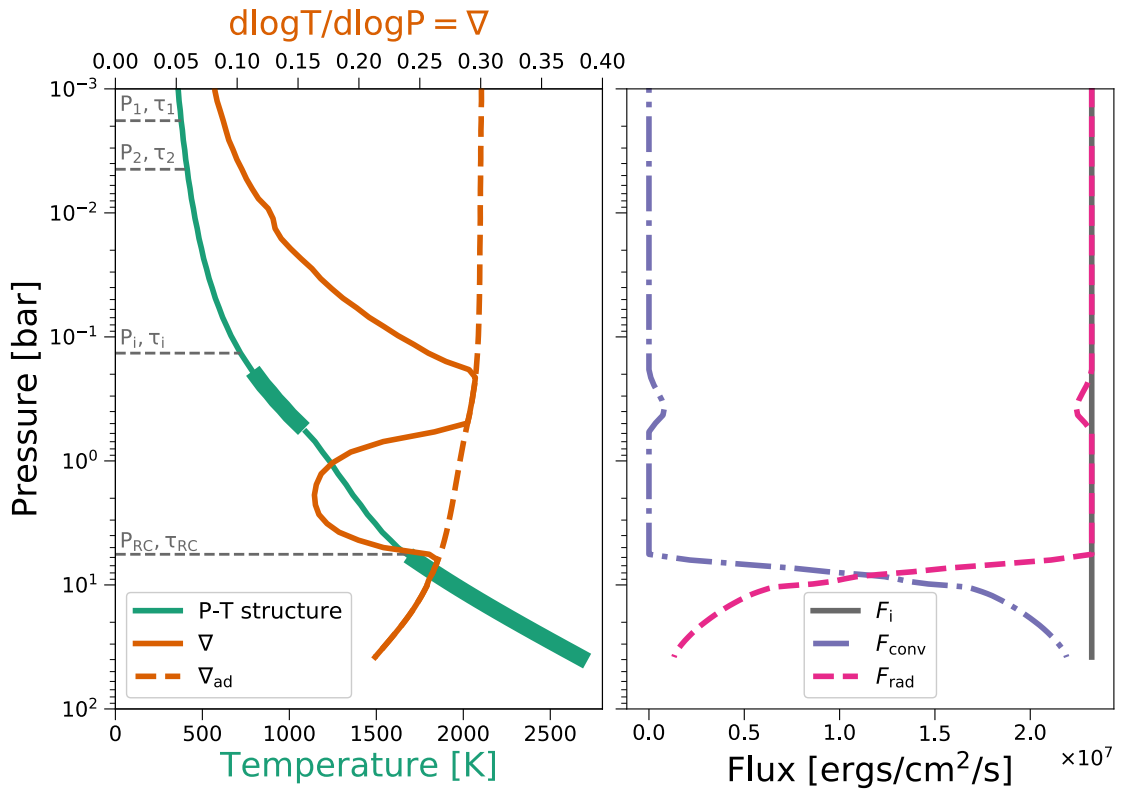
**Figure 2.1:** An example pressure-temperature profile along with processes influencing its structure from the 1D radiative-convective equilibrium model `ATMO`. This model has $T_{\text{eff}} = 800\,\text{K}$ and $\log(g) = 3.5$. The left panel shows the temperature structure (*green line*) as a function of pressure, the atmospheric temperature gradient $\nabla$ (*solid orange line*) and the local adiabatic gradient $\nabla_{\text{ad}}$ (*dashed orange line*). The model has two convectively unstable regions (*thickened green line*) within which $\nabla = \nabla_{\text{ad}}$. The right panel shows the internal heat flux $F_{\text{i}} = \sigma T_{\text{eff}}^4$ (*solid grey line*) which is carried by the convective flux (*dot-dashed purple line*) and the radiative flux (*dashed pink line*).

Convection in brown dwarfs has been shown to be adiabatic (Baraffe et al. 2002). Applying the ideal gas law and approximating the convection as adiabatic gives the condition for an unstable lapse rate, known in Astrophysics as the Schwarzschild criterion, as

$$-\frac{dT}{dz} > \frac{g}{c_P}. \tag{2.8}$$

Including the equation of hydrostatic equilibrium (Eq. (2.2)) this becomes

$$\nabla_T = \frac{d\log T}{d\log P} > \frac{R_s}{c_P} = \nabla_{\text{ad}}, \tag{2.9}$$

where $R_s$ is the specific gas constant and $c_P$ is the local atmospheric heat capacity. There-

fore for lapse rates larger than the adiabatic lapse rate $\nabla_{\mathrm{ad}}$ , convection will ensue, which will redistribute heat in the convectively unstable region of the atmosphere. Note that this is the dry adiabatic lapse rate, i.e. assuming no water vapour is present in the atmosphere.

The specific gas constant $R_s$ is equal to $c_P - c_v$, and the ratio of the specific heats at constant pressure and constant volume, called the adiabatic index, is $\gamma = c_p/c_v$. Using these definitions, the adiabatic lapse rate can alternatively be written as

$$\nabla_{\mathrm{ad}} = \frac{\gamma - 1}{\gamma}. \tag{2.10}$$

At high pressures and densities in brown dwarf atmospheres the optical depth is large and the dominant energy transport mechanism is convection. Thermal photons are efficiently absorbed and/or scattered and cannot transport the internal heat flux. Convection therefore drives the deep atmosphere temperature profile, $\nabla_T$, to closely follow the convective adiabat, $\nabla_{\mathrm{ad}}$. This is shown in Fig. 2.1 where $\nabla_T = \nabla_{\mathrm{ad}}$ in convective regions of the atmosphere (left panel, thickened green line and orange lines, note that $\nabla_T$ is denoted as $\nabla$ in this Figure).

### 2.1.6 Radiation

At lower pressures and densities in the atmosphere, the optical depth decreases, thermal photons are not absorbed or scattered as frequently, and the dominant energy transport mechanism becomes radiation. The internal heat is radiated away through opacity windows meaning the temperature gradient begins to decrease with decreasing pressure, and the atmosphere becomes stable to convection, i.e. $\nabla_T < \nabla_{\mathrm{ad}}$. The location of the transition between convective and radiative atmospheric layers is known as the radiative-convective boundary, and the pressure level at which this occurs, $P_{\mathrm{RC}}$, is illustrated in Fig. 2.1.

To illustrate the physics taking place, Fig. 2.2 shows radiative properties local to a selection of radiative and convective model levels. The pressure levels indicated in Fig. 2.2 correspond to the model presented in Fig. 2.1, and thus these figures are best considered concurrently. First, we introduce the concept that each model level with temperature $T$ acts as a blackbody in thermal equilibrium, meaning the emitted spectral energy density
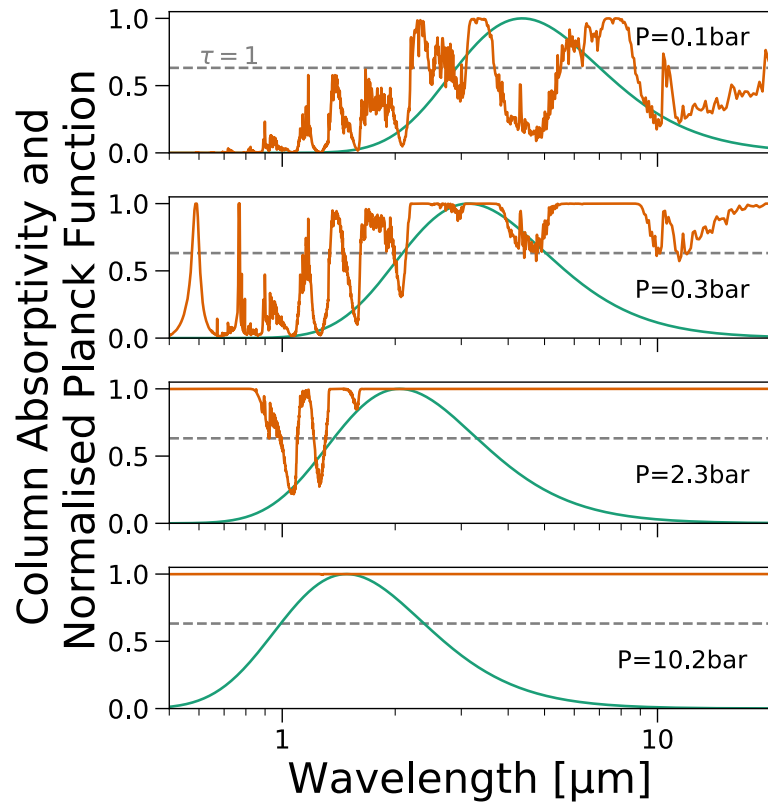
**Figure 2.2:** Spectra of the normalised local Planck function (*green*) and column absorptivity (*orange*) (i.e. $1 - e^{-\tau}$) with each subplot indicating the pressure level of the model atmosphere. The $\tau = 1$ level is shown by the horizontal dashed grey line.

of radiation follows Planck's law,

$$B_\lambda = \frac{2hc^2}{\lambda^5} \frac{1}{\exp\left(\frac{hc}{\lambda k_B T}\right) - 1}, \tag{2.11}$$

where $h$ is Planck's constant, $c$ is the speed of light and $k_B$ is Boltzmann's constant. The spectral energy density $B_\lambda$ has units of $W/sr/m^{-3}$, and is normalised and plotted as the green line in Fig. 2.2. The peak in emission can be seen shifting to longer wavelengths for model levels with lower pressures, due to the temperature dependence in Eq. (2.11).

Second we introduce the absorptivity ($A_\lambda$) of the column of gas above an atmospheric layer,

$$A_\lambda = 1 - \exp\left(-\tau\right). \tag{2.12}$$

Here $\tau$ is the optical depth at a given wavelength integrated from the top of the atmosphere down to the pressure level indicated in each subplot of Fig. 2.2. Plotted as the grey dashed line in Fig. 2.2 is the $\tau = 1$ absorptivity level, above which the medium is considered optically thick and below which it is considered optically thin.

At the highest pressure model level shown in Fig. 2.2, the absorptivity of the atmosphere is high across the wavelength range encompassing the Planck function. Emitted thermal radiation is efficiently absorbed or scattered, and thus the model level is convective as shown in Fig. 2.1. Moving to a lower pressure of 2.3 bar, opacity windows appear in the near-infrared between $1 - 2\,\mu$m lowering the absorptivity of the atmosphere in this wavelength range. This overlaps with the local Planck function, meaning thermal photons are radiated away through these opacity windows and the internal heat is carried by the radiative flux (see Fig. 2.1). At 0.3 bar the absorptivity continues to decrease across many wavelengths due to wavelength dependent molecular opacity (discussed in more detail in Chapter 3, and the peak of the Planck function shifts to longer wavelengths, aligning itself with a strong $CH_4$ absorption band at $\sim 3\,\mu$m. Despite the internal heat flux being predominantly carried by the radiative flux through wavelength regions of low absorptivity, the strong absorption at the peak of the Planck function heats the atmosphere, increasing the atmospheric temperature gradient $\nabla_T$ such that the atmospheric layer becomes convectively unstable. This forms a "detached" convective zone (shown in Fig. 2.1) within which $\nabla_T = \nabla_{ad}$ and the convective flux is non-zero. It is common that multiple such zones can form in a model atmosphere as the local Planck function aligns with different wavelength regions of strong molecular opacities. Finally at 0.1 bar, the column absorptivity continues to decrease across many wavelengths, and the peak of the Planck function moves into a region of low absorptivity. The model level is therefore stable to convection and the internal heat is once again carried solely by the radiative flux. The atmosphere remains radiative to the top of the atmosphere as the optical depth continues to decrease.

### 2.1.7 Observable emission

As seen in Fig. 2.2, thermal photons travel through opacity windows of low absorptivity in radiative atmospheric layers, and are emitted from the top of the atmosphere. Through

this emission brown dwarfs radiate away their internal heat and cool over time. The top panel of Fig. 2.3 shows the emission spectrum from the top of the model atmosphere. The wavelength dependent opacity in brown dwarf atmospheres leads to the emitted flux being strongly wavelength dependent, and composed of emission from many different layers of the atmosphere.

To quantify the contribution of different model levels to the emission from the top of the atmosphere, we introduce the contribution function $C\mathcal{F}$ (Drummond et al. 2018), defined as

$$C\mathcal{F} = B_\lambda \frac{d[\exp(-\tau)]}{d[\log(P)]}. \tag{2.13}$$

Note that $C\mathcal{F}$ has units of $Wm^{-2}ster^{-1}$, however it is common to present the normalised
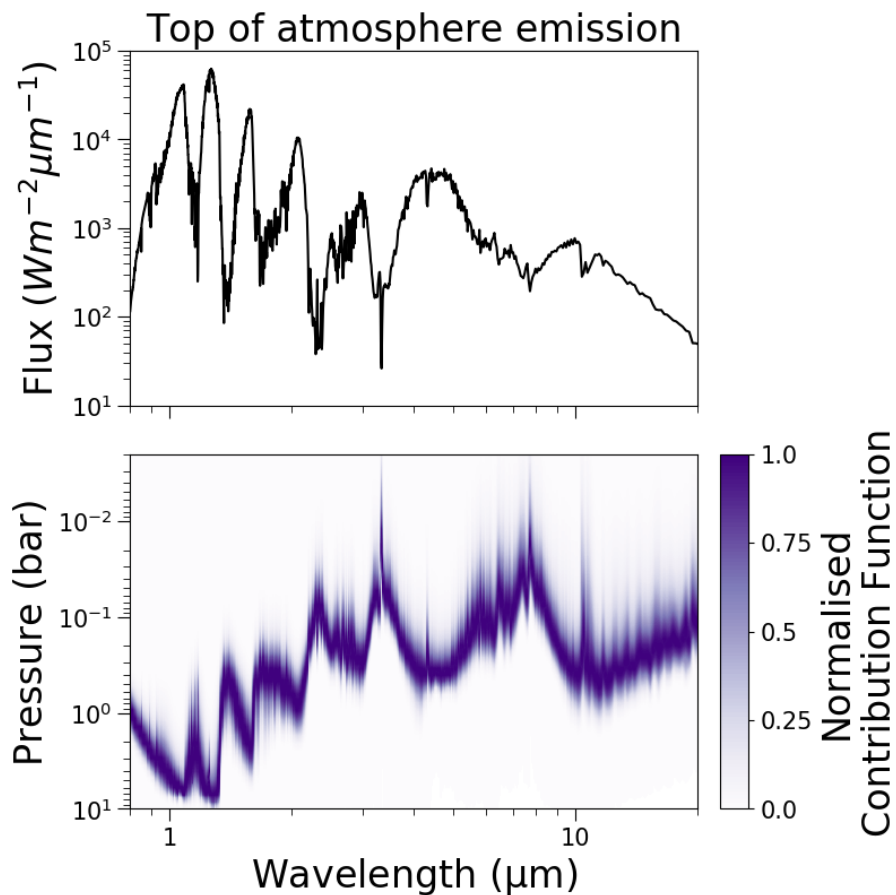


**Figure 2.3:** Top: Emission spectrum from the top of an ATMO model atmosphere. Bottom: Contour plot of the normalised contribution function, illustrating the pressure levels of the model atmosphere contributing to the emission from the top of the atmosphere at a given wavelength.

contribution function $\overline{CF}$, such that the atmospheric layer that contributes the most to the top of atmosphere emission has $\overline{CF}$ = 1. It is the normalised contribution function $\overline{CF}$ that is presented in the bottom panel of Fig. 2.3. Examining Eq. (2.13), the peak in $CF$ at a given wavelength will occur when $\tau$ = 1 since this will give the maximum gradient in $d[\exp(-\tau)]/d[\log(P)]$, and thus represents the location of the photosphere. It can be seen in Fig. 2.3 that wavelength regions of high emitted flux are formed at high pressures as the $\tau$ = 1 level lies deep in the atmosphere due to low opacity. Conversely, wavelength regions of low emitted flux are formed at lower pressures as the $\tau$ = 1 level lies higher in the atmosphere due to strong opacity.

It is the top of atmosphere emission from 1D models that can be compared to observations. The flux, $F_\lambda$, can be scaled to that of an observed object by multiplying by $R^2/D^2$, where $R$ is the radius and $D$ is the distance to the object.

## 2.2 Radiative transfer

Here I discuss the fundamentals of radiative transfer in stellar and planetary atmospheres. These details are readily available in the literature, and are presented in more depth in e.g. Rybicki & Lightman (1986); Thomas & Stamnes (2002). Radiative transfer in ATMO is also discussed in Amundsen (2015); Goyal (2019).

### Specific intensity

The fundamental quantity of radiative transfer considered here is the specific intensity (or spectral radiance) $I$, which is defined as the energy ($E$) transported by a beam of radiation at position $x$ per unit area ($A$), time ($t$), frequency ($\nu$) and solid angle ($\Omega$). A beam of radiation travelling in direction $\hat{k}$ has intensity

$$I(x, \hat{k}, \nu, t) = \frac{dE}{dA \cos\Theta \, d\Omega \, dt \, d\nu}, \tag{2.14}$$

where $\Theta$ is the angle between the direction of propagation and the unit normal of the area $dA$. An important property of the specific intensity is its implicit invariance with

distance i.e. the specific intensity remains constant along a beam of radiation provided there is no absorption, scattering or emission between the source and receiver. This is due to the solid angle dependence of $I$ which implicitly accounts for the inverse square law of radiative propagation. We now drop the position and time notation in the quantity $I$ and its subsequently derived moments for clarity.

**Plane parallel geometry**

One-dimensional models generally employ plane parallel geometry when treating radiative transfer in the atmosphere. In the plane parallel approximation, the atmosphere is divided into multiple plane parallel layers as illustrated in Fig. 2.4, each with a local temperature, pressure and density ($T$, $P$ and $\rho$ respectively). The plane parallel approximation is valid when the radial extension of the modelled atmosphere is negligible compared to the bulk radius of the object. Horizontal variations in the radiative properties are neglected by assuming azimuthal symmetry.

**Formulating the radiative transfer equation**

We now formulate a basic form of the radiative transfer equation in plane parallel geometry, which considers the change in specific intensity $dI$ of a beam of radiation over a path length $dS$, travelling at an angle $\theta$ to the normal of the plane parallel model level, given as

$$\mu\frac{dI(\nu,\mu)}{dS} = -\alpha(\nu)I(\nu,\mu) - \sigma(\nu)I(\nu,\mu) + \alpha(\nu)B(\nu,T) + \sigma(\nu)J(\nu). \tag{2.15}$$

Here $\mu$ is the cosine of the angle $\theta$. The formulation of the radiative transfer equation is illustrated in Fig. 2.4. The coefficients $\alpha(\nu)$ and $\sigma(\nu)$, describe the loss of intensity per unit length due to absorption or scattering from the beam of radiation respectively, meaning the first two terms in Eq. (2.15) represent decreases in the specific intensity, and are hence negative. The third term in Eq. (2.15) represents the gain (addition) in intensity of the beam of radiation due to thermal emission. Assuming local thermodynamic equilibrium, the emission is given by Kirchoff's law of thermal radiation as the product of the absorption
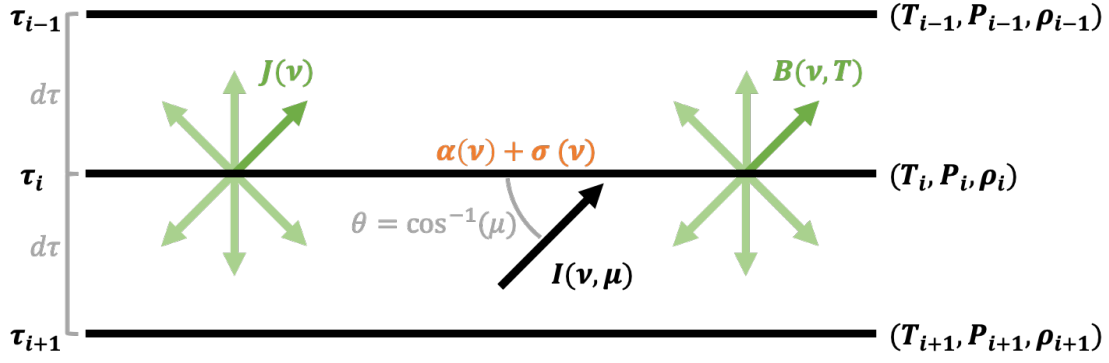
**Figure 2.4:** Illustration of plane parallel radiative transfer in a 1D model atmosphere. Plane parallel model levels are shown as horizontal black lines with a given optical depth $\tau$ and a local temperature, pressure and density ($T$, $P$ and $\rho$ respectively). A beam of radiation with specific intensity $I(\nu, \mu)$ incident at an angle $\theta$ to the $\tau_i$ model level is shown as the black arrow. Green quantities represent gains in intensity to the beam of radiation due to isotropic scattering from other beam directions $J(\nu)$ and Planck emission $B(\nu, T)$. Darker green arrows represent gains in the same direction $\mu$ as the incident beam of radiation. Orange quantities represent decreases in intensity of the beam of radiation due to absorption ($\alpha(\nu)$) and scattering ($\sigma(\nu)$).

coefficient $\alpha(\nu)$ and the Planck function $B(\nu, T)$ which is inherently isotropic.

The final term of Eq. (2.15) represents the gain (addition) in specific intensity due to the scattering of radiation from other directions into the beam direction. In this term, $J(\nu)$ is the intensity averaged over solid angle, i.e.

$$J(\nu) = \frac{1}{4\pi} \int_\Omega I(\nu, \mu) d\Omega \qquad (2.16)$$

which in plane parallel geometry assuming azimuthal symmetry becomes

$$
\begin{aligned}
J(\nu) &= \frac{1}{4\pi} \int_0^{2\pi} \int_{-1}^1 I(\nu, \mu) d\mu d\phi \\
&= \frac{1}{2} \int_{-1}^1 I(\nu, \mu) d\mu,
\end{aligned}
\qquad (2.17)
$$

where $\phi$ is the azimuthal angle. The mean intensity $J(\nu)$ is known as the zeroth moment of the specific intensity $I$. The gain in intensity due to scattering is given by

$$E_{\text{scatt}}(v, \mu) = \frac{1}{4\pi} \int_0^{2\pi} \int_{-1}^1 I(v, \mu) p(\mu, \phi, \mu', \phi') d\mu' d\phi'$$
$$= \frac{1}{2} \int_{-1}^1 I(v, \mu) p(\mu, \mu') d\mu' \tag{2.18}$$

where $p$ is the scattering phase function representing the contribution of scattered radiation from direction $(\mu', \phi')$ into the direction $(\mu, \phi)$. Assuming isotropic scattering and azimuthal symmetry, the phase function is normalised to unity, meaning that the gain in intensity due to scattering is equivalent to taking the mean intensity of all solid angles, i.e. $E_{\text{scatt}}(v, \mu) = J(v)$.

Replacing the gradient $d/dS$ with the derivative with respect to optical depth in Eq. (2.1) and recognising that the extinction coefficient $k(v) = \alpha(v) + \sigma(v)$, the radiative transfer equation can be simplfied to

$$\mu \frac{dI(v, \mu)}{d\tau} = -I(v, \mu) + S(v, \mu) \tag{2.19}$$

where $S$ is the source function defined as

$$S(v, \mu) = \frac{\alpha(v)B(v, T) + \sigma(v)J(v)}{\alpha(v) + \sigma(v)}$$
$$= \epsilon B(v, T) + (1 - \epsilon)J(v). \tag{2.20}$$

Here $\epsilon$ is the photon destruction probability defined as $\epsilon = \frac{\alpha(v)}{\alpha(v)+\sigma(v)}$.

**Solving the radiative transfer equation**

The radiative transfer equation (RTE hereafter, Eq. (2.19)) is generally difficult to solve since the source function contains an integral involving the quantity $I$ we are solving for through the mean intensity $J$ (Eq. (2.17)). This complexity is due to scattering, since to know how much radiation a layer of the atmosphere scatters into a component of the

local radiation field, requires knowledge of the local radiation field at all angles, which in turn requires knowledge of the amount of radiation other atmospheric layers have already scattered. Given this complexity, many numerical techniques have been developed to solve the radiative transfer problem in planetary and substellar atmospheres (Thomas & Stamnes 2002).

Radiative transfer is solved by `ATMO` using the discrete ordinate method, which samples a given number of ray directions ($\mu$) using Gauss-Legendre quadrature. Solving the RTE is split into an upwelling stream of radiation $I^+$ towards lower pressures, i.e. for ray directions $\mu = 0 \rightarrow 1$, and a downwelling stream $I^-$ towards higher pressures, i.e. $\mu = -1 \rightarrow 0$. A pair of boundary conditions are required to specify the downwelling radiation from the top of the atmosphere, and the upwelling radiation from the bottom of the atmosphere. At the top of the atmosphere, the downwelling intensity is assumed to be zero. The upwelling intensity from the bottom of the atmosphere is assumed to have some contribution from deeper layers, and is given by

$$I(\nu, \mu) = B(\nu, T) + \mu \frac{dB(\nu, T)}{d\tau}, \tag{2.21}$$

following Mihalas (1970). Here the gradient terms allows for a contribution to the thermal radiation from deeper atmospheric layers, and the factor of $\mu$ ensures that vertical streams of radiation have a higher contribution from the deep atmosphere.

The RTE itself is solved by `ATMO` in each model level in its integral form, given as

$$I(\tau, \nu, \mu) = -I_0(\nu, \mu) \exp\left(-\left|\frac{\tau - \tau_0}{\mu}\right|\right) + \int_{\tau_0/\mu}^{\tau/\mu} \frac{1}{\mu} S(\tau, \nu, \mu) \exp\left(\tau' - \left|\frac{\tau}{\mu}\right|\right) d\tau', \tag{2.22}$$

where $I_0$ is the incident radiation, and $\tau_0$ is the optical depth at the top of the atmosphere. Since the source function depends on the zeroth moment of the specific intensity, it is necessary to solve the Eq. (2.22) iteratively, with the initial calculation being performed with no scattering, i.e. $S(\tau, \nu, \mu) = B(\nu, T)$, and then on subsequent iterations computes

corrections to the source function including scattering, multiplied by a convergence acceleration factor applied in each layer. We direct the reader to Bueno & Bendicho (1995) for more information on this technique to solving the radiative transfer equation, known as a Gauss-Siedel type $\Lambda$ acceleration scheme.

**The radiative flux**

The flux $F(\nu)$ of radiation, otherwise known as the first moment of the specific intensity, is defined as

$$F(\nu) = \int_{\Omega} I(\nu, \mu) d\Omega, \tag{2.23}$$

which in plane parallel geometry assuming azimuthal symmetry becomes

$$\begin{aligned} F(\nu) &= \int_0^{2\pi} \int_{-1}^1 I(\nu, \mu) \mu d\mu d\phi \\ &= 2\pi \int_{-1}^1 I(\nu, \mu) \mu d\mu. \end{aligned} \tag{2.24}$$

Once the RTE has been solved in each model level, the zeroth and first moments, $J(\nu)$ and $F(\nu)$ respectively, can be calculated. To obtain the radiative flux in Eq. (2.7), we integrate $F(\nu)$ over frequency to obtain the bolometric flux $F_{\rm rad}$ in each model level i.e.

$$F_{\rm rad} = \int_0^{\infty} F(\nu) d\nu, \tag{2.25}$$

which can then be used to test for radiative-convective equilibrium.

## 2.3 Convection and mixing length theory

Convection can be modelled through mixing length theory, which uses dimensional scaling arguments to model convective fluxes. The idea behind this theory is that a displaced fluid parcel will conserve its properties over a characteristic length, known as the mixing

length, before mixing with the surrounding fluid. This approach models convection as the diffusion of heat through a turbulent medium, with the turbulent diffusivity given as

$$K_h = v_{\text{conv}} l, \tag{2.26}$$

where $l$ is the mixing length and $v_{\text{conv}}$ is the characteristic transport velocity. The mixing length is typically given in terms of the pressure scale height $H$ as $l = \alpha H$, where $\alpha$ is a free parameter.

The convective flux in `ATMO` is computed using the mixing length theory presented by (Henyey et al. 1965)

$$F_{\text{conv}} = \frac{1}{2} \rho c_P T v_{\text{conv}} \alpha \nabla, \tag{2.27}$$

where $\rho$ is the density, $c_P$ is the specific heat at constant pressure, $T$ is the temperature, and the convective efficiency $\nabla$ is

$$\nabla = \frac{\Gamma}{\Gamma + 1} (\nabla_T - \nabla_{\text{ad}}). \tag{2.28}$$

Here $\nabla_T$ is the temperature gradient as in Eq. (2.9), and $\nabla_{\text{ad}}$ is the adiabatic gradient.

We refer the reader to Henyey et al. (1965) and Gustafsson et al. (2008) for details on the computation of the convective velocity $v_{\text{conv}}$ and the efficiency parameter $\Gamma$. It is assumed that the convective flux is zero in convectively stable regions.

## 2.4   Finding the Pressure-Temperature Profile

Finding the pressure-temperature profile of a 1D model atmosphere in radiative-convective and hydrostatic equilibrium is typically done iteratively (Marley & Robinson 2015). In `ATMO`, a first guess pressure and temperature is assigned to each model level, and then the model iterates the P-T structure using a Newton-Raphson solver until Eq. (2.2) and Eq. (2.7)

are equated to a desired level of accuracy. On each iteration, chemical abundances are calculated for the current P-T structure (see Chapter 3, Section 3.1), opacities obtained from pre-computed look-up tables for individual gases (see Chapter 3, Section 3.2), and the radiative and convective fluxes calculated (Section 2.2 and Section 2.3 respectively). The P-T structure is generally considered converged in ATMO when radiative-convective flux balance and hydrostatic-equilibrium is satisfied to an accuracy of $\leq 1 \times 10^{-3}$ in each model level.

# Chapter 3

# Chemistry and Opacities

This Chapter is organised into two parts. In Section 3.1, I describe the chemical schemes used by `ATMO`, present improvements regarding the equation of state, and discuss the self-consistent coupling of a chemical relaxation scheme to model non-equilibrium chemistry due to vertical mixing. In Section 3.2, I present the atomic and molecular opacities used by `ATMO`, and detail the calculation of opacity tables.

## 3.1 Chemistry

### 3.1.1 Initial elemental abundances

Constructing a model atmosphere requires initial elemental abundances from which to derive the chemical composition. In models of brown dwarfs and giant exoplanets an appropriate and common assumption is to use solar elemental abundances i.e. the overall composition of the molecular cloud from which the solar system formed. This assumes that the modelled object, be it a brown dwarf or giant exoplanet, formed from similar material to our solar system. These primordial elemental abundances are typically derived from spectroscopic measurements of the Sun's photosphere or from mass spectroscopy of chondritic meteorites (Asplund et al. 2009; Lodders 2019).

Photospheric abundances are believed to approximately reflect the primordial composition of the solar system (Asplund et al. 2009), with notable exceptions of He and Li.

| Element | $N_i/N_H$ | Source |
|---|---|---|
| H | $1.000 \times 10^0$ | |
| He | $9.550 \times 10^{-2}$ | Asplund et al. (2009) (protosolar) |
| C | $3.162 \times 10^{-4}$ | Caffau et al. (2011) (photosphere) |
| N | $7.244 \times 10^{-5}$ | Caffau et al. (2011) (photosphere) |
| O | $5.754 \times 10^{-4}$ | Caffau et al. (2011) (photosphere) |
| Na | $1.738 \times 10^{-6}$ | Asplund et al. (2009) (photosphere) |
| K | $1.288 \times 10^{-7}$ | Caffau et al. (2011) (photosphere) |
| Si | $3.236 \times 10^{-5}$ | Asplund et al. (2009) (photosphere) |
| Ar | $2.512 \times 10^{-6}$ | Asplund et al. (2009) (photosphere) |
| Ti | $8.9125 \times 10^{-8}$ | Asplund et al. (2009) (photosphere) |
| V | $8.511 \times 10^{-9}$ | Asplund et al. (2009) (photosphere) |
| S | $1.445 \times 10^{-5}$ | Caffau et al. (2011) (photosphere) |
| Cl | $3.162 \times 10^{-7}$ | Asplund et al. (2009) (photosphere) |
| Mg | $3.981 \times 10^{-5}$ | Asplund et al. (2009) (photosphere) |
| Al | $2.818 \times 10^{-6}$ | Asplund et al. (2009) (photosphere) |
| Ca | $2.188 \times 10^{-6}$ | Asplund et al. (2009) (photosphere) |
| Fe | $3.311 \times 10^{-5}$ | Caffau et al. (2011) (photosphere) |
| Cr | $4.365 \times 10^{-7}$ | Asplund et al. (2009) (photosphere) |
| Li | $1.820 \times 10^{-9}$ | Asplund et al. (2009) (meteorites) |
| Cs | $1.202 \times 10^{-11}$ | Asplund et al. (2009) (meteorites) |
| Rb | $3.311 \times 10^{-10}$ | Asplund et al. (2009) (photosphere) |
| F | $3.631 \times 10^{-8}$ | Asplund et al. (2009) (photosphere) |
| P | $2.884 \times 10^{-7}$ | Caffau et al. (2011) (photosphere) |

**Table 3.1:** Elemental abundances used by `ATMO`

Diffusion and gravitational settling over the 4.56 Gyr lifetime of the sun mean that the protosolar He abundance is 0.05 dex higher than the present day photospheric abundance. Lithium burning has depleted the Sun of Li, and thus the primordial solar Li abundance is obtained from mass spectroscopy of meteorites.

The `ATMO` model atmospheres presented throughout this thesis are generated using solar elemental abundances from Asplund et al. (2009) and Caffau et al. (2011). These sources tabulate logarithmic abundances on a scale relative to hydrogen such that $\log(\epsilon_H) = 12$ (see Lodders 2019), meaning the logarithmic abundance for a given element $i$ is

$$\log(\epsilon_i) = 12 + \log\left(\frac{N_i}{N_H}\right), \tag{3.1}$$

where $N_i$ and $N_H$ are the number of atoms of elements $i$ and $H$ respectively. The elemental abundances $N_i/N_H$ used in `ATMO` are shown in Table 3.1.

The composition of an astrophysical object such as a star or brown dwarf is often defined by the hydrogen, helium and metal mass fractions $X$, $Y$ and $Z$ respectively. These mass fractions are defined as

$$
\begin{aligned}
X &= \frac{m_{\mathrm{H}}}{M}, \\
Y &= \frac{m_{\mathrm{He}}}{M}, \\
Z &= \sum_{i > \mathrm{He}} \frac{m_i}{M} = 1 - X - Y,
\end{aligned} \tag{3.2}
$$

where $M$ is the total mass of the system, and $m_{\mathrm{H}}$, $m_{\mathrm{He}}$ and $m_i$ are the fractional masses of the hydrogen, helium and metals the system contains. Here "metals" refers to all elements heavier than helium, and the mass fraction $Z$ is commonly termed the metallicity.

Alternatively, the metallicity can be expressed as a ratio of the number of atoms of all metals $N_{\mathrm{M}}$ to the number of hydrogen atoms $N_{\mathrm{H}}$, defining a metallicity factor [M/H] as

$$
[\mathrm{M/H}] = \log\left(\frac{N_{\mathrm{M}}}{N_{\mathrm{H}}}\right) - \log\left(\frac{N_{\mathrm{M}}}{N_{\mathrm{H}}}\right)^{\mathrm{Sun}}, \tag{3.3}
$$

where the second term on the right hand side comprises solar values. Note that it is common in the stellar community to use a metallicity factor [Fe/H] defined similarly to Eq. (3.3) but with the ratio of the number of iron atoms to the number of hydrogen atoms used instead, i.e. $N_{\mathrm{Fe}}/N_{\mathrm{H}}$ instead of $N_{\mathrm{M}}/N_{\mathrm{H}}$.

Rearranging Eq. (3.3) we obtain the expression

$$
\frac{N_{\mathrm{M}}}{N_{\mathrm{H}}} = \left(\frac{N_{\mathrm{M}}}{N_{\mathrm{H}}}\right)^{\mathrm{Sun}} \times 10^{[\mathrm{M/H}]}. \tag{3.4}
$$

The initial elemental abundances of elements heavier than helium in `ATMO` can be changed through the metallicity factor [M/H]. Solar metallicity therefore refers to [M/H] = 0, with

the elemental abundances set to the values inferred to be the primordial composition of the solar system, and [M/H] = 1 would increase the abundances of the metals by an order of magnitude.

### 3.1.2 Chemical equilibrium

**Gibbs free energy minimisation**

Once we have set the initial elemental abundances, our goal is to find the equilibrium distribution of these elements among atomic, molecular and condensate species in the atmosphere. This can be done by minimising the Gibbs free energy of a mixture of species for a fixed pressure and temperature. The method of minimising the Gibbs free energy to find the equilibrium composition of the atmosphere in `ATMO` has been presented in Drummond (2017), and I provide a brief review here. The Gibbs free energy is a thermodynamic potential analogous to mechanical potential, whereby a thermodynamic system will spontaneously minimise the Gibbs free energy to reach an equilibrium state. The Gibbs free energy $G$ is defined as

$$G = H - TS \tag{3.5}$$

where $H$ is enthalpy, $T$ temperature and $S$ entropy.

The enthalpy of formation of a chemical species can be thought of as a measure of its energy content, and the change in enthalpy $\Delta H$ quantifies the heat absorbed or released in chemical reactions as molecular bonds are broken and formed. Since physical systems tend to spontaneously move towards states of lower energy, equilibrium favours reactions that give a minimum in $\Delta H$. Additionally, the second law of thermodynamics implies that the equilibrium configuration of a thermally isolated system will have maximum entropy. Spontaneous processes in a thermally isolated system will therefore proceed in the direction of maximum entropy. Through these two principles, we can conclude that minimising the Gibbs free energy of a thermodynamic system will give the equilibrium chemical composition.

The chemical potential of a species is the energy that can be absorbed or released due to a change in the species particle number density through, for example, a chemical reaction or phase transition.  When the temperature, pressure and concentrations of all other species in the mixture are held constant, the chemical potential $\mu$ of a species $j$ is defined as

$$\mu_j = \left(\frac{\partial G}{\partial N_j}\right)_{T,P,N_{i\neq j}}, \tag{3.6}$$

where $N_j$ is the number of moles of species $j$ per kilogram of the total mixture.

Given the definition of the chemical potential, Eq. (3.6), we can write the Gibbs free energy of a system of $J$ chemical species at constant pressure and temperature as

$$G = \sum_{}^{J} \mu_j N_j. \tag{3.7}$$

To find the equilibrium composition of $J$ species at a constant pressure and temperature, the Gibbs free energy, Eq. (3.7), is minimised subject to the constraint of elemental conservation, i.e. conserving the total amount of each element in the total mixture of chemical species. This is expressed mathematically as

$$\sum_{j=1}^{J} a_{ij} N_j - b_i = 0, \tag{3.8}$$

where $i = 1, \ldots, I$ and $I$ is the total number of different elements in the mixture, $a_{ij}$ is the number of atoms of element $i$ in species $j$, and $b_i$ is the total number of atoms of element $i$ per kg of the mixture.

ATMO solves for the chemical equilibrium composition in each model level by minimising Equation (3.7) subject to the condition of Eq. (3.8) following the procedure outlined in Gordon & McBride (1994), which uses the method of Lagrange multipliers and Newton-Raphson iterations to solve the system of linear equations.

The method of Gibbs minimisation of Gordon & McBride (1994) allows for the treatment of condensation. First, a mixture containing only gas-phase species is used in the calculation, and is converged to a state of minimum $G$. Once this has been achieved, a test is performed to assess whether adding one or more condensate species will further minimise $G$. If this test is satisfied, then the condensate species which reduces $G$ the most is added to the calculation, and the new mixture is re-converged to a state of minimum $G$. Only one species is added to the mixture at a time, and this process is repeated until $G$ can no longer be reduced by the addition of condensate species to the mixture.

**Local and Rainout Condensation**

`ATMO` considers two options when calculating chemical equilibrium abundances including condensate species (Drummond 2017; Goyal et al. 2019):

1. Local condensation - when condensate species form, the gas-phase abundances of elements contained within the condensate species are depleted locally in each model level. Each model level is treated independently and has the same initial elemental abundances.

2. Rainout condensation - when condensate species form, the gas-phase abundances of elements contained within the condensate species are depleted from the current model level and all levels above (towards lower pressures). Each model level is therefore not independent and can have different initial elemental abundances, as elements contained within condensates are progressively depleted along the P-T profile, from high to low pressures in the atmosphere.

The local condensation approach assumes that the formation of condensate species in a given atmospheric layer does not affect the availability of elements for the formation of species elsewhere at other pressure levels in the atmosphere. In contrast, the rainout condensation approach assumes that when condensate species form, they settle or sink in the atmosphere, depleting the elements available to form species at lower pressures in the atmosphere.

Evidence for rainout condensation has been found in the retrieved abundances of

alkali metals in late T and Y dwarfs (Line et al. 2017; Zalesky et al. 2019). Therefore, the rainout condensation approach is used in the `ATMO` models presented in later chapters in this thesis.

**Thermochemical data**

Calculating the chemical equilibrium abundances requires thermochemical data on each individual species included in the mixture. McBride et al. (1993, 2002) present such data in the convenient form of coefficients of polynomials that have been fitted to the thermodynamic data of many species. These fits are performed over a temperature range typically between 200 K and 6000 K and a constant reference pressure of 1 bar. These polynomials are easily digestible by `ATMO`, and the general form is dimensionless and given by

$$\frac{C_P^o(T)}{R} = \sum_{i=1}^{I} a_i T^{q_i}.$$

(3.9)

Here $C_P^0$ is the heat capacity at a constant pressure of a given species, $R$ is the universal gas constant, $a_i$ are the polynomial coefficients, $q_i$ are integer temperature exponents. Typically, $I = 7$ and $q_i = -2, \ldots, 4$.

The enthalpy, entropy and chemical potential of an individual species can be related thermodynamically to $C_P^o(T)$ as

$$\frac{H^o(T)}{RT} = \frac{b_1}{T} + \frac{\int C_P^o(T) dT}{RT}$$

(3.10)

$$\frac{S^o(T)}{R} = b_2 + \int \left( \frac{C_P^o(T)}{RT} \right) dT$$

(3.11)

$$\frac{\mu^o(T)}{RT} = \frac{H^o(T)}{RT} - \frac{S^o(T)}{R}$$

(3.12)

where $b_1$ and $b_2$ are integration constants.

Since these thermodynamic quantities are defined at a standard reference pressure, it is necessary to convert to any pressure and temperature in a given `ATMO` model level.

Following Gordon & McBride (1994), for gas phase species this can be done with the relation

$$\mu_j(T, P) = \mu_j^o(T) + RT \ln \left( P_j \right),$$ (3.13)

where $P_j$ is the partial pressure of species $j$. This can be expressed in terms of the total pressure of the system,

$$\mu_j(T, P) = \mu_j^o(T) + RT \ln \left( P \right) + RT \ln \left( \frac{N_j}{N} \right).$$ (3.14)

For condensate species, the relationship is simply $\mu_j(T, P) = \mu_j^o(T)$ (Drummond 2017).

### 3.1.3 Non-equilibrium chemistry

The Gibbs energy minimisation procedure for calculating atmospheric abundances is only valid when assuming the atmosphere is in chemical equilibrium. The chemistry of an atmosphere can be driven out of equilibrium due to processes that happen on timescales faster than the net chemical reaction timescales that bring the atmosphere back to equilibrium with the local surroundings. Non-equilibrium chemistry due to vertical mixing is a prevalent feature in the solar system and throughout the brown dwarf cooling sequence, as discussed in Section 1.3.2.

Since the Gibbs energy minimisation procedure is based on thermodynamic principles and does not contain information regarding chemical timescales, physical processes such as vertical mixing which can drive the atmospheric chemistry away from equilibrium cannot be modelled using this approach. To model such non-equilibrium processes, chemical kinetics schemes are used in 1D codes such as ATMO, which deal directly with a network of chemical reactions. Chemical kinetics schemes solve the continuity equation, which describes the net rate of change of each species $j$ in the mixture due to the production and loss of the species through chemical reactions. Discretised in a 1D column model such as ATMO, the continuity equation can be written as

$$\frac{\partial n_j}{\partial t} = \mathcal{P}_j - \mathcal{L}_j - \frac{\partial \phi_j}{\partial z},$$
                                                                                         (3.15)

where $n_j$ is the number density of species $j$, $\mathcal{P}_j$ and $\mathcal{L}_j$ are the production and loss terms respectively (Drummond et al. 2016; Drummond 2017). The $\partial \phi_j / \partial z$ term describes the vertical net transport of species $j$ into the system, and thus setting $\partial \phi_j / \partial z = 0$, i.e. assuming no net chemical transport, and solving Eq. (3.15) for each species will give the chemical equilibrium composition. Diffusion processes contributing to the vertical net transport of species are encapsulated within the single flux term $\phi_j$. Within this term is the eddy diffusion coefficient $K_{zz}$, which is poorly constrained and often treated as a free parameter in 1D atmosphere models. The eddy diffusion coefficient can be used to estimate the typical mixing timescale in the atmosphere as $t_{\mathrm{mix}} \sim H_P^2 / K_{zz}$ (Lodders & Fegley 2006), where $H_P$ is the pressure scale height.

The chemical conversion of one species to another follows a sequence of reactions forming a pathway, and the production and loss terms for each species are derived from complex chemical kinetic networks containing thousands of these reactions (Moses et al. 2011; Venot et al. 2012). The continuity equation (Eq. 3.15) must be solved for each species included in the calculation, and since $\mathcal{P}_j$ and $\mathcal{L}_j$ depend on the number density of other species in the mixture through the chemical network, the system comprises of $J$ coupled ordinary differential equations (ODEs), where $J$ is the total number of species. This system of ODEs is solved for a steady state in which $\partial n_j / \partial t = 0$, and details on how this is implemented in `ATMO` can be found in (Drummond 2017).

**Chemical relaxation**

The chemical timescales of each reaction along a chemical conversion pathway can differ by many orders of magnitude. Solving the system of coupled ODEs in the chemical kinetics scheme can therefore be a stiff problem, and generating self-consistent models with a coupled chemical kinetics scheme in a 1D or 3D atmosphere model can be computationally expensive and lead to inconsistent convergence. To address this, chemical relaxation schemes such as those presented in Cooper & Showman (2006); Tsai et al. (2018) have therefore been developed to treat disequilibrium chemistry in brown dwarf and exoplanet

atmospheres.

Chemical relaxation schemes take the approach of replacing the chemical network with a source/sink term that depends on a chemical timescale. The relaxation method rewrites Eq. (3.15) for a given species as

$$\frac{dn}{dt} = -\frac{n - n_{\text{EQ}}}{\tau_{\text{chem}}},\tag{3.16}$$

where $n_{\text{EQ}}$ is the equilibrium number density and $\tau_{\text{chem}}$ is the chemical timescale. Here the production and loss terms in Eq. (3.15) have been replaced by a source/sink term that relaxes $n$ to $n_{\text{EQ}}$ on a given chemical timescale. Whether the species in question attains chemical equilibrium depends on the competition with dynamical mixing timescales. Since Eq. (3.16) for a given species is not coupled to the equation for other species in the mixture, the system of equations is much easier to solve.

A key challenge of chemical relaxation schemes is finding the chemical timescale, which is pre-computed from the chemical networks employed by chemical kinetics schemes. As the chemical timescales of each reaction along a chemical conversion pathway can vary by several orders of magnitude, the slowest reaction along the fastest pathway, known as the rate-limiting reaction, is used to determine the chemical timescale in Eq. (3.16). Tsai et al. (2018) develop a method of identifying the rate limiting reactions for different pressure/temperature regimes in a given chemical network, and thus obtaining the chemical timescale. They find the rate-limiting reactions for 500 to 3000K, and 0.1mbar to 1kbar, and include 6 species in the scheme, $H_2O$, $CO$, $CO_2$, $CH_4$, $N_2$ and $NH_3$.

To calculate non-equilibrium chemical abundances in ATMO we have self-consistently implemented the chemical relaxation scheme of Tsai et al. (2018). We choose to adopt this chemical relaxation scheme over full chemical kinetics networks for computational efficiency and consistent convergence throughout the grid when solving for a self-consistent P-T profile. The relaxation method is more computationally efficient as it avoids the need to solve the large, stiff system of ordinary differential equations needed when using full chemical kinetics networks. The P-T profile is reconverged on the fly while integrating

over time for the non-equilibrium abundances every 50 iterations of the numerical solver. Reconverging the profile more often than every 50 iterations gives negligible differences in the final P-T structure, abundances and emission spectrum. The chemistry is integrated for a minimum of $1 \times 10^{10}$ s, and is considered converged and in a steady state when $dn/n < 1 \times 10^{-2}$ and $(dn/n)/dt < 1 \times 10^{-4}$ for all species, where $n$ is the species number density. This self-consistent non-equilibrium chemistry approach is similar to that used in hot Jupiter models presented in Drummond et al. (2016).

### 3.1.4   Equation of State

Once the chemical composition of the atmosphere has been obtained, an equation of state is required to obtain properties such as the gas density $\rho(P,T)$, specific heat $C_P(P,T)$, and adiabatic gradient $\nabla_{\text{ad}}$ throughout the atmosphere. The relatively low densities and temperatures of brown dwarf atmospheres mean the gas can be assumed to be ideal (Saumon et al. 1995), and thus the density in each model level can be obtained using the ideal gas law,

$$\rho(P,T) = \frac{mP}{k_B T}. \tag{3.17}$$

Here $m$ is the mean molecular weight of the gas, typically measured in g/mol, which depends on the chemical composition of the atmosphere and is calculated as

$$m = \sum_{j=1}^{J_g} A_j m_j \tag{3.18}$$

where $A_j$ is the mole fraction of species $j$, $m_j$ is the species mean molecular weight, and $J_g$ is the number of gas phase species.

The specific heat and adiabatic gradient of the atmosphere can be obtained from the chemical composition using the NASA polynomials as described in Section 3.1.2, and are calculated in each ATMO model level as

$$C_P = \frac{k_B}{m} \sum_{j=1}^{J_g} A_j \left( \frac{C_P^o}{R} \right)_j, \tag{3.19}$$

$$\nabla_{\text{ad}} = \frac{1}{\sum_j^{J_g} A_j \left( \frac{C_P^o}{R} \right)_j}. \tag{3.20}$$

The quantity $(C_P^o/R)_j$ is obtained from thermodynamic data at a standard reference pressure, as described in Section 3.1.2. The pressure dependence of $C_P$ and $\nabla_{\text{ad}}$ is taken into account through the chemical composition, i.e. $A_j$, which is calculated with the Gibbs energy minimisation scheme using the chemical potential converted to any pressure and temperature in a given model level (see Eq. (3.14)).

Whilst generating models with ATMO using adiabatic gradient derived from the NASA polynomials, it was noticed that the temperature gradient in high effective temperature models ($T_{\text{eff}} > 2000\,\text{K}$) significantly differed when compared to other established models in the literature such as BT-COND (Allard et al. 2012). The ATMO models predicted much steeper temperature gradients, and thus higher temperatures at high pressures in the atmosphere.

Figure 3.1 shows the adiabatic gradient as a function of temperature computed from NASA polynomials (green line), along with the mole fractions of $H_2$, H and He as a function of temperature, for a $T_{\text{eff}} = 2400\,\text{K}$, $\log(g) = 4.0$ model. At low temperatures, the atmosphere is $H_2$ dominated meaning the gas is primarily diatomic, giving $\gamma \sim 1.4$ and $\nabla_{\text{ad}} \sim 0.28$. At higher temperatures the atmosphere becomes H dominated meaning the gas is monatomic, giving $\gamma \sim 1.66$ and $\nabla_{\text{ad}} \sim 0.4$. The NASA polynomials capture the transition from a $H_2$ dominated diatomic gas to a H dominated monatomic gas, but do not take into account the dissociation energy involved in the $H_2 \rightarrow 2H$ conversion. The dissociation energy modifies the internal energy of the gas, and thus the specific heat and adiabatic gradient.

The adiabatic gradient and the specific heat can alternatively be loaded from equation of state tables from Saumon et al. (1995) (hereafter SCVH95). SCVH95 present ther-
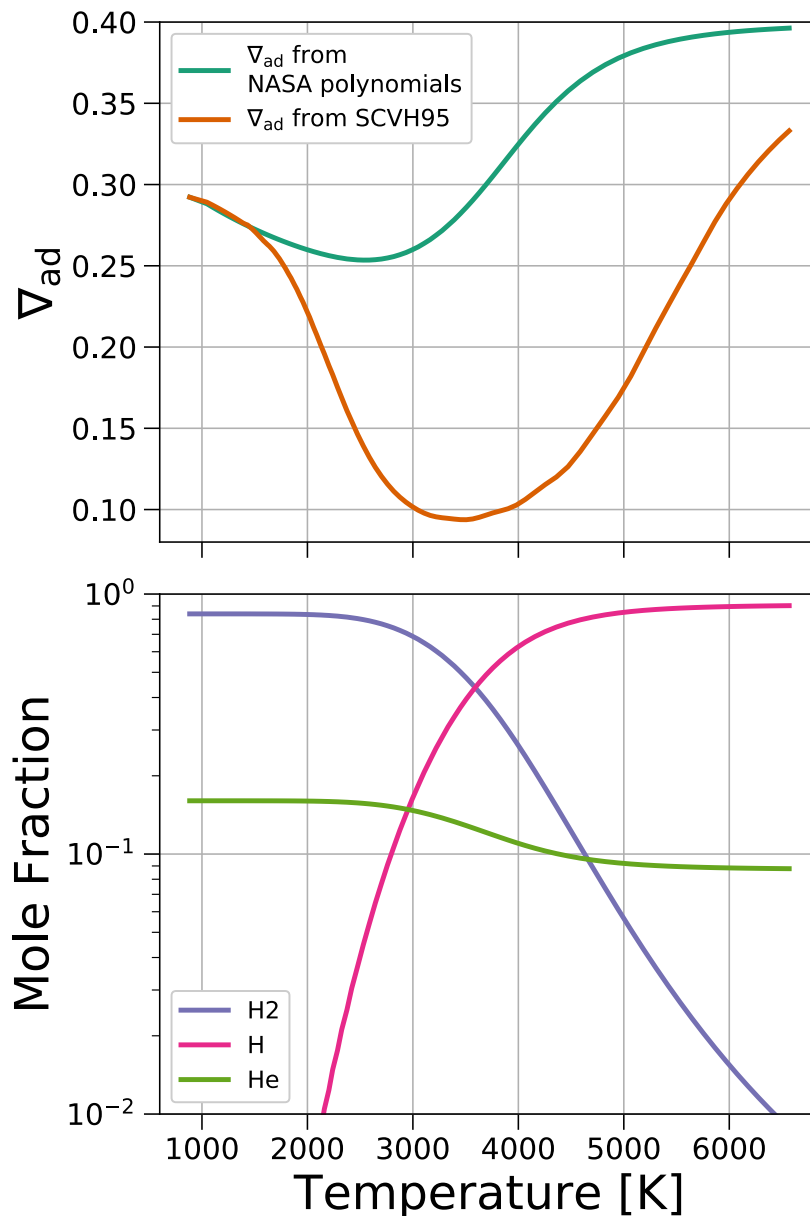
**Figure 3.1:** Top: Adiabatic gradient as a function of temperature calculated from the NASA polynomials (*green line*) and the SCVH95 (*orange line*) EOS for a fixed $T_{eff} = 2400\,$K, $\log(g) = 4.0$ pressure-temperature profile (hotter green profile in Fig. 3.2). Bottom: Mole fraction as a function of temperature for species contributing to the adiabatic gradient for the same atmospheric model.

modynamic calculations for hydrogen and helium mixtures covering a wide range in pressures and temperatures applicable for the atmospheres and interiors of low-mass stars, brown dwarfs and giant planets. The tabulated results account for non-ideal interactions important at high densities in a brown dwarf interior, and can also recover the ideal gas thermodynamics valid in the lower densities of the atmosphere. Figure 3.1 shows the adiabatic gradient from SCVH95 (orange line) for the same $T_{eff} = 2400\,$K, $\log(g) = 4.0$
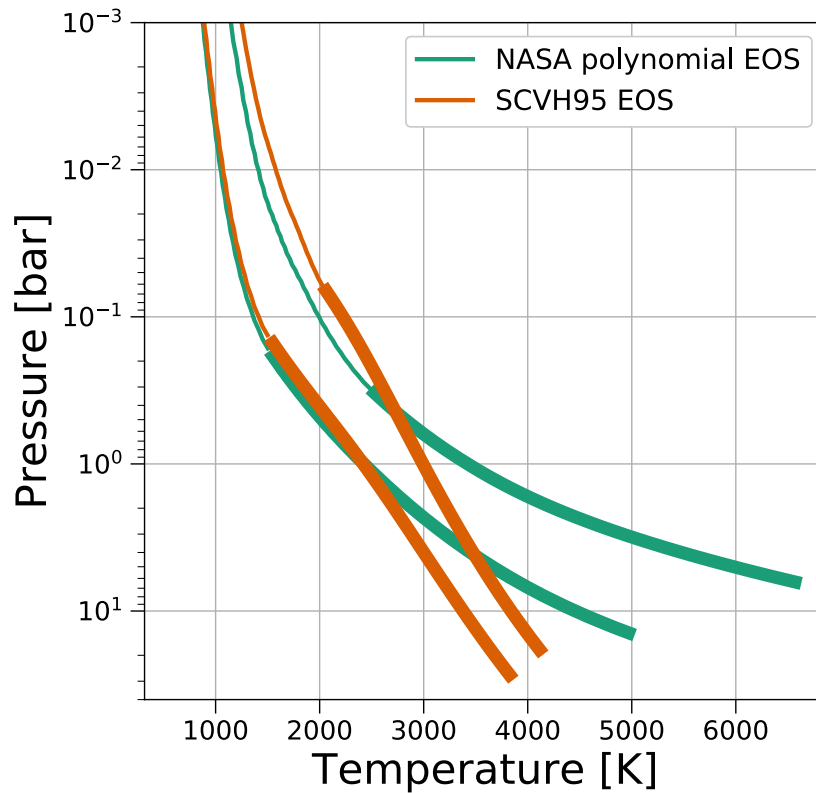
**Figure 3.2:** Pressure-temperature profiles from `ATMO` for $T_{\text{eff}}$ = 2000, 2400 K and $\log(g)$ = 4.0 calculated with the adiabatic gradient from NASA polynomials (*green line*) and the SCVH95 EOS (*orange line*). Convective regions are indicated by the thickened lines.

pressure-temperature profile. The SCVH95 EOS similarly predicts $\nabla_{\text{ad}} \sim 0.28$ in the diatomic $H_2$ region, but predicts a much lower minimum of $\nabla_{\text{ad}} \sim 0.1$ in the dissociation region. This is due to the effects of dissociation energy being taken into account in the SCVH95 EOS.

It was thus concluded that the NASA polynomials were not sufficient in modelling the adiabatic gradient in $T_{\text{eff}} > 2000$ K models where the atmosphere is hot enough to transition from being $H_2$ to H dominated. The SCVH95 EOS must therefore be used to capture the $H_2 \rightarrow 2H$ dissociation energy and correctly model the adiabatic gradient. The EOS tables from SCVH95 were therefore coupled to the `ATMO` code, to give the gas density, entropy, specific heat, adiabatic index and adiabatic gradient for a given pressure and temperature. A solar metallicity helium mass fraction $Y$ = 0.275 (Asplund et al. 2009) is used in `ATMO` to be consistent with previous models (Baraffe et al. 1998, 2003; Chabrier et al. 2000b). Since we are using a metal-free EOS, the presence of metals with mass fraction $Z$ can be mimicked by an equivalent He mass fraction $Y_{\text{eq}} = Y + Z$ (Chabrier & Baraffe

1997). `ATMO` uses $Z = 0.0169$ giving $Y_{\text{eq}} = 0.2919$ as input to the SCVH95 EOS tables.

Figure 3.2 shows self-consistent `ATMO` P-T profiles for $T_{\text{eff}} = 2000, 2400\ K$ and $\log(g) = 4.0$, calculated with the adiabatic gradient from the NASA polynomials and from the SCVH95 EOS. Models calculated with the SCVH95 EOS have shallower temperature gradients and are significantly cooler at high pressures in the atmosphere. This is due to the lower SCVH95 adiabatic gradient in the region of $H_2$ dissociation, which sets the temperature gradient in the convective region of the atmosphere. Temperature profiles computed with the SCVH95 EOS are in better agreement with other established models in the literature, such as the BT-COND models (Allard et al. 2012).

## 3.2  Opacities

Once the chemical abundances have been obtained, the opacities of important absorbers must be considered in brown dwarf and giant exoplanet atmosphere models. In this Section I review the calculation of atomic and molecular opacities for use in `ATMO`. Such calculations have been extensively detailed in Amundsen et al. (2014); Amundsen (2015); Goyal (2019).

### 3.2.1  Absorption cross-sections

The opacity of a species at a particular frequency of radiation arises from the transition between energy levels of the atom or molecule. Individual spectral absorption lines can be described by three parameters: the wavenumber of the centre of the line ($\tilde{v}_0$), the line intensity ($S(T)$) and the line profile ($\phi(\tilde{v} - \tilde{v}_0)$). The absorption cross-section $\sigma$ (or absorption coefficient per unit number density) for a given wavenumber $\tilde{v}$ is then the product of the line intensity $S_i$ and the line profile $\phi_i$ for a given transition $i$, i.e.

$$\sigma(\tilde{v}) = S_i(T)\phi_i(\tilde{v} - \tilde{v}_0). \tag{3.21}$$

The line profile $\phi(\tilde{v} - \tilde{v}_0)$ is normalised such that the integrated area under an individual line is equal to $S_i(T)$, meaning broader lines have higher opacity in the line wings

and lower opacity in the line centre, and vice versa for less broad lines. We now review the calculation of the line intensities and the line profiles.

**Line lists**

The necessary information for calculating line intensities can be found in large databases referred to as line lists, which typically tabulate either Einstein coefficients or oscillator strengths of transitions in a molecule or atom. If we consider two discrete energy levels in an atom or molecule there are three processes which can change the state of the system, each described by an Einstein coefficient. The lower energy level has energy $E$ and the upper level has energy $E + h\nu_0$, where $h$ is plancks constant and $\nu_0$ is the frequency of radiation. In the absence of a radiation field, the system can spontaneously transition from the upper to the lower energy level, emitting a photon with energy $h\nu_0$. The probability per unit time of this spontaneous emission occurring is described by the Einstein coefficient $A_{ul}$. In the presence of a radiation field, the system can transition from the lower to upper energy state by absorbing a photon of energy $h\nu_0$, or can transition from from the upper to lower state due to the radiation field stimulating the upper energy level. These processes depend on the energy density of the local radiation field, and thus the probability per unit time per unit energy density of the radiation field for absorption and stimulated emission are described by the Einstein coefficients $B_{lu}$ and $B_{ul}$ respectively.

The three Einstein coefficients are related to each other (Rybicki & Lightman 1986) by

$$A_{ul} = 8\pi hc\tilde{\nu}_0^3 B_{ul}, \tag{3.22}$$

$$g_l B_{lu} = g_u B_{ul}, \tag{3.23}$$

where $g_l$ and $g_u$ are the lower and upper level degeneracies respectively, and $c$ is the speed of light. Since the Einstein coefficients are independent of temperature, and knowing any of the three coefficients is sufficient to describe the probability of a transition, it is convenient for line lists to tabulate transitions with a corresponding Einstein coefficient

(typically $A_{ul}$) and information on the upper and lower energy levels. Occasionally, line lists tabulate oscillator strengths (or $gf$ values) instead of an Einstein coefficient. The oscillator strength can also be thought of as describing the probability of a transition, and is related to the Einstein $A_{ul}$ coefficient through

$$g_u A_{ul} = \frac{8\pi e^2 \tilde{\nu}_0^2}{m_e c} g_l f_{lu}, \tag{3.24}$$

where $e$ is the electron charge, $m_e$ the mass of the electron, and $f_{lu}$ is the oscillator strength of the transition.

One of the most widely used sources of line lists used in atmosphere models is the HITRAN database (Rothman et al. 2013). This database gives line lists at a reference temperature of 296 K and includes line intensities valid at the temperatures found in the Earth's atmosphere. Temperatures in brown dwarfs and exoplanets can reach several thousand Kelvin, meaning molecules present in the atmosphere can be excited to occupy high energy levels, and thus undergo significantly more transitions than at lower temperatures. It has been shown that the HITRAN line lists, whilst accurate for Earth's atmosphere, can underestimate the opacity at higher temperatures by many orders of magnitude (Amundsen 2015). This has led to the development of high temperature line list databases such as HITEMP (the high temperature version of HITRAN) (Rothman et al. 2010) and ExoMol (Tennyson et al. 2016), which more accurately capture the opacity in hot brown dwarf and exoplanet atmospheres. These high temperature line lists are predominantly theoretical, and are based on quantum chemistry simulations tuned to experimental results where available (Tennyson & Yurchenko 2012). The opacities used by `ATMO` are calculated from line lists mainly from the ExoMol database. The sources of opacity used in `ATMO` models throughout this work are listed in Table 3.2.

**Line intensities**

The relationship between the Einstein coefficient $A_{ul}$ and the spectral line intensity of a transition between an upper $u$ and lower $l$ state resulting is given by

**Table 3.2:** Opacity database used by `ATMO`.

| Species | Source |
|---------|--------|
| $H_2$-$H_2$, $H_2$-He | Richard et al. (2012) |
| $H^-$ | John (1988) |
| $H_2O$ | Barber et al. (2006) |
| $CO_2$ | Tashkun & Perevalov (2011) |
| CO | Rothman et al. (2010) |
| $CH_4$ | Yurchenko & Tennyson (2014) |
| $NH_3$ | Yurchenko et al. (2011) |
| Na, K, Li, Rb, Cs, Fe | Heiter et al. (2015) |
| TiO | Plez (1998) |
| VO | McKemmish et al. (2016) |
| FeH | Wende et al. (2010) |
| $PH_3$ | Sousa-Silva et al. (2015) |
| HCN | Barber et al. (2014) |
| $C_2H_2$, $H_2S$ | Rothman et al. (2013) |
| $SO_2$ | Underwood et al. (2016) |

$$S_{u,l}(T) = I_a \frac{A_{ul}}{8\pi c \tilde{\nu}_{u,l}^2} \frac{g_u e^{-E_l/k_B T}}{Q(T)} \left(1 - e^{-hc\tilde{\nu}_{u,l}/k_B T}\right), \tag{3.25}$$

where $I_a$ is the fractional isotopic abundance, $c$ is the speed of light, $E_l$ is the energy of the lower level of the transition, $g_u$ is the degeneracy of the upper level, $k_B$ is Boltzmann's constant, $T$ is the temperature, $Q(T)$ is the partition function, and $\tilde{\nu}_{u,l}$ is the wavenumber of the transition. Many line list sources such as HITRAN are tabulated at a reference temperature $T_0$. It is possible to calculate the line intensity at any given temperature using

$$S_{u,l}(T) = S_{u,l}(T_0) \frac{Q(T_0)}{Q(T)} \frac{e^{-E_l/k_B T}}{e^{-E_l/k_B T_0}} \frac{\left(1 - e^{-hc\tilde{\nu}_{u,l}/k_B T}\right)}{\left(1 - e^{-hc\tilde{\nu}_{u,l}/k_B T_0}\right)}. \tag{3.26}$$

Note that the internal partition function $Q(T)$ is typically provided with the line list.

**Line broadening**

The line profile $\phi(\tilde{\nu} - \tilde{\nu}_0)$ spreads the line intensity over a wavenumber region, and is dependant on the temperature, pressure and composition of the atmosphere. In an atmosphere, there are two processes which dominate the broadening of spectral lines: Doppler and pressure broadening.

At low pressures and high temperatures the line profile is dominated by Doppler effects from the thermal motion of particles altering the frequency of radiation. This Doppler broadening of a spectral line has a Gaussian line shape function given by

$$\phi(\tilde{\nu} - \tilde{\nu}_0) = \frac{1}{\alpha_D} \sqrt{\frac{\ln 2}{\pi}} \exp\left(-\frac{\ln 2(\tilde{\nu} - \tilde{\nu}_0^2)}{\alpha_D^2}\right), \tag{3.27}$$

with $\alpha_D$ the Doppler half-width at half maximum, which is given by

$$\alpha_D = \frac{\tilde{\nu}_0}{c} \sqrt{2 \ln 2 \frac{k_B T}{m}}. \tag{3.28}$$

where $m$ is the molecular mass. It can be seen that Doppler broadening is effective at higher temperatures and for lower mass molecules.

At higher pressures in an atmosphere, collisions between particles reduce the lifetime of the upper and lower energy states, leading to a broadening of the spectral line known as pressure broadening. The line shape for pressure broadening is characterised by a Lorentzian line profile,

$$\phi_L(\tilde{\nu} - \tilde{\nu}_0) = \frac{1}{\pi} \frac{\alpha_L}{(\tilde{\nu} - \tilde{\nu}_0)^2 + \alpha_L^2}, \tag{3.29}$$

where $\alpha_L$ is the pressure broadened half-width at half maximum. The width $\alpha_L$ depends on the pressure, temperature and composition of the atmosphere in a complex way, but in brown dwarf and exoplanet models it is often approximated as (Sharp & Burrows 2007)

$$\alpha_L(P_z, T) = \sum_z \alpha_L^z(P_z, T_0) \left(\frac{T_0}{T}\right)^{n_z} \frac{P_z}{P_0}, \tag{3.30}$$

where $z$ is the perturbing species, $T_0$ and $P_0$ are a reference temperature and pressure, $P_z$ is the partial pressure of species $z$ and $n_z$ is the temperature exponent. The total pressure broadened width is the sum of the pressure broadened widths for all perturbing species.

Since the Lorentz width depends on the partial pressure of the perturbing species, only the most abundant species need to be considered, and hence the opacities used in `ATMO` only consider broadening by $H_2$ and He. We note that in high metallicity atmospheres pressure broadening from other perturbing molecules may become important, however this should not affect the solar metallicity models presented throughout this work.

The values of $\alpha_L(P_0, T_0)$ and $n_z$ in Eq. (3.30) are obtained from literature sources mostly gathered from experimental data, and are tabulated at approximately room temperature and pressure. The values of $\alpha_L(P_0, T_0)$ and $n_z$ must therefore be extrapolated to different pressures and temperatures in the absence of available data. Furthermore, $\alpha_L(P_0, T_0)$ and $n_z$ are only known for a small fraction of transitions in the line list, and must again be extrapolated to pressure broaden all transitions. Pressure broadening is therefore a significant uncertainty and challenge in the brown dwarf and exoplanet modelling community, and laboratory experiments are needed to tackle this issue.

### Calculating opacity tables

The methodology for calculating opacities for use in `ATMO` is presented in detail in Amundsen et al. (2014). The absorption coefficients are calculated on a wavenumber grid spanning $0 - 50000 \, \text{cm}^{-1}$ at a resolution of $0.001 \, \text{cm}^{-1}$, in order to capture the large number of spectral lines and strong wavenumber dependence of the opacity. Each line is broadened including both Doppler and pressure broadening with collisions from $H_2$ and He. This is done on a pressure temperature grid, with 40 logarithmically spaced pressure points from $10^{-9} - 10^3 \, \text{bar}$, and 20 logarithmically spaced temperature points in the range $70 - 3000 \, \text{K}$. There will exist large pressure-temperature regions where Doppler and pressure broadening are comparably important. Therefore a convolution of the Doppler and Lorentz profiles is used, known as the Voigt profile (see Amundsen (2015) for details). It is not necessary to compute the Voigt profile out to arbitrarily large distances from the line centre, and numerical considerations regarding line wing cutoffs are discussed in Amundsen et al. (2014).

### 3.2.2   The correlated-$k$ method

Once absorption cross-sections have been calculated, the opacity of select atoms and molecules can be included in 1D atmosphere models and used to solve the radiative transfer equation, as discussed in Section 2.2.  The radiative transfer equation must be solved at a sufficiently high wavenumber resolution to capture the opacity of all line transitions of an atom or molecule, a method known as line-by-line radiative transfer. `ATMO` can solve the radiative transfer equation at the wavenumber resolution of the opacity tables ($\Delta\tilde{\nu} = 0.001\text{cm}^{-1}$), which is at a sufficiently high resolution to be considered equivalent to line-by-line.  While this is the most accurate method of solving the radiative transfer equation, this resolution yields $10^7$ monochromatic calculations in each model level, which becomes computationally unfeasible particularly when iterating for a consistent P-T structure.  It has been shown that binning opacities into larger wavenumber bins or sampling the opacities at a lower resolution can lead to substantial errors when combining cross-sections of different gases (Amundsen et al. 2014; Garland & Irwin 2019).  Therefore care must be taken to reduce the computational expense of solving the radiative transfer equation while maintaining accuracy.

The correlated-$k$ method is a commonly used technique with roots in Earth atmospheric science (Goody et al. 1989; Lacis & Oinas 1991; Edwards & Slingo 1996), which has been successfully applied in brown dwarf and exoplanet models (Amundsen et al. 2014, 2017; Malik et al. 2017) to improve computational efficiency while maintaining acceptable accuracy when solving the radiative transfer equation. The key idea behind this technique is that the absorption coefficient will take similar values at several wavenumbers within a spectral interval, and therefore by considering the distribution of opacities we can replace integrals over wavenumber with more well-behaved integrals over a new independent variable. For example, consider the transmission $\mathcal{T}$ of radiation between $\tilde{\nu}_1$ and $\tilde{\nu}_2$ through a homogeneous medium, given by

$$\mathcal{T}(u) = \frac{1}{\tilde{\nu}_2 - \tilde{\nu}_1} \int_{\tilde{\nu}_1}^{\tilde{\nu}_2} e^{-k(\tilde{\nu})u} d\tilde{\nu}. \tag{3.31}$$

Here $u$ is the column mass density and $k(\tilde{\nu})$ is the mass absorption coefficient.  As dis-

cussed previously, solving this integral requires a high wavenumber resolution in order to capture the complex wavenumber dependence of $k(\tilde{\nu})$. However, recognising that the same value of $k(\tilde{\nu})$ will be encountered at several wavenumbers, we can combine the calculation at these wavenumbers by considering the frequency distribution of absorption coefficients $f(k)$. The fraction (or probability) of absorption coefficients between $k$ and $k + dk$ is $f(k)dk$. Following Lacis & Oinas (1991), Eq. (3.31) can be rewritten as

$$\mathcal{T}(u) = \int_0^\infty f(k)e^{-ku}dk. \tag{3.32}$$

This integral can be simplified further by considering the cumulative frequency distribution of absorption coefficients, defined as $g(k) = \int_0^k f(k')dk'$, which gives the probability of an absorption coefficient having a value less than $k$. Since the cumulative distribution is a smooth, monotonically increasing function of $k$, it can be inverted to give $k(g)$, which is known as the $k$-distribution. In the $k$-distribution, $g$ acts as a pseudo wavenumber variable. The transmission can then be written in terms of this $k$-distribution as

$$\mathcal{T}(u) = \int_0^1 e^{-k(g)u}dg. \tag{3.33}$$

The transmission over a homogeneous path can therefore be calculated by evaluating an integral over wavenumber, frequency distribution or $k$-distribution (Eq. (3.31), Eq. (3.32) and Eq. (3.33) respectively). While all three calculations are exact and provide the same result, performing the integral over the smooth, monotonic $k$-distribution provides much greater computational efficiency. Typically, only ~10 characteristic absorption coefficients of a $k-$distribution, known as $k-$coefficients, are needed to evaluate the integral in Eq. (3.33), which can then be used to solve the radiative transfer equation.

In a homogeneous atmosphere, this $k-$distribution method is exact and equivalent to a line-by-line calculation since the $g(k)$ mapping of opacities from wavenumber space is the same along any given path. Of course, real atmospheres are not homogeneous, with different atmospheric layers having different pressures, temperatures and compositions. This means that the $g(k)$ mapping of opacities from wavenumber space in one model

level can differ to that in another model level, and can lead to the mixing of wavenumbers throughout the atmosphere. This limitation can in part be overcome by choosing narrow spectral intervals, or carefully selecting interval boundaries so that only one absorber dominates each interval. The $k-$distributions can then be assumed to be correlated throughout atmosphere, leading to this technique being termed the correlated-$k$ method.

A correlated-$k$ database was created by Amundsen et al. (2014) which can be used by ATMO to solve the radiative transfer equation. The database consists of tables of $k-$coefficients for each individual opacity source, calculated on the same pressure-temperature grid as the full resolution absorption coefficient files. The $k-$ coefficients are calculated with the open source UK Met Office radiative transfer code SOCRATES (Edwards 1996; Edwards & Slingo 1996), which is described in Amundsen et al. (2014); Amundsen (2015). The tables are provided at 32-, 500-, and 5000-band spectral resolutions. The spacing in the 32-band files is shown in Table 4 of Amundsen et al. (2014), and these tables are used by ATMO when iterating for a consistent P-T structure. The 500 and 5000 bands are evenly spaced in wavenumber between 1 and $50000 \text{cm}^{-1}$, and the 5000-band tables are used to generate emission spectra shown in this work. The $k$-coefficients are mixed within the ATMO code using the methods described in Amundsen et al. (2017).

### 3.2.3   Iron opacity

Whilst developing models of brown dwarfs in this work, it was noticed that for high effective temperature models ($T_{\text{eff}} > 2000 \text{K}$) the top of atmosphere emission spectra exhibited large emission between $0.2 - 0.4 \mu\text{m}$, an example of which is shown in Fig. 3.3 in the spectrum without Fe opacity. The peak in emission for brown dwarfs lies in the near-infrared with significantly less emission at shorter wavelengths. This large flux window is therefore not realistic as it exceeds the flux in the near-infrared, and is likely due to a missing opacity source in this wavelength region. Sharp & Burrows (2007) discuss important opacity sources in this wavelength region, with the most important absorber being gaseous iron (see their Section 2.5). Indeed, iron has a comparable abundance to other major absorbing species in a $T_{\text{eff}} = 2000 \text{K}$ model atmosphere, and is more abundant than sodium and potassium. Therefore, we calculated Fe opacity for use in ATMO following the methods and
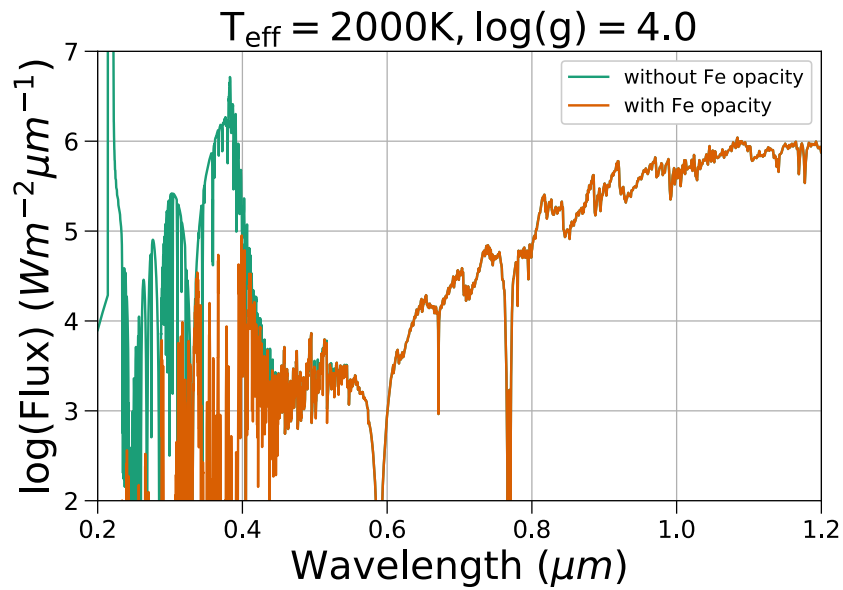
**Figure 3.3:** `ATMO` emission spectra calculated with (*orange*) and without (*green*) gaseous Fe opacity.

physics described in Section 3.2.1 and Section 3.2.2.

The line list for iron was taken from the VALD database (Heiter et al. 2015), which tabulates the oscillator strength (or $gf$ value) of $\sim 96,000$ transitions. The partition function, needed to obtain the line intensities (see Eq. (3.26)), was obtained from Sauval & Tatum (1984), which is the same source as used for the alkali metals. As discussed in Section 3.2.1, the parameters required to calculate pressure broadened line widths from collisions with $H_2$ and He are typically taken from literature sources. Unfortunately, no data were found in the literature on the pressure broadening of Fe lines from collisions with $H_2$. This is because Fe is more commonly used as an opacity source in stellar atmospheres where the temperatures are sufficiently high to dissociate molecular hydrogen. Therefore, pressure broadened line widths were calculated with Van der Waals coefficients included in the VALD line list using Equation 23 of Sharp & Burrows (2007). The use of Van der Waals coefficients to calculate pressure broadened line widths from collisions with $H_2$ and He is outlined in Amundsen (2015). A fixed factor cutoff of 1000 times the sum of the pressure and Doppler broadened line width from the centre of each line was applied to the Voigt profiles in the Fe absorption coefficient calculations. Note that in this fixed factor cutoff there is also a maximum line width applied of $100 \, \mathrm{cm}^{-1}$.

The absorption cross-section of Fe is shown in Fig. 3.4 for a pressure of 100 bar and
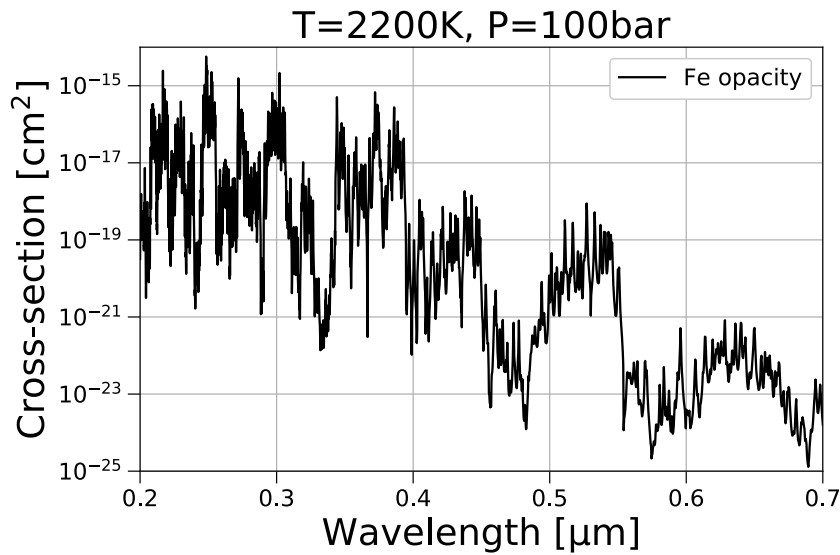
**Figure 3.4:** Absorption cross-section of atomic iron at 100 bar and 2200 K.

a temperature of 2200 K, which can be directly compared to Figure 10 of Sharp & Burrows (2007). We find good agreement between the absorption cross-section of atomic Fe calculated in this work and that presented in Sharp & Burrows (2007). Note the opacity of Fe is not calculated for wavelengths longer than $1\mu$m, as the opacity becomes negligible compared to other dominant opacity sources in the atmosphere.

Emission spectra calculated with and without Fe opacity are shown in Fig. 3.3. It can be seen that including Fe opacity reduces the flux emerging between 0.2 and $0.4\mu$m, causing the flux in this wavelength region to become small compare to the near-infrared. It is thus concluded that including Fe opacity in `ATMO` is important for modelling the emission of high effective temperature ($T_{\text{eff}} > 2000$ K) brown dwarfs.

We have also shown that gaseous Fe opacity is important in models of extremely irradiated hot Jupiters, as shown in a new grid of self-consistent `ATMO` models (Goyal et al. 2020). The large cross-sections of Fe at ultraviolet and optical wavelengths lead to strong absorption of incoming stellar radiation. This causes heating in the upper atmosphere at low pressures, and subsequently cools the deeper atmosphere at higher pressures. Thus, Fe opacity plays in important role in forming temperature inversions in hot Jupiter atmospheres.

# Chapter 4

# Potassium Line Shapes

## 4.1 The role of potassium in brown dwarf atmospheres

The alkali metals sodium Na and potassium K play a key role in brown dwarf atmospheres. They are abundant in the gas phase until they condense into KCl and $Na_2S$ (Lodders 1999), and have strong resonance doublets at $\sim 0.59\,\mu$m and $\sim 0.77\,\mu$m, respectively, that are present in late L and T dwarfs (Kirkpatrick et al. 1999; Burgasser et al. 2003b). The line shapes are determined by the potential field of $H_2$ perturbing the ground and excited states of the alkali atom, and in brown dwarf atmospheres these resonance lines become broadened out to thousands of angstroms away from the line core, shaping the visible and red-optical spectra of brown dwarfs. As such, Lorentzian line profiles are not sufficient to model the collisional broadening effects on these alkali metals (Allard & Kielkopf 1982; Burrows et al. 2000, 2002; Allard et al. 2019), and more detailed quantum mechanical calculations of the interaction potentials of these collisions are required to accurately model Na and K line shapes.

Both Burrows et al. (2003) and Allard et al. (2007b) (hereafter BV03 and A07) have presented alkali broadening calculations which can be used in 1D radiative-convective models of brown dwarfs and exoplanets. BV03 calculate the interaction potentials of the ground and excited states of Na and K perturbed by $H_2$ and He as a function of distance and orientation angle. Using these potentials BV03 computed absorption line profiles out

to thousands of angstroms from the line core. A07 similarly compute interaction potentials of Na and K perturbed by $H_2$ and He, and used the semi-classical unified line shape theory of Allard et al. (1999) to calculate the collisional profiles of the Na- and K-$H_2$ resonance lines.

Previous works with `ATMO` have used both the BV03 and A07 broadening treatments (Tremblin et al. 2015; Tremblin et al. 2016) as it remains unclear which performs best when reproducing observations. The BV03 profiles used in `ATMO` are implemented in Baudino et al. (2015). Baudino et al. (2017) benchmarked the BV03 and A07 alkali broadening schemes in a 1D radiative-convective equilibrium model showing large uncertainties in the predicted transmission spectra of hot Jupiters and the emission spectra of brown dwarfs. When generating the grid of brown dwarf atmosphere models in this work we found similar uncertainties. In particular, the differences in opacity in the far-red wing of the K doublet cause substantial differences in the predicted near-infrared spectra where the peak in brown dwarf emission lies. This has motivated us to implement the new K resonance line profiles presented in Allard et al. (2016) (hereafter A16). The A16 line profiles follow the same framework as A07, with improvements on the determination of the intermediate- and long-range part of the $K - H_2$ potential and the inclusion of spin-orbit coupling.

This Chapter is organised as follows. Details of the implementation of the new A16 potassium line shapes for use in `ATMO` are shown in Section 4.2. In Section 4.3, I compare these new line shapes to those previously used in `ATMO`, and examine the impact of these new line shapes on 1D radiative-convective models in Section 4.4. These results have been published in Phillips et al. (2020b).

## 4.2   Implementing new potassium line shapes

The opacity of potassium is calculated following the methodology described in Section 3.2. The line list is obtained from the VALD database (Heiter et al. 2015), which tabulates the oscillator strength of 1128 transitions of the K atom. Doppler and pressure broadening effects are included when calculating line profiles. The VALD line list contains van der Waals coefficients, which are used to calculate pressure broadened line widths (Sharp &

Burrows 2007) for all lines except for the K resonance doublet at $\sim 0.77\,\mu$m. For these lines, we use updated resonant line shapes from A16.

The wing profiles from A16 are tabulated as coefficients of density expansion of the dipole autocorrelation function. For a review on the density expansion of atomic spectra, the reader is referred to Royer (1971); Allard et al. (1994, 1999), and Section 3.3 of Allard et al. (2019) for a brief review of its use in opacity tables. The cross-section in the line wing profile is calculated from these tables using

$$\sigma_{\text{wing}}(\Delta\omega) = \pi r_0 f \exp\left(-\frac{n_p}{n_0}v_n\right) \sum_{i=1}^{N_{\text{exp}}} \left(\frac{n_p}{n_0}\right)^i p_i(\Delta\omega), \tag{4.1}$$

where $\Delta\omega$ is the frequency given in wavenumbers (cm$^{-1}$) relative to the unperturbed line centre of the transition, $n_p$ is the perturber density, $n_0$ is the reference perturber density at which the table was calculated, and $v_n$ is a normalisation factor. The density expansion coefficients $p_i$ are tabulated at a given $\Delta\omega$ up to order $N_{\text{exp}}$. In the A16 tables, $N_{\text{exp}} \sim 20$, whereas in the A07 tables $N_{\text{exp}} \sim 3$. This higher order expansion makes the A16 line wing profiles valid up to perturber densities of $1\times10^{21}$ cm$^{-3}$, whereas the A07 line wing profiles are only valid up to perturber densities of $1 \times 10^{19}$ cm$^{-3}$. The factor $\pi r_0 f$ acts as an area normalisation constant for the line profile integrated over $\Delta\omega$ (Allard et al. 2019), where $r_0$ is the classical radius of the electron and $f$ is the oscillator strength of the transition. The tables are provided for the D1 and D2 component of the K resonance doublet, which correspond to the $4s^2S_{1/2} - 4p^2P_{3/2,1/2}$ transitions in the atom. These tables are provided at a reference perturber density of $n_0 = 1\times10^{21}$cm$^{-3}$ and for a range of temperatures. The K resonance lines broadened by H$_2$ are provided at temperatures of 600, 820, 1000, 1500, 2000, and 3000 K. The K resonance lines broadened by He are provided at temperatures of 500, 800, 1000, 1500, 2000, 2500 and 3000 K.

While the line wing profiles are calculated from the density expansion coefficients, the profile in the line core is modelled with a Lorentzian profile with parameters calculated from the same unified line shape theory (Allard et al. 1999). The line core is determined by distant encounters that alter the lifetime of states in the K atom and can thus be modelled

**Figure 4.1:** Absorption cross-section of potassium broadened by $H_2$ calculated at $P = 10$ bar and $T = 1500$ K, which corresponds to a $H_2$ perturber density of $n_{H_2} = 4 \times 10^{19}$ cm$^{-3}$. The absorption cross-section is shown as the solid black line, with the contribution of the Lorentzian core and pressure broadened wing profiles shown as dotted red and blue lines repectively.

with a Lorentzian, while the line wings are determined by distant encounters that shift the energy levels in the K atom (Allard et al. 1999; Burrows et al. 2003). The Lorentzian core must be convolved with the line wings, which is done separately for the D1 and D2 component by taking the maximum cross-section between the core and wing at a given wavenumber. This process is shown in Fig. 4.1 at $P = 10$ bar and $T = 1500$ K, and is generally found to give a smooth junction between the core and wing profile, provided the sampling in wavenumbers is sufficiently high ($\Delta\omega = 0.01$ cm$^{-1}$).

Once the Lorentzian core and wing profiles have been combined for the D1 and D2 components, the total opacity from the resonance doublet will be the summation of each component. The contribution of each component to the total K opacity is shown in Fig. 4.2 calculated for $P = 10$ bar and $T = 1500$ K, which corresponds to $n_{H_2} = 4 \times 10^{19}$ cm$^{-3}$. The blue wing of the resonance doublet can be seen to be shaped by the broadening of the D2 component, and the far red wing is formed from the broadening of the D1 component.

To understand how the K line shapes change throughout the atmosphere, the variations of the D1 and D2 components with perturber density and temperature are shown in Fig. 4.3 and Fig. 4.4 respectively. The opacity in the wings increases linearly with $H_2$ number density in Fig. 4.3, except in the blue wing of the D2 component. The opacity in the blue wing of the D2 component does not vary linearly with density due to multi-
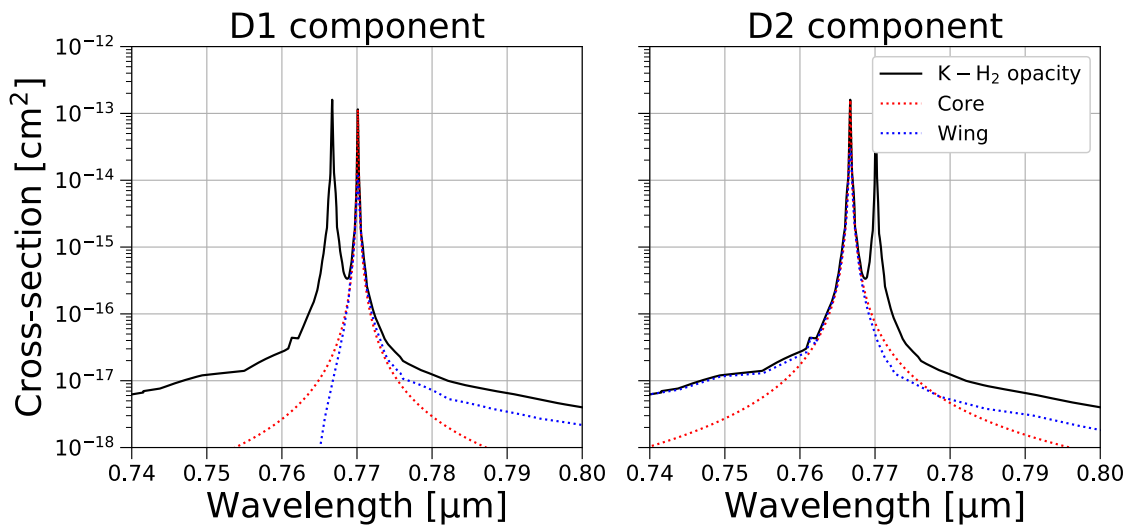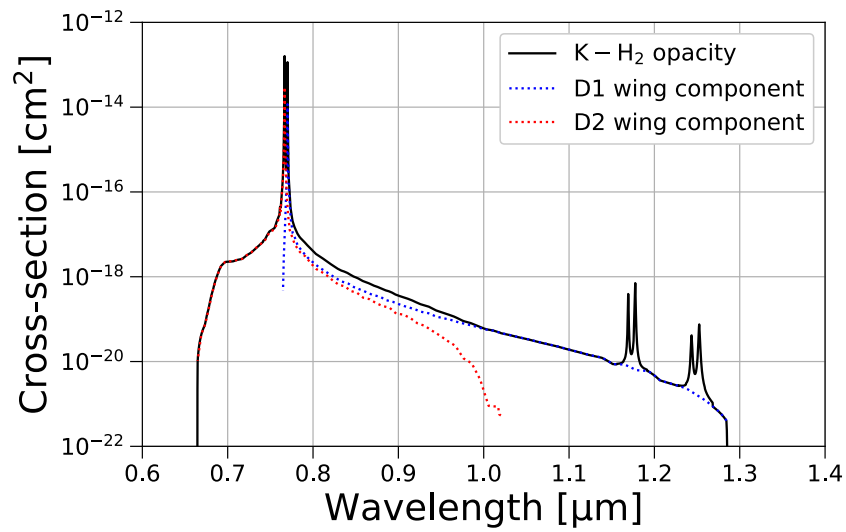
**Figure 4.2:** Absorption cross-section of potassium broadened by $H_2$ calculated at $P = 10$ bar and $T = 1500$ K, which corresponds to a $H_2$ perturber density of $n_{H_2} = 4 \times 10^{19}$ cm$^{-3}$. The absorption cross-section is shown as the solid black line, with the contribution of the D1 and D2 components shown as dotted blue and red lines respectively.
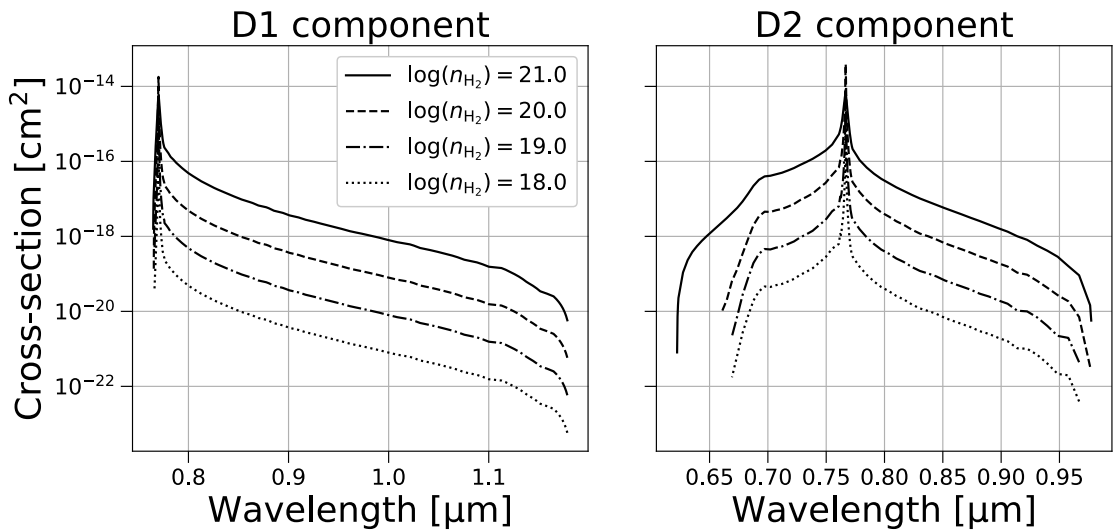


**Figure 4.3:** Variation of the D1 and D2 component wing profiles with number density of $H_2$, given in the legend with units cm$^{-3}$. The temperature is 1000 K.

ple perturber effects causing quasi-molecular line satellites (Allard et al. 2007b). A first line satellite can be noticed at $\sim 0.69\,\mu$m due to K-$H_2$, and a second satellite appears for $n_{H_2} = 10^{21}$ cm$^{-3}$ at $\sim 0.63\,\mu$m due to K-($H_2)_2$ (Allard et al. 2016). The broadening of the line wings increases with temperature, which can be seen in Fig. 4.4. At high temperatures, the D1 component extends into the near-infrared, and can thus have a significant impact on the emitted radiation from a model atmosphere.

Since $H_2$ is the most abundant species in brown dwarf and giant exoplanet atmo-
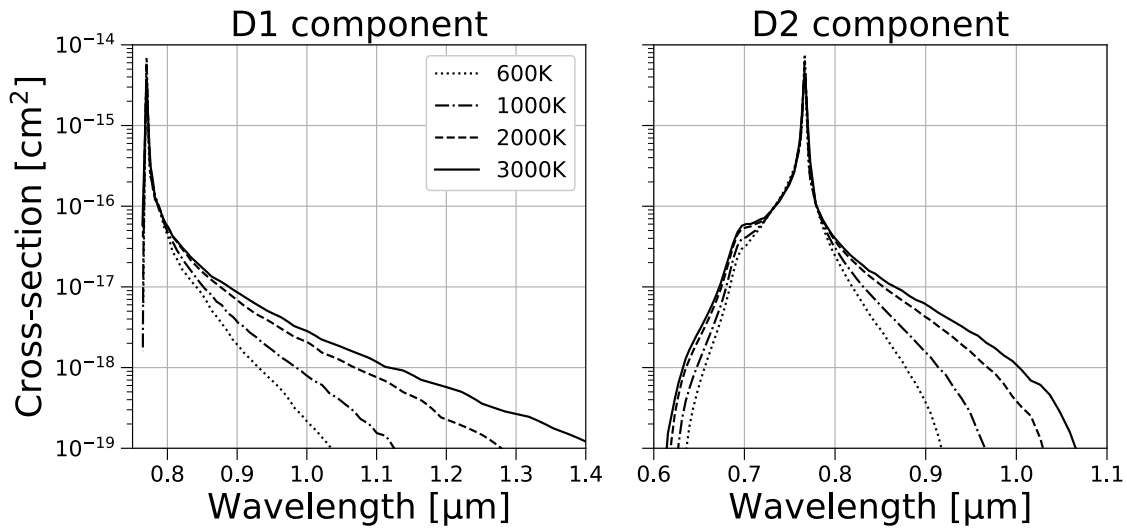
**Figure 4.4:** Variation of the D1 and D2 component wing profiles with temperature. The $H_2$ perturber density is $n_{H_2} = 1 \times 10^{21}$ cm$^{-3}$.

spheres, the opacity from the K resonance doublet is dominated by broadening from $H_2$. However, while less abundant, He also contributes to the broadening of the resonance doublet. The Lorentzian core and line wings are joined for K$-$He in the same manner as for K $-$ $H_2$. The opacities of K $-$ $H_2$ and K $-$ He are summed to obtain the total opacity, and are each weighted by the expected abundance in brown dwarf atmospheres. To do this, the number fraction of H is assumed to be $A_H = 0.91183$ (Amundsen 2015), with the number fraction of He being $A_{He} = 1 - A_H$. The dominant form of hydrogen is assumed to be $H_2$, meaning the partial pressure of a given perturber, denoted by the subscript $p$, can be calculated using

$$P_p = P \frac{A_p}{\frac{A_H}{2} + A_{He}},$$ 

(4.2)

where $P$ is the total pressure of the gas. The broadening from $H_2$ and He can then be calculated using the number density calculated from the ideal gas equation using the partial pressure of each species.

The contribution to the total opacity of K $-$ $H_2$ and K $-$ He is shown in Fig. 4.5, which is calculated at $P = 10$ bar and $T = 1500$ K. This pressure and temperature correspond to $n_{H_2} = 4.1 \times 10^{19}$ cm$^{-3}$ and $n_{He} = 7.8 \times 10^{18}$ cm$^{-3}$. The opacity can be seen to be dominated

$$n_{H_2} = 4.1 \times 10^{19} \, cm^{-3}, \, n_{He} = 7.8 \times 10^{18} \, cm^{-3}$$
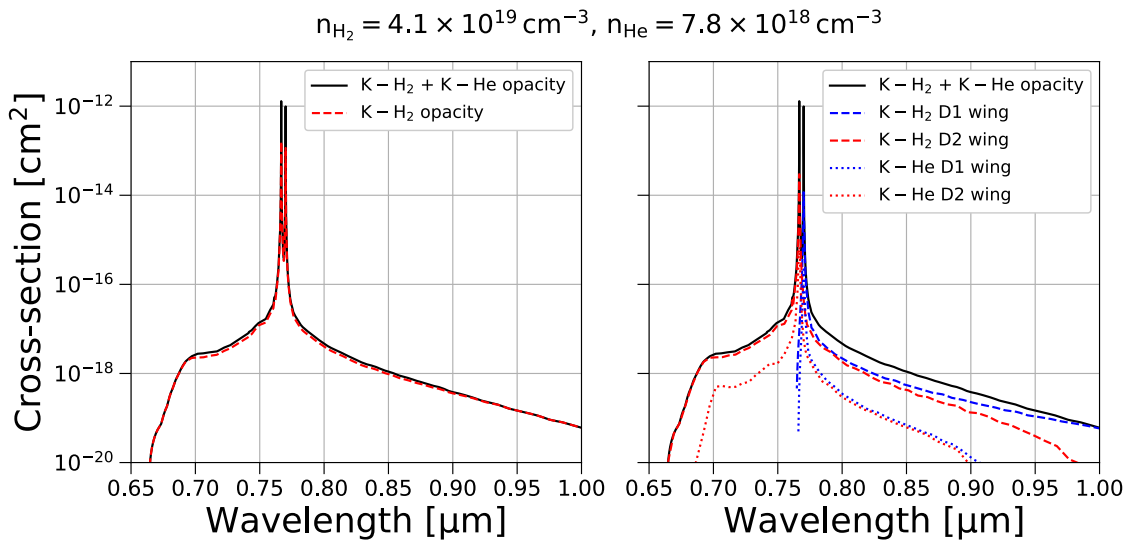


**Figure 4.5:** Left: Absorption cross-section of potassium calculated with broadening from $H_2$ and He (*solid black line*), and calculated with broadening solely from $H_2$ (*dashed red line*). Right: Absorption cross-section of potassium calculated with broadening from $H_2$ and He (*solid black line*), with the contribution of the D1 (*red*) and D2 (*blue*) components broadened by $H_2$ and He (*dashed and dotted lines respectively*).

by $K - H_2$ since $H_2$ is more abundant than He. However, $K - He$ has a small contribution to the opacity, particularly in the blue wing satellite feature between $0.7 - 0.75 \, \mu m$, and it also increases the peak of the resonance lines due to the smaller number density of He giving a less broad Lorentzian core.

## 4.3  Comparisons with other line shapes

In Fig. 4.6 I show the absorption cross section of potassium employed in `ATMO` using broadening schemes from BV03, A07, and A16, at pressures and temperatures typical of the red-optical to near-infrared photosphere of T-type brown dwarfs. The top panel displays the K opacity for P=1 bar and T=1500 K. This corresponds to a $n_{H_2} < 10^{19} \, cm^{-3}$ regime within which both the A07 and A16 profiles are valid. Therefore, the A07 and A16 wing profiles predict a similar strength quasi-molecular $K - H_2$ line satellite in the blue wing at $\sim 0.7 \, \mu m$, which is not captured by the BV03 wing profiles. The bottom panel of Fig. 4.6 shows the K absorption cross section at a higher pressure of 50 bar corresponding to a $10^{19} \, cm^{-3} < n_{H_2} < 10^{21} \, cm^{-3}$ regime within which the A07 tables are no longer valid, while the A16 profiles are. The A07 profiles therefore predict a much weaker line satellite than the A16 profiles. At both 1 and 50 bar, the opacity differs considerably in the red wing at $\sim 1 \, \mu m$, with the BV03 profiles giving significantly less absorption than the A07
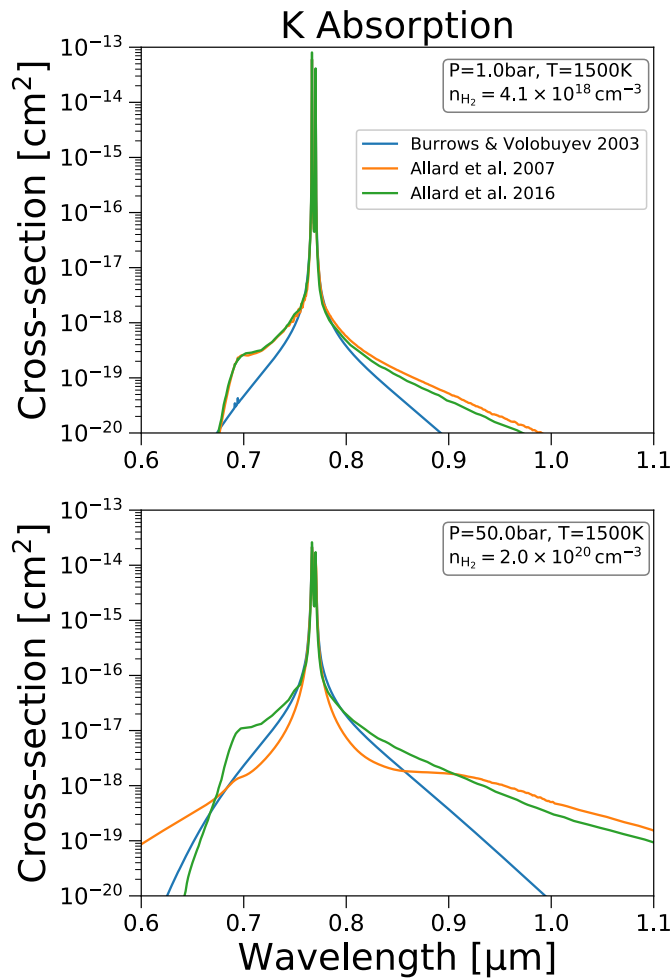
**Figure 4.6:** Absorption cross section of potassium calculated with different broadening treatments for the D1 and D2 resonance doublet, at a pressure of 1 bar and a temperature of 1500K (top panel) and a pressure of 50 bar and a temperature of 1500K (bottom panel).

and A16 profiles.

## 4.4   Impact on atmosphere models

We now investigate the impact K resonance line shapes have on 1D atmosphere models from `ATMO`. Figure 4.7 shows a synthetic red-optical and near-infrared emission spectrum of a $T_{\mathrm{eff}} = 800\,\mathrm{K}$, $\log(g) = 5.0$ T-type brown dwarf calculated with the BV03, A07, and A16 broadening schemes. The red-optical spectra in the left panel shows the difference in the emission around the potassium D1 and D2 resonance doublet. There is a noticeable difference between the emission in the blue wing around $\sim 0.7\,\mu m$ due to the $\mathrm{K} - \mathrm{H_2}$ quasi-molecular feature predicted by A07 and A16 compared to BV03. The lower absorption in the red wing in the BV03 case leads to more flux emerging through the $Y$ band at $\sim 1\,\mu m$
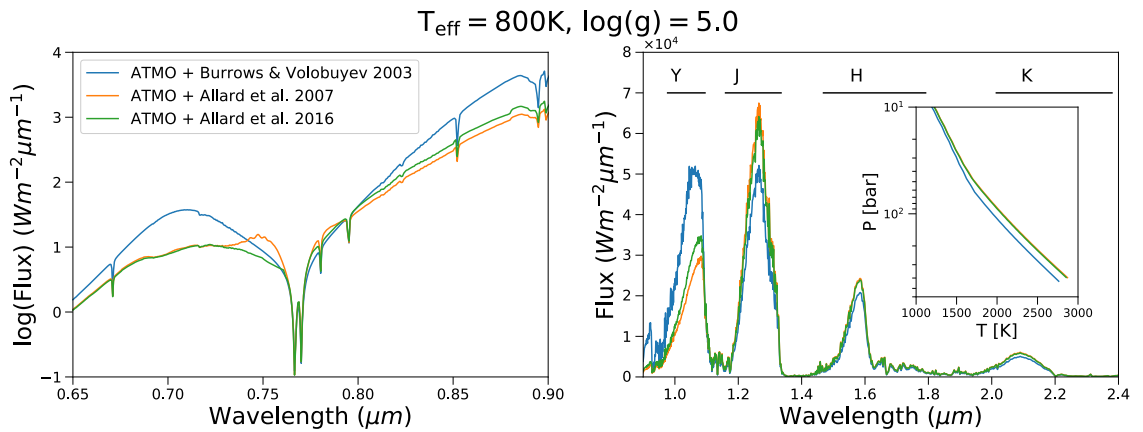
**Figure 4.7:** Comparison of the emission spectra from the top of the atmosphere for $T_{\text{eff}}$ = 800K and log(g) = 5.0 calculated with alkali broadening from BV03; A07; A16. Indicated in the right plot are the locations of the Mauna Kea near-infrared filters.

compared to the A07 and A16 cases. The large differences in opacity in the BV03 profiles compared to the A07 and A16 profiles also causes differences in the temperature profile when reconverging the atmospheric structure to find radiative-convective equilibrium. P-T profiles generated including BV03 alkali opacity are several hundred Kelvin cooler for pressures above 5 bar than profiles generated with A07 and A16 opacity. This leads to the redistribution of flux across the near-infrared seen in the right panel of Fig. 4.7. We note that this flux distribution only occurs if the model is generated self-consistently with a reconverged P-T structure when switching between opacity sources.

The biggest effect the K resonance lines have on the synthetic spectrum is in the Y band due to the extent of the red wing of the D1 component. Figure 4.8 shows the absolute Y band magnitude as a function of effective temperature in model grids calculated with BV03, A07 and A16 broadening schemes. At high effective temperatures in Fig. 4.8 there is no difference in the Y band magnitudes due to different K resonance line broadening schemes since the main of source of opacity in the Y band is FeH. At lower effective temperatures, the K-$H_2$ redwing begins to influence the Y band magnitide. This is caused by FeH becoming less abundant due to the rainout of Fe, and an increase in the number density of $H_2$ in these cooler atmospheres. Models calculated with the BV03 line profiles profiles predict brighter Y band magnitudes than A07 by up to $\sim 0.8$ mag for log($g$) = 5.0 and $\sim 0.5$ mag for log($g$) = 3.5. The differences in Y band magnitudes become more pronounced at higher gravity due to these atmospheres being cooler and denser, which
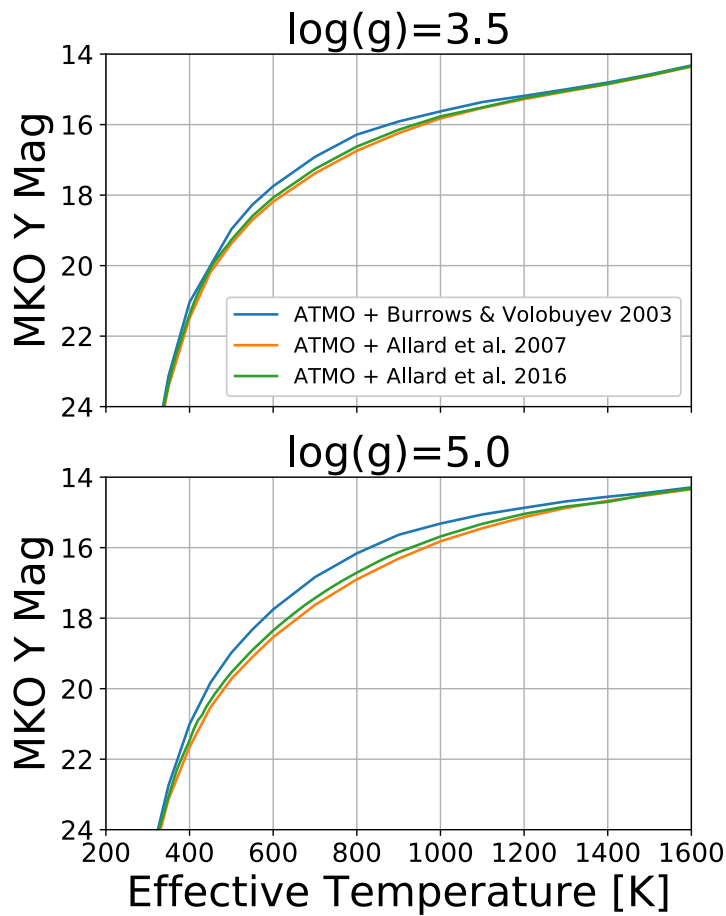
**Figure 4.8:** Absolute Y band magnitude as a function of effective temperature for $\log(g) = 3.5$ (top panel) and $\log(g) = 5.0$ (bottom panel). A constant radius of $0.1\,R/R_{\mathrm{sun}}$ was used to compute the magnitudes.

increases the opacity in the red wing of the resonance doublet. It can therefore be concluded that K resonant line broadening will be most significant in older, cooler brown dwarfs.

# Chapter 5

# A New Set of Atmosphere and Evolution Models

In this chapter, we present a new set of coupled atmosphere and evolutionary models for brown dwarfs and giant exoplanets, which we have termed `ATMO` 2020. This set of models is published in Phillips et al. (2020b), and includes numerous improvements to the input physics for modelling substellar objects. The 1D atmosphere code `ATMO` is used to generate self-consistent models with equilibrium chemistry and non-equilibrium chemistry due to vertical mixing. We include updated line lists for important molecular absorbers and improved line shapes for the pressure broadened potassium resonance lines. Finally, these atmosphere models are coupled to an interior structure model which uses a new $H - He$ equation of state from Chabrier et al. (2019) including ab initio quantum molecular dynamics calculations.

The chapter is organised as follows. In Section 5.1 we outline the details of the grid and the tools used to generate the models. The main results and features of the grid are presented in Section 5.2. The grid is then compared to others in the literature in Section 5.3 to highlight model improvements. Finally, we summarise this Chapter in Section 5.4.

## 5.1  Grid set-up and methods

### 5.1.1  Model grid

The model set consists of a grid of solar metallicity atmosphere models spanning $T_{\text{eff}} = 200 - 3000\,\text{K}$ and $\log(g) = 2.5 - 5.5$ ($g$ in cgs units), with steps of $100\,\text{K}$ for $T_{\text{eff}} > 600\,\text{K}$, $50\,\text{K}$ for $T_{\text{eff}} < 600\,\text{K}$, and $0.5$ in $\log(g)$. We note that we extend our grid of models to $T_{\text{eff}} = 3000\,\text{K}$ in order to follow the evolution of the most massive brown dwarfs from very early stages starting from hot luminous initial models. However, the range of validity of our atmosphere models is $T_{\text{eff}} \lesssim 2000\,\text{K}$ since we do not include some sources of opacity (e.g. some hydrides and condensates) that form at higher temperatures.

We generate three atmosphere grids with different chemistry schemes spanning this parameter range. The first is calculated assuming chemical equilibrium, and the second and third are calculated assuming non-equilibrium chemistry due to vertical mixing with different mixing strengths. Each model in each of the grids is generated with the `ATMO` code, and consists of a pressure-temperature (P-T) profile, chemical abundance profiles, and a spectrum of the emergent flux at the top of the atmosphere. The `ATMO` code is described in detail in Chapter 2, with the chemistry schemes and opacity database used by the model described in Chapter 3. The models are all publicly available for download[1][2].

The P-T profiles from the model atmosphere grid are then used as outer boundary conditions for the interior structure model to follow the evolution of $0.0005 - 0.075\,\text{M}_\odot$ objects from $0.001 - 10\,\text{Gyr}$. We follow the evolution of the object's effective temperature, luminosity, radius, gravity, and absolute magnitudes in a range of photometric filters. Absolute magnitudes are derived by calculating the flux density in a given photometric filter for each spectrum in the atmosphere grid. The flux density can then be interpolated to the $T_{\text{eff}}$ and $\log(g)$ for a given mass and age, and the corresponding radius used to compute the absolute magnitude. The zero point is calculated from a Vega spectrum. The evolutionary tracks for a given mass are also publicly available for download[1][2].

---

[1] http://opendata.erc-atmo.eu
[2] http://perso.ens-lyon.fr/isabelle.baraffe/ATMO2020/.

### 5.1.2  One-dimensional atmosphere model - `ATMO`

The one-dimensional atmosphere model `ATMO` used to generate atmosphere models in this grid has been previously discussed in detail in Chapter 2 and Chapter 3 of this thesis. We briefly summarise the model here for completeness.

The P-T structure is solved by `ATMO` on a logarithmic optical depth grid defined in the spectral band between 1.20 and 1.33 $\mu$m. We use 100 model levels, with the outer boundary condition in the first model level fixed at a pressure of $10^{-5}$ bar and given an optical depth of $\tau \sim 10^{-4} - 10^{-7}$ depending on $\log(g)$. The inner boundary condition in the last model level is not fixed in pressure and given an optical depth of $\tau = 1000$. A first guess pressure and temperature is assigned to each model level, and then the model iterates the P-T structure towards radiative-convective and hydrostatic equilibrium using a Newton-Raphson solver. On each iteration, chemical abundances are calculated for the current P-T structure, opacities are obtained from pre-computed look-up tables for individual gases, and the radiative and convective fluxes are calculated. The P-T structure is generally considered converged when radiative-convective flux balance and hydrostatic equilibrium is satisfied to an accuracy of $\leq 1 \times 10^{-3}$ in each model level.

`ATMO` can calculate chemical abundances assuming thermodynamic equilibrium or assuming non-equilibrium chemistry due to vertical mixing in the atmosphere. The chemistry schemes used in this work are discussed in detail in Section 3.1. Once the chemical abundances have been computed, the opacities used by `ATMO` are loaded from pre-computed correlated-$k$ tables for individual gases. The calculation of these opacities is discussed in detail in Section 3.2, and the specific improvements regarding the potassium resonance line broadening implemented in this thesis are outlined in Chapter 4. The opacities are combined within the code using the random overlap method with resorting and rebinning to get the total mixture opacity (Amundsen et al. 2017). This method ensures the opacities are completely consistent with the pressure, temperature, and abundances on every iteration.

The radiative flux is computed by solving the integral form of the radiative transfer equation in 1D plane-parallel geometry following Bueno & Bendicho (1995), which

is discussed in Section 2.2. We include isotropic scattering and sample 16 ray directions with a discrete ordinate method using Gauss-Legendre quadrature. The convective flux is computed using mixing length theory (Henyey et al. 1965) as discussed in Section 2.3, with a mixing length of 2 times the local pressure scale height. The adiabatic gradient is computed using EOS tables from Saumon et al. (1995), as discussed in Section 3.1.4.

### 5.1.3 Interior structure and evolution model

Calculations of interior structure and evolutionary models are based on the Lyon stellar evolution code, and are described in detail in Chabrier & Baraffe (1997); Baraffe et al. (1998, 2003). The structure models are based on the coupling between interior profiles and the chemical equilibrium atmospheric structures described previously at an optical depth $\tau = 1000$. We note that this is deeper than in previous models which used $\tau = 100$ to couple the atmosphere to the interior. However, the radial extension of the atmosphere at $\tau = 1000$ is still negligible compared to the total radius of the object, and thus the Stefan-Boltzmann condition ($L = 4\pi\sigma R^2 T_{\mathrm{eff}}^4$) is still satisfied. We use a solar metallicity helium mass fraction $Y = 0.275$ (Asplund et al. 2009) to be consistent with previous models (Baraffe et al. 1998; Chabrier et al. 2000b; Baraffe et al. 2003). Since we are using a metal-free EOS, the presence of metals with mass fraction $Z$ can be mimicked by an equivalent He mass fraction $Y_{\mathrm{eq}} = Y + Z$ (Chabrier & Baraffe 1997). We use $Z = 0.0169$ giving $Y_{\mathrm{eq}} = 0.2919$.

The main change in terms of inner structure input physics concerns the EOS. In this work we use the new EOS for H–He mixtures presented by Chabrier et al. (2019), which includes ab initio quantum molecular dynamics calculations in the regime of pressure dissociation and ionisation. This is a significant improvement over the semi-analytic H–He EOS of Saumon et al. (1995) (SCVH95) used in this regime in previous models (Baraffe et al. 1998; Chabrier et al. 2000b; Baraffe et al. 2003).

For the sake of comparison, we have also computed a set of evolutionary models with the SCVH95 EOS to determine the impact of the new EOS. We note that the SCVH95 EOS is used in the atmosphere models (see Section 3.1.4). There is, however, no difference between the SCVH EOS and the new EOS of Chabrier et al. (2019) in the atmospheric P-T
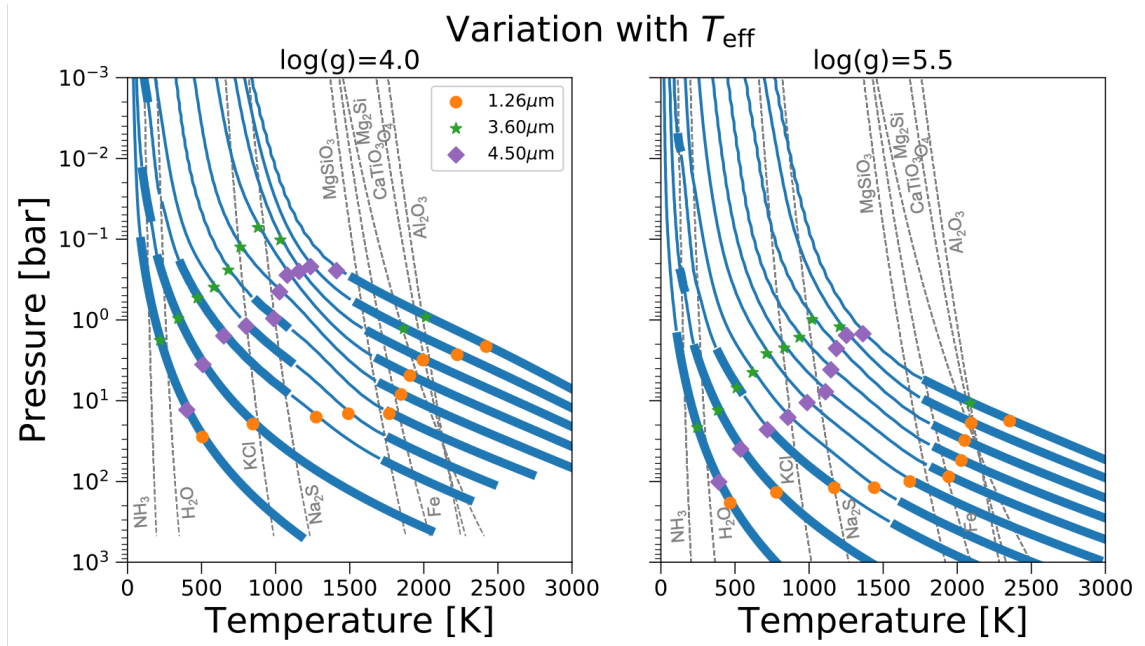
**Figure 5.1:** Self-consistent atmospheric P-T structures from the `ATMO` 2020 model grid. Each panel shows P-T structures with $T_{eff}$ =200, 300, 450, 600, 800, 1000, 1200, 1400, 1600, and 1800 K from left to right respectively, with $\log(g)$ = 4.0 (left panel) and $\log(g)$ = 5.5 (right panel). The condensation curves of major condensing species are shown as grey dashed lines. Convectively unstable regions of the model atmosphere are shown as thickened solid lines. Finally, the 1.26, 3.6 and 4.5 $\mu$m photospheres are shown as coloured markers on the profiles.

regime, which is close to a perfect gas. There is thus no inconsistency when using the SCVH EOS in the atmosphere models and the new EOS in the inner structure models.

## 5.2 The ATMO 2020 model grid

### 5.2.1 Atmospheric temperature structures

Self-consistent, chemical equilibrium P-T profiles from the `ATMO` 2020 model grid are shown in Figures 5.1 and 5.2. Figure 5.1 shows the variation of the P-T profiles with $T_{eff}$ at constant surface gravities of $\log(g)$ = 4.0 and $\log(g)$ = 5.5. Convective regions typically lie deep in the atmosphere, where the optical depth is high, thermal photons cannot propogate far, and radiative energy transport is inefficient. At cooler $T_{eff}$, detached convective zones appear at lower pressures in the P-T profiles, as the local Planck function in the model atmosphere aligns with regions of strong molecular opacity (this is discussed in Chapter 2, Section 2.1). Detached convective zones appear for $T_{eff} \leq 800$ K at $\log(g)$ = 4.0, and $T_{eff} \leq 450$ K at $\log(g)$ = 5.5, and are separated from the deep convective zones by radiative regions, within which the opacity is low enough for radiative transport to be efficient.
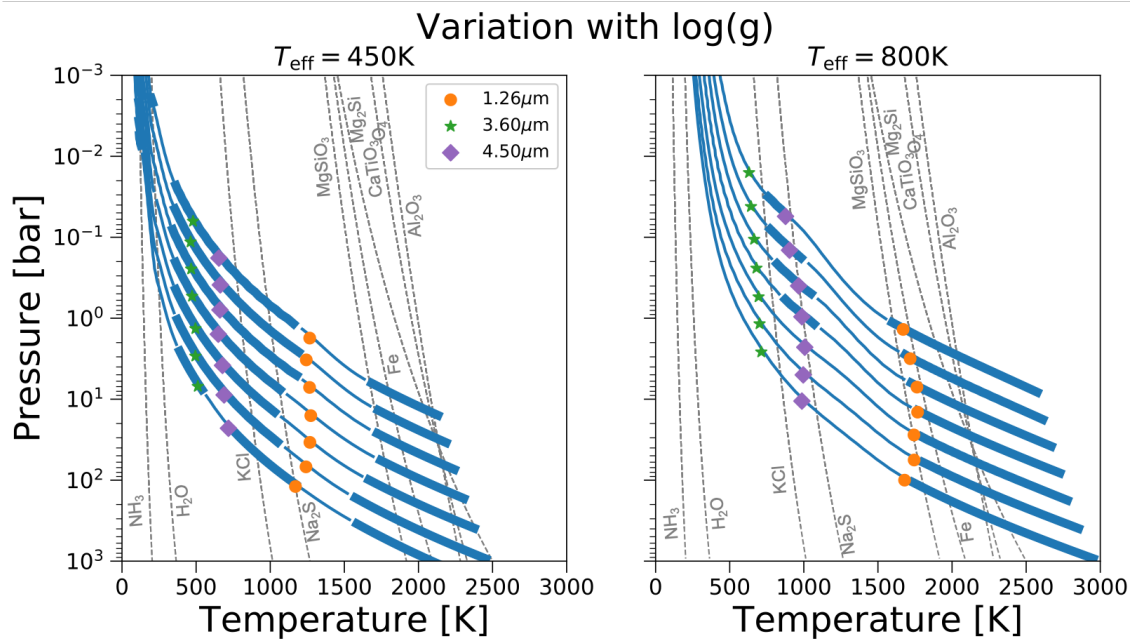
**Figure 5.2:** Same as Fig. 5.1, but showing P-T structures with $\log(g) = 2.5, 3.0, 3.5, 4.0, 4.5, 5.0$ and $5.5$ from top to bottom respectively, with $T_{\text{eff}} = 450\,\text{K}$ (*left panel*) and $T_{\text{eff}} = 800\,\text{K}$ (*right panel*).

Indicated on the profiles shown in Fig. 5.1 are the locations of the 1.26, 3.6 and 4.5 $\mu$m photospheres, which have been located using the contribution function (Eq. (2.13)). The general trend is that the photosphere moves to higher pressures with decreasing $T_{\text{eff}}$, as the local temperature of the atmosphere decreases. The 3.6 $\mu$m photosphere initially moves to lower pressures in the atmosphere between $T_{\text{eff}} = 1400\,\text{K}$ and $T_{\text{eff}} = 1600\,\text{K}$ for $\log(g) = 4.0$, and $T_{\text{eff}} = 1600\,\text{K}$ and $T_{\text{eff}} = 1800\,\text{K}$ for $\log(g) = 5.5$. This is due to $CH_4$ beginning to absorb at 3.6 $\mu$m, as it begins to be the dominant form of carbon in the upper atmosphere. The 4.5 $\mu$m photosphere gradually moves towards higher pressures, and undergoes the largest shift towards higher pressures between $T_{\text{eff}} = 1200\,\text{K}$ and $T_{\text{eff}} = 800\,\text{K}$ for $\log(g) = 4.0$, and $T_{\text{eff}} = 1400\,\text{K}$ and $T_{\text{eff}} = 1000\,\text{K}$ for $\log(g) = 5.5$. This is due to CO becoming less abundant as the dominant form of carbon becomes $CH_4$, which removes opacity from the 4.5 $\mu$m wavelength region and shifts the photosphere to higher pressure.

Figure 5.2 shows the variation of the P-T profiles with $\log(g)$ at constant effective temperatures of $T_{\text{eff}} = 450\,\text{K}$ and $T_{\text{eff}} = 800\,\text{K}$. At a given pressure level, lower gravity atmospheres have a higher local temperature. An alternative way of expressing this is that at a given optical depth, lower gravity atmospheres have lower pressures. This can be seen from the location of the 1.26, 3.6, and 4.5 $\mu$m photospheres, which are located at

lower pressures for lower gravity atmospheres, and higher pressures for higher gravity atmospheres. This can be best explained through the pressure scale height of the atmosphere (Eq. (2.5)). Consider the column density of gas $N$, from a reference location in the atmosphere with local density $n_0$, vertically to infinity. In an isothermal atmosphere with constant gravity, the column density is $N = n_0 H_P$ (Fortney 2018). Since lower gravity atmospheres have larger scale heights, the column density $N$ will increase in lower gravity atmospheres, which will increase the optical depth at a given pressure level. The photosphere will therefore lie at lower pressures in the atmosphere.

### 5.2.2  Chemistry and opacities

Figure 5.3 shows the chemical equilibrium abundances of molecules that play an important role in shaping the emission from `ATMO 2020` model atmospheres. Chemical equilibrium abundances for several values of $T_{\text{eff}}$ and $\log(g)$ are shown.

At $T_{\text{eff}} = 1200\,\text{K}$, the dominant form of carbon is $CH_4$ in the cooler upper atmosphere, and CO in the warmer deep atmosphere. Note some carbon is contained within $CO_2$, however its abundance is several orders of magnitude lower than CO and $CH_4$. The transition between CO and $CH_4$ occurs at $\sim 0.1\,\text{bar}$ for $\log(g) = 4.0$, and $\sim 15\,\text{bar}$ for $\log(g) = 5.5$, due to lower gravity atmospheres being warmer at a given pressure level (see Fig. 5.2). This transition moves to higher pressures in the atmosphere with decreasing $T_{\text{eff}}$, and by $T_{\text{eff}} = 300\,\text{K}$ the model atmosphere is completely $CH_4$ dominated at all pressures for both surface gravities shown in Fig. 5.3.

The dominant form of nitrogen is $N_2$ at $T_{\text{eff}} = 1200\,\text{K}$ for both surface gravities shown in Fig. 5.3. At $T_{\text{eff}} = 800\,\text{K}$, $N_2$ is the dominant form of nitrogen in the warmer deep atmosphere, and $NH_3$ is more abundant in the cooler upper atmosphere. Similarly to the CO to $CH_4$ transition, the $N_2$ to $NH_3$ transition occurs at higher pressures for higher $\log(g)$ and decreasing $T_{\text{eff}}$. In the $T_{\text{eff}} = 300\,\text{K}$ models shown, the atmosphere is almost completely $NH_3$ dominated at both values of $\log(g)$.

The most abundant molecule is generally $H_2O$, except at high pressures in the $T_{\text{eff}} = 1200\,\text{K}$ and $T_{\text{eff}} = 800\,\text{K}$, $\log(g) = 4.0$ model atmospheres in which CO is more abundant.
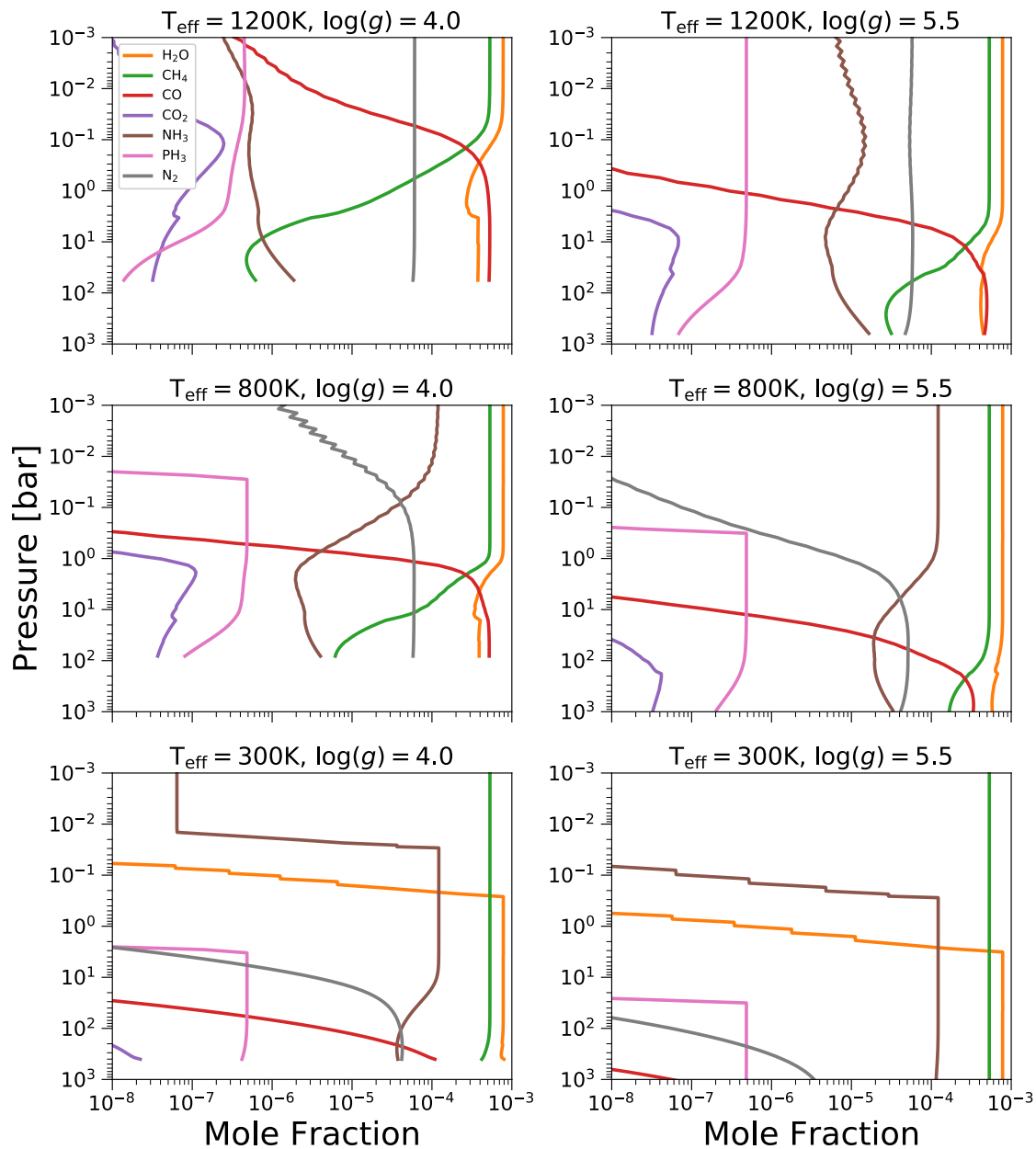
**Figure 5.3:** Chemical abundance profiles of $H_2O$, $CH_4$, $CO$, $CO_2$, $NH_3$, $PH_3$, and $N_2$ of self-consistent `ATMO` models generated under the assumption of chemical equilibrium. Columns display models with different surface gravities, and rows display models with different effective temperatures, as indicated in the plot titles.

In these model atmospheres, the $H_2O$ abundance can be seen increasing with decreasing pressure as $CO$ becomes less abundant, which frees O to form $H_2O$. In the coolest model atmospheres shown in Fig. 5.3, $H_2O$ condenses in the upper atmosphere, depleting its gas phase abundance. Similarly, $NH_3$ also condenses, depleting its gas phase abundance at lower temperatures (and thus pressures) than $H_2O$. The condensation level depends on $\log(g)$, with $H_2O$ and $NH_3$ condensing at higher pressures in higher gravity atmospheres,
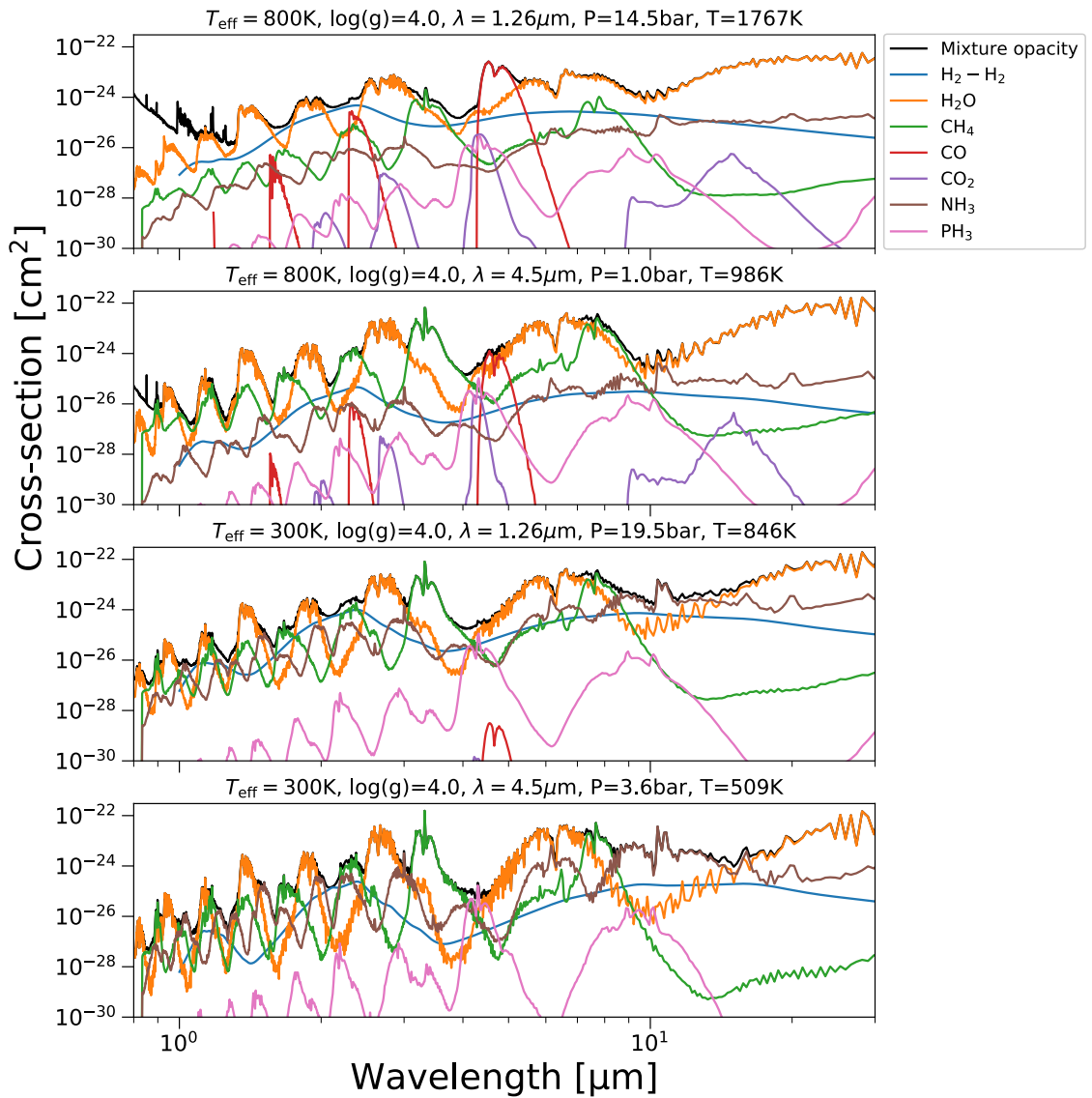
**Figure 5.4:** Abundance weighted cross-sections of the main molecular opacity sources in T and Y dwarf atmospheres. Each panel shows the opacity at the pressures and temperatures of the photosphere at a given wavelength indicated in the plot titles. The opacities are taken from models with $T_{\text{eff}} = 800\,\text{K}$ and $T_{\text{eff}} = 300\,\text{K}$, $\log(g) = 4.0$, as indicated in the plot titles.

due to high gravity atmospheres being cooler at a given pressure level.

Phosphine ($PH_3$), while less abundant than other molecules shown in Fig. 5.3, can also impact the emission spectra from a model atmosphere. Its abundance becomes significantly depleted at low pressures in the $T_{\text{eff}} = 800\,\text{K}$ and $T_{\text{eff}} = 300\,\text{K}$ model atmospheres in Fig. 5.3, due to the condensation of phosphoric acid ($H_3PO_4$). This causes phosphorous (P) to rainout of the atmosphere, depleting the abundance of $PH_3$.

The absorption cross-sections of $H_2O$, $CH_4$, $CO$, $CO_2$, $NH_3$ and $PH_3$ are shown in

Fig. 5.4. Each panel shows abundance weighted cross-sections at the pressures and temperatures of the 1.26 and 4.5 $\mu$m photospheres of the $T_{eff}$ = 800, 300 K and $\log(g)$ = 4.0 model atmospheres. This Figure serves to highlight how the wavelength dependent opacities of these molecules in brown dwarf and giant exoplanet atmospheres shape the emitted flux. $H_2O$ is the most prominent source of opacity across the spectrum, and has strong absorption bands at all pressures and temperatures shown. $H_2 - H_2$ collisionally induced absorption (CIA) adds a continuum like opacity to the spectrum, peaking at $\sim$ 2.4 $\mu$m. $H_2 - H_2$ CIA contributes to the total opacity around $\sim$ 2.4 $\mu$m and $\sim$ 4.0 $\mu$m at high atmospheric pressures.

In the $T_{eff}$ = 800 K model atmosphere, $CH_4$ opacity is stronger at 1 bar than at 14.5 bar in the atmosphere, due to its higher abundance (see Fig. 5.4). Conversely, CO and $CO_2$ opacity are stronger at 14.5 bar than at 1 bar, and influence the opacity in the $\sim$ 4.5 $\mu$m spectral region. In the cooler $T_{eff}$ = 300 K model atmosphere, $CH_4$ opacity has strengthened and has absorption bands at multiple wavelengths across the spectrum. The opacity from CO and $CO_2$ has weakened to have no influence on the total mixture opacity, and instead the $\sim$ 4.5 $\mu$m spectral region is shaped by $PH_3$ and $H_2O$ opacity. The absorption of $NH_3$ also increases in the $T_{eff}$ = 300 K model atmosphere to influence multiple wavelengths, in particular the $\sim$ 10 $\mu$m region.

### 5.2.3 Emission spectra

Figure 5.5 shows chemical equilibrium `ATMO` 2020 emission spectra for a range of $T_{eff}$ and $\log(g)$. The emission spectra are formed by the P-T profiles shown in Fig. 5.1, the chemical abundances shown in Fig. 5.3 and the opacities shown in Fig. 5.4. Absorption bands from $H_2O$, $CH_4$ and $NH_3$ increase with decreasing $T_{eff}$, carving out defined flux peaks which emerge through opacity windows. Surface gravity also has an impact on the emitted flux at a given $T_{eff}$, particularly in the K-band due to $H_2 - H_2$ CIA. Higher gravity atmospheres have lower flux in the K-band, due to higher photospheric pressures increasing the $H_2 - H_2$ CIA at this wavelength. Other differences in the low and high gravity spectra are primarily due to differing $CH_4$ and $NH_3$ abundances.
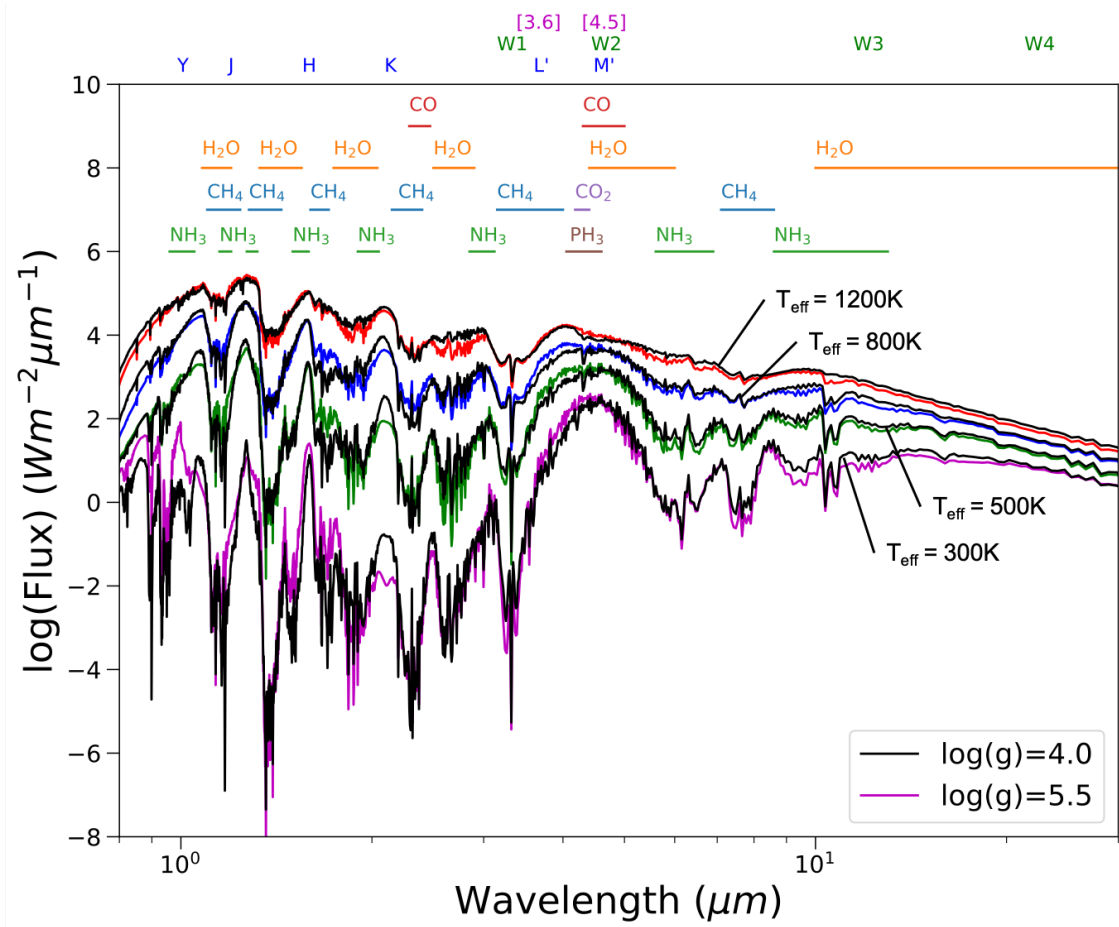
**Figure 5.5:** Emission spectra of self-consistent `ATMO` model atmospheres generated under the assumption of chemical equilibrium. Four effective temperatures are shown ($T_{\text{eff}}$ = 1200, 800, 500, 300 K) at two gravities ($\log(g)$ = 4.0, 5.5). Overplotted at the top are the approximate locations of molecular absorption features, and the locations of the Mauna Kea, WISE and *Spitzer* IRAC photometric filters.

### 5.2.4   Models with vertical mixing

Atmosphere models with non-equilibrium chemistry due to vertical mixing are calculated with `ATMO` using the self-consistently coupled Tsai et al. (2018) chemical relaxation scheme as described in Section 3.1.3. Vertical mixing in the atmosphere is parametrised using the eddy diffusion coefficient $K_{zz}$ in cm$^2$s$^{-1}$ (see Section 3.1.3), and is assumed to be constant throughout the atmosphere. We scale the eddy diffusion coefficient with surface gravity since the typical dynamical timescale $t$ can be approximated as

$$t \sim \frac{H_P^2}{K_{zz}} \propto \frac{1}{g^2 K_{zz}}, \tag{5.1}$$

where $H_P$ is the atmospheric scale height. Within this approximation, we keep the dy-
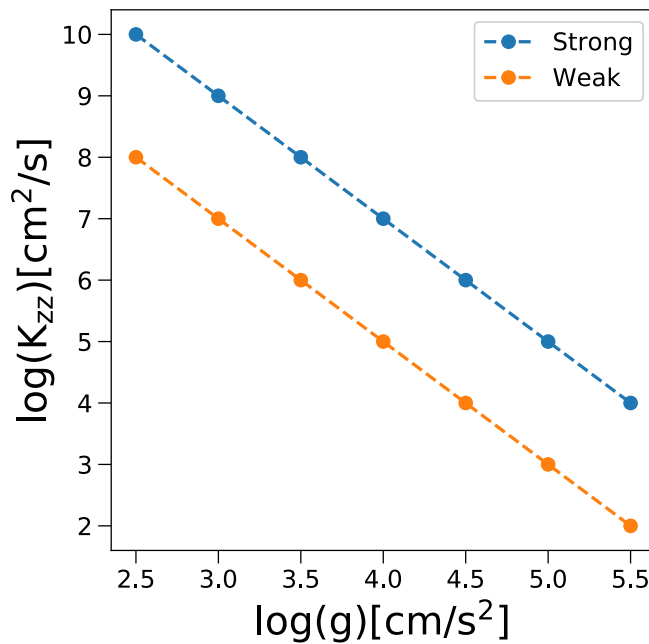
**Figure 5.6:** Vertical mixing relationships with surface gravity (strong and weak; see text) used in the generation of non-equilibrium atmosphere models in this work.

namical timescale $t$ constant by changing the value of $K_{zz}$ by an order of magnitude for a $\log(g)$ step of 0.5 within the grid. We generate atmosphere model grids with two $K_{zz}$ scaling relationships with surface gravity as shown in Figure 5.6; we refer to these relationships as 'strong' and 'weak' mixing throughout this work.

Our choice of mixing strengths come from approximate values in the literature which have been found to provide reasonable comparisons to observations of late T and Y dwarfs. For example, Leggett et al. (2017) found $K_{zz}$ values in the range $10^4$-$10^6$ cm$^2$/s provided reasonable comparison to the [4.5]-$M$ colours of late T and Y dwarfs for model sequences with a constant gravity of $\log(g) = 4.5$ (see their Figure 7). We have therefore adopted to set $\log(K_{zz}) = 4$ and $\log(K_{zz}) = 6$ in the 'weak' and 'strong' cases respectively at $\log(g) = 4.5$ and scale $K_{zz}$ with gravity.

We note that $K_{zz}$ has often been estimated by assuming it is the same diffusion coefficient as that derived from mixing length theory of convection, i.e. $D_{mix} \sim l_{mix}v_{mlt}$, with $l_{mix}$ the mixing length and $v_{mlt}$ the convective velocity (Gierasch & Conrath 1985; Ackerman & Marley 2001). This however has to be extrapolated to the convectively stable radiative regions of the atmosphere where a number of complex processes such as
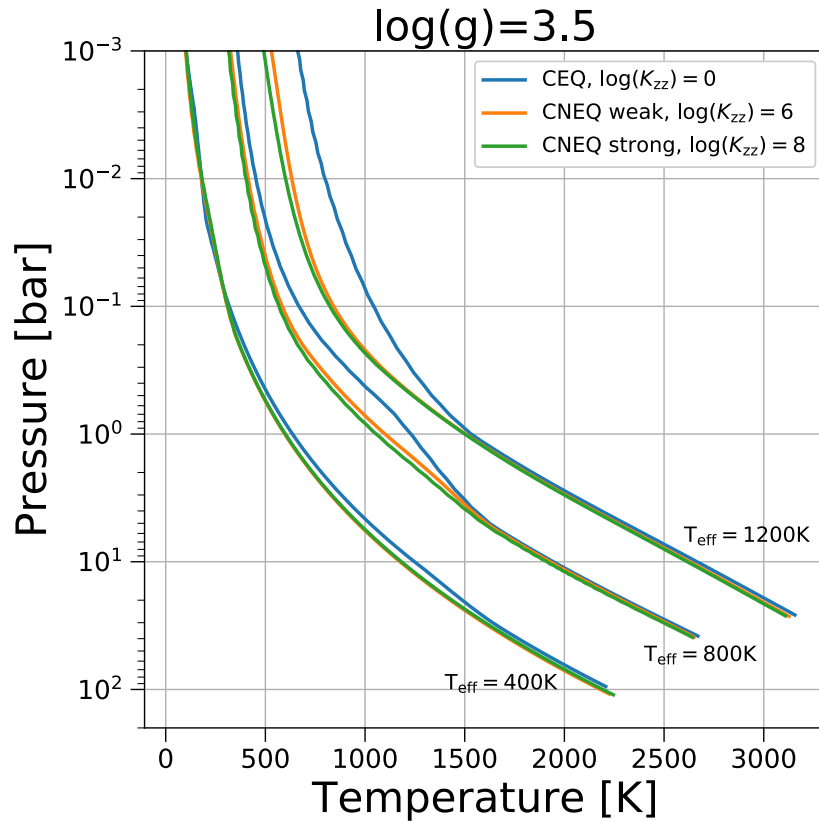
**Figure 5.7:** Self-consistent atmospheric P-T structures calculated assuming chemical equilibrium (CEQ) and non-equilibrium chemistry due to vertical mixing with different mixing strengths (CNEQ) indicated in the legend, for $T_{\mathrm{eff}} = 400, 800$ and $1200\,\mathrm{K}$.

gravity waves and convective overshooting (Freytag et al. 1996; Kupka et al. 2018) may drive the mixing. The value of $K_{zz}$ has also been approximated from 3D numerical simulations of hot Jupiters including passive tracer transport (Parmentier et al. 2013; Zhang & Showman 2018). These approaches to estimating $K_{zz}$ have their limitations and none has provided a quantitative picture that has reached a consensus in the community. In this work we therefore choose to adopt a simpler approximation for $K_{zz}$ to examine the trends of non-equilibrium chemistry in colour-magnitude diagrams (Chapter 6), and we leave more sophisticated studies of $K_{zz}$ for future work.

Figure 5.7 shows self-consistent P-T structures calculated with ATMO assuming chemical equilibrium and non-equilibrium due to vertical mixing in the weak and strong $K_{zz}$ cases. We choose to show here a low gravity of $\log(g) = 3.5$, and hence high $K_{zz}$ values, to give large, clear differences between the equilibrium and non-equilibrium chemistry models. Non-equilibrium chemistry models produce P-T structures with cooler upper at-

mospheres compared to chemical equilibrium models. This difference decreases towards lower effective temperatures. Models with stronger vertical mixing give cooler temperatures in the atmosphere than models with weaker vertical mixing, a difference which again decreases with decreasing effective temperature.

The differences in the self-consistent P-T structures can be understood by examining the chemical abundance profiles, which are shown in Figure 5.8. At $T_{\text{eff}}$ = 1200 K, the dominant carbon bearing species in the cooler, upper atmosphere is $CH_4$ and in the warmer, deeper atmosphere is CO. Vertical mixing acts to bring CO from the deep atmosphere into the upper atmosphere on timescales shorter than the chemical timescale converting CO to $CH_4$. This therefore increases the CO abundance and depletes the $CH_4$ abundance in the upper atmosphere. While significantly less abundant than CO, $CO_2$ is similarly mixed into the upper atmosphere in Figure 5.8.

The abundance of $CH_4$ is quenched by up to 2 orders of magnitude in both the weak and strong mixing cases in the $T_{\text{eff}}$ = 1200 K models in Figure 5.8. The $H_2O$ abundance is also quenched by up to a factor of ~ 3. $H_2O$ and $CH_4$ are two of the most significant opacity sources in model brown dwarf atmospheres, and therefore the depleted abundances of these species in models including vertical mixing lowers the opacity in the upper atmosphere. This results in P-T structures that are cooler in the upper atmosphere as seen in Figure 5.7.

Models with stronger vertical mixing quench species from deeper in the atmosphere due to shorter mixing timescales, which leads to stronger depletion of $CH_4$ and a larger increase in the abundance of CO. In the $T_{\text{eff}}$ = 1200 K, $\log(K_{zz})$ = 8 model the quenched mole fraction of methane is $3.7 \times 10^{-6}$, whereas in the $T_{\text{eff}}$ = 1200 K, $\log(K_{zz})$ = 6 model the quenched mole fraction is $1.4 \times 10^{-5}$. This difference in abundance translates into a difference in opacity, and causes models with strong vertical mixing to be cooler in the upper atmosphere than models with weak vertical mixing in Figure 5.7.

At lower effective temperatures the dominant carbon bearing species becomes $CH_4$ throughout the atmosphere, as can be seen in the $T_{\text{eff}}$ = 400 K models in Figure 5.8. The change in $CH_4$ abundance due to vertical mixing is therefore smaller at lower effective
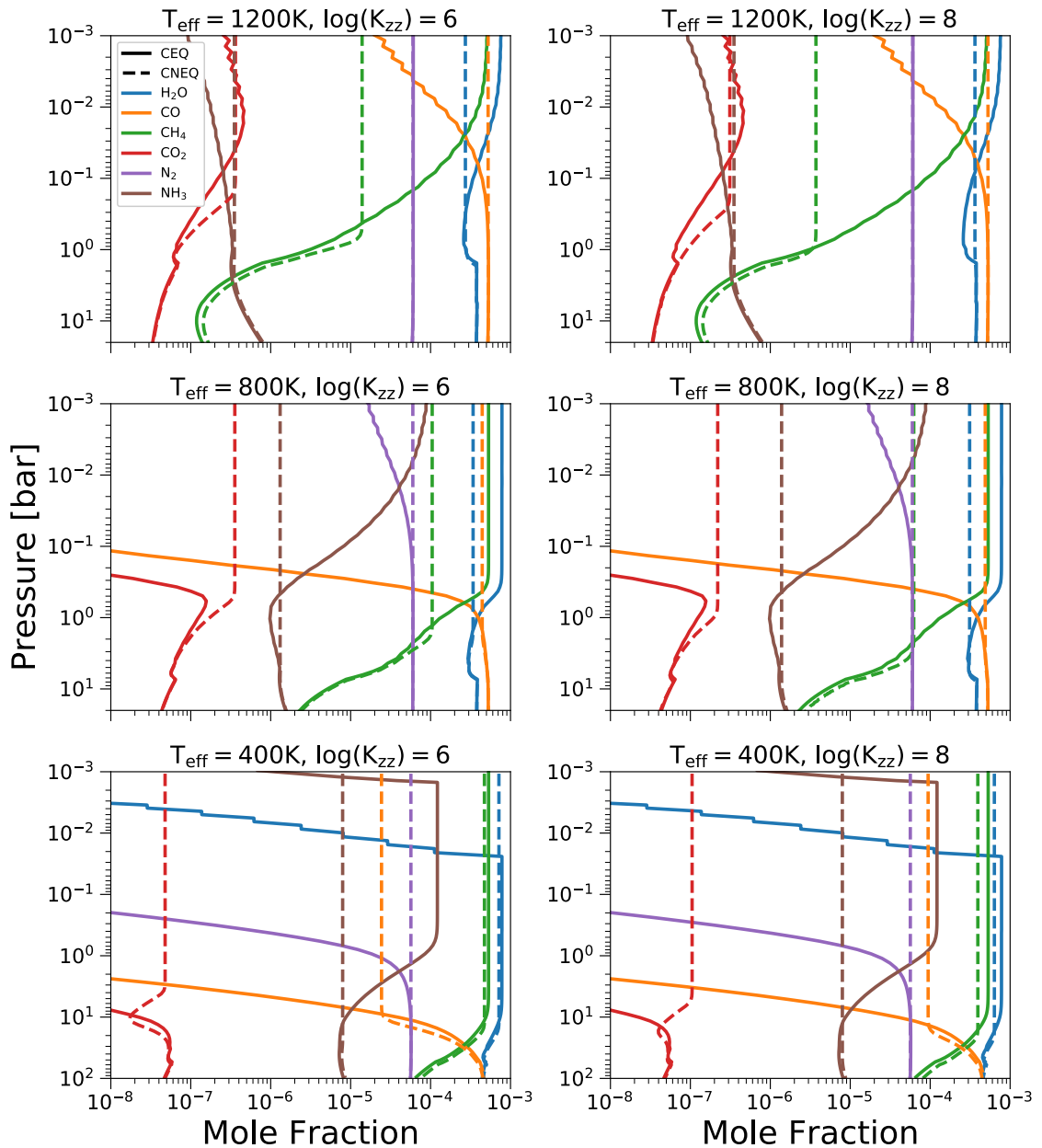
**Figure 5.8:** Chemical abundance profiles of $H_2O$, CO, $CH_4$, $CO_2$, $N_2$, and $NH_3$ of self-consistent `ATMO` models generated under the assumption of chemical equilibrium (solid lines) and non-equilibrium chemistry due to vertical mixing (dashed lines). Non-equilibrium models calculated with the weak and strong $K_{zz}$ mixing relationship are shown in the left and right columns respectively. The rows display models with different effective temperatures, as indicated in the plot titles. These chemical abundance profiles correspond to the P-T profiles shown in Figure 5.7 and have $\log(g) = 3.5$. Note that in some cases the abundance profile of a given species lies below the profile of another species.

temperatures, giving a smaller change in opacity in the upper atmosphere. This causes smaller temperature differences in the P-T structures calculated with and without vertical mixing at lower effective temperatures, as seen in Figure 5.7.

At low effective temperatures the nitrogen chemistry of the atmosphere begins to

become important in a role similar in nature to the carbon chemistry at higher temperatures. In the $T_{eff} = 400\,K$ models in Figure 5.8, the dominant nitrogen bearing species in the cooler upper atmosphere is $NH_3$, and in the warmer deeper atmosphere is $N_2$. Vertical mixing acts to bring $N_2$ from the deep atmosphere into the upper atmosphere on timescales shorter than the chemical timescale converting $N_2$ to $NH_3$. The abundance of $N_2$ therefore increases in the upper atmosphere and the $NH_3$ abundance becomes depleted by approximately an order of magnitude. The depletion of $NH_3$ in the upper atmosphere becomes greater in models with stronger vertical mixing. The condensation of $H_2O$ can also be seen in the chemical equilibrium abundances in the $T_{eff} = 400\,K$ model in Figure 5.8. Including vertical mixing brings gas phase $H_2O$ into a region of the atmosphere that would otherwise be absent of $H_2O$ due to condensation.

The changes in the abundances of $H_2O$, CO, $CH_4$, $CO_2$, $N_2$ and $NH_3$ due to vertical mixing impact the emission spectra from the model atmosphere, as shown in Figure 5.9. In the $T_{eff} = 800\,K$ and $T_{eff} = 1200\,K$ non-equilibrium chemistry models, the depleted $CH_4$ abundance lowers the opacity in absorption bands at $\sim 1.6\,\mu m$, $\sim 2.15\,\mu m$, $\sim 3.15\,\mu m$ and $\sim 7.1\,\mu m$. This gives brighter $H$ and $L'$ bands in the non-equilibrium spectra, which becomes enhanced with stronger vertical mixing. The $K$-band flux is lower in the $T_{eff} = 800\,K$ and $T_{eff} = 1200\,K$ non-equilibrium spectra due to the P-T profiles being cooler than the equilibrium models. This causes the model levels in which the $K$-band flux is generated to be shifted to slightly higher pressures where $H_2 - H_2$ collisionally induced absorption is stronger.

The abundances of CO and $CO_2$ are increased by many orders of magnitude in the upper atmosphere under non-equilibrium chemistry due to vertical mixing in all models shown in Figure 5.8. Despite $CO_2$ being several orders of magnitude less abundant than CO, both CO and $CO_2$ have strong absorption features at $\sim 4.3\,\mu m$ and $\sim 4.18\,\mu m$, respectively, and their increased abundances lower the flux at these wavelengths in the $W2$ and $M'$ bands in the non-equilibrium spectra shown in Figure 5.9. Since higher values of $K_{zz}$ mix CO and $CO_2$ from deeper in the atmosphere where they are more abundant, the $W2$ and $M'$ band flux depend strongly on $K_{zz}$.

At lower effective temperatures $NH_3$ absorption features can begun to be seen in
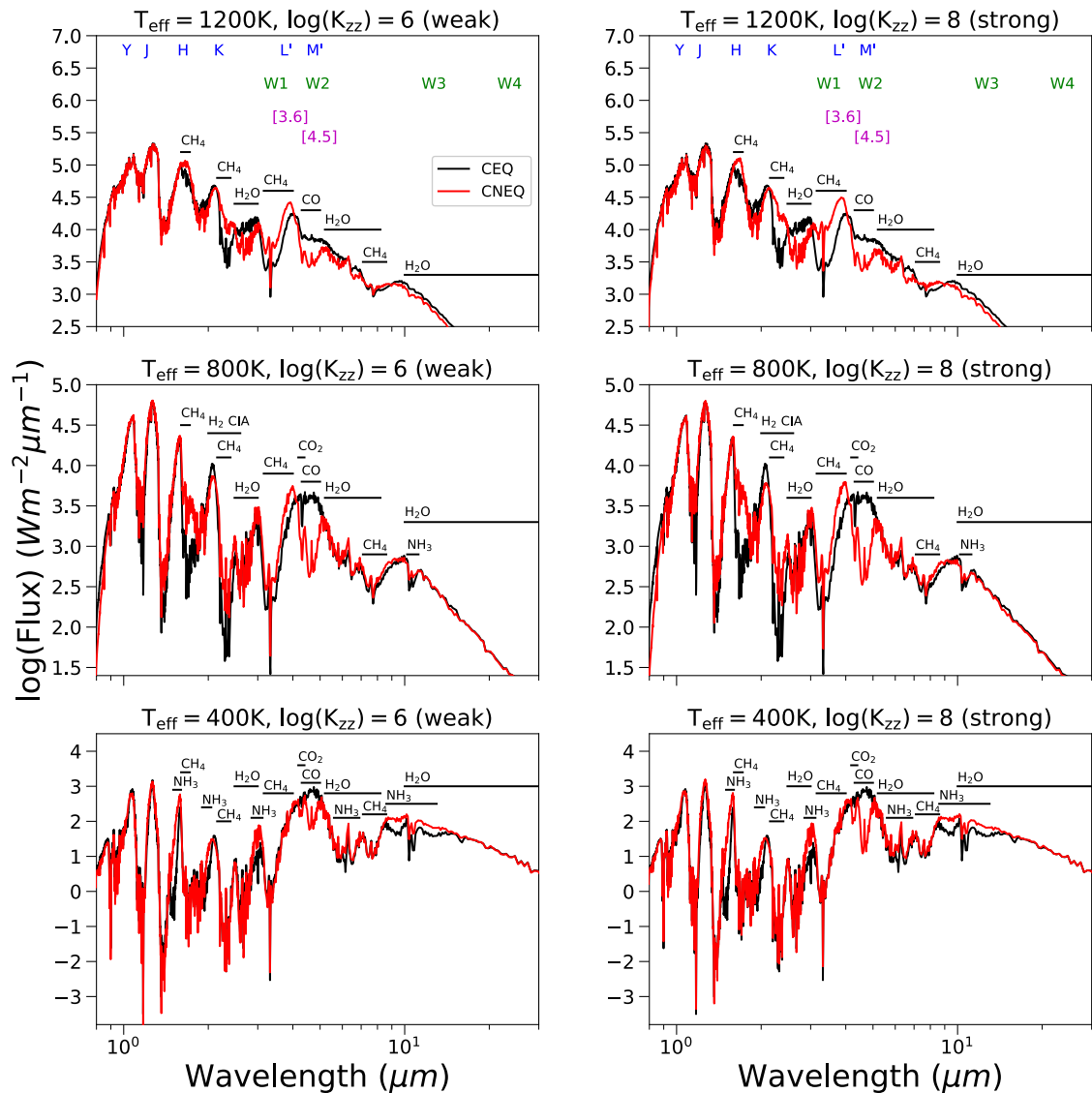
**Figure 5.9:** Emission spectra of self-consistent ATMO model atmospheres generated under the assumption of chemical equilibrium (black) and non-equilibrium chemistry due to vertical mixing (red). Non-equilibrium models calculated with the weak and strong $K_{zz}$ mixing relationship are shown in the left and right columns respectively. The rows display models with different effective temperatures, as indicated in the plot titles. These emission spectra correspond to the P-T profiles and chemical abundance profiles in Figure 5.7 and Figure 5.8 respectively, and all models shown here have $\log(g) = 3.5$. Overplotted for clarity are the approximate locations of molecular absorption features causing differences between the equilibrium and non-equilibrium spectra. Also indicated in the top plots are the locations of the Mauna Kea near-infrared photometric filters (blue bars), the WISE infrared filters (green bars), and *Spitzer* IRAC filters (magenta bars).

the emission spectra. In the $T_{\text{eff}} = 800$ K models, a $NH_3$ absorption feature is seen at $\sim 10.2\,\mu$m. Since vertical mixing quenches the abundance of ammonia, the flux emitted through this $NH_3$ absorption band increases in models with non-equilibrium chemistry. At lower effective temperatures in the $T_{\text{eff}} = 800$ K models, the equilibrium abundance of ammonia increases, the absorption feature at $\sim 10.2\,\mu$m becomes more prominent, and $NH_3$ absorption features at $\sim 1.5\,\mu$m, $\sim 1.9\,\mu$m, $\sim 2.85\,\mu$m, $\sim 5.6\,\mu$m, and $\sim 8.6\,\mu$m also
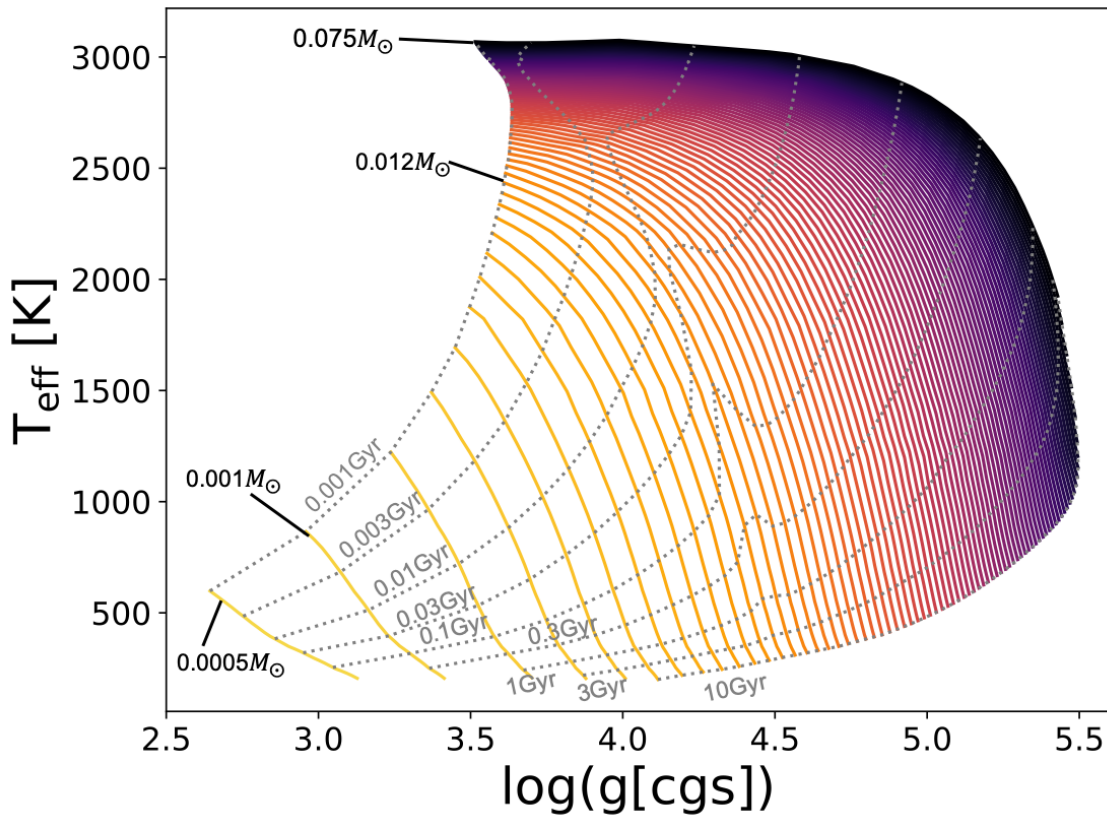
**Figure 5.10:** Evolution of the effective temperature and surface gravity of the `ATMO` 2020 models, for masses of $0.0005\,M_\odot$ and $0.001 - 0.075\,M_\odot$ in steps of $0.001\,M_\odot$ (*coloured lines*). Isochrones are also shown as grey dotted lines, with ages of $0.001, 0.003, 0.01, 0.03, 0.1, 0.3, 1.0, 3.0$ and $10.0\,$Gyr.

appear in the spectra. In models with non-equilibrium chemistry due to vertical mixing, the quenching of ammonia increases the flux emitted through these wavelengths, in particular brightening the $H$ and $W3$ bands.

### 5.2.5   Evolutionary tracks

The chemical equilibrium atmospheric temperature structures presented in Section 5.3.1 are used to couple the non-grey atmosphere to the interior structure, and calculate evolutionary tracks for a range of substellar masses. Figure 5.10 shows the evolution of $T_{\text{eff}}$ and $\log(g)$ as a function of mass and age. The evolution proceeds from left to right, as a given object contracts to higher gravity and cools to lower effective temperature. This Figure shows how a given $T_{\text{eff}}$ and $\log(g)$ from the atmospheric model grid can be used to infer a mass and age of an object.

One of the major improvements of the interior structure model in this work is the use

of the EOS of Chabrier et al. (2019), over the older EOS of Saumon et al. (1995) (see Section Section 5.1.3). Figure 5.11 shows evolutionary tracks calculated with these different EOSs. There are notable differences for the highest masses, with the new EOS predicting slightly cooler, less luminous objects at old ages close to the stellar–substellar transition. The new EOS also slightly changes the cooling curve around the deuterium burning minimum mass, which can be seen in the $0.012\,M_\odot$ track.

The right column of Figure 5.11 shows evolutionary tracks magnified for objects close to the substellar boundary. The largest difference occurs for a 10 Gyr old $0.071\,M_\odot$ object, which is now predicted to be $\sim 180\,$K cooler in effective temperature and $\sim 0.25\,$dex less luminous with the new EOS. We note, however, that we do not expect our evolutionary tracks to be accurate at the $0.001\,M_\odot$ level, as other uncertainties in the evolution model such as small changes in the helium mass fraction can cause changes to the cooling curves comparable to those caused by the new EOS. Therefore, distinguishing between the new and the old EOS will be challenging, and for this reason we avoid providing an exact value for the mass at the substellar boundary predicted by our new models.

To illustrate the impact of the new EOS we show the interior temperature and density profiles of a $0.075\,M_\odot$, 10 Gyr object in Figure 5.12. The new EOS of Chabrier et al. (2019) gives an object up to $\sim 5\%$ cooler and $\sim 8\%$ denser in the core. This therefore raises the theoretical stellar–substellar boundary by 1-2% in mass, as the interior is now cooler and denser, thus more degenerate ($\psi \propto T/\rho^{2/3}$, where $\psi$ is the degeneracy parameter equal to the ratio of the thermal energy $kT$ to the electron Fermi energy $kT_F$ (Chabrier & Baraffe 1997)) for a given mass and age. This results in a change in the cooling curves at masses near the stellar–substellar boundary, with objects cooling to lower $T_{\text{eff}}$.

## 5.3 Comparisons to other models

Throughout this Section, we present and compare the new set of atmosphere models and evolutionary tracks to others available in the literature in order to highlight model improvements. Alongside previously published ATMO models, we choose two families of brown dwarf models that are widely used in the community for comparison, the Lyon
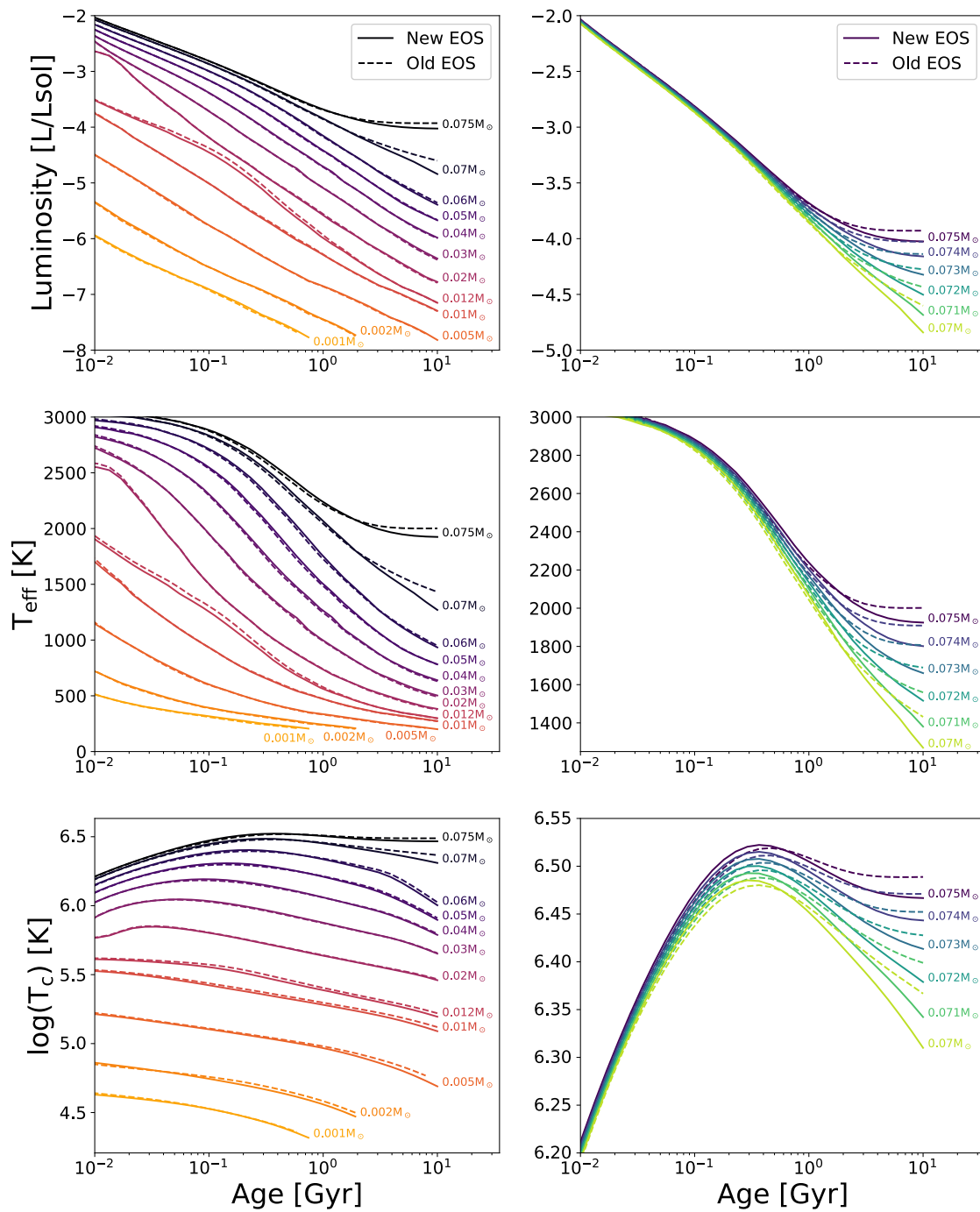
**Figure 5.11:** Luminosity, effective, and central temperature (from top to bottom) as a function of age calculated with the new EOS from Chabrier et al. (2019) (solid lines) and the older EOS of Saumon et al. (1995) (dashed lines). These models are calculated with `ATMO` surface boundary conditions, as described in the text. Each column displays a different selection of masses, indicated by colour-coded annotations placed next to the curves calculated with the new EOS.

group and the Saumon & Marley group.

The Lyon group use the model atmosphere code Phoenix for application to stellar and substellar atmospheres (Allard & Hauschildt 1995; Hauschildt et al. 1999), which have
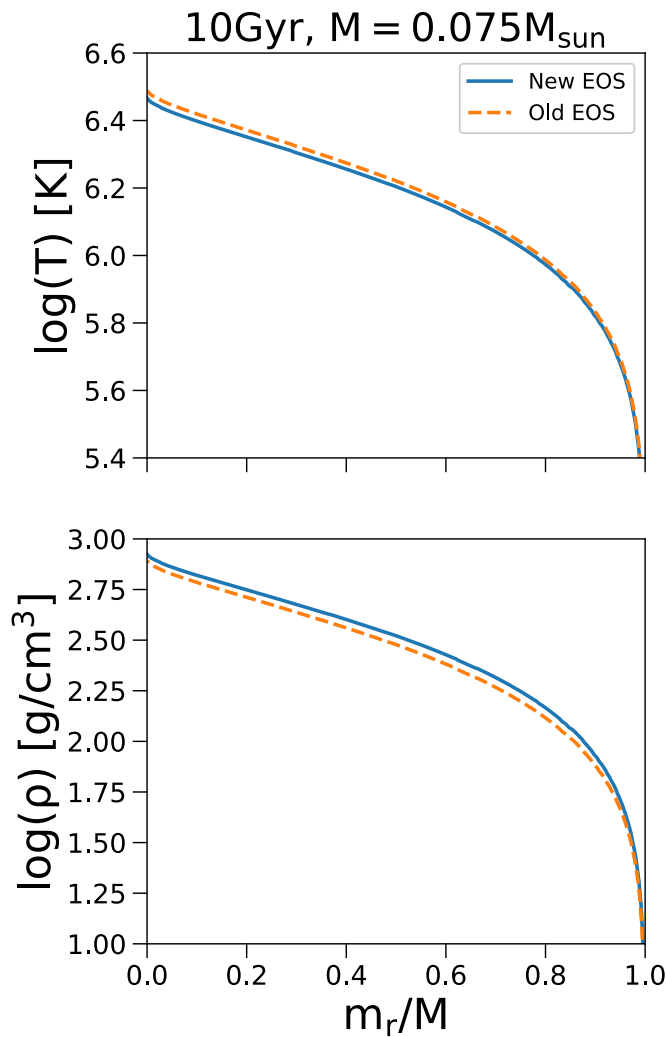
**Figure 5.12:** Interior temperature (top) and density (bottom) as a function of normalised radial mass profile of the simulated object. Solid blue lines are generated using the new EOS of Chabrier et al. (2019), and the dashed orange lines are generated using the older EOS of Saumon et al. (1995).

been succesfully used to describe the evolution of low-mass stars (e.g. Baraffe et al. (2015)). Both Chabrier et al. (2000b) and Baraffe et al. (2003) presented evolutionary calculations for brown dwarfs using grids of Phoenix model atmospheres from Allard et al. (2001), labelled "AMES-Dusty" and "AMES-Cond", respectively. The AMES-Dusty models included dust opacity and are valid for hot (i.e. massive and/or young) brown dwarfs, whereas the AMES-Cond models neglected dust opacity representing the case where all condensates have settled below the photosphere, and are valid for cooler brown dwarfs.

The second set of brown dwarf models we use for comparisons are from the Saumon & Marley group, who applied and developed a 1D radiative-convective code originally designed for solar system atmospheres to brown dwarfs (McKay et al. 1989; Marley et al.

1996, 2002; Burrows et al. 1997). Evolutionary models from this group were presented in Saumon & Marley (2008), who varied the cloud sedimentation efficiency (see Ackerman & Marley (2001)) within their atmospheric outer boundary condition to investigate the impact of clouds on brown dwarf evolution. Most recently, this group has been developing a new set of atmosphere and evolution models named Sonora (Marley et al. 2017, Marley et al., in prep). While yet to be published, these models are already being used by the community to model brown dwarfs and interpret observations (e.g. Nielsen et al. 2019; De Rosa et al. 2019; Kitzmann et al. 2020; Zhang 2020; Miles et al. 2020). Currently, the Sonora model grid consists of chemical equilibrium model atmospheres with three different metallicities, [M/H] = −0.5, 0.0, 0.5, and spans a similar effective temperature and surface gravity range to the ATMO 2020 grid.

### 5.3.1　Atmospheric temperature structures

The ATMO chemical equilibrium temperature structures are compared to the AMES-Cond and Sonora models in Fig. 5.13 and Fig. 5.14 respectively. Temperature structures are shown for $\log(g)$ = 4.0, $\log(g)$ = 5.0 and $T_{\mathrm{eff}}$ between 200 and 2400 K. The effect of surface gravity on the temperature structure of the atmosphere can be seen in these figures. Lower surface gravity objects are hotter at a given pressure level in the atmosphere, or alternatively, have lower pressures for a constant optical depth.

Significant differences in the temperatures structures from the ATMO and AMES-Cond can be seen in Fig. 5.13, for a given $T_{\mathrm{eff}}$ and $\log(g)$. The ATMO profiles are typically warmer than AMES-Cond for $T_{\mathrm{eff}} < 1200$ K in the $\log(g)$ = 4.0 case, and $T_{\mathrm{eff}} < 2000$ K in the $\log(g)$ = 5.0 case. There are numerous model improvements that could contribute to these differences since the AMES-Cond grid was generated. Most notably, improved high-temperature line lists including significantly more transitions for crucial species such as $H_2O$, $CH_4$, and $NH_3$, have increased the atmospheric opacity leading to warmer temperature profiles in this $T_{\mathrm{eff}}$ range. A good agreement with the Sonora temperature profiles in this $T_{\mathrm{eff}}$ range can be seen in Fig. 5.14, which similarly use improved high-temperature line lists to calculate opacities in the atmosphere model.

The ATMO $T_{\mathrm{eff}}$ = 200 K models are slightly cooler in the deep atmosphere compared to
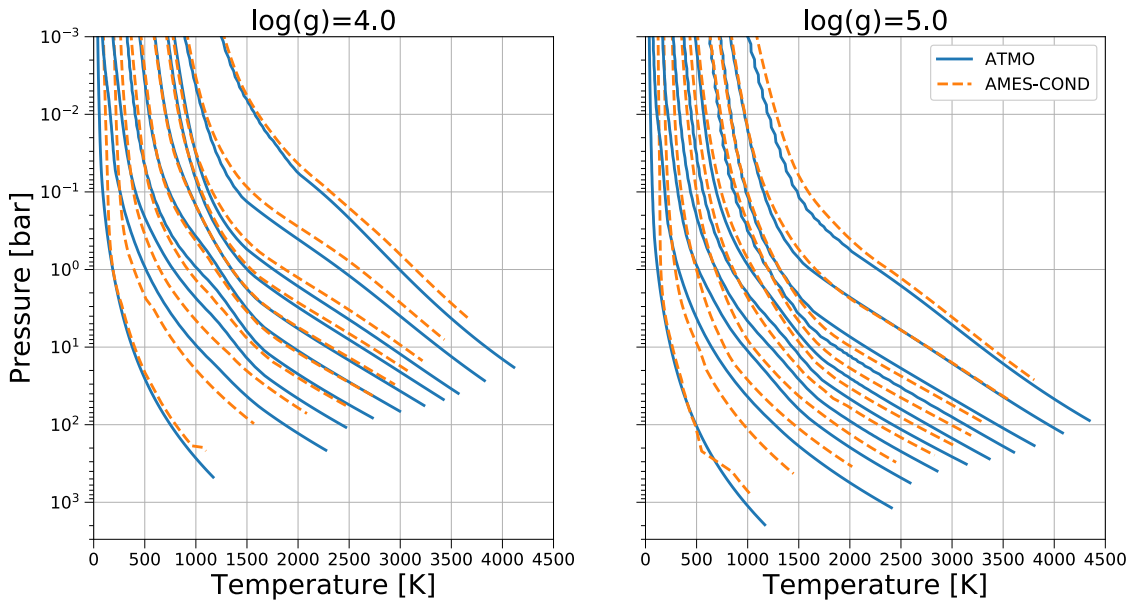
**Figure 5.13:** Self-consistent atmospheric P-T structures from this work (solid blue lines) and from the AMES-Cond models of B03 (dashed orange lines) for $\log(g) = 4.0$ (left panel), $\log(g) = 5.0$ (right panel), and $T_{\text{eff}} = 200, 400, 600, 800, 1000, 1200, 1400, 1600, 2000,$ and $2400\text{K}$ (from left to right in each panel).
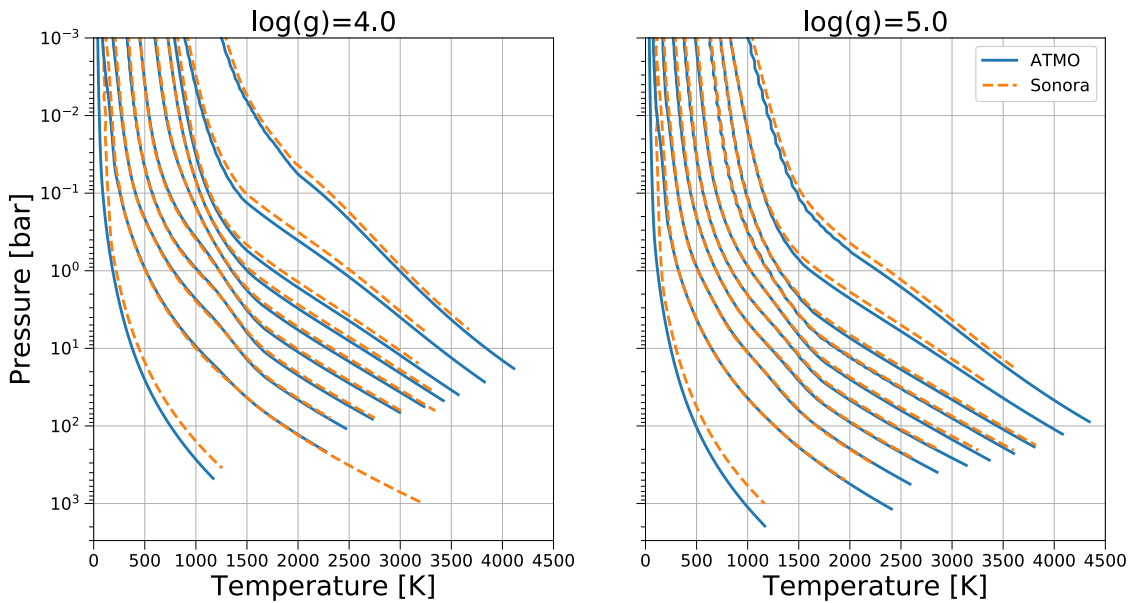


**Figure 5.14:** Same as Fig. 5.13 but with the Sonora atmosphere models

the AMES-Cond and Sonora models in Fig. 5.13 and Fig. 5.14. Since details of the Sonora models are yet to be published, and the Phoenix models were generated in 2001, it is difficult to confidently conclude the cause of the cooler ATMO profiles at $T_{\text{eff}} = 200\,\text{K}$. However, one likely cause is subtle differences in the treatment of low-temperature equilibrium chemistry and condensation, since the temperature structure at these cool temperatures is highly sensitive to the condensation of $H_2O$ and $NH_3$.

# M ≥ 0.02M⊙
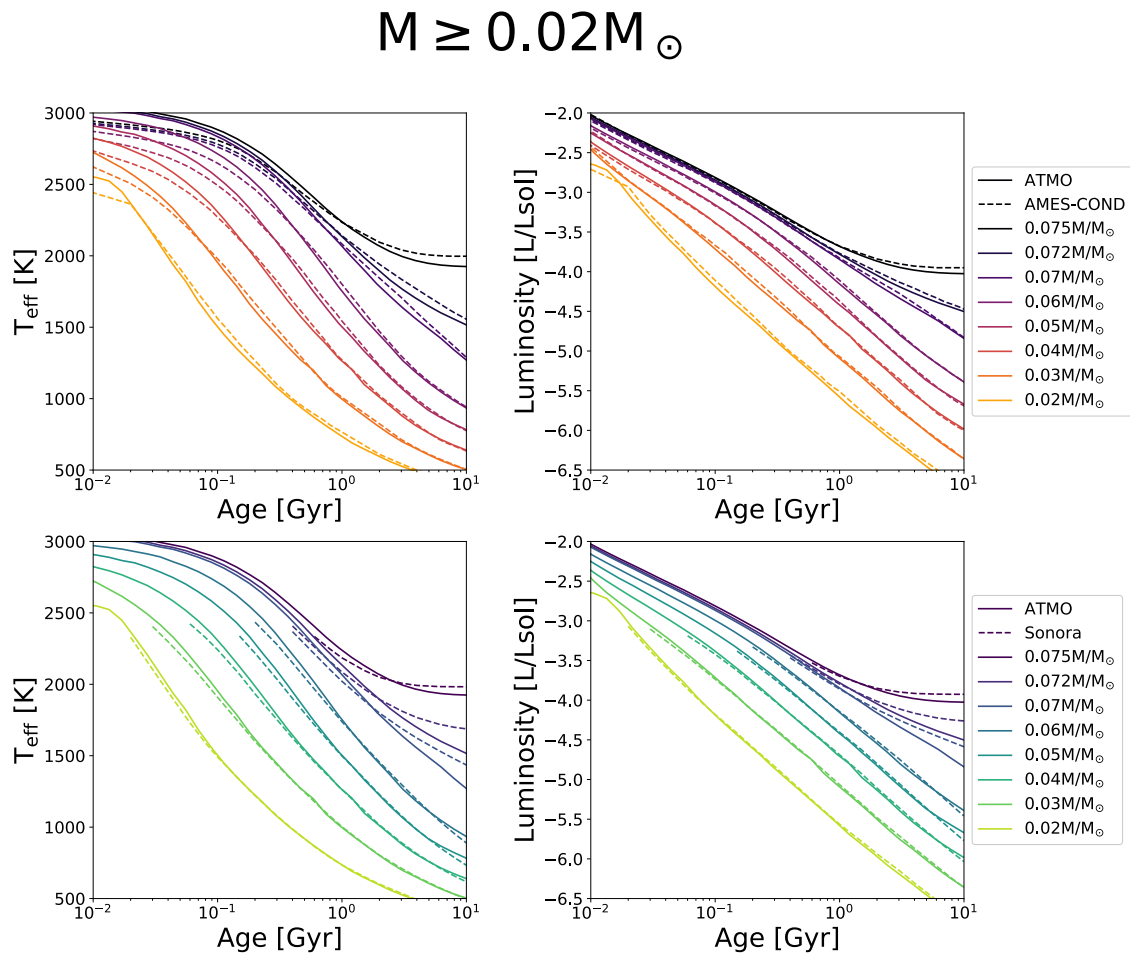


**Figure 5.15:** Evolution of the effective temperature and luminosity for substellar masses $\geq 0.2\,M_\odot$ from this work (solid lines), from the AMES-Cond models of B03 (dashed lines, top), and the Sonora models (dashed lines, bottom).

At higher effective temperatures, ATMO profiles tend to be cooler than the AMES-Cond and Sonora models for $T_{\rm eff} > 1200\,K$ in the $\log(g) = 4.0$ case, and $T_{\rm eff} > 2000\,K$ in the $\log(g) = 5.0$ case. This suggests we may be missing opacity at higher temperatures. We do not include the opacity of some metal oxides and metal hydrides which can be important in shaping the temperature profiles at high $T_{\rm eff}$ (Malik et al. 2019). This is only important for high-$T_{\rm eff}$ objects (i.e. massive and/or young brown dwarfs), and will therefore not affect the evolutionary calculations of cool T–Y objects presented in this work.

## 5.3.2 Evolutionary tracks

The evolutionary tracks from this work and from the AMES-Cond and Sonora calculations are compared in Figure 5.15, which shows the evolution of the effective temperature and luminosity for masses $\geq 0.02\,M_\odot$. As previously discussed, the new EOS used in this

# M ≤ 0.02M⊙
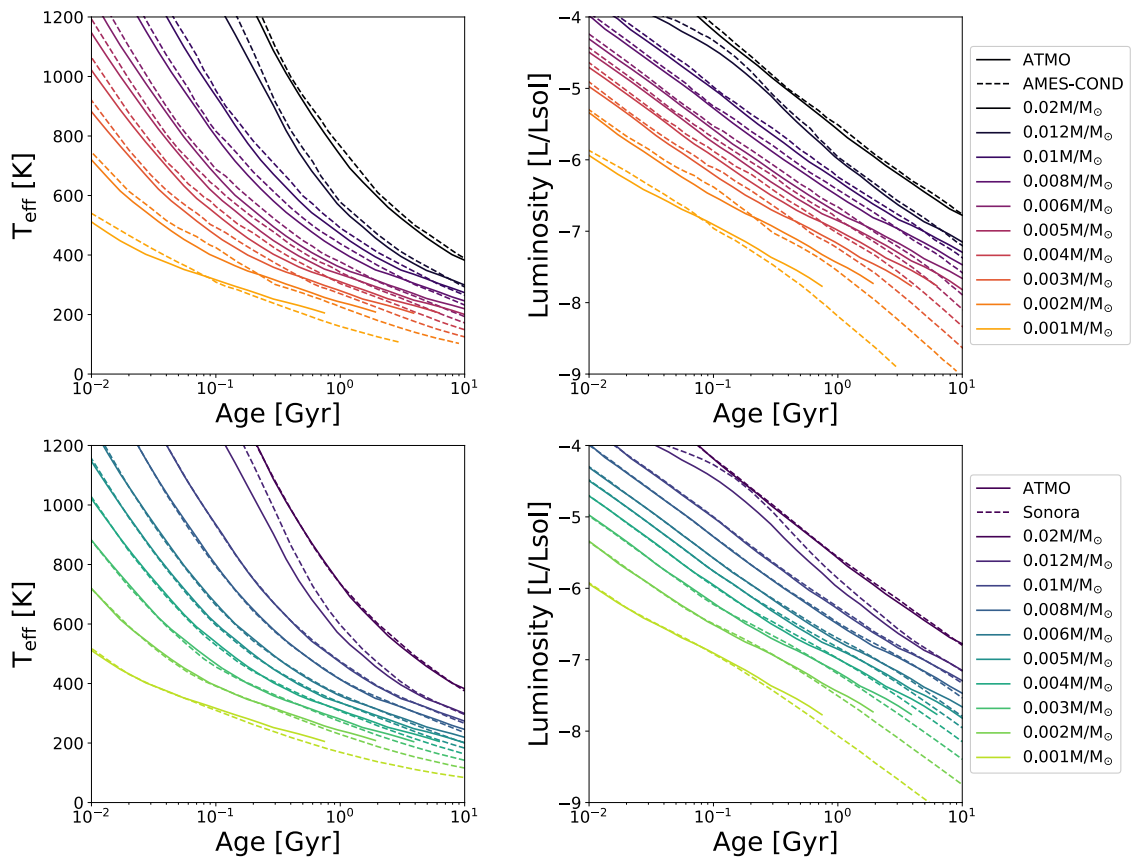


**Figure 5.16:** Same as Figure 5.15 but for masses ≤ 0.2 M⊙.

work raises the hydrogen and deuterium minimum burning mass, causing changes in the cooling curves at high masses and around $0.012\,M_\odot$, respectively. Indeed, the `ATMO` tracks can be seen to be cooler and less luminous than both the AMES-Cond and `Sonora` tracks at high masses and old ages, likely due to the usage of the new EOS. The AMES-Cond tracks were calculated with the old EOS, while it is not current known what EOS was used in the `Sonora` calculations. We also note that small changes in the effective helium mass fraction can also induce changes in the evolutionary tracks qualitatively similar to that induced by the new EOS. The effective helium mass fraction could therefore be another cause of differences between the `ATMO` and `Sonora` calculations.

At young ages, the `ATMO` tracks tend to be warmer and more luminous than the AMES-Cond and `Sonora` models in Figure 5.15. This is likely due to the cooler pressure-temperature profiles at high $T_{\rm eff}$ used as surface boundary conditions (see Figure 5.13

and Figure 5.14), which stems from some missing condensate and hydride opacity in the `ATMO` models. At lower masses and cooler effective temperatures, the `ATMO` and `Sonora` tracks show good agreement stemming from the similar atmospheric P-T profiles in this $T_{\mathrm{eff}}$ range (see Figure 5.14).

Figure 5.16 compares the `ATMO` evolutionary tracks with the AMES-Cond and `Sonora` tracks for masses $\leq 0.02\,\mathrm{M_{\odot}}$. The biggest differences arise for $0.012\,\mathrm{M_{\odot}}$, i.e. around the deuterium burning limit, due to the usage of the new EOS in the `ATMO` models. There is also a change in the shape of the evolutionary curves at these lower masses due to changes in the atmospheric temperature structures used as the surface boundary conditions. At younger ages, or for $T_{\mathrm{eff}} > 350\,\mathrm{K}$, the `ATMO` tracks are cooler and less luminous than the AMES-Cond tracks due to the warmer temperature structures, as shown in Figure 5.13. At older ages, or for $T_{\mathrm{eff}} < 350\,\mathrm{K}$, the `ATMO` tracks switch to being warmer and more luminous than the AMES-Cond tracks, due to the cooler temperature structures at the very lowest $T_{\mathrm{eff}}$ seen in Figure 5.13. This can also be seen in the comparisons with the `Sonora` tracks. The `ATMO` and `Sonora` tracks show good agreement for $T_{\mathrm{eff}} > 350\,\mathrm{K}$, a $T_{\mathrm{eff}}$ region in which the temperature structures also show good agreement (see Figure 5.14). For $T_{\mathrm{eff}} < 350\,\mathrm{K}$, the `ATMO` tracks become warmer and more luminous than the `Sonora` tracks, due to the temperature structures being cooler at the lowest $T_{\mathrm{eff}}$ (see Figure 5.14).

### 5.3.3   Emission spectra

The AMES-Cond grid of the Lyon group was labelled as such due to the NASA-AMES line lists used to calculate the opacity of $H_2O$ and TiO. Since the calculation of these models there have been significant improvements in high-temperature line lists for these species, in particular the BT2 $H_2O$ line list from Barber et al. (2006). A new BT-Cond grid of Phoenix model atmospheres with updated opacities was presented by Allard et al. (2012), which spans $T_{\mathrm{eff}} = 800 - 3000\,\mathrm{K}$.

Figure 5.17 shows comparisons of emission spectra from `ATMO` and BT-Cond for a selection of effective temperatures and surface gravities. Differences in the emission spectra can be seen in the $H$ and $K$ bands due to the updated $CH_4$ line list (Yurchenko & Tennyson 2014) used by `ATMO`. This updated line list adds opacity to the red side of the $H$ band peak at
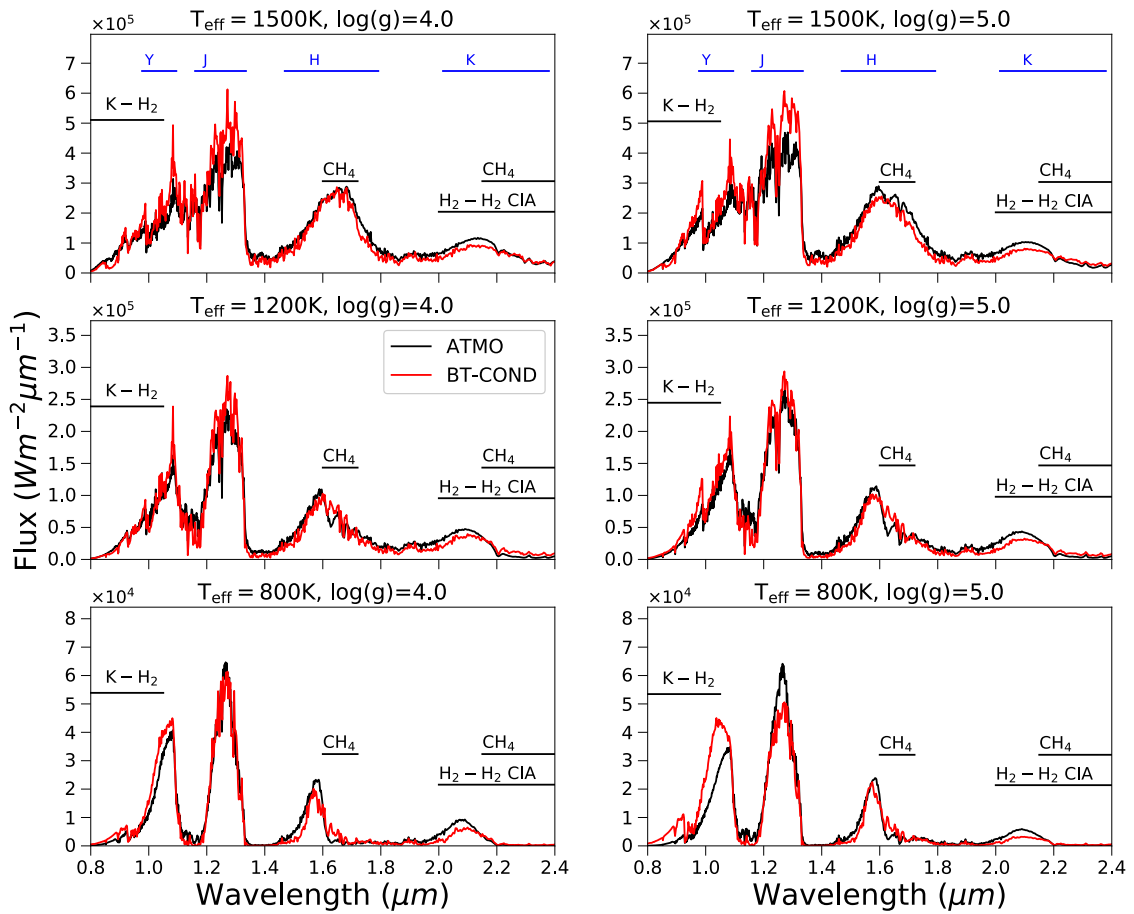
**Figure 5.17:** Synthetic near-infrared emission spectra from `ATMO` compared with models from the BT-Cond grid (Allard et al. 2012) for a range of effective temperatures and $\log(g) = 4.0$ (left) and $\log(g) = 5.0$ (right). Overplotted are the approximate locations of absorption features causing differences between the spectra. Also indicated in the top plots are the locations of the Mauna Kea near-infrared photometric filters (blue bars).

~ 1.6 $\mu$m, altering the shape of the $H$ band. Furthermore, improved $H_2 - H_2$ collisionally induced absorption used by `ATMO` from Richard et al. (2012) can be seen increasing the flux emitted through the $K$ band, an effect also seen by Saumon et al. (2012). At $T_{eff} = 800$ K differences can be seen in the $Y$ band at $\lambda \sim 1 \mu m$, due to the red wing of the potassium resonance doublet. As shown in Chapter 4, different potassium resonance line broadening schemes can lead to large differences in the flux emitted through the $Y$ and $J$ bands. Furthermore, differences in the condensation schemes between `ATMO` and AMES-Cond can affect the potassium abundance, leading to further differences in opacity in the $Y$ band.

The emission spectra from the `ATMO` 2020 model atmosphere grid and previously published `ATMO` models from Tremblin et al. (2015) are shown in Figure 5.18. Tremblin et al. (2015) presented a grid of `ATMO` model atmospheres, showing how non-equilibrium
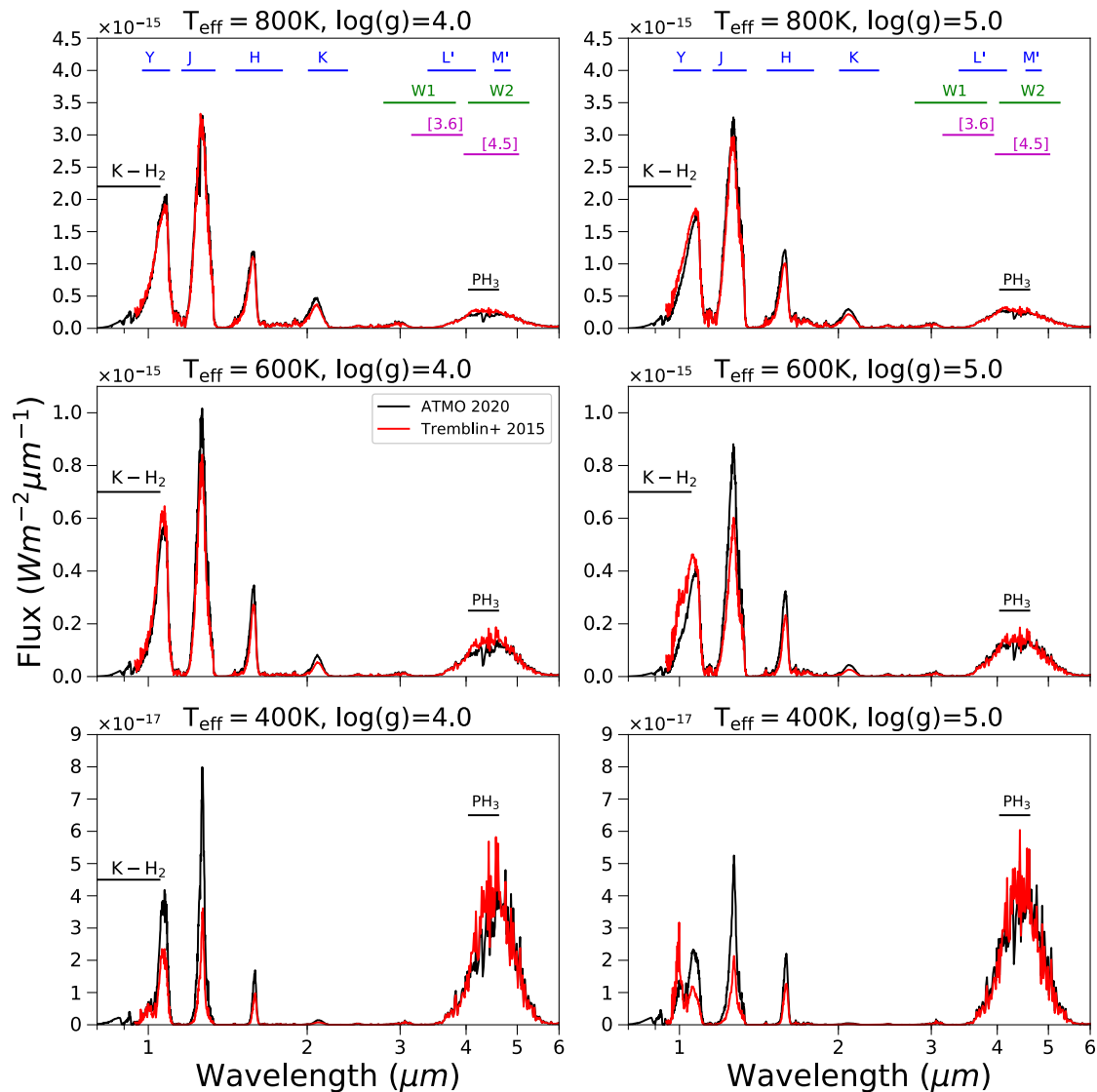
**Figure 5.18:** Synthetic infrared emission spectra from the ATMO 2020 model grid compared with previously published ATMO models from Tremblin et al. (2015) for a range of effective temperatures and $\log(g) = 4.0$ (left) and $\log(g) = 5.0$ (right). Overplotted are the approximate locations of absorption features causing differences between the spectra. Also indicated in the top plots are the locations of the Mauna Kea near-infrared photometric filters (blue bars), *WISE* photometric filters (green bars), and *Spitzer* IRAC photometric filters (magenta bars).

chemistry and alterations to the temperature structure can reproduce spectral observations of cool late T and Y dwarfs. Here we compare to the chemical equilibrium models from this grid with no modifications to the thermal structure, to illustrate how model improvements have impacted the synthetic emission spectra from ATMO.

Differences in the $Y$ band due to the red wing of the potassium resonance doublet can be seen in Figure 5.18. The Tremblin et al. (2015) models used K resonance line broadening from Allard et al. (2007b), and assumed local condensation to remove potas-

sium from the gas phase at higher temperatures into alkali feldspars to reduce the strong Y band absorption. The lower potassium red wing absorption in the Allard et al. (2016) profiles used in the `ATMO` 2020 models, and the use of rainout condensation allowing potassium to remain in the gas phase to lower temperatures, causes differences in the $Y$ band in these models.

A phosphine (PH$_3$) absorption feature can be seen in the `ATMO` 2020 models at ~ 4.05 $\mu$m, that is absent from the Tremblin et al. (2015) spectra. The Tremblin et al. (2015) models included 12 opacity sources not including PH$_3$, whereas the `ATMO` 2020 models include 22 opacity sources including PH$_3$. These additional opacity sources in the `ATMO` 2020 models become important at low effective temperatures, adding opacity to the model atmosphere and leading to warmer temperature structures than the Tremblin et al. (2015) models. The impact of this can be seen in the emission spectra of the $T_{\mathrm{eff}} = 400\,$K models in Figure 5.18, where the `ATMO` 2020 models are brighter in the near-infrared $Y$, $J$, $H$ and $K$ bands due to the warmer temperatures in the atmosphere.

The emission spectra from `ATMO` and `Sonora` models are shown in Figure 5.19 for a selection of effective temperatures and surface gravities. The spectra generally show good agreement, likely due to improved opacities used by both models that have previously caused differences with the BT-Cond models. Similarly to the Tremblin et al. (2015) models, there appears to be additional opacity in the `ATMO` models due to PH$_3$ in the blue side of the $4 - 5\,\mu$m flux window. The `Sonora` models appear to be either missing PH$_3$ opacity or predicting a much lower abundance than `ATMO`. At the lowest effective temperature of $200\,$K the `ATMO` and `Sonora` spectra begin to differ. As seen in Figure 5.14, `ATMO` predicts a cooler temperature profile than `Sonora` at $T_{\mathrm{eff}} = 200\,$K. As such, the flux emitted by `ATMO` is generally lower than `Sonora` across all wavelengths, apart from $\lambda > 15\,\mu$m. In this wavelength region, the opacity is dominated by H$_2$O. Since the `ATMO` models are cooler, more H$_2$O is removed from the gas phase as it condenses, leading to more flux being emitted at $\lambda > 15\,\mu$m.
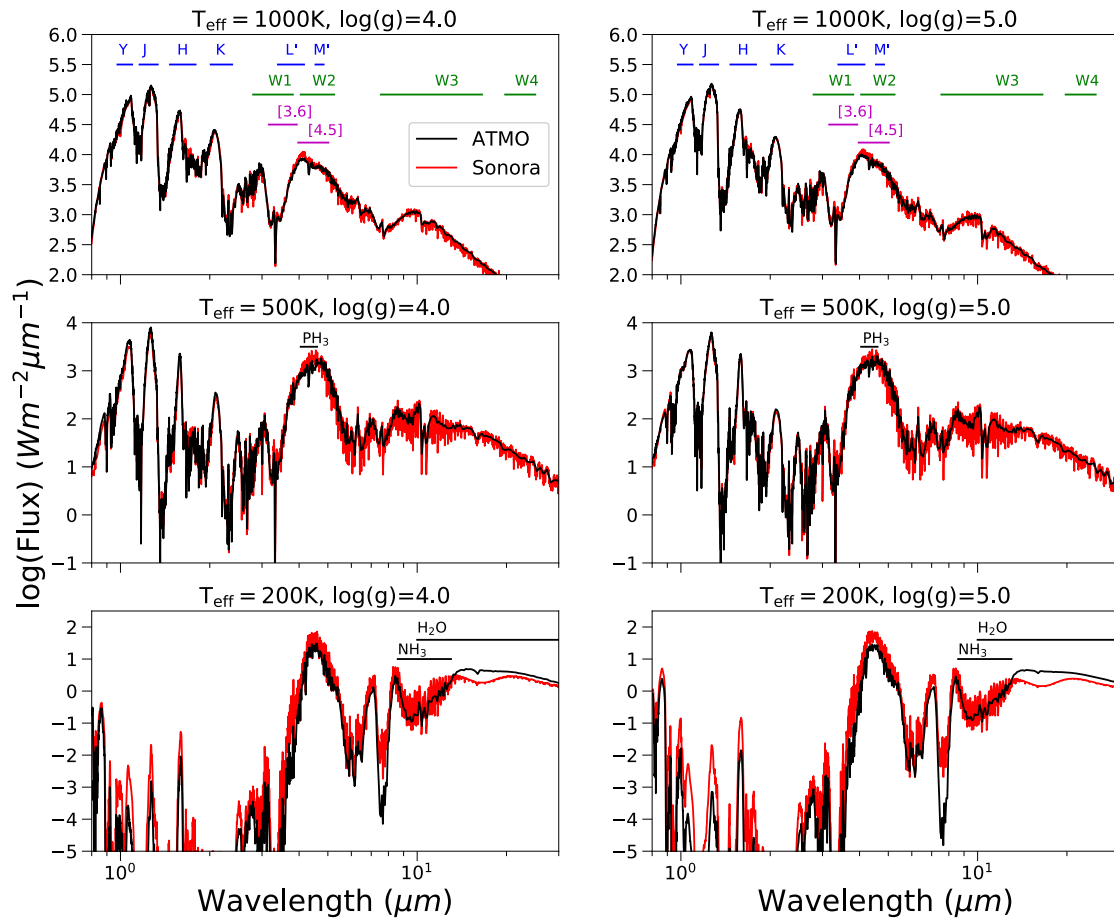
**Figure 5.19:** Synthetic emission spectra from the `ATMO 2020` and `Sonora` model grids for a range of effective temperatures and surface gravities, as indicated in the plot titles. Note that the `Sonora` spectra are presented at a higher resolution than the `ATMO` spectra. Overplotted are the approximate locations of absorption features causing differences between the spectra. Indicated in the top plots are the locations of the Mauna Kea near-infrared photometric filters (blue bars), *WISE* photometric filters (green bars), and *Spitzer* IRAC photometric filters (magenta bars).

## 5.4 Summary and conclusions

In this Chapter, I have presented a new set of substellar atmosphere and evolution models applicable to cool brown dwarfs and directly imaged giant exoplanets, named `ATMO` 2020. The atmosphere model grid is generated with the 1D code `ATMO`, and spans $T_{\text{eff}} = 200 - 3000\,\text{K}$, $\log(g) = 2.5 - 5.5$ with both equilibrium and non-equilibrium chemistry due to different strengths of vertical mixing. This grid of atmosphere models has been used as the surface boundary condition for the interior structure model to calculate the evolution of $0.0005 - 0.075\,M_\odot$ objects. I have highlighted numerous theoretical modelling improvements through comparisons to other models sets in the literature. The main conclusions from this Chapter are as follows:

- The `ATMO` 2020 atmospheric temperature structures are warmer than previous models due to improved high temperature line lists of important molecular absorbers adding opacity to the 1D model atmosphere. These high temperature line lists contain significantly more line transitions required to accurately capture the opacity in brown dwarf and exoplanet atmospheres, also altering the predicted emission spectra.

- There are notable changes to the cooling tracks of substellar objects due to the usage of a new H-He equation of state and the warmer atmospheric temperature structures used as surface boundary conditions. The new EOS raises the mass of the stellar-substellar boundary by $\sim 1 - 2\%$, and alters the cooling tracks around the hydrogen and deuterium burning minimum masses. The warmer outer boundary conditions changed the shape of the cooling curves in the low-mass brown dwarf regime, with a $1\,M_{Jup}$ object being cooler and less luminous at ages $< 0.1\,Gyr$, and warmer and brighter for ages $> 0.1\,Gyr$.

- Good agreement is found between the `ATMO` 2020 and `Sonora` models. The temperature structures and emission spectra are largely similar except at the highest effective temperatures where `ATMO` may be missing some hydride opacity, and at the lowest effective temperatures where the `ATMO` models tend to be cooler than the `Sonora` models. It is unclear what is causing the differences between the models at $T_{eff} = 200\,K$. However we note that the temperature structures and emission spectra are highly sensitive to condensation of major species and the treatment of equilibrium chemistry at these low temperatures.

- Including self-consistent non-equilibrium chemistry due to vertical mixing leads to cooler temperatures in the upper atmosphere due to the quenching of $CH_4$ and $H_2O$. This impact on the temperature structure is weakly dependent on mixing strength, and reduces towards lower effective temperatures as the equilibrium composition of the atmosphere becomes $CH_4$ dominated. The quenching of $CH_4$, and also $NH_3$ at lower effective temperatures, reduces the opacity of their respective absorption features brightening multiple regions of the synthetic emission spectra, in particular the $H$ and $L'$ photometric bands. The largest impact on the synthetic emission

spectra from vertical mixing is the increased CO and $CO_2$ absorption in the $4-5\,\mu$m flux window. The abundances of these species are increased by many orders of magnitude as they are mixed from the deep atmosphere. This is strongly dependent on the mixing strength, and thus it is concluded that CO and $CO_2$ absorption in the $4-5\,\mu$m flux window can be used to calibrate $K_{zz}$ in cool substellar atmospheres.

# Chapter 6

# Comparisons to observations

In this Chapter I extensively compare the `ATMO` 2020 model set presented in Chapter 5 to observational datasets of substellar objects. These comparisons serve to illustrate the numerous modelling improvements included in the `ATMO` 2020 model set over previous calculations in the literature, such as the new H-He EOS, improved high temperature linelists, improved K resonance line broadening, and the inclusion of self-consistent non-equilibrium chemistry due to vertical mixing. Alongside highlighting and validating these improvements, these comparisons also highlight current shortcomings in the modelling of cool brown dwarfs in reproducing observational features along the cooling sequence, thus motivating future work in these areas. The majority of these comparisons to observations have been published in Phillips et al. (2020b).

The Chapter is organised as follows. In Section 6.1 I compare the `ATMO` 2020 evolutionary tracks, along with other calculations in the literature, to dynamical mass measurements of brown dwarfs. In Section 6.2 I compare the new models to other models and observational datasets in colour-magnitude diagrams. I present comparisons of the new models to the observed spectra of cool brown dwarfs across the T-Y transition in Section 6.3. Following these spectral comparisons, I present preliminary work in tuning the `ATMO` 2020 models with the effective adiabatic index $\gamma_{\text{eff}}$ following Tremblin et al. (2019), to better reproduce the observed emission spectra of late T and Y dwarfs. Finally, I summarise the Chapter and draw conclusions in Section 6.4.

## 6.1   Dynamical masses

Dynamical mass measurements of brown dwarfs from astrometric monitoring programs of binary systems provide useful tests for evolutionary models (e.g. Dupuy & Liu (2017)). A reliable measurement of a brown dwarf mass helps break the degeneracy between its fundamental parameters. Recently, Brandt et al. (2019) presented a dynamical mass measurement of the first imaged brown dwarf Gl 229 B of $70 \pm 5\,M_{Jup}$. This measurement joins a growing list of massive T dwarfs that are challenging evolutionary models by having higher than expected masses for their observed luminosity (e.g. Bowler et al. (2018); Dieterich et al. (2018); Dupuy et al. (2019); Sahlmann et al. (2020)). Evolutionary models tend to predict that these systems must be older than expected to have cooled to their observed luminosity, often in tension with age estimates from host star activity or kinematics.

We show in Figure 6.1 the luminosity as a function of mass for ultracool dwarfs with dynamical mass measurements including Gl 229 B. In this figure we show isochrones from this work calculated with the new and old EOSs, along with isochrones from Baraffe et al. (2003), the `Sonora` models, and the hybrid cloud tracks of Saumon & Marley (2008). The new EOS can be seen predicting cooler, less luminous objects in this figure for old high-mass objects, since the hydrogen burning minimum mass has been raised and objects in this mass range cool faster. For a $70\,M_{Jup}$ object at an age of 10 Gyr, the `ATMO` tracks calculated with the new EOS are $\sim 0.1$ dex less luminous than the AMES-Cond and `Sonora` tracks, and $\sim 0.4$ dex less luminous than the hybrid cloud tracks of Saumon & Marley (2008).

As discussed by Brandt et al. (2019), the evolutionary models of B03 and SM08 are only compatible with a mass of $70 \pm 5\,M_{Jup}$ for Gl 229 B if the system is old (7-10 Gyr), in some tension with the 2-6 Gyr age estimate of the host star from kinematics and stellar activity. The `ATMO` tracks calculated with the new EOS may help relieve some of the tension surrounding the age of the system given that high-mass objects are predicted to be cooler and less luminous at a given age. We note, however, that the difference between the old and new EOS is not observationally significant given the uncertainty on the mass measurement of Gl 229 B shown in Figure 6.1.
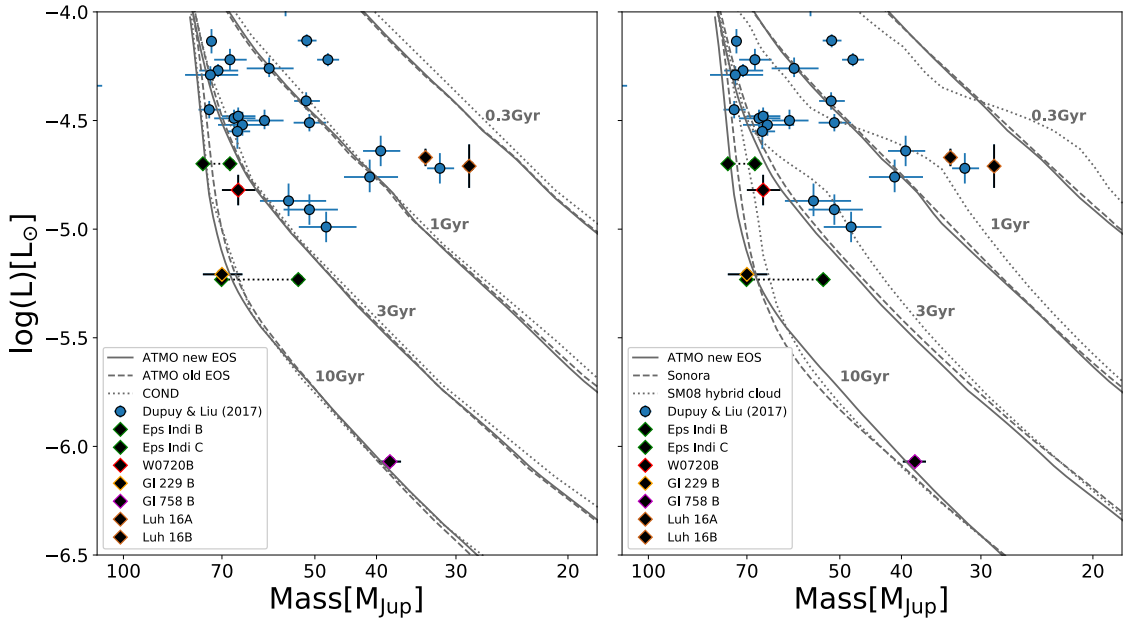
**Figure 6.1:** Luminosity as a function of mass for ultracool dwarfs that have dynamical mass measurements. `ATMO` isochrones from this work calculated using the new EOS from Chabrier et al. (2019) and the older EOS of Saumon et al. (1995) are plotted as solid and dashed grey lines respectively in the left panel. Isochrones from the AMES-Cond models of Baraffe et al. (2003) are plotted as dotted grey lines in the left panel, and isochrones from the `Sonora` models and the hybrid cloud models of Saumon & Marley (2008) are plotted in the right panel with dashed and dotted lines respectively. Most mass measurements are from Dupuy & Liu (2017) and are plotted as blue circles, with other literature measurements plotted as black diamonds (Bowler et al. 2018; Lazorenko & Sahlmann 2018; Dupuy et al. 2019; Brandt et al. 2019). Both mass measurements of $\epsilon$ Indi BC from Cardoso (2012) and Dieterich et al. (2018) are plotted, and we refer the reader to Dupuy et al. (2019) for a discussion on these conflicting mass measurements. We indicate key objects with coloured outlines.

## 6.2 Colour-magnitude diagrams

In this section we compare the new `ATMO` 2020 model set presented in this thesis, along with the AMES-Cond and `Sonora` models, to observational datasets in colour-magnitude diagrams. In Section 6.2.1 we show diagrams involving the Mauna Kea $Y$, $J$, $H$ and $K$ photometric filters, which cover the peak in emission of L and early T dwarfs. The peak in emission for cooler late T and Y dwarfs shifts to longer wavelengths, with a large percentage of flux emitted through the $3.5 - 5.5\,\mu$m flux window. In Section 6.2.2 we therefore show diagrams involving photometric filters that cover longer wavelengths, including the $3.5 - 5.5\,\mu$m flux window.

### 6.2.1 Near-infrared diagrams

In Figures 6.2 through 6.5, we present near-infrared colour-magnitude diagrams (CMDs) including $Y$, $J$, $H$ and $K$ band photometry from the database of ultracool parallaxes (Dupuy

& Liu 2012; Dupuy & Kraus 2013). We exclude from the dataset the known and suspected binaries, young low-gravity objects, and low-metallicity objects. In these diagrams, the data show the M and L dwarf population for $J$ or $H < 14$, which gets progressively redder for cooler objects, and the sharp change to bluer colours for the methane dominated T dwarfs at $J$ or $H \sim 14.5$ known as the L-T transition. The cool T and Y dwarf objects for which the models presented in this work are most applicable, lie below $J$ or $H \sim 15$.

Figure 6.2 shows near-infrared CMDs including $0.1 - 5.0\,\text{Gyr}$ isochrones with photometry derived from ATMO chemical equilibrium atmosphere models, to illustrate the variation of the predicted colours with age. The $0.1 - 5.0\,\text{Gyr}$ isochrone range is chosen to approximately capture the typical age range of field brown dwarfs inferred from mass and luminosity measurements (Dupuy & Liu 2017). The $J - H$ and $J - K$ colours predicted by ATMO are too blue compared to the data. The colours of the cool T and Y dwarf population below $J \sim 15$ are not well reproduced, however the isochrones do begin to redden and reconverge with the observed $J - H$ colours of the Y dwarfs, which lie below $J \sim 21$. Unlike the $J - H$ and $J - K$ colours, the $H - K$ colours of cool T–Y-type objects lying below $H \sim 15$ are well reproduced by the ATMO isochrones, with the spread in age reasonably encapsulating the data. The fact that the ATMO models predict too blue $J - H$ and $J - K$ colours compared to the data, but are able to reproduce the $H - K$ colours of cool T and Y dwarfs, indicates that there is a problem with the current models in the $J$-band. It has been shown that additional physics not currently included in the ATMO models such as reductions in the temperature gradient due to thermochemical instabilities (Tremblin et al. 2015; Tremblin et al. 2016) and/or cloud opacity (Morley et al. 2012; Charnay et al. 2018) can reduce the flux in the $J$ band and better reproduce the red $J - H$ and $J - K$ colours of late T dwarfs.

The $Y - J$ colours in Figure 6.2 are captured by the ATMO isochrones for T type brown dwarfs between $J \sim 15 - 18\,\text{mag}$, before becoming too red at cooler temperatures between $J \sim 22 - 24$. As shown in Chapter 4, the $Y$-band magnitude is formed by the red wing of the K resonance doublet, and thus the $Y - J$ colours are dependent on the choice of K resonance line broadening. We show this dependence on the $Y - J$ colours in Figure 6.3, which shows 1 Gyr isochrones with photometry derived from chemical equilibrium ATMO models
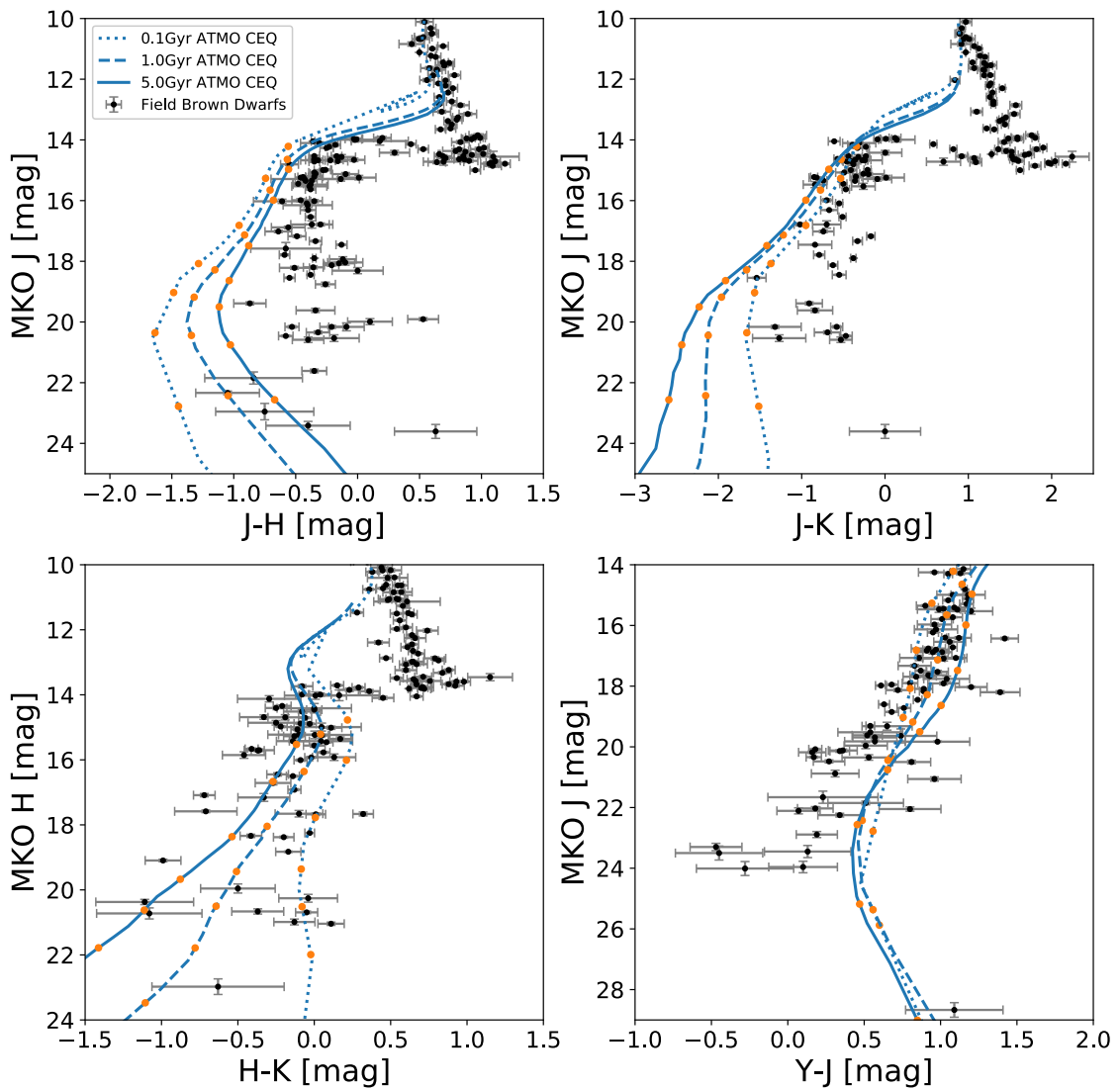
**Figure 6.2:** Near-infrared colour-magnitude diagrams involving the Mauna Kea $Y$, $J$, $H$ and $K$ photometric filters. The photometry of field brown dwarfs are plotted as black circles, with the data taken from the database of ultracool parallaxes. The data is filtered to only include field brown dwarfs from Dupuy & Liu (2012) and Dupuy & Kraus (2013). Isochrones from `ATMO` 2020 chemical equilibrium models are plotted as blue lines, with orange markers on each isochrones indicating $T_{\mathrm{eff}} = 1000, 800, 600, 500, 450, 400$ and $350\,\mathrm{K}$.

calculated with potassium resonance line broadening from Burrows & Volobuyev (2003) (BV03), Allard et al. (2007b) (A07) and Allard et al. (2016) (A16). The isochrone including BV03 broadening is too blue for T dwarf objects with $J < 20$, due to the low opacity in the red wing of the potassium resonance doublet (see Figure 4.6). The stronger opacity in the red wing of the potassium doublet from the A07 and A16 broadening treatments give redder $Y - J$ colours, with the A16 isochrone best matching the data for $J < 20$. For cooler objects with $J > 22$, all the isochrones become too red compared to the observed $Y - J$ colours of Y dwarfs, before reconverging with the WISE 0855 data point at $J \sim 29$. Given
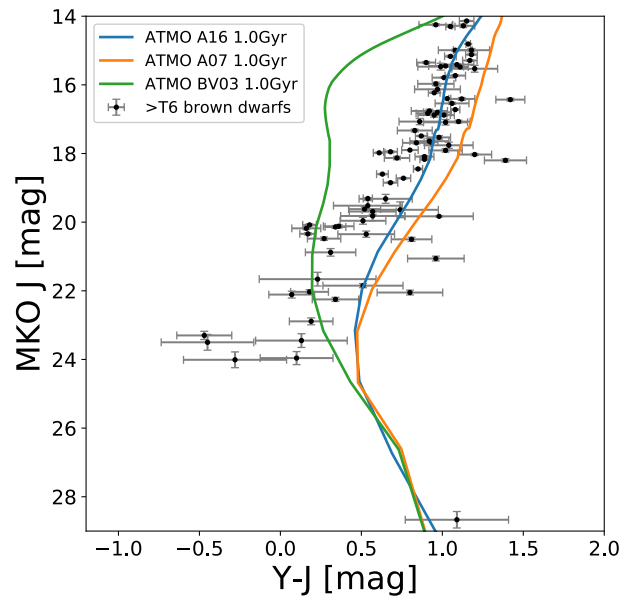
**Figure 6.3:** $Y - J$ colour as a function of absolute $J$-band magnitude. Photometry of >T6 brown dwarfs are plotted as black circles, with data from the database of ultracool parallaxes (Dupuy & Liu 2012; Dupuy & Kraus 2013) and updated photometry from Leggett et al. (2019) and references therein. 1 Gyr isochrone from chemical equilibrium ATMO models calculated with Allard et al. (2016) (blue), Allard et al. (2007b) (orange) and Burrows & Volobuyev (2003) (green) K resonance line broadening are shown.

the improvements to the potassium resonance line broadening discussed in Chapter 4, this could indicate that the current modelling of potassium chemistry is incorrect. Potassium appears to remain in the gas phase and suppress the $Y$ band flux in the current models to lower temperatures than observed. This is further discussed in Section 6.3.3.

In Figure 6.4 we show the near-infrared CMDs including 1 Gyr isochrones from the ATMO 2020, AMES-Cond and Sonora chemical equilibrium models. The ATMO and Sonora tracks predict broadly similar colours in all diagrams, whereas the older AMES-Cond tracks predict significantly different colours primarily due to outdated opacities. The $J-H$ colours are best reproduced by the AMES-Cond models, with both the ATMO and Sonora isochrones predicting colours that are too blue compared to the data. This is caused by the outdated physics used within the AMES-Cond models, which lack $CH_4$ and $NH_3$ opacity in the $H$ band due to the incomplete line lists used at the time. The brighter AMES-Cond $H$ band therefore gives redder $J - H$ colours that coincidentally more closely match the data compared to the ATMO and Sonora tracks, which use more complete $CH_4$ and $NH_3$ line lists. These more complete line lists have added opacity to the $H$ band since the generation of the AMES-Cond models.
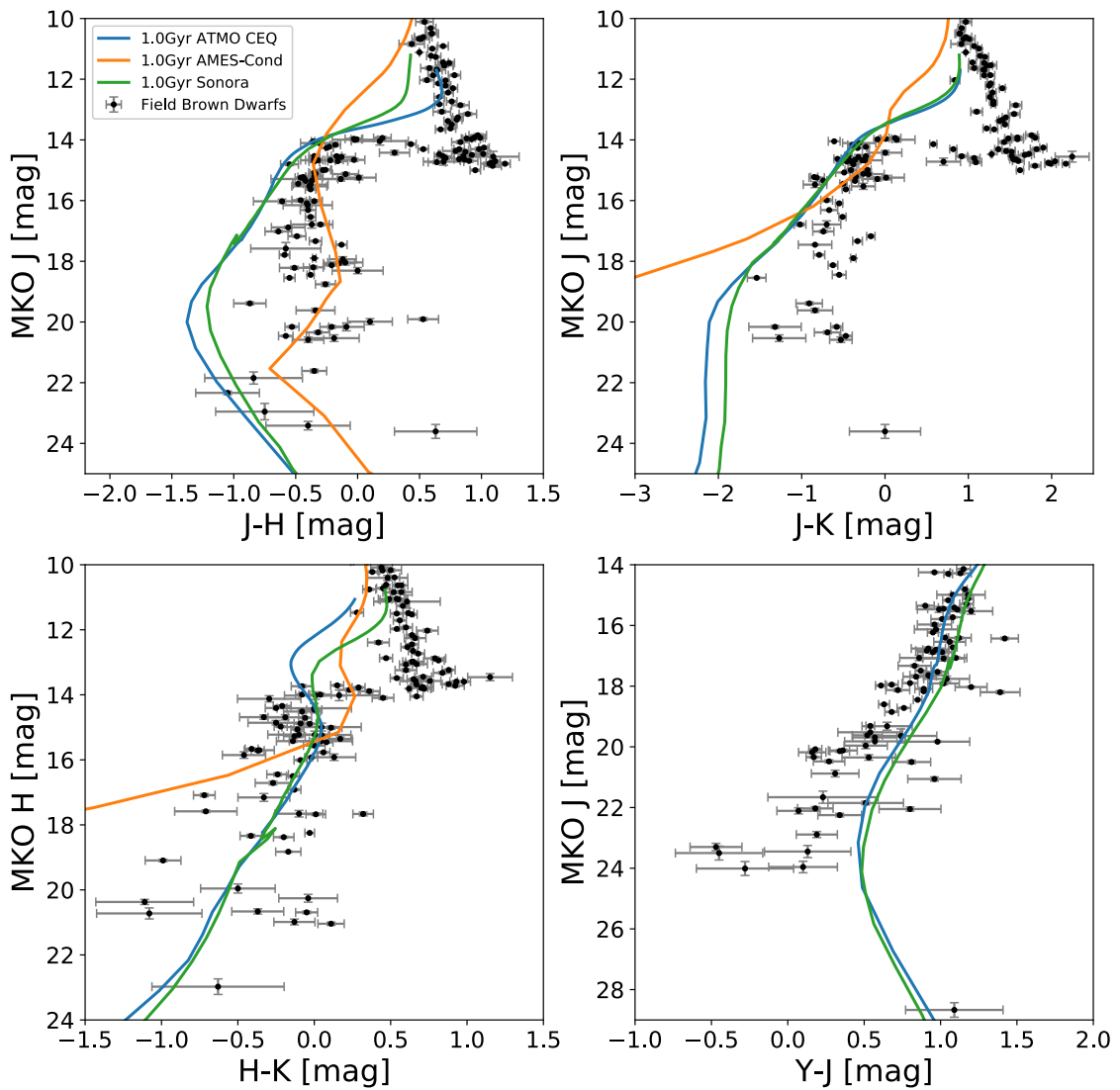
**Figure 6.4:** Same as Figure 6.2, but with 1 Gyr isochrones from `ATMO` 2020 (blue), AMES-Cond (orange) and `Sonora` (green) chemical equilibrium models. Note that the AMES-Cond models are not shown in the $Y - J$ diagram due to the $Y$ band photometry not being included in the available evolutionary tables.

In the $J - K$ and $H - K$ diagrams in Figure 6.4, the AMES-Cond models get progressively bluer compared to the `ATMO` and `Sonora` tracks for objects above $J \sim 17$ and $J \sim 16$. This is due to outdated $H_2 - H_2$ collisionally induced absorption used by the AMES-Cond models over-predicting the opacity in the $K$-band. The updated $H_2 - H_2$ CIA from Richard et al. (2012) used by the `ATMO` and `Sonora` models predicts a brighter $K$-band, and improves the comparison with observations in these CMDs (see also Saumon et al. (2012)). The AMES-Cond models are not shown in the $Y - J$ diagram due to the $Y$ band photometry not being included in the available evolutionary tables. The `Sonora` isochrone predicts slightly redder $Y - J$ colours than `ATMO`, similar to the isochrone calcu-
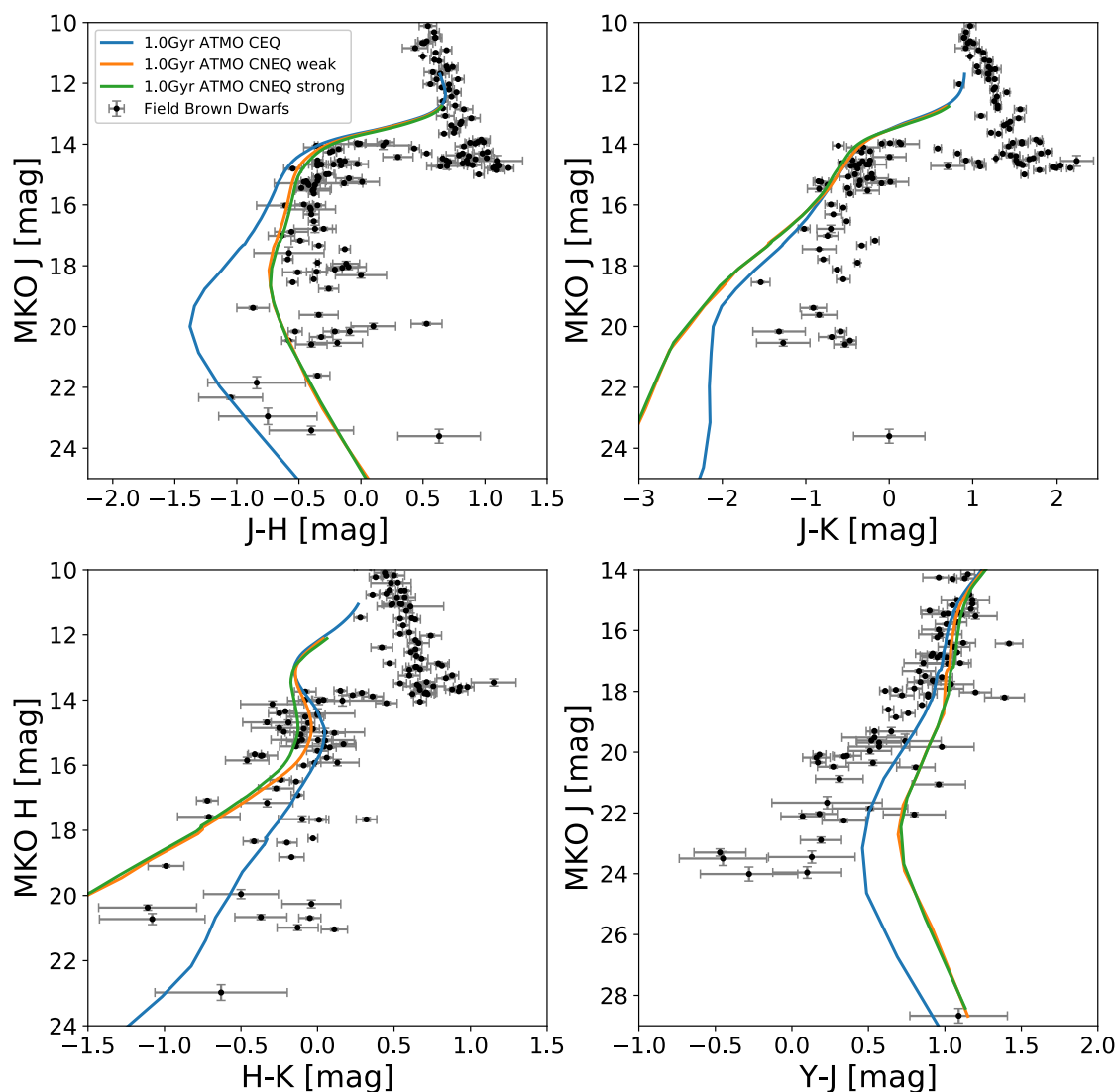
**Figure 6.5:** Same as Figure 6.2, but with 1 Gyr isochrones from chemical equilibrium models (blue) and non-equilibrium chemistry models with weak (orange) and strong (green) vertical mixing from the `ATMO 2020` model set.

lated with A07 potassium resonance line broadening shown in Figure 6.3.

In Figure 6.5, we show 1 Gyr `ATMO` isochrones with photometry derived from chemical equilibrium and non-equilibrium atmosphere models to illustrate the impact of vertical mixing on the predicted colours of cool brown dwarfs. Vertical mixing can be seen reddening the predicted $J - H$ colours compared to chemical equilibrium tracks, moving the isochrones towards the observed $J - H$ colours of T dwarfs. This is due to vertical mixing quenching $CH_4$ and $NH_3$, lowering the opacity and increasing the flux through the $H$ band. The difference between the weak and strong vertical mixing tracks in the $J - H$ diagram is small. This is due to the abundance of methane only varying by a small factor at

the quench levels corresponding to the differing vertical mixing strengths (see Figure 5.8).

Unlike the $J-H$ colours, including non-equilibrium chemistry due to vertical mixing moves the isochrone away from the observed $J-K$ and $H-K$ colours of cool T and Y dwarfs. This is due to non-equilibrium chemistry giving cooler P-T profiles (see Figure 5.7) thus increasing the strength of $H_2 - H_2$ collisionally induced absorption in the $K$-band. This reduces the flux in the $K$-band, and gives bluer $J - K$ and $H - K$ colours. The quenching of $CH_4$ and $NH_3$ also brightens the $H$-band and contributes to the reddening of the $H - K$ colours when including vertical mixing. The cooler P-T profiles given by assuming non-equilibrium due to vertical mixing also alters the $Y$ and $J$ band magnitudes, and gives redder $Y - J$ colours.

### 6.2.2 3.5–5.5 micron flux window diagrams

Cool T–Y-type brown dwarfs emit a large percentage of their total energy through the 3.5 to 5.5 $\mu m$ flux window, at longer wavelengths probed by the $Y$, $J$, $H$, and $K$ filters considered in the CMDs presented in Section 6.2.1. The *WISE* $W1$ and $W2$, the *Spitzer* IRAC [3.6] and [4.5], and the MKO $L'$ and $M'$ filters probe this wavelength region and can provide useful photometry by which to characterise cool brown dwarfs. In Figures 6.6 through 6.8, we present CMDs involving these photometric filters. The photometric data of >T6 type brown dwarfs presented in these Figures are taken from Leggett et al. (2017); Martin et al. (2018); Smart et al. (2018); Theissen (2018); Leggett et al. (2019); Kirkpatrick et al. (2019) and references therein.

Figure 6.6 shows a selection of CMDs including $0.1 - 5.0$ Gyr isochrones with photometry derived from ATMO chemical equilibrium atmosphere models, to illustrate the variation of the predicted colours with age. The $J - [4.5]$ colours are reasonably well reproduced by the ATMO chemical equilibrium isochrones for objects with $T_{\text{eff}} < 600$ K ($J - [4.5] > 4$). For warmer objects with $T_{\text{eff}} > 600$ K ($J - [4.5] < 4$) the predicted colours are slightly too red. Similarly, the tight $H - W2$ correlation with $H$ band magnitude is well reproduced by the ATMO chemical equilibrium isochrones. The predicted colours are again slightly too red for warmer objects, with the discrepancy decreasing with effective temperature. The $L'$ magnitude is underpredicted by the ATMO isochrones for $H - L' > 3$,
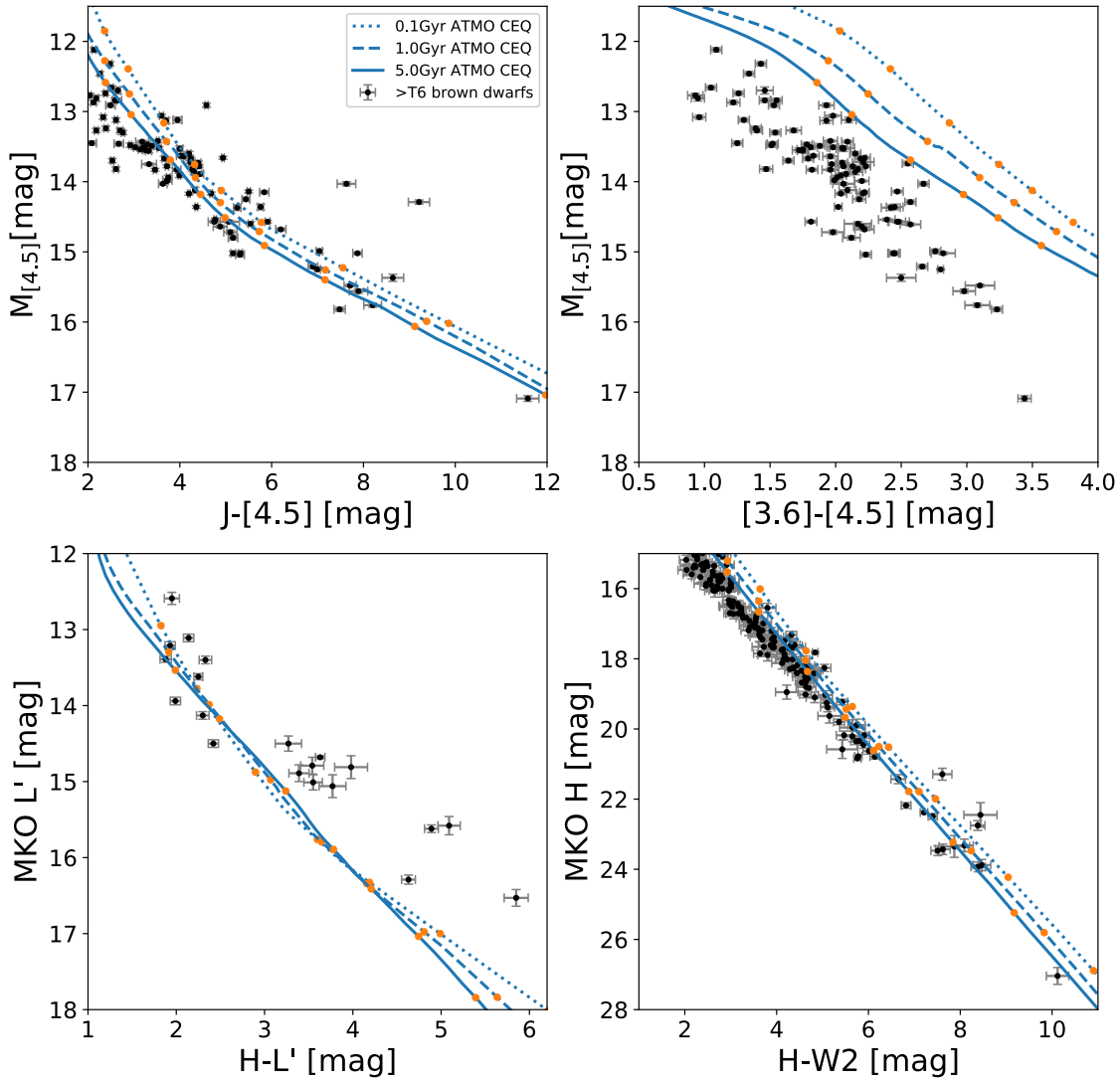
**Figure 6.6:** Colour-magnitude diagrams involving photometric filters that cover the $3.5 - 5.5\,\mu$m flux window. The photometry of >T6 brown dwarfs are plotted as black circles, with the data taken from Leggett et al. (2017); Martin et al. (2018); Smart et al. (2018); Theissen (2018); Leggett et al. (2019); Kirkpatrick et al. (2019) and references therein. Isochrones from ATMO 2020 chemical equilibrium models are plotted as blue lines, with orange markers on each isochrones indicating $T_{\rm eff} = 1000, 800, 600, 500, 450, 400, 350, 300$ and $250$ K.

corresponding to objects with $T_{\rm eff} < 600$ K. This is a long-standing issue in the understanding of cool brown dwarfs, whereby the $\lambda = 3.6 - 4.0\,\mu$m model fluxes are too low compared to observations of cool brown dwarfs (Leggett et al. 2012, 2013, 2015, 2017; Leggett et al. 2019), a discrepancy that increases with decreasing $T_{\rm eff}$. The ATMO $[3.6] - [4.5]$ colours are too red compared to the data, clearly indicating that the ATMO $[4.5]$ band magnitudes are too bright. The $[3.6] - [4.5]$ colours are also affected by the ATMO $[3.6]$ band magnitudes being too faint compared to the data, since the $[3.6]$ band covers a similar wavelength range to the $L'$ band.
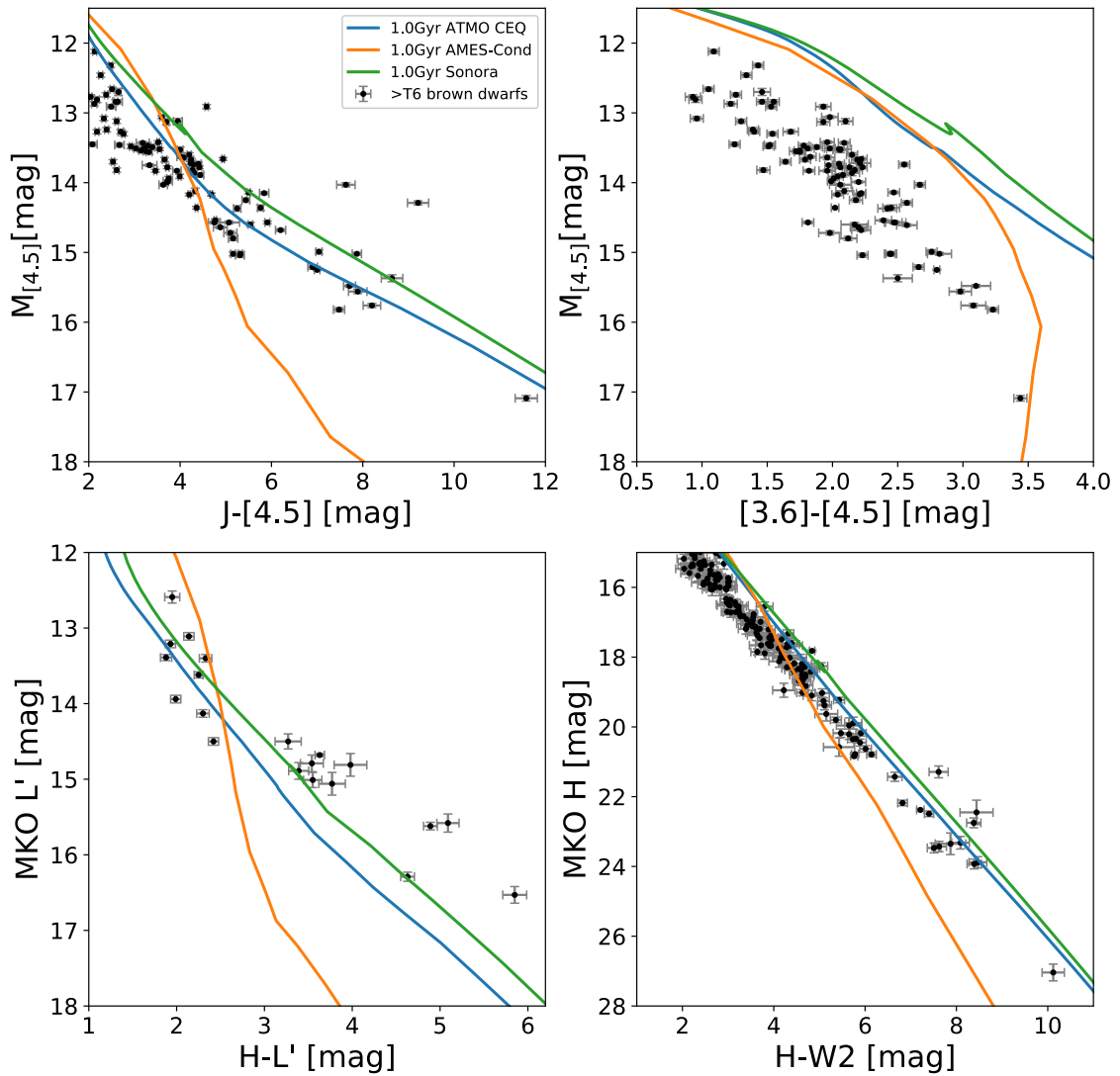
**Figure 6.7:** Same as Figure 6.6, but with 1 Gyr isochrones from `ATMO` 2020 (blue), AMES-Cond (orange) and `Sonora` (green) chemical equilibrium models.

In Figure 6.7 we show CMDs including 1 Gyr isochrones from the `ATMO` 2020, AMES-Cond and `Sonora` chemical equilibrium models. The AMES-Cond isochrones tend to be fainter than the `ATMO` and `Sonora` isochrones for cool Y dwarf objects in photometric bands that cover the $3.5-5.5$ $\mu$m flux window. This is due to the cooler atmospheric temperature structures given by the AMES-Cond models (see Figure 5.13). The `Sonora` isochrones are slightly brighter than the `ATMO` isochrones in $L'$, [4.5] and $W2$ band magnitude, likely due to differing $PH_3$ absorption as discussed in Section 5.3.3 and shown in Figure 5.19. This means the `Sonora` isochrones have redder $J-[4.5]$, $[3.6]-[4.5]$, $H-L'$ and $H-W2$ colours compared to the `ATMO` isochrones, but generally show the same trends.
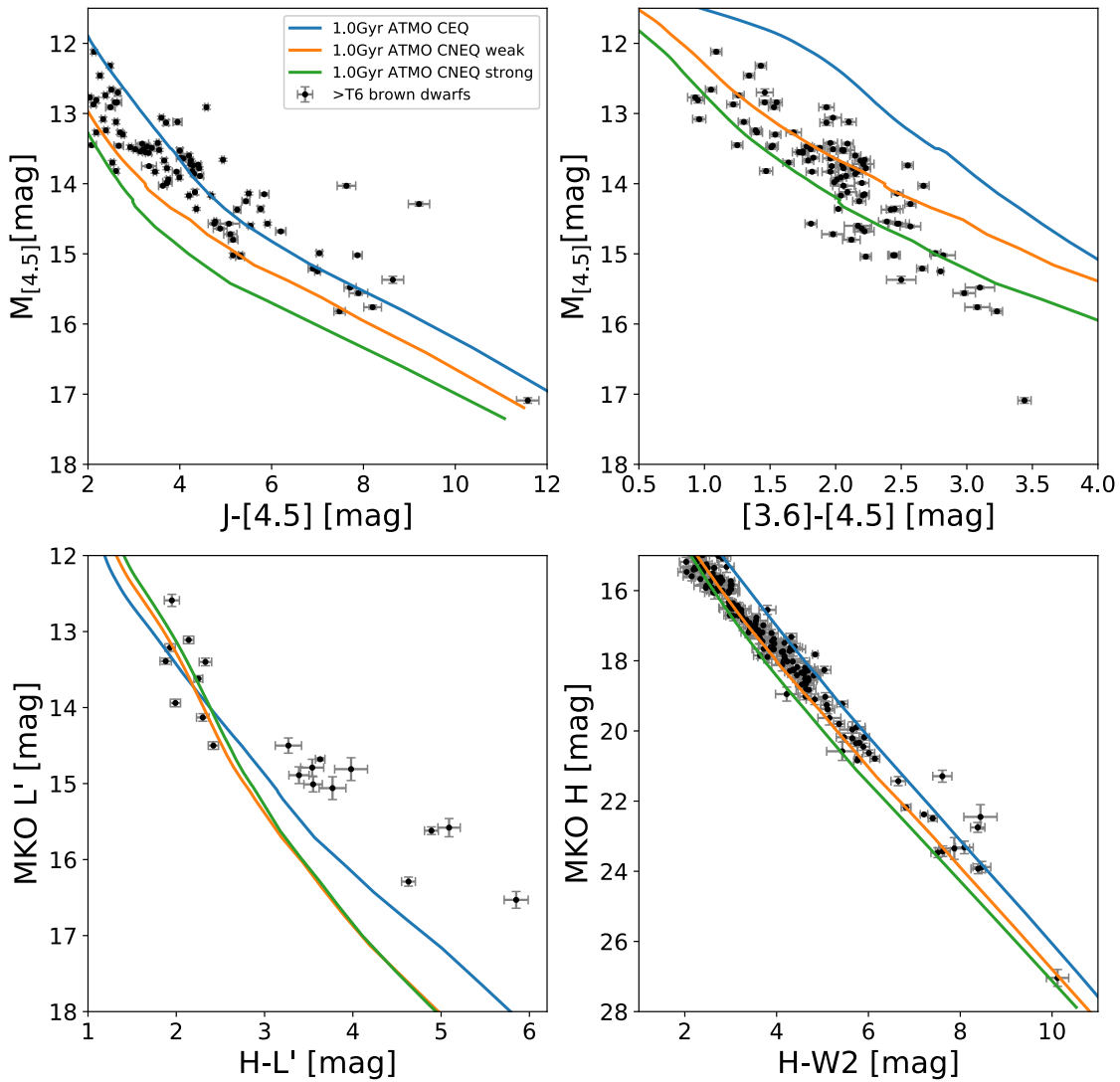
**Figure 6.8:** Same as Figure 6.6, but with 1 Gyr isochrones from chemical equilibrium models (blue) and non-equilibrium chemistry models with weak (orange) and strong(green) vertical mixing from the `ATMO 2020` model set.

In Figure 6.8, we show 1 Gyr `ATMO` isochrones with photometry derived from chemical equilibrium and non-equilibrium atmosphere models to illustate the impact of vertical mixing on the predicted colours of cool brown dwarfs. Including non-equilibrium chemistry due to vertical mixing reduces the $W2$ and $[4.5]$ band magnitudes due to increased CO and $CO_2$ absorption, the quenching of $CH_4$ brightens the $L'$ and $[3.6]$ bands, and the quenching of both $CH_4$ and $NH_3$ brightens the $H$ band. This yields bluer $J − [4.5]$, $[3.6]−[4.5]$, and $H−W2$ colours. The observed $J−[4.5]$ colours are reasonably well encapsulated by the chemical equilibrium and weak vertical mixing isochrones, indicating that variations in the strength of vertical mixing in these objects could explain their observed

colours. The strong mixing tracks are too blue compared to the data. A similar conclusion can be drawn from the $H-W2$ colours, where the weak vertical mixing tracks provide the best comparison to the data. Given the tight correlation of $H-W2$ colour with $H$-band magnitude, and the dependence of $H-W2$ colour on vertical mixing, this CMD could be used to calibrate vertical mixing in cool brown dwarfs and constrain the values of $K_{zz}$ that should be used in atmosphere models.

The predicted $[3.6]-[4.5]$ colours are improved by the inclusion of vertical mixing, with both the strong and weak vertical mixing tracks matching the observed population of T and Y dwarfs. However, the tracks diverge from the $[3.6]-[4.5]$ colours of the coolest objects, predicting colours that are far too red. In the $H-L'$ diagram, including non-equilibrium chemistry due to vertical mixing can increase the $\lambda \sim 3.6-4.0\,\mu$m flux as $CH_4$ is quenched in the atmosphere, lowering the opacity in the $L'$ band. However, as the $H$ band also brightens when including vertical mixing the $H-L'$ colours become bluer, moving the tracks away from the observed population of late T and Y dwarf compared to chemical equilibrium tracks. As noted by Leggett et al. (2019) and Morley et al. (2018), the discrepancy between the models and the observed $\lambda \sim 3.6-4.0\,\mu$m flux is likely due to processes happening in these atmospheres that are not currently captured by 1D radiative-convective models, such as thermochemical instabilities, cloud clearing, or breaking gravity waves. The inclusion of such processes in 1D atmosphere models may improve the comparisons to data in the $H-L'$ and $[3.6]-[4.5]$ diagrams.

## 6.3 Spectral comparisons to observations

In this Section, we show comparisons of our models to spectra and photometry of cool T–Y-type brown dwarfs. Our methodology here is to compare models to the data by eye, guided by values of $T_{\text{eff}}$, $\log(g)$, and $R$ obtained from other studies in the literature and which are consistent with our new evolutionary tracks. Our by-eye comparison serves to illustrate model improvements and current shortcomings in reproducing cool brown dwarf spectra, and we leave more thorough grid fitting analyses to future work.

### 6.3.1 Gliese 570 D

Gliese 570 D is a late T dwarf companion to a ternary star system $\sim 5.8$ pc parsecs away from the sun (Burgasser et al. 2000; van Leeuwen 2007). It has a T7.5 spectral type and is one of the most thoroughly studied T dwarfs to date. Age indicators from the host star indicate an age in the range $1-5$ Gyr (Geballe et al. 2001; Liu et al. 2007). Gliese 570 D has been the target of a number of grid fitting studies, which have estimated $T_{\text{eff}} = 800-820$ K, $\log(g) = 5.00-5.27$ and $L = 2.88-2.98\, L_{\odot}$ (Geballe et al. 2001, 2009; Saumon et al. 2006; Saumon et al. 2012). This object has also been used as a benchmark for brown dwarf retrieval studies, which obtain a slightly cooler $T_{\text{eff}} = 715$ K and a surface gravity $\log(g) = 4.8$ (Line et al. 2015, 2017). Red-optical and near-infrared spectra are from Burgasser et al. (2003b, 2004).

We compare $T_{\text{eff}} = 800$ K, $\log(g) = 5.0$ chemical equilibrium models calculated with different K resonance line broadening schemes to the red-optical and near-infrared spectra of Gliese 570 D (Burgasser et al. 2003b, 2004) in Figure 6.9. We find a radius of $R/R_{\odot} = 0.082$ provides the best match to the observed spectrum for this $T_{\text{eff}}$ and $\log(g)$. Using our new evolutionary tracks, these parameters indicate an age of 5 Gyr and a mass of $46\,M_{\text{Jup}}$ for Gliese 570 D, in agreement with previous works (Saumon et al. 2006). We note that non-equilibrium chemistry models do not impact the near-infrared spectrum within this wavelength range since the $K_{\text{zz}}$ value is low for this high gravity.

The models with A16 K resonance line broadening provide the best match to the data. There is an excellent agreement in the $Y$ band where the redwing of the K resonance doublet influences the spectrum. In models with A07 K broadening the opacity in the redwing is too strong giving too little flux in the $Y$ band, whereas in models with BV03 broadening too much flux emerges in the $Y$ band due to the lower opacity in the K redwing. A further improvement in the models can be seen in the $H$ band, where the improved methane line list provides a much more satisfactory comparison to the data than models with a less complete line list (Saumon et al. 2012). The $K$ band is nicely reproduced due to the collisionally induced absorption from Richard et al. (2012), as previously shown in Saumon et al. (2012). The flux in the $J$ band is overpredicted by the model with A16 K broadening. We speculate that a more in-depth fitting study investigating the effects of
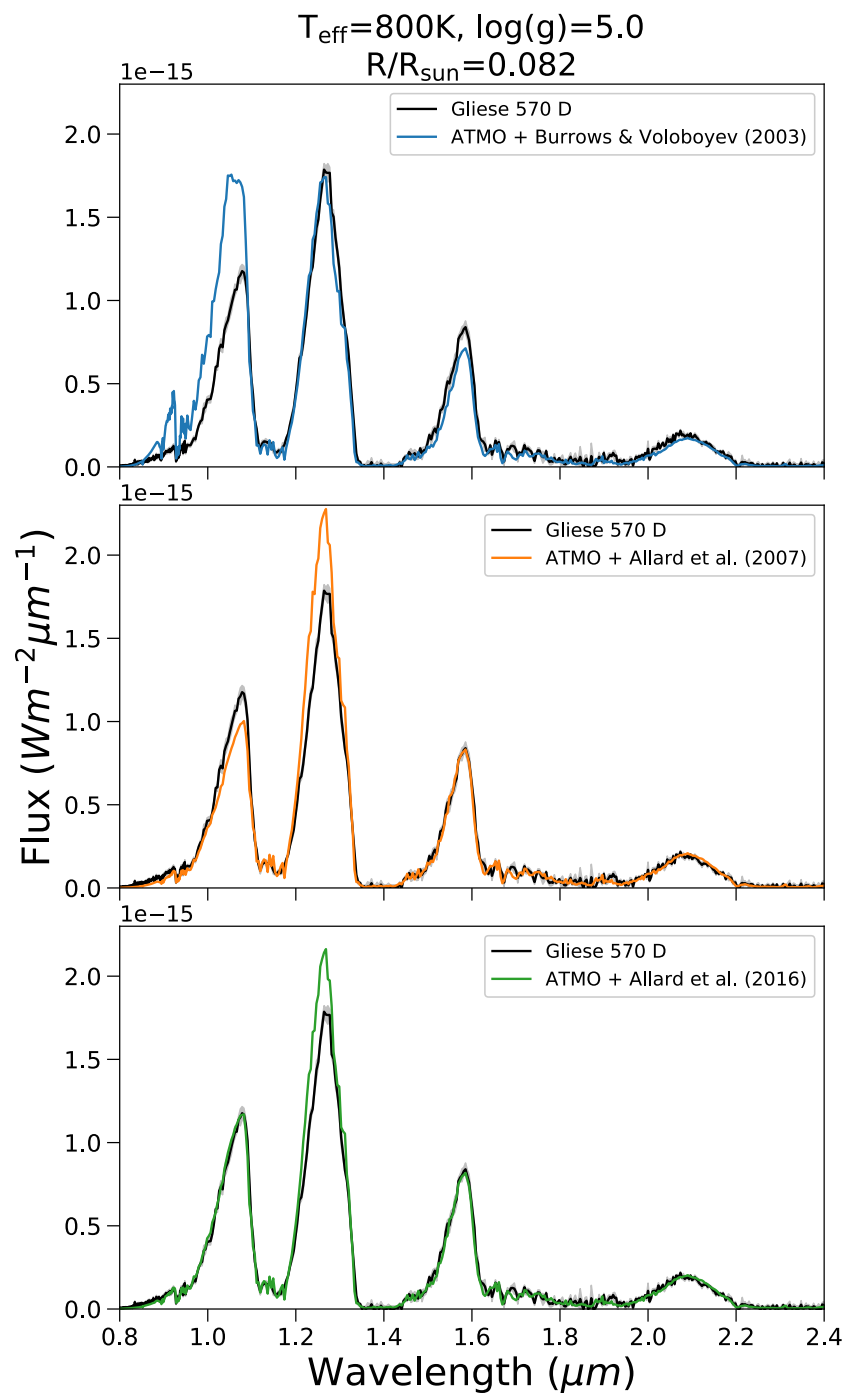
**Figure 6.9:** Model comparisons to the absolutely flux calibrated near-infrared spectrum of the T7.5 dwarf Gliese 570 D (Burgasser et al. 2000). Three models are shown all calculated self-consistently using K resonance line broadening from BV03 (top), A07 (middle), and A16 (bottom), for $T_{eff}$ = 800 K, $\log(g)$ = 5.0, and $R/R_\odot$ = 0.082.

metallicity and/or thermo-chemical instabilities may help further improve the fit in the *J*

band.

### 6.3.2 The T–Y transition

In Figure 6.10 we show a comparison of the `ATMO` 2020 models calculated with equilibrium and non-equilibrium chemistry to spectra and photometry of objects spanning the T–Y transition. We compare them to the T9 spectral standard UGPS 0722 (Lucas et al. 2010; Leggett et al. 2012), a well-studied cool dwarf that has been estimated to have $T_{\mathrm{eff}} = 505 \pm 10\,$K, a mass of $3 - 11\,$M$_{\mathrm{Jup}}$, and an age range between 60 Myr and 1 Gyr using the SM08 models (Leggett et al. 2012). We compare $T_{\mathrm{eff}} = 500\,$K, $\log(g) = 4.0$ chemical equilibrium and non-equilibrium models to this object, finding that these models overpredict the flux in the *Y* and *J* bands at $\sim 1.0\,\mu m$ and $\sim 1.2\,\mu m$, respectively. This has been noted by other authors (e.g. Leggett et al. (2012)), with sulfide clouds (Morley et al. 2012) or a reduced temperature gradient (Tremblin et al. 2015) invoked to redden the spectrum at these short near-infrared wavelengths. This is further explored in Section 6.3.4.

At longer wavelengths, the shape of the *K* band at $\sim 2.1\,\mu m$ appears to be better reproduced by the model including non-equilibrium chemistry. The *Spitzer* IRAC channel 2 and *WISE W*2 photometric points at $\sim 4.5\,\mu m$ and $\sim 4.6\,\mu m$, respectively, are lower than that predicted with the chemical equilibrium model, implying the presence of enhanced CO absorption brought about through vertical mixing in the atmosphere (see Figure 5.9 and Section 5.2.4). Both the strong and weak mixing non-equilibrium models overpredict the CO absorption in the IRAC ch2 and *W*2 bands, implying that the strength of vertical mixing is overestimated in the current model set-up. Decreasing the eddy diffusion coefficient $K_{\mathrm{zz}}$ further may improve the comparison to the photometric points in the $4 - 5\,\mu m$ flux window for this object.

Observations of the Y0- and Y1-type objects WISE 1206 and WISE 1541 (Cushing et al. 2011; Schneider et al. 2015) are shown in the middle and bottom panels of Figure 6.10, respectively. Using the cloud-less models of SM08, Schneider et al. (2015) estimate $T_{\mathrm{eff}} \sim 400 - 450\,$K and $\log(g) = 4.0 - 4.5$ for the Y0 object WISE 1206. Zalesky et al. (2019) ran retrieval analysis on a sample of Y dwarfs including WISE 1541, retrieving $T_{\mathrm{eff}} \sim 325\,$K $\log(g) \sim 5.0$ for this object, in line with comparisons to cloud-free forward models presented in Leggett et al. (2013). Here we compare $T_{\mathrm{eff}} = 420\,$K, $\log(g) = 4.5$ models to WISE 1206 and $T_{\mathrm{eff}} = 330\,$K, $\log(g) = 4.0$ models to WISE 1541. We use a lower value of
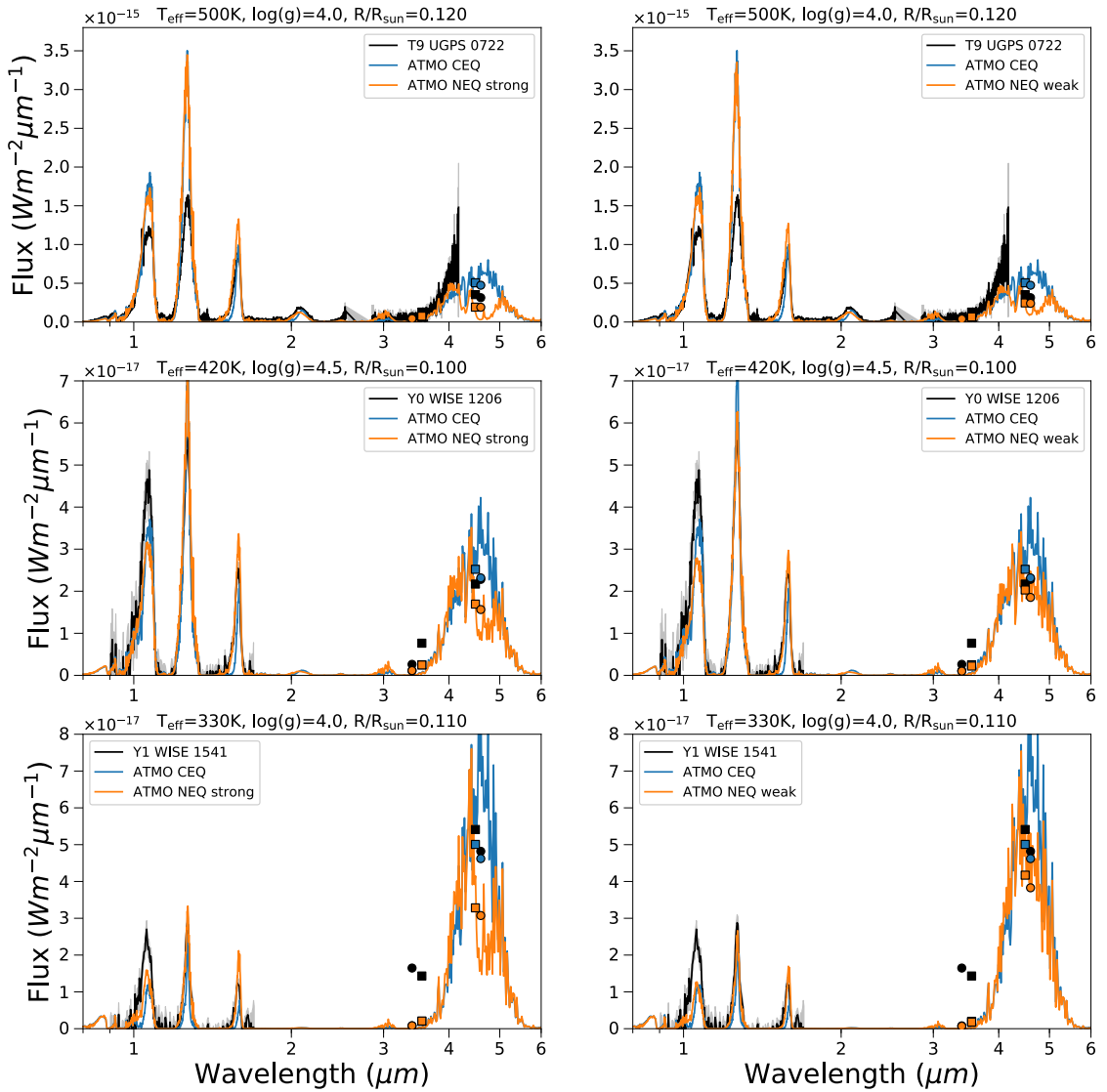
**Figure 6.10:** Comparison of the chemical equilibrium (blue) and non-equilibrium (orange) `ATMO` 2020 models to sample spectra (black) forming a T–Y spectral sequence. The left and right columns display non-equilibrium models with the strong and weak $K_{zz}$ mixing relationships with surface gravity, respectively. *Spitzer* IRAC photometry is plotted as squares and *WISE* photometry as circles. The top panel shows the observed spectrum of the T9 dwarf UGPS 0722 (Lucas et al. 2010; Leggett et al. 2012), with *Spitzer* IRAC and *WISE* photometric points from Kirkpatrick et al. (2012). The middle and bottom panels show the $0.9 - 1.7\ \mu m$ *HST* WFC3 spectra of the Y0- and Y1-type dwarfs WISE 1206 and WISE 1541 (Schneider et al. 2015), with *Spitzer* IRAC photometry also from Schneider et al. (2015) and *WISE* photometry from Cutri et al. (2013).

the surface gravity for WISE 1541 than obtained by previous studies since $\log(g) = 5.0$ does not agree with our evolutionary tracks at this $T_{\text{eff}}$.

The *J*- and *H*-band brightness and shape is better reproduced by the non-equilibrium models for both objects. This is due to the quenching of $NH_3$ reducing the opacity in these bands (see Figure 5.9 and Tremblin et al. (2015)). The strong mixing non-equilibrium chemistry model overpredicts the CO absorption in the $4 - 5\ \mu m$ flux window for the
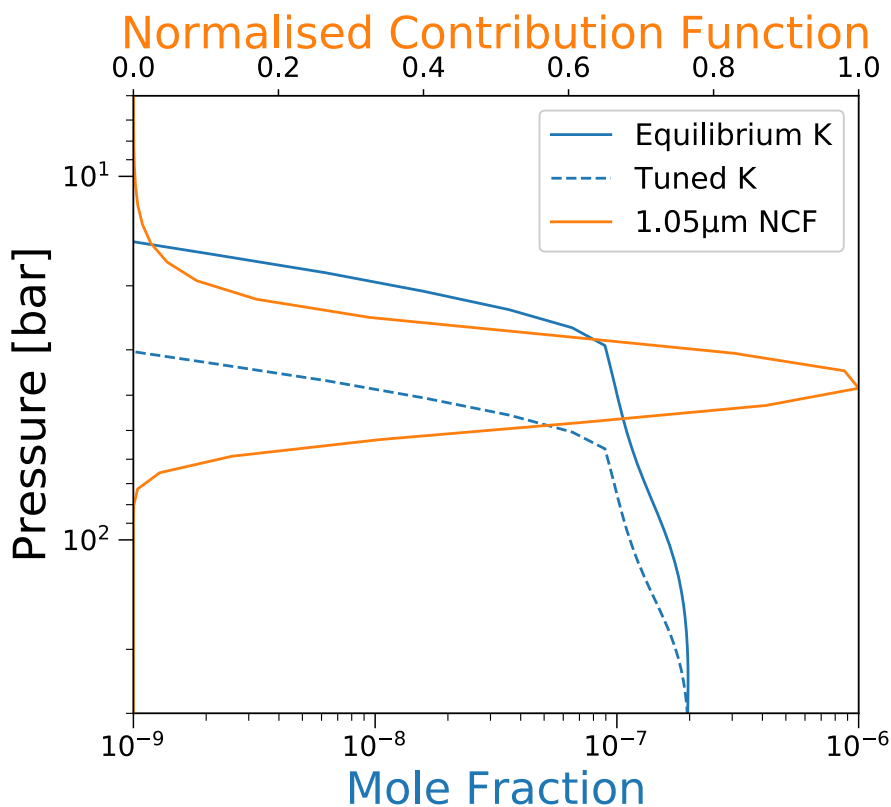
**Figure 6.11:** The equilibrium (solid blue line) and tuned (dashed blue line) mole fraction of potassium in the $T_{\text{eff}} = 420\,\text{K}$, $\log(g) = 4.5$, NEQ weak model atmosphere used to model the emission spectrum of WISE 1206 in Figure 6.10 and 6.12. The normalised contribution function at the 1.05 $\mu$m peak of the $Y$ band is shown as the orange line.

warmer WISE 1206 object, while the weaker mixing model better reproduces the photometric points in this wavelength range. The strong and weak mixing non-equilibrium chemistry models both overpredict the CO absorption in the cooler WISE 1541 object, with the equilibrium model better reproducing the *WISE* and *Spitzer* photometry.

### 6.3.3   Tuning the potassium abundance

The $Y$-band flux at $\sim 1\,\mu m$ is underpredicted for WISE 1206 and WISE 1541 in Figure 6.10 by the current models, an issue also seen by the model comparisons in Schneider et al. (2015). We note that the $K - H_2$ opacity is important in this wavelength region; however, given the improvements to the K resonant line broadening outlined in Chapter 4, we do not attribute this discrepancy to shortcomings in the K opacity. Instead, we note that reducing the K abundance by artificially altering the KCl condensation level in the model atmosphere can rectify the difference between model and data in the $Y$ band.
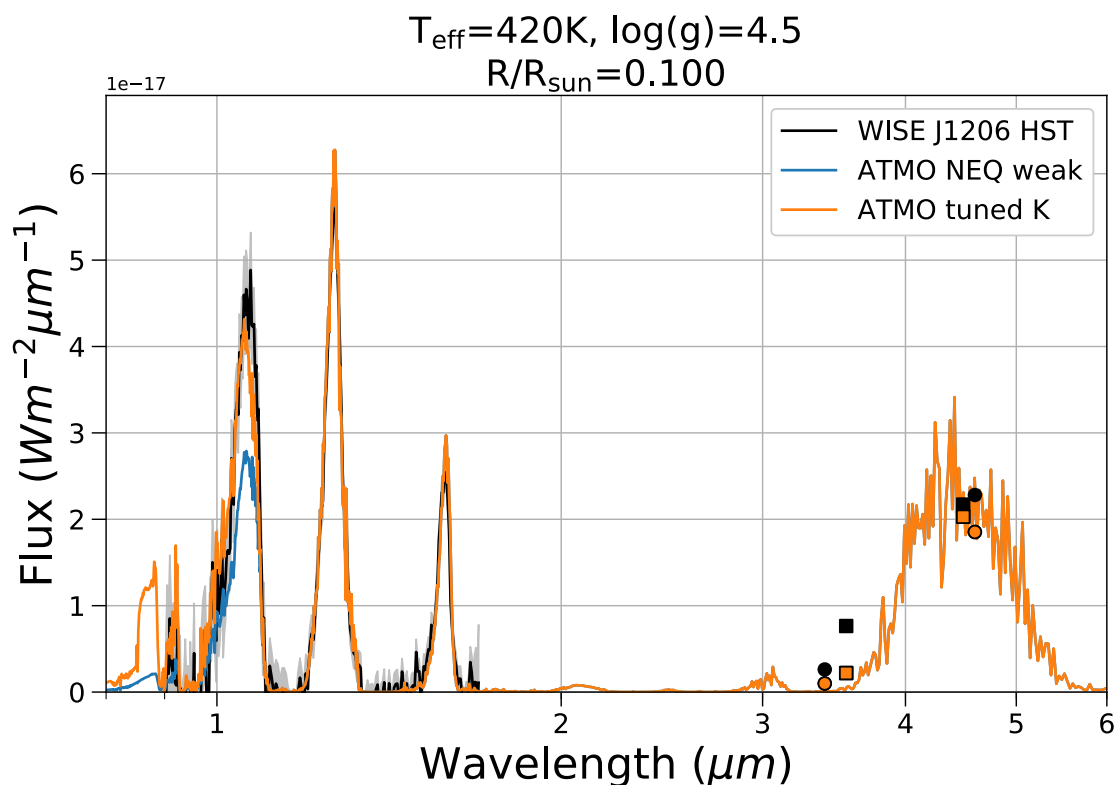
**Figure 6.12:** Comparison of the $T_{\text{eff}}$ = 420 K, $\log(g)$ = 4.5, `ATMO` 2020 weak vertical mixing model emission spectrum with equilibrium (blue) and tuned (orange) potassium abundance, to the observed spectra and photometry of WISE 1206.

The process of artificially tuning the potassium abundance to better match the data is shown in Figures 6.11 and 6.12. Figure 6.11 shows the abundance of K in the atmosphere corresponding to the $T_{\text{eff}}$ = 420 K, $\log(g)$ = 4.5, weak vertical mixing model used to model WISE 1206 in Figure 6.10. Potassium is sufficiently abundant in the unmodified, equilibrium model between $30 - 40$ bar where the 1.05 $\mu$m contribution function peaks. The opacity of $K - H_2$ therefore suppresses the flux in the $Y$ band. The K abundance can however be artificially tuned so that it is reduced by approximately an order of magnitude between $30 - 40$ bar in the peak of the 1.05 $\mu$m contribution function. This reduces the $K - H_2$ opacity and increases the flux passing through the $Y$ band, better matching the observed emission of WISE 1206 as illustrated in Figure 6.12.

We therefore posit that the current modelling of the potassium chemistry, including potentially its condensation into KCl and/or the thermochemical data used to calculate the equilibrium abundances, is slightly incorrect. This should be investigated more thoroughly in future work.

### 6.3.4   Tuning the effective adiabatic index

As discussed in Section 6.3.2, the current `ATMO` 2020 models overpredict the flux in the $Y$ and $J$ bands of late T dwarf objects such as UGPS 0722. This has been noted by other authors (e.g. Leggett et al. (2012)), with sulfide clouds (Morley et al. 2012) or a reduced temperature gradient (Tremblin et al. 2015) invoked to redden the spectrum at these short near-infrared wavelengths. Here we explore the process of reducing the temperature gradient of the model atmosphere to resolve the discrepancy between model and data.

The suggested mechanism reducing the temperature gradient in brown dwarf atmospheres is radiative convective instabilities triggered by chemical transitions such as $CO \rightarrow CH_4$ and $N_2 \rightarrow NH_3$ (Tremblin et al. 2019). The reduction in the temperature gradient can be mimicked in `ATMO` models through the effective adiabatic index $\gamma_{\mathrm{eff}}$. We recall from Section 2.1 that the adiabatic gradient which sets the temperature gradient in convectively unstable regions of the atmosphere can be written as

$$\nabla_{\mathrm{ad}} = \frac{\gamma - 1}{\gamma}, \tag{6.1}$$

where $\gamma$ is the adiabatic index obtained from the (Saumon et al. 1995) EOS tables as discussed in Section 3.1.4. The adiabatic index $\gamma$ can be replaced with a user defined effective adiabatic index $\gamma_{\mathrm{eff}}$ in Equation (6.1), which changes the temperature gradient in the convectively unstable regions of the atmosphere. Reductions in the temperature gradient through $\gamma_{\mathrm{eff}}$ have been shown to reproduce several observed features of brown dwarfs, including the L-T transition (Tremblin et al. 2016), extremely red young low-gravity objects (Tremblin et al. 2017b), and the red colours of cool late T dwarf objects (Tremblin et al. 2015).

Figure 6.13 shows P-T profiles used to model the late T dwarf UGPS 0722. The corresponding emission spectra from these model atmospheres are compared to the observed spectrum of UGPS 0722 in Figure 6.14. The unmodified $T_{\mathrm{eff}} = 500$ and $550\,\mathrm{K}$ models (blue and orange respectively) both overpredict the flux in the $Y$ and $J$ band at $\sim 1.05\,\mu\mathrm{m}$ and $\sim 1.2\,\mu\mathrm{m}$ respectively. The $Y$ and $J$ band flux is formed at pressures of $10 - 30\,\mathrm{bar}$ in the at-
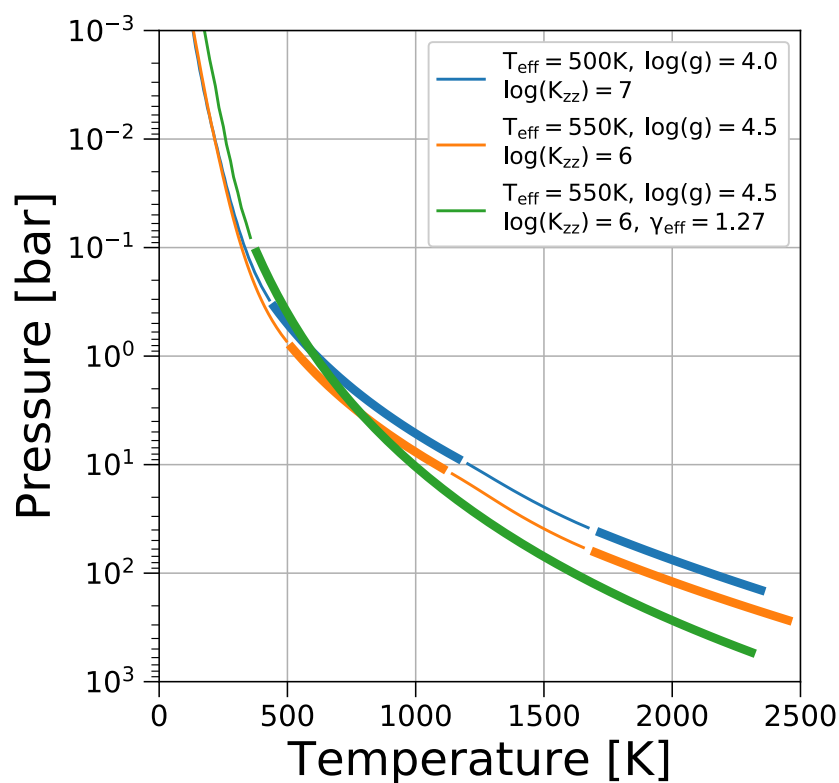
**Figure 6.13:** Pressure-temperature profiles used to model the late T dwarf UGPS 0722. Convectively unstable regions of the atmosphere are shown as thickened lines. The model atmosphere with a modified temperature gradient through the effective adiabatic index is shown in green.

mosphere. The P-T profile with $\gamma_{eff} = 1.27$ (green model) reduces the temperature at these pressure levels, thus reducing the flux emitted through the $Y$ and $J$ bands and matching the spectrum of UGPS 0722 well at these wavelengths. At longer wavelengths the spectrum in the $3.5 - 5.5\,\mu m$ flux window is well reproduced by the $T_{eff} = 540\,K$, $\gamma_{eff} = 1.27$ model, capturing both the slope between $3.5 - 4.2\,\mu m$, and the CO absorption in the $M'$ spectrum from Miles et al. (2020). Note that, since the $\gamma_{eff} = 1.27$ profile is cooler in the deep atmosphere, the value of $K_{zz}$ has been increased to $K_{zz} = 10^7\,cm^2s^{-1}$ compared to the strong and weak mixing relationships used in the ATMO 2020 models to quench a sufficient amount of CO to reproduce the $M'$ spectrum. This further highlights how CO absorption in the $3.5 - 5.5\,\mu m$ flux window can be used to calibrate vertical mixing in cool brown dwarf atmospheres.
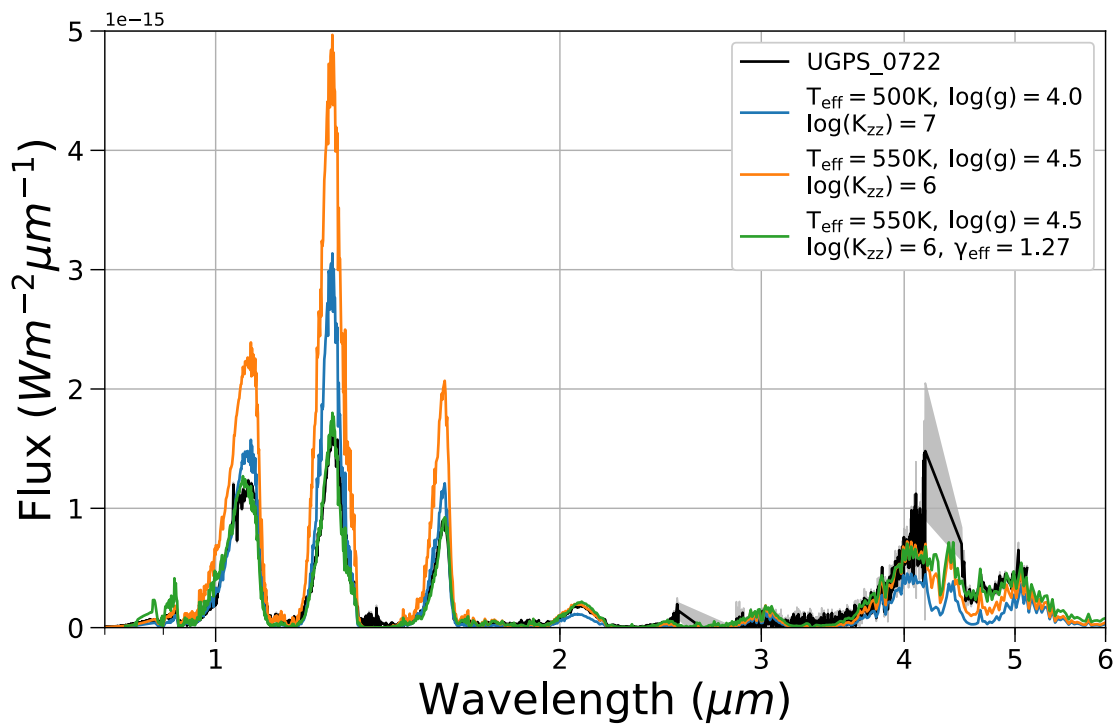
**Figure 6.14:** Comparison of `ATMO` model emission spectra to the observed spectrum of UGPS 0722 (Lucas et al. 2010; Leggett et al. 2012; Miles et al. 2020). The corresponding P-T profiles of the models shown here are shown in Figure 6.13. The spectrum corresponding to the model atmosphere with a modified temperature gradient through the effective adiabatic index is shown in green.

## 6.4   Summary and Conclusions

In this Chapter, I have presented extensive comparisons of the `ATMO` 2020 model set, along with other model sets in the literature, to observational datasets. These observational datasets include brown dwarf dynamical mass measurements (Section 6.1), photometry of large samples of field brown dwarfs (Section 6.2), and infrared emission spectra of individual objects (Section 6.3). The comparisons of the `ATMO` 2020 models to these observational datasets serve to illustrate numerous modelling improvements presented in this thesis, as well as highlight the current shortcomings in the modelling of cool brown dwarfs, thus motivating future research. The main conclusions from this Chapter are as follows:

- The new H-He EOS of Chabrier et al. (2019) used in the calculation of the `ATMO` 2020 evolutionary tracks helps relieve some tension between T dwarfs such as Gl 229 B with unexpectedly high dynamical mass measurements and evolutionary models. Evolutionary models tend to predict that these systems must be older than age estimates from host star activity and/or kinematics to have cooled to their observed lu-

minosity. The new EOS predicts high mass objects cool faster, to lower temperatures and luminosities than previous models, thus reducing the discrepancy in derived ages. It must however be noted that the difference in evolutionary tracks calculated with the old and new EOS is not observationally significant given the uncertainty on typical dynamical mass measurements.

- The new potassium resonance line shapes of Allard et al. (2016) implemented in the ATMO 2020 models have been validated through comparisons to the observed $Y - J$ colours of cool brown dwarfs and the emission spectrum of a typical mid-late T dwarf, Gliese 570 D. The $Y$ band at $\sim 1.05\,\mu$m is best reproduced by models including the new line shapes, with models computed with potassium resonance line shapes from Allard et al. (2007b) and Burrows & Volobuyev (2003) predicting too strong and too little absorption, respectively, in the far red wing.

- Despite the improvements to the K resonant line broadening, the $Y$-band flux of the Y dwarfs WISE 1206 and WISE 1541 is underpredicted by the current models, giving $Y - J$ colours that are too red compared to the observed Y dwarf population. We have demonstrated that this discrepancy can be rectified by artificially reducing the potassium abundance to mimick the condensation into KCl occuring at higher pressures in the model atmosphere. This reduces the $K - H_2$ opacity and increases the flux passing through the $Y$ band, better matching the observed emission of the Y dwarf WISE 1206. We therefore posit that the current modelling of potassium chemistry, including potentially its condensation into KCl and/or the thermochemical data used to calculate the equilibrium abundances is slightly incorrect, and should be investigated in future work.

- Comparisons of the ATMO 2020 models to the observed spectra of Y dwarfs indicate the quenching of ammonia is key in reproducing near-infrared emission from these objects, in agreement with the results of Leggett et al. (2015); Tremblin et al. (2015). Comparisons of the models to photometry probing the $3.5 - 5.5\,\mu$m flux window also supports the presence of non-equilibrium CO and $CO_2$ abundances. Since the abundances of CO and $CO_2$ depend strongly on the value of $K_{zz}$ (the parameter commonly used to model vertical mixing in 1D atmosphere codes), the $3.5 - 5.5\,\mu$m

flux window is a useful observational diagnostic of $K_{zz}$ in cool brown dwarf atmospheres, as demonstrated recently by Miles et al. (2020).

- We have demonstrated that reducing the temperature gradient in a 1D model atmosphere through the effective adiabatic index can successfully reproduce the emission spectrum of the late T dwarf UGPS 0722 over the full $1 - 5\,\mu$m wavelength range. The reduction in the temperature gradient is thought to be driven by the $CO \rightarrow CH_4$ and $N_2 \rightarrow NH_3$ chemical transitions triggering convective instabilities (Tremblin et al. 2019). This cools the deep layers of the atmosphere and lowers the flux emitted through the $Y$, $J$ and $H$ bands. Reducing the temperature gradient can thus impact the predicted $J-H$, $J-K$, $H-L'$ colours of brown dwarfs that have found to be insufficiently modelled by the current ATMO 2020 models through comparisons to observations in colour-magnitude diagrams in this Chapter. This therefore provides motivation to expand on this initial grid of atmosphere models, by reducing the temperature gradient through the effective adiabatic index.

# Chapter 7

# Summary and future work

## 7.1 Summary and conclusions

A reliable model of the atmosphere and its evolution over time lies at the core of our understanding of brown dwarfs and giant exoplanets. The atmosphere regulates the rate at which these objects cool, and imprints its temperature structure and chemical composition onto the emitted thermal radiation. The study of brown dwarfs and giant exoplanets is being driven by ever-improving instrumentation becoming sensitive to cooler objects, which are providing the opportunity to study Jovian-like worlds outside of our solar system. In this thesis I have presented a new set of atmosphere and evolution models applicable for the coolest T/Y brown dwarfs and giant exoplanets, termed `ATMO` 2020. These models are important for placing mass and age constraints on newly discovered objects and understanding the rich chemistry and physics taking place in their atmospheres.

In Chapter 2 I reviewed the physics and techniques used in one-dimensional atmosphere models, with a particular focus on the `ATMO` code which I have used throughout this thesis to generate the new set of atmosphere models. `ATMO` solves for the temperature structure of the atmosphere in radiative and convective flux balance with a given internal heat flux, and computes the emission spectrum from the top of the atmosphere for comparisons to observations. The two major components of the `ATMO` code are therefore the radiative transfer and convection modules, which are detailed in Section 2.2 and Sec-

tion 2.3 respectively. To find the temperature structure of the atmosphere, ATMO iterates towards radiative-convective equilibrium, which is discussed in Section 2.4.

The main input physics to the ATMO code is the chemistry schemes and the opacity sources that are used in the model atmosphere, which is the focus of Chapter 3. In Section 3.1, I review the different chemistry schemes used in the ATMO 2020 model atmospheres. These include the calculation of chemical equilibrium abundances with rainout condensation, and the inclusion of non-equilibrium chemistry due to vertical mixing using a fully coupled chemical relaxation scheme. I also demonstrate that an equation of state that takes into account $H_2 \rightarrow 2H$ dissociation energy is required to correctly model the adiabatic gradient in atmospheres with $T_{\mathrm{eff}} > 2000\,\mathrm{K}$. In Section 3.2, I discuss the calculation of atomic and molecular opacity tables from large line lists for use in radiative transfer calculations within ATMO. I present calculations of gaseous Fe opacity, an important absorber at short wavelengths ($0.2 - 0.4\,\mu$m) which we show can play an important role in forming temperature inversions in hot Jupiter atmospheres.

The alkali metals are key opacity sources in brown dwarf atmospheres. In particular, the potassium resonance lines at $\sim 0.77\,\mu$m are broadened due to the high atmospheric densities of $H_2$, and can dominate the $0.7 - 1.0\,\mu$m spectrum of late L and T dwarfs. In Chapter 4, I present the implementation of new resonant line shapes from Allard et al. (2016) in the calculation of potassium opacity tables for ATMO. I outline the junction of the Lorentzian line cores and the pressure broadened wings, and review how the line wing shape depends on temperature and $H_2$/He perturber number density. The new resonant line shape calculations improve upon previous calculations principally on their validity at high atmospheric densities ($n_{H_2} > 10^{19}\,\mathrm{cm}^{-3}$), which leads to differences in the predicted opacity in the blue wing satellite feature and the far-red wing. I compare synthetic emission spectra calculated with these new K line shapes to others commonly used in the literature, showing that there is a large impact on the predicted Y- and J-band flux due to these different line shapes. These differences are larger in high gravity atmospheres due to higher $H_2$ number densities, meaning the new K resonant line shapes are most important for old and/or massive brown dwarfs.

In Chapter 5 I present the ATMO 2020 set of atmosphere and evolutionary models

for cool brown dwarfs and directly imaged giant planets. The atmosphere grid spans $T_{\text{eff}} = 200 - 3000\,\text{K}$, $\log(g) = 2.5 - 5.5$ with both equilibrium and non-equilibrium chemistry due to different strengths of vertical mixing. This grid of atmosphere models is used as the surface boundary condition for an interior structure model to calculate the evolution of $0.0005 - 0.075\,M_\odot$ objects. I highlight theoretical modelling improvements through comparisons to other model sets, finding that there are notable changes to the cooling tracks and predicted emission of substellar objects. These changes are brought about by two major modelling improvements. First the use of a new hydrogen and helium EOS (Chabrier et al. 2019) in the interior structure model has raised the hydrogen and deuterium burning minimum masses, causing changes in the cooling tracks around these masses. Second, improved high temperature line lists for important molecular absorbers have added opacity to the 1D model atmosphere, changing the predicted emission spectra and leading to warmer temperature structures, which alter the shape of the cooling tracks of substellar objects in the low-mass brown dwarf regime. I demonstrate the impact of self-consistent non-equilibrium chemistry due to vertical mixing on 1D model atmospheres, and highlight how CO and $CO_2$ absorption in the $4 - 5\,\mu$m flux window can be used to calibrate vertical mixing in cool substellar atmospheres. The results from Chapter 5 are fully summarised and concluded in Section 5.4.

Finally, in Chapter 6 I compare the ATMO 2020 model set to observational datasets of substellar objects. I show that the new H-He EOS used in the calculation of the ATMO 2020 evolutionary tracks helps relieve some tension between T dwarfs with unexpectedly high dynamical mass measurements and evolutionary models. I validate the implementation of the new potassium line shapes presented in Chapter 4 through the observed $Y - J$ colours of cool brown dwarfs and the emission spectrum of a typical mid-late T dwarf. Finally, I demonstrate that non-equilibrium chemistry due to vertical mixing is supported through comparisons to near-infrared photometry and emission spectra of cool T/Y brown dwarfs. These comparisons further illustrate the numerous modelling improvements included in the ATMO 2020 model set, but also serve to highlight the current shortcomings in the modelling of cool brown dwarfs. Despite the improvements to the K resonant line broadening, the Y-band flux of Y dwarfs appears to be underpredicted by the current models, and I demonstrate that this discrepancy can be rectified by artificially

reducing the potassium abundance in the model atmosphere. The near-infrared colours of late-T dwarfs are also significantly redder than those predicted by the current models, and I demonstrate that this discrepancy can be improved by reducing the temperature gradient in a 1D model atmosphere. The results from Chapter 6 are fully summarised and concluded in Section 6.4.

## 7.2   Future work

There are a number of possible avenues to build upon my existing work in forward modelling of substellar atmospheres, and several natural extensions to the `ATMO 2020` model set presented in this thesis. I finish by outlining these ideas for future work.

### 7.2.1   Non-solar metallicity models

The atmosphere models presented in this thesis were all generated assuming solar metallicity elemental abundances. A natural extension to the `ATMO 2020` model grid is therefore exploring the effect of non-solar metallicities on the predicted cooling and emission of substellar objects. Spectroscopic signatures of metallicity through the C/O ratio have been cited as a method of inferring the formation mechanism of an object, and hence its classification as a planet or brown dwarf (Bowler 2016). However, such signatures could be degenerate with other atmospheric processes such as non-equilibrium chemistry due to vertical mixing. My work self-consistently coupling a non-equilibrium chemistry scheme in the `ATMO 2020` models therefore provides an ideal starting point for future studies into disentangling the spectral signatures of non-equilibrium chemistry and non-solar metallicity. This could be a key step in finding observational differences between planets formed by accretion in a protoplanetary disk and cool brown dwarfs formed by gravitational collapse of interstellar material.

### 7.2.2   Opacities and alkali broadening

In this thesis, I have demonstrated the importance of molecular opacities in shaping the temperature structures and synthetic spectra of cool brown dwarfs and giant exoplanets. Line lists of important absorbers are being continuously updated and improved. For ex-

ample, several new line lists have been published since the generation of the ATMO 2020 models, including $H_2O$ (Polyansky et al. 2018), TiO (McKemmish et al. 2019) and $CO_2$ (Yurchenko et al. 2020). Future work integrating these updated opacities into ATMO will be undertaken, and the impact on the temperature structures, synthetic spectra, and cooling tracks will be investigated.

I have also shown that the new potassium resonant line shapes used in this work improve the near-infrared spectral comparisons to mid-late T dwarfs. Further work must be undertaken to validate these line shapes not only in the near-infrared, but also at red-optical wavelengths where line shape calculations differ in the blue wing of the resonance doublet. The blue wing displays a satellite feature brought about by $K - H_2$ quasi-molecular absorption that has previously been detected in the T dwarf $\epsilon$ Indi Ba (Allard et al. 2007a), and can be a useful diagnostic of temperature and metallicity (Allard et al. 2007b). Accurately modelling the optical spectrum requires taking into account the pressure broadened line shapes of other alkali metals such as Na and Li. Recently, Allard et al. (2019) presented improvements on the line shapes of the Na resonance doublet, finding a change in the blue wing of the doublet in the predicted emission spectra of self-luminous atmospheres. I am working to include these new Na resonance line shapes in ATMO, and future work to validate these improvements on the alkali opacity at red optical wavelengths must be undertaken.

### 7.2.3 Non-equilibrium chemistry

To model non-equilibrium chemistry due to vertical mixing, I consistently coupled the chemical relaxation scheme of Tsai et al. (2018) to ATMO, considering the non-equilibrium abundances of $H_2O$, CO, $CO_2$, $CH_4$, $N_2$ and $NH_3$. I adopted this relaxation scheme over a full kinetics network for computational efficiency and consistent convergence throughout the grid when solving for a self-consistent P–T profile. This relaxation scheme is more computationally efficient as it avoids the need to solve the large, stiff system of ordinary differential equations needed when using full chemical kinetics networks. Despite these advantages, the abundances obtained from chemical relaxation schemes are not always accurate, and can differ from those obtained from full chemical kinetics networks by up to

an order of magnitude (Tsai et al. 2018). Recent efforts have been made to develop reduced chemical kinetics networks which improve computational efficiency while maintaining accurate chemical abundance profiles (Venot et al. 2019). In future work, I will investigate the benefits of using such reduced chemical networks over the relaxation scheme used in the `ATMO` 2020 models.

Additionally, while I have considered the non-equilibrium abundances of the primary carbon- and nitrogen-bearing molecules with the relaxation scheme, future models should include additional species thought to be impacted by vertical mixing. Non-equilibrium signatures of HCN may become apparent in high-gravity objects with vigorous mixing (Zahnle & Marley 2014), and $PH_3$ and $GeH_4$, both of which are signatures of vertical mixing in Jupiter's atmosphere, as well as $C_2H_2$ and $CH_3D$, could impact the mid-infrared spectra of the coolest brown dwarfs (Morley et al. 2018). Furthermore, present chemical kinetics models do not consider condensate species. As such, the models essentially assume that mixing of species into the upper atmosphere happens on timescales much shorter than condensation timescales. Such an assumption is important for $H_2O$ and $NH_3$, which condense in the upper atmospheres of cool brown dwarfs in chemical equilibrium. Incorporating condensation timescales would involve combining kinetic cloud formation models such as the Helling & Woitke model (Woitke & Helling 2003, 2004; Helling & Woitke 2006; Helling et al. 2008) with a gas-phase chemical kinetics scheme. While this coupling is technically challenging and beyond the scope of this work, coupled gas-cloud kinetics models are required to correctly determine the abundances of $H_2O$ and $NH_3$, which are critical species governing the temperature structure and thermal emission from cool Y dwarf atmospheres.

### 7.2.4   Clouds and thermo-compositional convection

The most apparent example of shortcomings in the current `ATMO` 2020 models is the inability to reproduce the sharp change in near-infrared colors at the L-T transition and the red colors of cool late T dwarf objects. Currently, there are two competing theories on the physical process responsible for these observational features: clouds and thermo-compositional convection.

Including clouds in 1D atmosphere codes has been widely shown to reproduce the L-T transition and the red colors of late-T dwarfs through variations in cloud model parameterisations concerning, for example, the cloud sedimentation efficiency or cloud patchiness (Allard et al. 2001; Burrows et al. 2006; Saumon & Marley 2008; Marley et al. 2010; Morley et al. 2012, 2014b; Charnay et al. 2018). One such parametric cloud model widely used in the brown dwarf and exoplanet communities is the `EddySed` cloud formation code (Ackerman & Marley 2001), which has been applied to the L-T transition (Saumon & Marley 2008; Marley et al. 2010) and late-T dwarfs (Morley et al. 2012). The code has already been used within the Exeter Exoplanet Theory Group to study the fully coupled effects of clouds in 3-dimensional models of hot Jupiter atmospheres (Lines et al. 2019). Future work self-consistently coupling the `EddySed` code to `ATMO` is needed to account for the clouds expected to form in brown dwarf atmospheres, and to enable studies into the role of clouds throughout the cooling sequence.

Recently, a new theory has been developed suggesting that chemical transitions such as $CO/CH_4$ and $N_2/NH_3$ in brown dwarf atmospheres can be responsible for triggering 'thermo-compositional diabatic convection' (Tremblin et al. 2019). This may reduce the temperature gradient in the atmosphere reddening the emission spectrum without the need to invoke clouds. Reductions in the temperature gradient through the adiabatic index $\gamma_{\mathrm{eff}}$ have been shown to reproduce several observed features of brown dwarfs, including the L-T transition (Tremblin et al. 2016), extremely red low gravity objects (Tremblin et al. 2017b), and the red colors of cool late T dwarfs (Tremblin et al. 2015). Motivated by this, I aim to expand on the initial grid of atmosphere models presented here by reducing the temperature gradient through the effective adiabatic index $\gamma_{\mathrm{eff}}$. The key goal is to study and calibrate how thermo-compositional diabatic convection may evolve and influence the brown dwarf cooling sequence.

## 7.3 Concluding statement

The work I have presented in this thesis provides the tools required to place mass and age constraints on cool brown dwarfs and giant exoplanets, and characterise the complex chemistry and physics taking place in their atmospheres. The comparisons of the `ATMO`

2020 model set to observational datasets validates the modelling improvements presented in this work, and reinforces the need for continued development of atmosphere and evolution models. The `ATMO` 2020 model set will be particularly useful for the next generation of telescopes and instrumentation such as the *James Webb Space Telescope* (*JWST*) and ground-based extemely large telescopes, which will be transformative in our ability to detect and characterise the coldest brown dwarfs and directly imaged planets.

# Bibliography

Ackerman, A. S. & Marley, M. S. 2001, The Astrophysical Journal, 556, 872

Allard, F., Allard, N. F., Homeier, D., et al. 2007a, Astronomy and Astrophysics, 474, L21

Allard, F. & Hauschildt, P. H. 1995, ApJ, 445, 433

Allard, F., Hauschildt, P. H., Alexander, D. R., & Starrfield, S. 1997, ARA&A, 35, 137

Allard, F., Hauschildt, P. H., Alexander, D. R., Tamanai, A., & Schweitzer, A. 2001, The Astrophysical Journal, 556, 357

Allard, F., Homeier, D., & Freytag, B. 2012, Philosophical Transactions of the Royal Society of London Series A, 370, 2765

Allard, N. & Kielkopf, J. 1982, Reviews of Modern Physics, 54, 1103

Allard, N. F., Koester, D., Feautrier, N., & Spielfiedel, A. 1994, Astronomy and Astrophysics Supplement Series, 108, 417

Allard, N. F., Royer, A., Kielkopf, J. F., & Feautrier, N. 1999, Phys. Rev. A, 60, 1021

Allard, N. F., Spiegelman, F., & Kielkopf, J. F. 2007b, Astronomy and Astrophysics, 465, 1085

Allard, N. F., Spiegelman, F., & Kielkopf, J. F. 2016, Astronomy and Astrophysics, 589, A21

Allard, N. F., Spiegelman, F., Leininger, T., & Molliere, P. 2019, A&A, 628, A120

Allers, K. N. & Liu, M. C. 2013, The Astrophysical Journal, 772, 79

Amundsen, D. S. 2015, PhD thesis, University of Exeter

Amundsen, D. S., Baraffe, I., Tremblin, P., et al. 2014, Astronomy and Astrophysics, 564, A59

Amundsen, D. S., Tremblin, P., Manners, J., Baraffe, I., & Mayne, N. J. 2017, Astronomy and Astrophysics, 598, A97

Apai, D., Radigan, J., Buenzli, E., et al. 2013, ApJ, 768, 121

Artigau, É. 2018, Variability of Brown Dwarfs, 94

Artigau, É., Bouchard, S., Doyon, R., & Lafrenière, D. 2009, The Astrophysical Journal, 701, 1534

Asplund, M., Grevesse, N., Sauval, A. J., & Scott, P. 2009, Annual Review of Astronomy & Astrophysics, 47, 481

Baraffe, I., Chabrier, G., Allard, F., & Hauschildt, P. H. 1998, Astronomy and Astrophysics, 337, 403

Baraffe, I., Chabrier, G., Allard, F., & Hauschildt, P. H. 2002, A&A, 382, 563

Baraffe, I., Chabrier, G., Barman, T. S., Allard, F., & Hauschildt, P. H. 2003, Astronomy and Astrophysics, 402, 701

Baraffe, I., Homeier, D., Allard, F., & Chabrier, G. 2015, A&A, 577, A42

Barber, R. J., Strange, J. K., Hill, C., et al. 2014, Monthly Notices of the Royal Astronomical Society, 437, 1828

Barber, R. J., Tennyson, J., Harris, G. J., & Tolchenov, R. N. 2006, Monthly Notices of the Royal Astronomical Society, 368, 1087

Barman, T. S., Macintosh, B., Konopacky, Q. M., & Marois, C. 2011, ApJ, 733, 65

Basri, G., Marcy, G. W., & Graham, J. R. 1996, ApJ, 458, 600

Baudino, J. L., Bézard, B., Boccaletti, A., et al. 2015, A&A, 582, A83

Baudino, J.-L., Mollière, P., Venot, O., et al. 2017, The Astrophysical Journal, 850, 150

Beichman, C., Gelino, C. R., Kirkpatrick, J. D., et al. 2014, ApJ, 783, 68

Best, W. M. J., Liu, M. C., Magnier, E. A., et al. 2017, ApJ, 837, 95

Bézard, B., Lellouch, E., Strobel, D., Maillard, J.-P., & Drossart, P. 2002, , 159, 95

Biller, B. 2017, The Astronomical Review, 13, 1

Biller, B. A. & Bonnefoy, M. 2018, Exoplanet Atmosphere Measurements from Direct Imaging, 101

Biller, B. A., Crossfield, I. J. M., Mancini, L., et al. 2013, ApJL, 778, L10

Biller, B. A., Vos, J., Bonavita, M., et al. 2015, ApJL, 813, L23

Biller, B. A., Vos, J., Buenzli, E., et al. 2018, AJ, 155, 95

Bowler, B. P. 2016, PASP, 128, 102001

Bowler, B. P., Dupuy, T. J., Endl, M., et al. 2018, The Astronomical Journal, 155, 159

Brandt, T. D., Dupuy, T. J., Bowler, B. P., et al. 2019, arXiv e-prints, arXiv:1910.01652

Bueno, T. J. & Bendicho, F. P. 1995, ApJ, 455, 646

Buenzli, E., Apai, D., Morley, C. V., et al. 2012, ApJL, 760, L31

Buenzli, E., Marley, M. S., Apai, D., et al. 2015, The Astrophysical Journal, 812, 163

Burgasser, A. J., Geballe, T. R., Leggett, S. K., Kirkpatrick, J. D., & Golimowski, D. A. 2006, The Astrophysical Journal, 637, 1067

Burgasser, A. J., Kirkpatrick, J. D., Burrows, A., et al. 2003a, ApJ, 592, 1186

Burgasser, A. J., Kirkpatrick, J. D., Cutri, R. M., et al. 2000, ApJL, 531, L57

Burgasser, A. J., Kirkpatrick, J. D., Liebert, J., & Burrows, A. 2003b, ApJ, 594, 510

Burgasser, A. J., Marley, M. S., Ackerman, A. S., et al. 2002, The Astrophysical Journal, 571, L151

Burgasser, A. J., McElwain, M. W., Kirkpatrick, J. D., et al. 2004, AJ, 127, 2856

Burningham, B., Leggett, S. K., Homeier, D., et al. 2011, Monthly Notices of the Royal Astronomical Society, 414, 3590

Burningham, B., Smith, L., Cardoso, C. V., et al. 2014, MNRAS, 440, 359

Burrows, A., Burgasser, A. J., Kirkpatrick, J. D., et al. 2002, The Astrophysical Journal, 573, 394

Burrows, A., Hubbard, W. B., Lunine, J. I., & Liebert, J. 2001, Reviews of Modern Physics, 73, 719

Burrows, A. & Liebert, J. 1993, Reviews of Modern Physics, 65, 301

Burrows, A., Marley, M. S., Hubbard, W. B., et al. 1997, The Astrophysical Journal, 491, 856

Burrows, A., Marley, M. S., & Sharp, C. M. 2000, The Astrophysical Journal, 531, 438

Burrows, A. & Sharp, C. M. 1999, The Astrophysical Journal, 512, 843

Burrows, A., Sudarsky, D., & Hubeny, I. 2006, The Astrophysical Journal, 640, 1063

Burrows, A., Sudarsky, D., & Lunine, J. I. 2003, The Astrophysical Journal, 596, 587

Burrows, A. & Volobuyev, M. 2003, The Astrophysical Journal, 583, 985

Caffau, E., Ludwig, H. G., Steffen, M., Freytag, B., & Bonifacio, P. 2011, Solar Physics, 268, 255

Cardoso, C. 2012, PhD thesis, University of Exeter

Chabrier, G. & Baraffe, I. 1997, Astronomy and Astrophysics, 327, 1039

Chabrier, G. & Baraffe, I. 2000, ARA&A, 38, 337

Chabrier, G., Baraffe, I., Allard, F., & Hauschildt, P. 2000a, ApJL, 542, L119

Chabrier, G., Baraffe, I., Allard, F., & Hauschildt, P. 2000b, The Astrophysical Journal, 542, 464

Chabrier, G., Mazevet, S., & Soubiran, F. 2019, The Astrophysical Journal, 872, 51

Charnay, B., Bézard, B., Baudino, J. L., et al. 2018, ApJ, 854, 172

Cooper, C. S. & Showman, A. P. 2006, The Astrophysical Journal, 649, 1048

Crossfield, I. J. M., Biller, B., Schlieder, J. E., et al. 2014, Nature, 505, 654

Cruz, K. L., Kirkpatrick, J. D., & Burgasser, A. J. 2009, AJ, 137, 3345

Cushing, M. C., Hardegree-Ullman, K. K., Trucks, J. L., et al. 2016, ApJ, 823, 152

Cushing, M. C., Kirkpatrick, J. D., Gelino, C. R., et al. 2011, The Astrophysical Journal, 743, 50

Cushing, M. C., Marley, M. S., Saumon, D., et al. 2008, The Astrophysical Journal, 678, 1372

Cushing, M. C., Rayner, J. T., & Vacca, W. D. 2005, ApJ, 623, 1115

Cushing, M. C., Roellig, T. L., Marley, M. S., et al. 2006, ApJ, 648, 614

Cushing, M. C., Vacca, W. D., & Rayner, J. T. 2004, PASP, 116, 362

Cutri, R. M., Wright, E. L., Conrow, T., et al. 2013, Explanatory Supplement to the AllWISE Data Release Products, Tech. rep.

Dantona, F. & Mazzitelli, I. 1985, ApJ, 296, 502

De Rosa, R. J., Esposito, T. M., Hirsch, L. A., et al. 2019, AJ, 158, 225

Dieterich, S. B., Weinberger, A. J., Boss, A. P., et al. 2018, The Astrophysical Journal, 865, 28

Drummond, B. 2017, PhD thesis, University of Exeter

Drummond, B., Carter, A. L., Hébrard, E., et al. 2019, MNRAS, 486, 1123

Drummond, B., Mayne, N. J., Manners, J., et al. 2018, ApJ, 869, 28

Drummond, B., Tremblin, P., Baraffe, I., et al. 2016, Astronomy and Astrophysics, 594, A69

Dupuy, T. J. & Kraus, A. L. 2013, Science, 341, 1492

Dupuy, T. J. & Liu, M. C. 2012, The Astrophysical Journal, 201, 19

Dupuy, T. J. & Liu, M. C. 2017, ApJS, 231, 15

Dupuy, T. J., Liu, M. C., Best, W. M. J., et al. 2019, The Astronomical Journal, 158, 174

Edwards, J. M. 1996, Journal of the Atmospheric Sciences, 53, 1921

Edwards, J. M. & Slingo, A. 1996, Quarterly Journal of the Royal Meteorological Society, 122, 689

Epchtein, N., de Batz, B., Capoani, L., et al. 1997, The Messenger, 87, 27

Esplin, T. L., Luhman, K. L., Cushing, M. C., et al. 2016, ApJ, 832, 58

Faherty, J. K., Beletsky, Y., Burgasser, A. J., et al. 2014, ApJ, 790, 90

Faherty, J. K., Burgasser, A. J., Walter, F. M., et al. 2012, ApJ, 752, 56

Faherty, J. K., Rice, E. L., Cruz, K. L., Mamajek, E. E., & Núñez, A. 2013, AJ, 145, 2

Faherty, J. K., Riedel, A. R., Cruz, K. L., et al. 2016, ApJS, 225, 10

Fegley, B. J. & Lodders, K. 1996, Astrophysical Journal Letters v.472, 472, L37

Fernandes, C. S., Van Grootel, V., Salmon, S. J. A. J., et al. 2019, ApJ, 879, 94

Filippazzo, J. C., Rice, E. L., Faherty, J., et al. 2015, The Astrophysical Journal, 810, 158

Fortney, J. J. 2018, arXiv.org, arXiv:1804.08149

Freytag, B., Ludwig, H. G., & Steffen, M. 1996, A&A, 313, 497

Gagné, J., Allers, K. N., Theissen, C. A., et al. 2018, ApJL, 854, L27

Gagné, J., Burgasser, A. J., Faherty, J. K., et al. 2015, ApJL, 808, L20

Gagné, J., Faherty, J. K., Burgasser, A. J., et al. 2017, ApJL, 841, L1

Gardner, J. P., Mather, J. C., Clampin, M., et al. 2006, Space Sci. Rev., 123, 485

Garland, R. & Irwin, P. G. J. 2019, arXiv e-prints, arXiv:1903.03997

Geballe, T. R., Saumon, D., Golimowski, D. A., et al. 2009, The Astrophysical Journal, 695, 844

Geballe, T. R., Saumon, D., Leggett, S. K., et al. 2001, ApJ, 556, 373

Gierasch, P. J. & Conrath, B. J. 1985, Energy conversion processes in the outer planets., ed. G. E. Hunt, 121–146

Golimowski, D. A., Leggett, S. K., Marley, M. S., et al. 2004, AJ, 127, 3516

Gonzales, E. C., Faherty, J. K., Gagné, J., Artigau, É., & Bardalez Gagliuffi, D. 2018, ApJ, 864, 100

Goody, R., West, R., Chen, L., & Crisp, D. 1989, J. Quant. Spec. Radiat. Transf., 42, 539

Gordon, S. & McBride, B. J. 1994, Computer program for calculation of complex chemical equilibrium compositions and applications

Goyal, J. M. 2019, PhD thesis, University of Exeter

Goyal, J. M., Mayne, N., Drummond, B., et al. 2020, arXiv e-prints, arXiv:2008.01856

Goyal, J. M., Mayne, N., Sing, D. K., et al. 2018, Monthly Notices of the Royal Astronomical Society, 474, 5158

Goyal, J. M., Mayne, N., Sing, D. K., et al. 2019, MNRAS, 486, 783

Goyal, J. M., Wakeford, H. R., Mayne, N. J., et al. 2019, Monthly Notices of the Royal Astronomical Society, 482, 4503

Gustafsson, B., Edvardsson, B., Eriksson, K., et al. 2008, Astronomy and Astrophysics, 486, 951

Hauschildt, P. H., Allard, F., & Baron, E. 1999, ApJ, 512, 377

Hayashi, C. & Nakano, T. 1963, Progress of Theoretical Physics, 30, 460

Heiter, U., Lind, K., Asplund, M., et al. 2015, Phys. Scr, 90, 054010

Helling, C. & Casewell, S. 2014, The Astronomy and Astrophysics Review, 22, 80

Helling, C., Dehn, M., Woitke, P., & Hauschildt, P. H. 2008, The Astrophysical Journal, 675, L105

Helling, C. & Woitke, P. 2006, Astronomy and Astrophysics, 455, 325

Henyey, L., Vardya, M. S., & Bodenheimer, P. 1965, Astrophysical Journal, 142, 841

Hubeny, I. 2017, MNRAS, 469, 841

Joergens, V. 2014, 50 Years of Brown Dwarfs: From Prediction to Discovery to Forefront of Research, Vol. 401

John, T. L. 1988, A&A, 193, 189

Jones, H. R. A. & Tsuji, T. 1997, The Astrophysical Journal, 480, L39

Jose, J., Biller, B. A., Albert, L., et al. 2020, ApJ, 892, 122

Kellogg, K., Metchev, S., Heinze, A., Gagné, J., & Kurtev, R. 2017, ApJ, 849, 72

Kirkpatrick, J. D. 2005, ARA&A, 43, 195

Kirkpatrick, J. D., Gelino, C. R., Cushing, M. C., et al. 2012, The Astrophysical Journal, 753, 156

Kirkpatrick, J. D., Henry, T. J., & Donald W McCarthy, J. R. 1991, The Astrophysical Journal

Kirkpatrick, J. D., Henry, T. J., & Liebert, J. 1993, The Astrophysical Journal, 406, 701

Kirkpatrick, J. D., Looper, D. L., Burgasser, A. J., et al. 2010, The Astrophysical Journal Supplement Series, 190, 100

Kirkpatrick, J. D., Martin, E. C., Smart, R. L., et al. 2019, The Astrophysical Journal Supplement Series, 240, 19

Kirkpatrick, J. D., Reid, I. N., Liebert, J., et al. 1999, The Astrophysical Journal, 519, 802

Kitzmann, D., Heng, K., Oreshenko, M., et al. 2020, ApJ, 890, 174

Knapp, G. R., Leggett, S. K., Fan, X., et al. 2004, The Astronomical Journal, 127, 3553

Kumar, S. S. 1963, The Astrophysical Journal

Kupka, F., Zaussinger, F., & Montgomery, M. H. 2018, MNRAS, 474, 4660

Lacis, A. A. & Oinas, V. 1991, Journal of Geophysical Research, 96, 9027

Lazorenko, P. F. & Sahlmann, J. 2018, A&A, 618, A111

Leggett, S. K., Cushing, M. C., Hardegree-Ullman, K. K., et al. 2016, ApJ, 830, 141

Leggett, S. K., Dupuy, T. J., Morley, C. V., et al. 2019, arXiv e-prints, arXiv:1907.07798

Leggett, S. K., Morley, C. V., Marley, M. S., & Saumon, D. 2015, The Astrophysical Journal, 799, 37

Leggett, S. K., Morley, C. V., Marley, M. S., et al. 2013, The Astrophysical Journal, 763, 130

Leggett, S. K., Saumon, D., Marley, M. S., et al. 2012, The Astrophysical Journal, 748, 74

Leggett, S. K., Tremblin, P., Esplin, T. L., Luhman, K. L., & Morley, C. V. 2017, ApJ, 842, 118

Lew, B. W. P., Apai, D., Zhou, Y., et al. 2016, ApJL, 829, L32

Line, M. R., Marley, M. S., Liu, M. C., et al. 2017, ApJ, 848, 83

Line, M. R., Teske, J., Burningham, B., Fortney, J. J., & Marley, M. S. 2015, ApJ, 807, 183

Lines, S., Mayne, N. J., Manners, J., et al. 2019, MNRAS, 488, 1332

Linsky, J. L. 1969, ApJ, 156, 989

Liu, M. C., Dupuy, T. J., & Allers, K. N. 2016, The Astrophysical Journal, 833, 96

Liu, M. C., Leggett, S. K., & Chiu, K. 2007, ApJ, 660, 1507

Lodders, K. 1999, The Astrophysical Journal, 519, 793

Lodders, K. 2004, Science, 303, 323

Lodders, K. 2019, arXiv e-prints, arXiv:1912.00844

Lodders, K. & Fegley, B., J. 2006, Chemistry of Low Mass Substellar Objects, ed. J. W. Mason, 1

Lodieu, N. 2018, Metal-Depleted Brown Dwarfs, 173

Lodieu, N., Espinoza Contreras, M., Zapatero Osorio, M. R., et al. 2017, A&A, 598, A92

Lodieu, N., Zapatero Osorio, M. R., Béjar, V. J. S., & Peña Ramírez, K. 2018, MNRAS, 473, 2020

Lucas, P. W., Tinney, C. G., Burningham, B., et al. 2010, MNRAS, 408, L56

Luhman, K. L. 2014, The Astrophysical Journal Letters, 786, L18

Mace, G. N., Kirkpatrick, J. D., Cushing, M. C., et al. 2013, ApJ, 777, 36

Macintosh, B., Graham, J. R., Barman, T., et al. 2015, Science, 350, 64

Madhusudhan, N., Burrows, A., & Currie, T. 2011, ApJ, 737, 34

Malik, M., Grosheintz, L., Mendonça, J. M., et al. 2017, AJ, 153, 56

Malik, M., Kitzmann, D., Mendonça, J. M., et al. 2019, The Astronomical Journal, 170

Manjavacas, E., Apai, D., Zhou, Y., et al. 2019, AJ, 157, 101

Marley, M. S. & Robinson, T. D. 2015, Annual Review of Astronomy and Astrophysics, 53, 279

Marley, M. S., Saumon, D., Cushing, M., et al. 2012, The Astrophysical Journal, 754, 135

Marley, M. S., Saumon, D., Fortney, J. J., et al. 2017, in American Astronomical Society Meeting Abstracts, Vol. 230, American Astronomical Society Meeting Abstracts #230, 315.07

Marley, M. S., Saumon, D., & Goldblatt, C. 2010, The Astrophysical Journal Letters, 723, L117

Marley, M. S., Saumon, D., Guillot, T., et al. 1996, Science, 272, 1919

Marley, M. S., Seager, S., Saumon, D., et al. 2002, The Astrophysical Journal, 568, 335

Marocco, F., Andrei, A. H., Smart, R. L., et al. 2013, The Astronomical Journal, 146, 161

Marocco, F., Caselden, D., Meisner, A. M., et al. 2019, ApJ, 881, 17

Martin, E. C., Kirkpatrick, J. D., Beichman, C. A., et al. 2018, ApJ, 867, 109

Martin, E. L., Basri, G., Delfosse, X., & Forveille, T. 1997, A&A, 327, L29

Mayor, M. & Queloz, D. 1995, Nature, 378, 355

McBride, B. J., Gordon, S., & Reno, M. A. 1993, Coefficients for calculating thermodynamic and transport properties of individual species, Tech. rep.

McBride, B, J., Zehe, M, J., & Gordon, S. 2002, NASA Glenn Coefficients for Calculating Thermodynamic Properties of Individual Species, Tech. rep.

McGovern, M. R., Kirkpatrick, J. D., McLean, I. S., et al. 2004, ApJ, 600, 1020

McKay, C. P., Pollack, J. B., & Courtin, R. 1989, , 80, 23

McKemmish, L. K., Masseron, T., Hoeijmakers, H. J., et al. 2019, MNRAS, 488, 2836

McKemmish, L. K., Yurchenko, S. N., & Tennyson, J. 2016, Monthly Notices of the Royal
    Astronomical Society, 463, 771

Meisner, A. M., Caselden, D., Kirkpatrick, J. D., et al. 2020, ApJ, 889, 74

Metchev, S. A., Heinze, A., Apai, D., et al. 2015, ApJ, 799, 154

Mihalas, D. 1970, Stellar atmospheres

Miles, B. E., Skemer, A. J. I., Morley, C. V., et al. 2020, arXiv e-prints, arXiv:2004.10770

Mohanty, S. & Basri, G. 2003, ApJ, 583, 451

Morgan, W. W. & Keenan, P. C. 1973, ARA&A, 11, 29

Morley, C. V., Fortney, J. J., Marley, M. S., et al. 2012, The Astrophysical Journal, 756, 172

Morley, C. V., Marley, M. S., Fortney, J. J., & Lupu, R. 2014a, The Astrophysical Journal
    Letters, 789, L14

Morley, C. V., Marley, M. S., Fortney, J. J., et al. 2014b, The Astrophysical Journal, 787, 78

Morley, C. V., Skemer, A. J., Allers, K. N., et al. 2018, ApJ, 858, 97

Morley, C. V., Skemer, A. J., Miles, B. E., et al. 2019, ApJL, 882, L29

Moses, J. I., Visscher, C., Fortney, J. J., et al. 2011, ApJ, 737, 15

Nakajima, T., Oppenheimer, B. R., Kulkarni, S. R., et al. 1995, Nature, 378, 463

Nelson, L. A., Rappaport, S., & Chiang, E. 1993, ApJ, 413, 364

Nielsen, E. L., De Rosa, R. J., Macintosh, B., et al. 2019, AJ, 158, 13

Noll, K. S., Geballe, T. R., & Marley, M. S. 1997, The Astrophysical Journal, 489, L87

Oppenheimer, B. R., Kulkarni, S. R., Matthews, K., & Nakajima, T. 1995, Science, 270, 1478

Oppenheimer, B. R., Kulkarni, S. R., Matthews, K., & van Kerkwijk, M. H. 1998, The Astrophysical Journal, 502, 932

Parmentier, V., Showman, A. P., & Lian, Y. 2013, A&A, 558, A91

Phillips, C. L., Bowler, B. P., Mace, G., Liu, M. C., & Sokal, K. 2020a, ApJ, 896, 173

Phillips, M. W., Tremblin, P., Baraffe, I., et al. 2020b, Astronomy and Astrophysics, 637, A38

Plez, B. 1998, Astronomy and Astrophysics, 337, 495

Polyansky, O. L., Kyuberis, A. A., Zobov, N. F., et al. 2018, MNRAS, 480, 2597

Radigan, J. 2014, ApJ, 797, 120

Radigan, J., Jayawardhana, R., Lafrenière, D., et al. 2012, ApJ, 750, 105

Radigan, J., Lafrenière, D., Jayawardhana, R., & Artigau, E. 2014, ApJ, 793, 75

Rebolo, R., Martin, E. L., Basri, G., Marcy, G. W., & Zapatero-Osorio, M. R. 1996, ApJL, 469, L53

Rebolo, R., Martin, E. L., & Magazzu, A. 1992, The Astrophysical Journal

Rebolo, R., Osorio, M. R. Z., & Martin, E. L. 1995, Nature, 377, 129

Richard, C., Gordon, I. E., Rothman, L. S., et al. 2012, Journal of Quantitative Spectroscopy and Radiative Transfer, 113, 1276

Roellig, T. L., Van Cleve, J. E., Sloan, G. C., et al. 2004, ApJS, 154, 418

Rothman, L. S., Gordon, I. E., Babikov, Y., et al. 2013, Journal of Quantitative Spectroscopy and Radiative Transfer, 130, 4

Rothman, L. S., Gordon, I. E., Barber, R. J., et al. 2010, Journal of Quantitative Spectroscopy & Radiative Transfer, 111, 2139

Royer, A. 1971, Phys. Rev. A, 3, 2044

Rybicki, G. B. & Lightman, A. P. 1986, Radiative Processes in Astrophysics

Sahlmann, J., Burgasser, A. J., Gagliuffi, D. C. B., et al. 2020, MNRAS

Saumon, D., Chabrier, G., & van Horn, H. M. 1995, Astrophysical Journal Supplement v.99, 99, 713

Saumon, D., Geballe, T. R., Leggett, S. K., et al. 2000, The Astrophysical Journal, 541, 374

Saumon, D. & Marley, M. S. 2008, The Astrophysical Journal, 689, 1327

Saumon, D., Marley, M. S., Abel, M., Frommhold, L., & Freedman, R. S. 2012, The Astrophysical Journal, 750, 74

Saumon, D., Marley, M. S., Cushing, M. C., et al. 2006, ApJ, 647, 552

Saumon, D., Marley, M. S., Leggett, S. K., et al. 2007, The Astrophysical Journal, 656, 1136

Sauval, A. J. & Tatum, J. B. 1984, Astrophysical Journal Supplement Series (ISSN 0067-0049), 56, 193

Schlaufman, K. C. 2018, ApJ, 853, 37

Schneider, A. C., Cushing, M. C., Kirkpatrick, J. D., et al. 2015, ApJ, 804, 92

Sharp, C. M. & Burrows, A. 2007, The Astrophysical Journal Supplement Series, 168, 140

Skrutskie, M. F., Schneider, S. E., Stiening, R., et al. 1997, Astrophysics and Space Science Library, Vol. 210, The Two Micron All Sky Survey (2MASS): Overview and Status., ed. F. Garzon, N. Epchtein, A. Omont, B. Burton, & P. Persi, 25

Smart, R. L., Bucciarelli, B., Jones, H. R. A., et al. 2018, MNRAS, 481, 3548

Sousa-Silva, C., Al-Refaie, A. F., Tennyson, J., & Yurchenko, S. N. 2015, Monthly Notices of the Royal Astronomical Society, 446, 2337

Stephens, D. C., Leggett, S. K., Cushing, M. C., et al. 2009, The Astrophysical Journal, 702, 154

Tarter, J. C. 1975, PhD thesis, California Univ., Berkeley.

Tashkun, S. A. & Perevalov, V. I. 2011, Journal of Quantitative Spectroscopy and Radiative Transfer, 112, 1403

Tennyson, J. & Yurchenko, S. 2018, Atoms, 6, 26

Tennyson, J. & Yurchenko, S. N. 2012, MNRAS, 425, 21

Tennyson, J., Yurchenko, S. N., Al-Refaie, A. F., et al. 2016, Journal of Molecular Spectroscopy, 327, 73

Theissen, C. A. 2018, ApJ, 862, 173

Thomas, G. E. & Stamnes, K. 2002, Radiative Transfer in the Atmosphere and Ocean

Tinney, C. G. & Tolley, A. J. 1999, MNRAS, 304, 119

Tremblin, P., Amundsen, D. S., Chabrier, G., et al. 2016, The Astrophysical Journal, 817, L19

Tremblin, P., Amundsen, D. S., Mourier, P., et al. 2015, The Astrophysical Journal Letters, 804, L17

Tremblin, P., Chabrier, G., Baraffe, I., et al. 2017a, ApJ, 850, 46

Tremblin, P., Chabrier, G., Mayne, N. J., et al. 2017b, ApJ, 841, 30

Tremblin, P., Padioleau, T., Phillips, M. W., et al. 2019, ApJ, 876, 144

Triaud, A. H. M. J., Lanotte, A. A., Smalley, B., & Gillon, M. 2014, MNRAS, 444, 711

Tsai, S.-M., Kitzmann, D., Lyons, J. R., et al. 2018, ApJ, 862, 31

Tsai, S.-M., Lyons, J. R., Grosheintz, L., et al. 2017, ApJS, 228, 20

Tsuji, T. 2002, ApJ, 575, 264

Tsuji, T. & Nakajima, T. 2003, The Astrophysical Journal, 585, L151

Tsuji, T., Nakajima, T., & Yanagisawa, K. 2004, The Astrophysical Journal, 607, 511

Underwood, D. S., Tennyson, J., Yurchenko, S. N., et al. 2016, Monthly Notices of the Royal Astronomical Society, 459, 3890

van Leeuwen, F. 2007, A&A, 474, 653

Venot, O., Bounaceur, R., Dobrijevic, M., et al. 2019, A&A, 624, A58

Venot, O., Hébrard, E., Agúndez, M., et al. 2012, Astronomy and Astrophysics, 546, A43

Vos, J. M., Biller, B. A., Bonavita, M., et al. 2019, MNRAS, 483, 480

Wende, S., Reiners, A., Seifahrt, A., & Bernath, P. F. 2010, Astronomy and Astrophysics, 523, A58

Wilson, P. A., Rajan, A., & Patience, J. 2014, A&A, 566, A111

Witte, S., Helling, C., Barman, T., Heidrich, N., & Hauschildt, P. H. 2011, Astronomy and Astrophysics, 529, A44

Woitke, P. & Helling, C. 2003, Astronomy and Astrophysics, 399, 297

Woitke, P. & Helling, C. 2004, Astronomy and Astrophysics, 414, 335

Wright, E. L., Eisenhardt, P. R. M., Mainzer, A. K., et al. 2010, AJ, 140, 1868

Yang, H., Apai, D., Marley, M. S., et al. 2016, ApJ, 826, 8

Yang, H., Apai, D., Marley, M. S., et al. 2015, ApJL, 798, L13

York, D. G., Adelman, J., Anderson, John E., J., et al. 2000, AJ, 120, 1579

Yurchenko, S. N., Barber, R. J., & Tennyson, J. 2011, Monthly Notices of the Royal Astronomical Society, 413, 1828

Yurchenko, S. N., Mellor, T. M., Freedman, R. S., & Tennyson, J. 2020, MNRAS, 496, 5282

Yurchenko, S. N. & Tennyson, J. 2014, Monthly Notices of the Royal Astronomical Society, 440, 1649

Zahnle, K. J. & Marley, M. S. 2014, ApJ, 797, 41

Zalesky, J. A., Line, M. R., Schneider, A. C., & Patience, J. 2019, ApJ, 877, 24

Zapatero Osorio, M. R., Martín, E. L., Bouy, H., et al. 2006, ApJ, 647, 1405

Zhang, X. 2020, arXiv e-prints, arXiv:2006.13384

Zhang, X. & Showman, A. P. 2018, ApJ, 866, 2

Zhang, Z., Liu, M. C., Best, W. M. J., et al. 2018, ApJ, 858, 41

Zhang, Z., Liu, M. C., Hermes, J. J., et al. 2020, ApJ, 891, 171

Zhang, Z. H., Burgasser, A. J., Gálvez-Ortiz, M. C., et al. 2019, MNRAS, 486, 1260

Zhang, Z. H., Homeier, D., Pinfield, D. J., et al. 2017a, MNRAS, 468, 261

Zhang, Z. H., Pinfield, D. J., Gálvez-Ortiz, M. C., et al. 2017b, MNRAS, 464, 3040

Zhou, Y., Apai, D., Schneider, G. H., Marley, M. S., & Showman, A. P. 2016, ApJ, 818, 176